Accelerated Curing of Concrete with Microwave Energy

by

Thanakorn Pheeraphan

B.S., Virginia Military Institute
May 1991

S.M.C.E., Massachusetts Institute of Technology
August 1993

Submitted to the Department of Civil and Environmental Engineering
in partial fulfillment of the requirements for the degree of

Doctor of Philosophy

at the

MASSACHUSETTS INSTITUTE OF TECHNOLOGY

February 1997

Author .....
Department of Civil and Environmental Engineering
December 31, 1996

Certified by .....
Christopher K. Y. Leung
Assistant Professor,Department of Civil and Environmental Engineering
Thesis Supervisor

Accepted by .....
Joseph M. Sussman
Chairman, Departmental Committee on Graduate Studies

Accelerated Curing of Concrete with Microwave Energy

by

Thanakorn Pheeraphan

Submitted to the Department of Civil and Environmental Engineering
on December 31, 1996, in partial fulfillment of the
requirements for the degree of
Doctor of Philosophy

Abstract

A high rate of strength development in concrete can benefit several operations in the construction industry such as precast concrete fabrication and concrete pavement repair. Current approaches to accelerate rate of strength development are not very satisfactory. Steam curing techniques, which provide slow rate of heating and non-uniform hydration products, can take over one day to reach sufficient strength. With chemical accelerators or rapid hardening cements, concrete may face long term durability problems which are currently not well understood. Microwave curing technique which can provide high rate of strength development and uniform heating is an alternative.

In this study, determination of optimal process, which provides high strength at both early and later stages, is obtained with help of feedback temperature control. Strength of up to 5,100 psi is obtained for microwave cured concrete within 4.5 hours while its 7-day strength is the same as that of normally cured concrete. Then the effects of microwave on the performances of concrete with different additives (e.g., concrete with superplasticizer admixture and air-entrained concrete) are investigated.

Another major objective of this research is to develop and verify the numerical model which can simulate microwave curing of concrete. The numerical model, called microwave heating model, basically combines electromagnetic power dissipation and heat transfer models together in order to compute the temperature distribution inside the material during the curing process. The power dissipation model uses finite-difference time-domain technique to solve electric and magnetic fields in Maxwell's equation in order to determine the steady state dissipated power. To compute the dissipated power during microwave curing, the evolution of permittivity of heated concrete is to be established. The traditional maturity concept, which is used to estimate strength development based on thermal history and curing time, is therefore used and the permittivity-maturity relation can then be established within the specified range of curing temperature. Once the steady state dissipated power is obtained, the heat transfer model is used to compute the temperature inside the material. The microwave heating model is then verified by comparison with the experimental results. The developed model provides a tool for the design of microwave applicators for practical processes.

Thesis Supervisor: Christopher K. Y. Leung
Title: Assistant Professor,Department of Civil and Environmental Engineering

To my family,
with all my love.

Acknowledgment

I would like to express my sincere appreciation to Prof. Christopher K.Y. Leung for his kindness, intelligence advice, warmly support and encouragement throughout my study here. He is the kind of advisor who is always there when I need him. To work with him, it has always been special and enjoyable.

I am truly honored and grateful to have Prof. Oral Buyukozturk, Prof. Jin A. Kong of the Department of Electrical Engineering and Computer Science, and Dr. Robert Shin of M.I.T. Lincoln Laboratory, in my thesis committee. Thank you for your valuable suggestion, comments, and time. Special thanks to Prof. Jin A. Kong for giving me a knowledge in the area of Electromagnetics and for providing access to the network analyzer system and excellent computer resources.

To Dr. Neal Burk and Mr. Ray Henderson of the W.R. Grace & Co. in Cambridge, thank you for providing access to the freezing and thawing facilities. Special thanks to Mr. Ray Henderson for helpful discussions and technical assistance related to freezing and thawing measurement.

Without helps in preparing my test equipment by Arthur and Stephen Rudolph, who have been nice to me for many years, my labwork and experiments would not be possible. Thank you.

Many thanks go to friends in Electrical engineering department: to Sean Shih, Dr. Joel Johnson and Dr. M. Ali Tassoudji for helpful discussions and assistance related to the measurement of permittivity, to Dr. Kevin Li and Jerry Akerson for useful discussion on the Finite-Difference Time-Domain technique and to Kit Lai for administrative work.

My appreciation also goes to all of my friends who always cheer me up, write me, support me, and help me fight through obstacles. Among those whose names deserved to be mentioned are Taweesak Bunleusin, Yiping Geng, Somsak Kittipiyakul, Chanathip Namprempre, Roong Poshyananda, and Nutteerat Wutthicharoen.

My academic study is all well taken care of by the Royal Thai Air Force and all of funds for experimental works are provided by Prof. Christopher K.Y. Leung.

Finally, I am deeply indebted to my family who always sends me love and support. Thank you!

Contents

List of Figures

List of Tables

Chapter 1

Introduction

1.1 Motivation

A high rate of strength development in concrete can benefit several operations in the construction industry such as precast concrete fabrication and concrete pavement repair. Current approaches to accelerate rate of strength development are not very satisfactory. Steam curing techniques, which provide slow rate of heating and non-uniform hydration products, can take over one day to reach sufficient strength. With chemical accelerators or rapid hardening cements, concrete may face long term durability problems which are currently not well understood. According to our preliminary results in [35], microwave curing of concrete can provide high rate of strength development while its later strength is reasonably high. It is therefore promising to develop microwave curing technique for practical applications.

In reality, it is impossible to carry out experiments for specimens with all possible sizes and geometries. To better understand the microwave curing process and to develop ways to extrapolate laboratory results (on cylinders of a particular size) to practical specimens, numerical models need to be developed. In this thesis, a numerical model to simulate microwave curing of concrete is developed and verified. With the model, guidelines to process various specimens in microwave applicators of different designs could be established. Successful development of this technique can potentially result in breakthroughs in the precast concrete

fabrication and pavement repair operations.

1.2 Objectives

The main objectives of this research are

1. to determine the optimal process providing high compressive strength at early age (4.5 hour) without significantly impairing the later age strength (7 day)
2. to study the effects of microwave on the performance of concrete with different additives (e.g., concrete with superplasticizer admixture and air-entrained concrete)
3. to develop a numerical tool to simulate microwave curing of concrete
4. to verify the numerical model with experiments

At the end of this work, it is expected that a numerical tool will be available for the development of microwave curing technique for practical applications.

1.3 Approach

As the first step, an optimal process, which provides good combination of early age (4.5 hour) and later age (7 day) compressive strength, is determined. By using feedback temperature control, we try to identify optimal processes with high energy efficiencies.

Then the freeze-thaw durability of microwave-cured air-entrained concrete is studied. This is important to infra-structural applications where air entrainment has to be introduced to resist severe freeze-thaw attack.

To compute the dissipated power during microwave heating in the numerical model, it is important to know the actual evolution of permittivity of heated concrete. Because concrete evolves with time and the actual evolution of permittivity of heated concrete at microwave frequency is difficult to obtain, the traditional maturity concept, which is widely used in predicting the strength of concrete based on its thermal history and its current state, is applied.

The next step is to develop the microwave heating model to simulate microwave heating of concrete in particular. The complete model consists of (i) power dissipation model using well established finite-difference time-domain technique to compute steady state dissipated power, (ii) heat transfer model using explicit finite-difference scheme to compute temperature, and (iii) permittivity-maturity relation to update permittivity. Then the model results will be verified with experiments.

1.4 Outline of the Thesis

This thesis contains eight chapters.

Chapter 1 is the introduction chapter. It includes the motivation of this research, the objectives, and approach, as well as the organization of this thesis.

In Chapter 2, the determination of optimized microwave curing process is illustrated with the use of feedback temperature control. The background of strength development of normal-cured and microwave-cured concrete are reviewed. The experimental program and its results are then discussed in details. The optimal process of mortar is obtained first and that of concrete is found in similar manner. Then concrete with various additives are tested to identify their optimal processes.

Chapter 3 presents the freeze-thaw durability of microwave cured air-entrained concrete. The backgrounds of frost damage of hardened concrete, factors controlling frost resistance of hardened concrete, and calculation of durability factor of concrete are given for basic understanding of freeze-thaw durability of concrete. The experimental program is described and the results from compressive strength test, freeze-thaw test, air-void characteristics determination are presented. The effects of various parameters on the freeze-thaw durability of microwave-cured concrete are discussed.

In Chapter 4, the measurement of complex permittivity of concrete are explained. The setup and procedure are given. The results illustrated the validity of the measurement. The concept of maturity is described and used to establish the permittivity-maturity relation to represent the evolution of permittivity of heated concrete at microwave frequency. In the appendix, derivation for related equation and an example of permit-

tivity calculation are presented.

In Chapter 5, the power dissipation model using finite-difference time-domain(FDTD) to compute the steady state dissipated power during the microwave curing is covered. The FDTD algorithm is explained and the complete illustrations of treatments of element at every possible condition (i.e., in free space, dielectric material, boundary conditions, excitation source and etc.) in the numerical model are presented. Calculation of dissipated power and the condition to check for steady state are discussed. Then the model is verified by comparison of field values and dissipated power distribution with the analytical solution or available numerical results in the literature. In the appendix, the analytical solution used in comparison of field values is included. In addition, this chapter illustrates the implemented finite-difference equations for computer simulation.

Chapter 6 describes the heat transfer model which is used to compute temperature after the steady state dissipated power is determined. The transient heat diffusion equation and its related components are discussed. Again, the implemented finite-difference equations for computer simulation are included. Then, the verification of the model is shown. In the appendix, the stability analysis is included.

In Chapter 7, the overview of the complete model for microwave curing of concrete is shown clearly. The calibration of input power is described to relate the numerical model to experimental results. Then the model is verified with concrete by performing simulations of microwave curing of concrete at various microwave power levels and comparing model and experimental results.

Chapter 8 summarizes the major findings and highlights the main conclusion. Recommendations for future work are also included.

Chapter 2

Determination of Optimal Process

2.1 Introduction

High *early* strength development is the primary objective of this work because the distinct advantage of microwave curing is the gain in strength at the early stage which is important in several operations in concrete construction industry such as precast concrete fabrication and concrete pavement repairing. At present, the common ways to accelerate concrete hardening are (i) curing at elevated temperatures with or without steam and pressure and (ii) use of chemical accelerators or special cement compositions. Due to its slow rate of heating and non-uniform heating, steam curing is inferior to microwave curing which can provide higher rate of strength development and more uniform heating. With chemical accelerators or special cements, concrete may face long term durability problems which are presently not well understood. From our results on microwave-cured concrete, high compressive strength at early and later stage can be obtained [35]. Therefore, microwave curing is a promising technique to be developed for practical applications. In order to develop this accelerated curing technique for the practical applications, it is of importance to determine the optimal process to show its potential benefits.

This chapter includes (i) background of strength development of concrete under normal curing and microwave curing, (ii) experimental program, (iii) compressive strength results of mortar, concrete, concrete

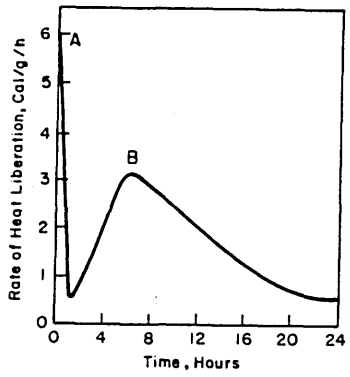

Figure 2-1: Heat liberation curve of a Portland cement paste at early time [Mehta, 1986]

with superplasticizer, and concrete with air-entrained admixture, (iv) splitting tensile strength result and photographs revealing pores and cracks of concrete, and (v) conclusion.

2.2 Background

2.2.1 Strength development of normal-cured concrete

In general, when a cement is hydrated, the heat of hydration data can be used to characterize its setting and hardening behavior. A typical plot of the heat liberation curve of a Portland cement paste is shown in Figure 2-1. The first peak (peak A) occurring a few minutes after mixing is largely due to the heat of solutions of aluminates from tricalcium aluminate and sulfates from gypsum [27]. Also, it corresponds to the formation of gelatinous colloidal coatings of hydration products around the cement grains [10]. Then, the heat liberation decreases rapidly as the solubility of aluminates is depressed due to the presence of sulfates in the solution [27].

At 4-8 hours after mixing, a rising of the second acceleration peak (peak B) represents the period of the final set (or beginning of hardening) which is accompanied by a high rate of strength development. This is mainly due to the growth of calcium silicate hydrate (C-S-H or a hydration product of calcium silicates) which in general provides most of the strength to concrete.

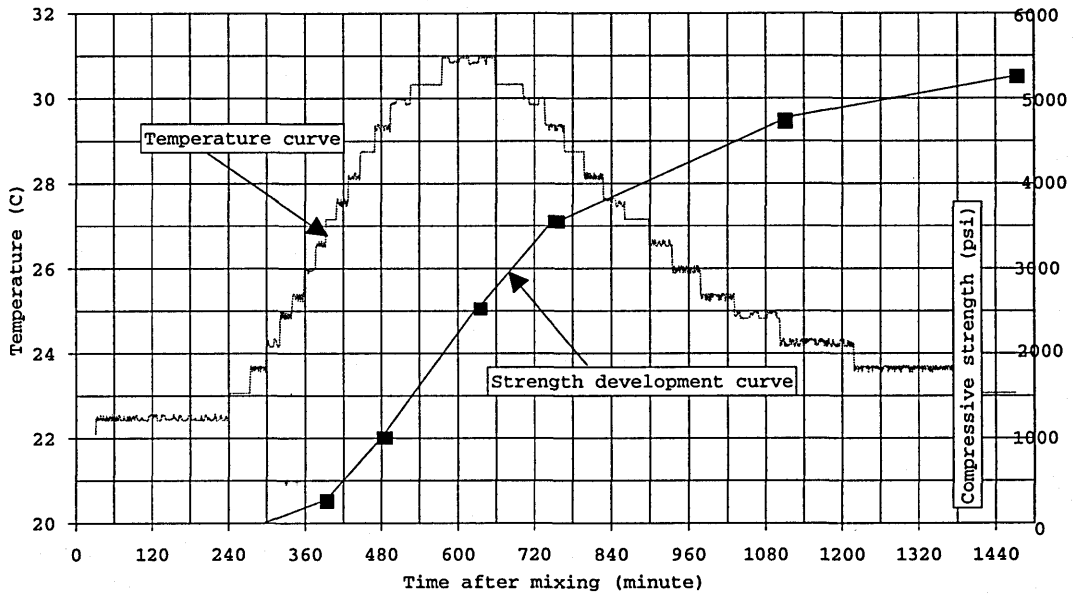

Figure 2-2: A graph of measured temperature versus time during the early hardening period of 0.40 w/c normal-cured concrete vs a graph of its strength development

To show the rate of strength development during the second peak period, the graph of measured temperature of 0.40 w/c normal-cured concrete during first 24 hours after mixing is plotted against the graph of its strength development as illustrated in Figure 2-2. It is clear that the second peak period correlates to the region where the rate of strength development is relatively high. Therefore, the specimen which is tested for strength a short while after reaching the second peak will have higher early strength than the one that is tested before or right at the peak. And, the early strength will be even higher if the specimen is allowed to go through the region of high strength development long enough before removal for capping and test. Note that once the temperature is reduced, the rate of strength development will become lower. Table 2.1 shows the result of its compressive strength over time. Apparently, the second acceleration period is very significant for strength development of concrete.

Table 2.1: The development of compressive strength of 0.40 w/c concrete under normal curing

Age (hour)	Compressive strength (psi)	7-day compressive strength (%)
0	0	0
8.0	1032.7	14.8
10.5	2571.2	36.9
12.5	3572.1	51.3
24.5	5234.4	75.2
168.0	6963.9	100

2.2.2 Strength development of microwave-cured concrete

Microwave, an electromagnetic wave with a wavelength of 1 mm - 1 m and a frequency range of 0.3 to 300 GHz, can be used as an energy source to heat dielectric materials composed of positive and negative poles. Water is an example of dielectric materials. When microwave transmits through a dielectric material, an internal electric field is generated inside the material, leading to a vibration or movement of the polar molecules to reduce the intensity of the electric field [45]. These movements are resisted by friction and inertial forces. Consequently, heat is generated and the temperature is elevated inside the material.

It is believed that the development of compressive strength due to microwave heating depends on two distinct effects:

1) Effect of accelerated cement hydration

2) Effect of increased porosity and microcracks

While microwave energy is being applied to the concrete specimen, the rate of cement hydration is accelerated because the increased curing temperature can shorten the induction period [16], which is the period during which the cement paste still remains in plastic state and there is very little hydration occurring, and can bring the second peak to occur at a much earlier time period. As a result, the rate of strength development at early age of microwave-cured concrete will be much faster than that of normal-cured concrete. Figure 2-3 shows an example of the curves of measured temperature during the early hardening period of 0.40

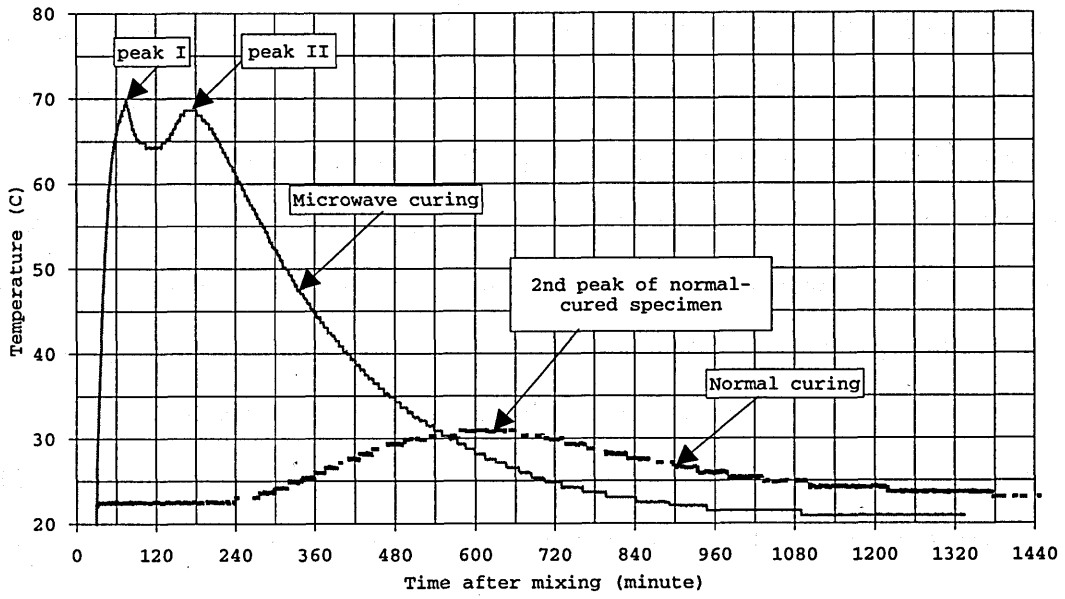

Figure 2-3: The curves of measured temperature versus time during the early hardening period of 0.40 w/c concrete under microwave curing and normal curing

w/c concrete under microwave curing and normal curing. For microwave curing, the initial peak (peak I) is mostly due to the application of microwave energy while the second peak (peak II) is owing to the cement hydration identical to the second peak of concrete under normal curing.

However, at later stage, the strength of specimens under microwave treatment can be lower than that of specimens under normal curing. This can be explained by the effect of increased porosity and microcracking which dominates the results at later age. During heating and maybe a short while afterwards, due to the difference in the thermal expansion coefficients of the concrete constituents (the thermal expansion coefficients of water and air are roughly 15 and 200 times, respectively, higher than that of the aggregate and the cement [18]), the greater expansion of water and air inside the specimen can result in an increase in both the porosity and the internal pressure, leading to the formation of microcracks inside the specimen. The strength at the later age of the treated specimens can therefore be less than the untreated ones. However, the later-age strength of microwave-cured specimen can be equal to or better than that of normal-cured specimen if the effect of increased porosity and microcracks is minimized.

Another important point is that before the application of microwave energy, it is essential for concrete to observe a substantial natural curing time in order to allow initial reaction of hydration involving dissolution of anhydrous cement constituents to their ionic forms into the solution; in other words, microwave energy should be applied at the beginning of the induction period of hydration. If concrete is not allowed to have sufficient initial reaction, quick precipitation of hydration products and rapid evaporation of water due to an elevated temperature can cause the formation of unfavorable hydrated products leading to a decrease in strength. An adverse effect will also be found if the application of microwave occurs after the structure of concrete has begun to form (or after the ionic mobility in the solution is restricted). It can be explained that since the structure of concrete has already formed, when microwave energy is applied, free water in the capillary pores can escape leaving behind partially empty voids. Consequently, the paste structure becomes more porous and strength is reduced. Therefore, to increase both early and later strength, differential expansion due to application of microwave energy should take place during the liquid/plastic stage so that the entrapped air can escape without any adverse effect and the excess water can be driven to the surface and get evaporated. When water evaporates, the concrete can densify as the capillary structure collapses.

The above statement is consistent with the works by Wu et al.[52] and Pheeraphan [35]. The permeability result by Wu et al. indicates that while microwave energy is applied to fresh concrete, its porosity is decreased due to the removal of water before setting resulting in the collapse of capillary voids and the densification of concrete. Additional result shows that when the starting times of microwave application are at 45 and 120 minutes after mixing, the 3-day compressive strength is decreased to 90% and 83% of the reference strength, which is the 3-day strength of the specimen with microwave energy applied right after mixing. The reduction of strength is explained by the fact that if microwave energy is applied after the network structure of concrete has already formed, porosity will not be reduced.

Similar results are obtained by Pheeraphan [35]. Using the 7-day strengths of normal-cured specimens as the baseline (100%) for each different delay time (defined as the time after water is mixed with cement), the 4.5-hour strengths of microwave-cured specimens whose delay times are 20, 30, and 61 minutes are 12.5%, 35.8%, and 29.3%, respectively. The corresponding values for 7-day strength are 69.5%, 70.3%, and 60.5%.

It is noticed that when the delay time is increased from 30 to 61 minutes, the strengths of microwave-cured specimens at both 4.5 hours and 7 days are decreased. The reduction of strength is due to the same reason described previously. In addition, Pheeraphan also observes that if fresh concrete is allowed to cure naturally for a substantial period of time before microwave application to have sufficient initial hydration, its early strength can be higher than that of the case where microwave energy is applied to fresh concrete right after mixing. It can be seen from the 4.5-hour results of specimens with 20- and 30-minute delay times that the former gains strength much slower than the latter at 4.5 hours while their 7-day strength in term of percentage are the same.

Therefore, it is important to experimentally determine the delay time in order to allow sufficient initial reaction of cement hydration while the concrete structure, that can restrict excess water to escape, has not begun to form yet.

Rate of heating is one of the most important factors on strength development of microwave-cured concrete. It can affect the occurrence of the second peak which is used to explain the gain of early strength. Based on the same explanation as described in the strength development of normal-cured concrete section, high early strength can be achieved if the specimen is removed for capping and test a short while after its second peak is reached. It can also be noted that the rate of heating affects not only the strength development at early age but later age. The effect will be discussed in a later section.

To conclude, the effect of accelerated cement hydration improves the early strength while in the long term, the adverse effect of increased porosity and internal microcracks becomes dominant and thus may reduce the later strength. The rate of heating as well as the location of the second acceleration peak are both significant factors for strength development of microwave-cured concrete.

2.3 Experimental Program

Preparation of material is first described, followed by the discussion of the feedback temperature control and its set-up. Then, the specimen preparation and curing process are explained.

2.3.1 Material preparation

Both mortar and concrete specimens are made with type III Portland cement but with different sources of sand. For mortar specimens, the cement/mortar sand ratio is fixed at 1:2. Mortar sand whose fineness modulus is 2.28 is supplied locally by B. Vitalini, Inc. from Milford in Massachusetts. For concrete specimens, the cement/Boston sand/pea gravel ratio is 1:1:1.5. Boston sand with 2.82 fineness modulus is obtained from Boston Sand and Gravel Co. while pea gravel is supplied from B. Vitalini, Inc.. Pea gravel is washed and dried in the conventional oven for one day. After 7 days in air, it is sieved to sizes between 0.371 inch (or 9.4 mm) and 0.093 inch (or 2.36 mm) before use.

WRDA-19 superplasticizer supplied by W.R. Grace & Co. is used to produce low w/c concrete. It is suggested by the supplier to add superplasticizer in a range of 6 to 20 fluid ounces per 100 lbs of cement. In the experiment, the ratio of 13.5 fluid ounces of WRDA-19 superplasticizer per 100 lbs of cement (or 4 grams of WRDA-19 per 1 lb. of cement) is used. It is added to the water before mixing.

To provide freeze-thaw resistance, Duravair-1000, a liquid air-entraining admixture supplied by W.R. Grace & Co., is used to produce air systems in concrete. Usually, air content should be in the range of 4-8% and can be produced with the typical addition rates range from 0.75 to 3 fluid ounces of Duravair-1000 per 100 lbs of cement (or 50 to 200 mL per 100 kg) as recommended by the supplier. The addition rate between this range is used in our experiments and the admixture is added to the water before mixing.

2.3.2 Feedback temperature control

In the experiments, a microwave oven model LBM1.2V fabricated by Cober Electronics, Inc. is employed. It can generate power at any level from 0 to 1200 watts. To achieve uniform heating, there are a mode stirrer and a turntable. In addition, the oven is supplied with a product temperature probe and an Analog Devices μMAC-1050 data acquisition system to monitor the internal temperature of the material and to allow the feedback control of microwave process. The probe should be inserted into the material so that the tip is positioned at the center. Figure 2-4 illustrates a configuration that protects the probe from concrete hardening and yet positions the tip at the center of the concrete.

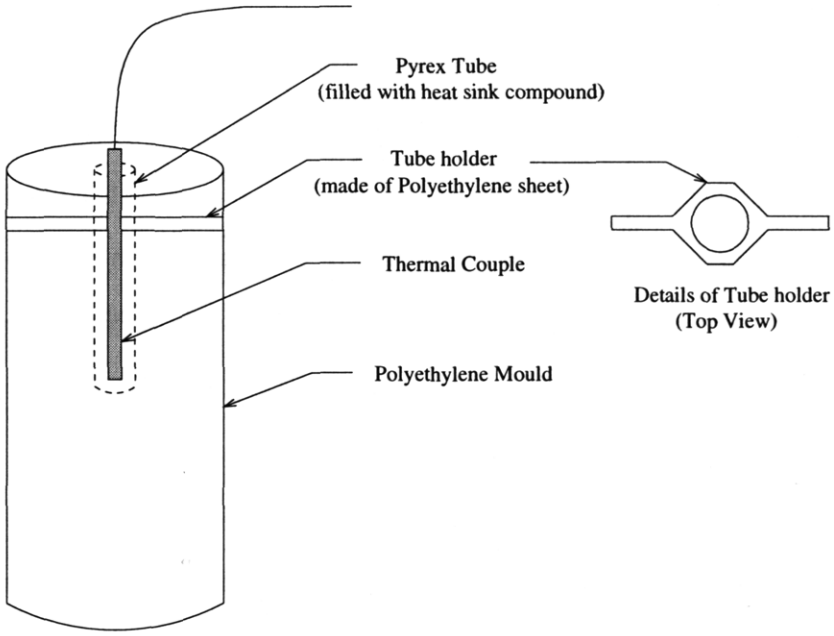

Figure 2-4: A polyethylene mould with temperature probe

The μMAC-1050 is installed with the RS-232 interface which can communicate data with the computer using the Labtech **Notebook** software. The analog signals sent to the μMAC-1050 from the devices, such as power and sample temperature, are converted to a digital format and can be collected by the computer via the interface and using the software. Therefore, the power and temperature can be measured and recorded. In addition, it is also possible to control the microwave power with the computer through the interface by setting up the analog output with the software.

The control process used with the Notebook is called Analog output closed-loop. It requires the input and output blocks. The input block is used to acquire the process data (input signal) from the controlled system to the Notebook while the output block is used to process this data through a control algorithm. A PID (Proportional-Integral-Derivative) algorithm is used to determine the output value based on the desired setup value. The output is then used to control the process. The sequences repeat until the end of the control.

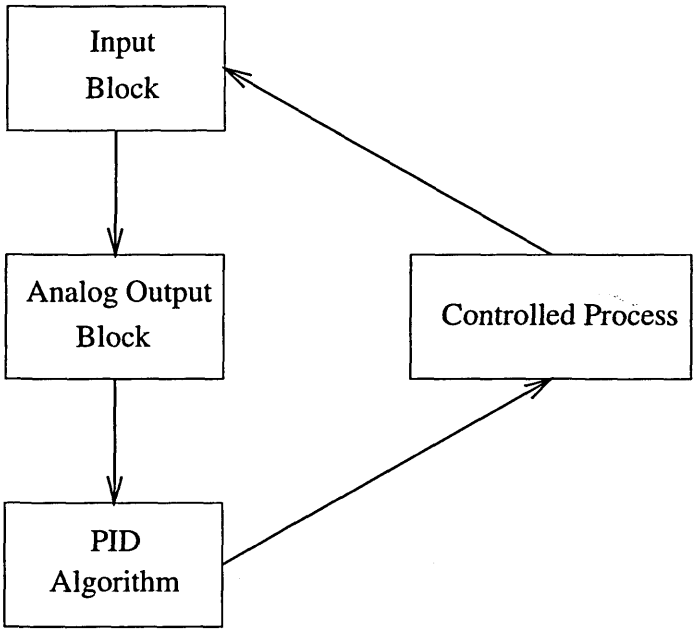

Figure 2-5: Analog PID output diagram [adapted from Labtech Notebook reference manual, 1992]

Figure 2-5 shows the Analog PID output diagram. The PID algorithm is shown below [21].

$$O(t) = P * e(t) + I * \int e(t')dt' + D * \frac{de}{dt}$$

where O(t) = output value,

e(t) = error (defined as desired setup value - input value),

P = Proportional constant,

I = Integral constant, and

D = Derivative constant

The values of P, I, and D determine the performance of the control. The steps to determine the optimum values of P, I, and D are listed in [21]. Because concrete is a complicated material, it is very difficult to determine the optimum P, I, and D values. For simplicity, we set I and D to zero and find the value of P which allows the cycle to approach equilibrium without overshooting the set point. From our initial work, the appropriate value of P is found to be 3. Thus, in this control process, P is set to 3 while I and D are set

to 0.

For the temperature control, the desired temperature will be set initially while the value of temperature at a particular moment will control the next microwave power level. The control algorithm will calculate the output value based on the desired temperature and the temperature at the moment. Then, the output value will be sent to control the microwave power to heat up the product. The setup value will be equal to the desired temperature divided by the scale factor of the product temperature which is 20°C per volt. Therefore, if the desired temperature is at 80°C, the setup value will be equal to 4.

In addition to setting the desired setup value to control the microwave power, it is also necessary to set the microwave percent power control which is located on the front panel of the microwave oven. The microwave percent power control is used as a power adjustment in manual control. In this work, when the microwave percent power control is set, for example to 50% or 600 watts, it will be referred to as "Max@600W." It is noted that even though the microwave percent power control is set to a certain value, the experimental results show the maximum power level does not agree with the set value. For example, if the microwave percent power control is set to 800 watts, the maximum power may turn out to be at 1200 watts instead. This is a limitation of the oven we employed.

2.3.3 Specimen preparation and curing process

Nine 3-inch by 6-inch specimens are casted in each batch. Six of them casted in polyethylene moulds are microwave-cured while the rests of them casted in plastic moulds are cured normally. To monitor the internal temperature, a probe is inserted in one of the microwave-cured specimens. In most of the mixing, thirty minutes after water is mixed with cement, sand and pea gravel, microwave energy is applied for 45 minutes unless indicated otherwise. The specimens except the one with the probe are then removed from the oven and covered with plastic sheets. At 3.5 hours after mixing, three microwave-cured specimens are removed from the moulds and capped for compression test at 4.5 hours. The rest of the specimens including the normal-cured specimens are then removed from the moulds after one day and cured in saturated-lime water at 23 ± 1.7°C (or 73.4 ± 3°F), according to ASTM C 192-90a, for 6 more days until testing.

For concrete with air-entraining admixture, nine 3-inch by 8-inch specimens are casted in each batch. Five of them are cured with the microwave energy. Temperature probe is not used in this experiment. To compare with the 14-days strength of normally cured concrete, the strength of microwave-cured concrete is measured at 4.5 hours and 14 days.

2.4 Results and Discussion

Mortar specimens with various heating rates are first investigated. Then, the trends identifying the optimal process for microwave-cured mortar specimens can be used to obtain the optimal process for microwave-cured concrete. After the optimal microwave process is determined for regular concrete, the investigation on the use of superplasticizer to obtain even higher early strength is performed. Lastly, concrete specimens with air-entraining admixture are investigated.

2.4.1 Mortar specimens

For mortar specimens with 0.50 w/c, five cases are investigated as follows:

- Case I: Constant power at 412 watts for 45 minutes
- Case II: Feedback temperature control at 60°C for 90 minutes (P=3 and "Max@600W")
- Case III: Feedback temperature control at 50°C for 20 minutes and at 80°C for 25 minutes (P=3 and "Max@800W" for both)
- Case IV: Feedback temperature control at 80°C for 45 minutes (P=3 and "Max@1200W")
- Case V: Constant power at 800 watts for 20 minutes and Feedback temperature control at 80°C for 25 minutes (P=3 and "Max@800W")

It should be noted that the 412-watt power used in Case I is the accurate value of power recorded in the computer when the dial on the oven is set to 400 watts. In earlier works ([35], [22] and [23]), this power level is referred to as 400 watts. To be more accurate, the value of 412 watts is used here.

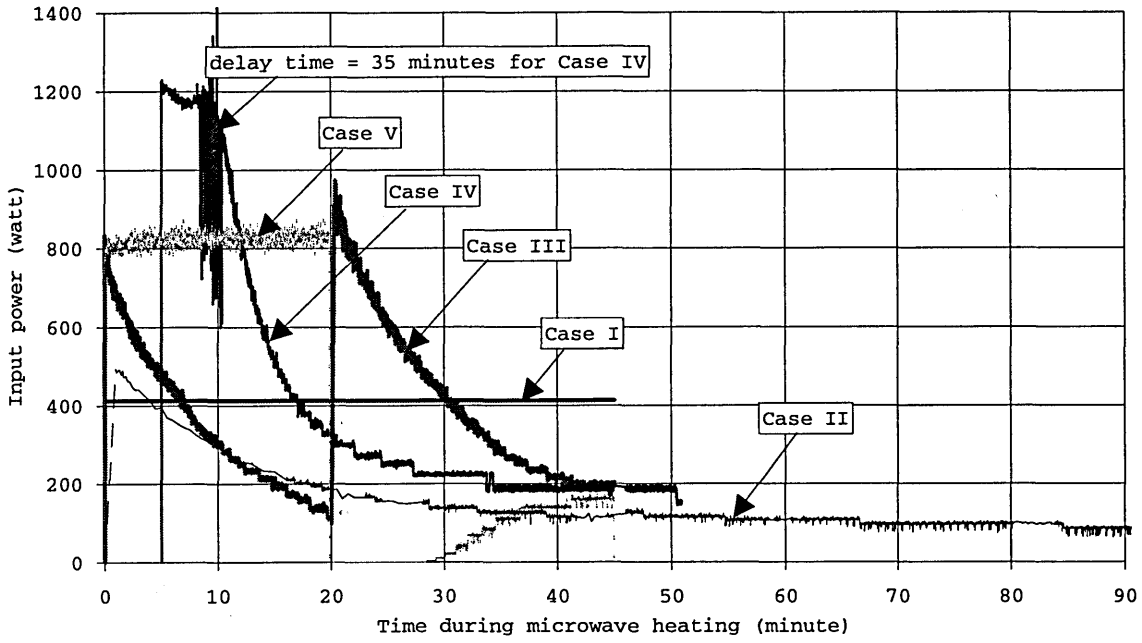

Figure 2-6: Power history plots for microwave-cured mortar specimens of Cases I, II, III, IV, and V (Time in x-axis = time during microwave processing)

Figure 2-6 shows the power histories of these cases while the plots of the measured temperature during and after microwave application are shown in Figure 2-7.

In Figure 2-7, the second peaks of Cases II, III, and IV occur at 45, 0, and -30 minutes after removal for capping, respectively. It is noted that -30 minutes *after* removal for capping means that 30 minutes *before* removing for capping. The temperature histories after microwave application of Cases I and V are not reported here because Case I is the optimal case for microwave process at a constant power [22] while the specimens in Case V are overheated.

The results of compressive strength at early and later stage of these cases are illustrated in Table 2.2 and Figure 2-8. It is clear that the results of Cases I and IV are similar but better than those of the others. The percent early strength gain of microwave-cured specimens of Case IV is higher than those of Cases II and III due to the fact that the second peak of Case IV occurs about 30 minutes before the time that the specimens are removed for capping which actually allows higher early strength development before the testing time. At

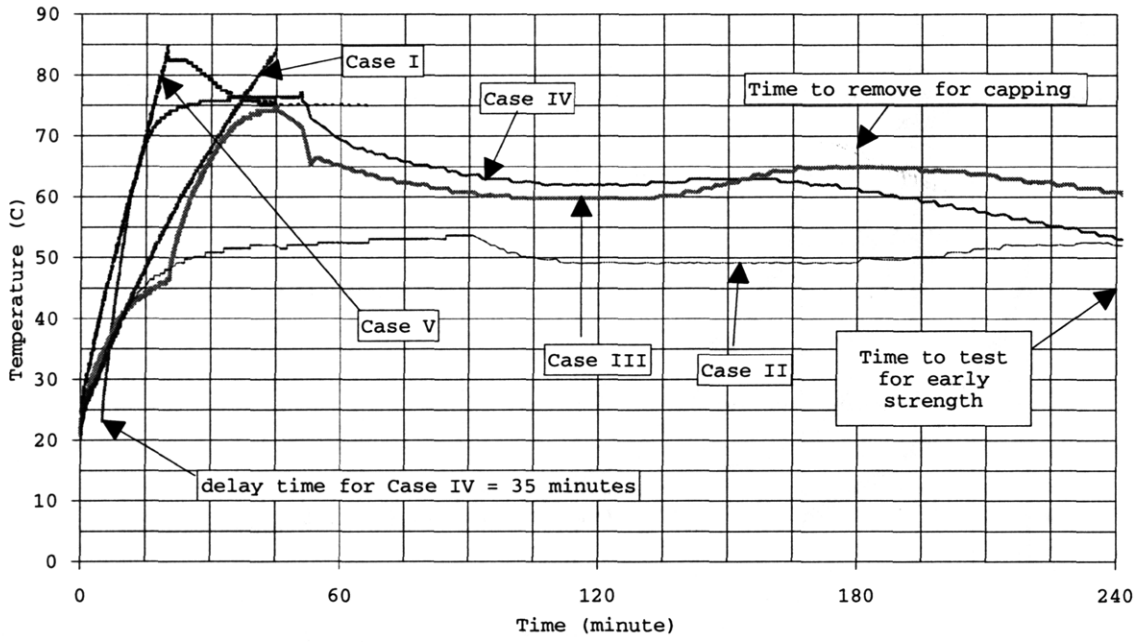

Figure 2-7: Temperature history plots for microwave-cured mortar specimens of Cases I, II, III, IV, and V (Time in x-axis = time during and after microwave processing)

later age, the strength development mostly depends on the rate of heating.

For Case V, its heating rate is so high that the rate of strength development is low. By examining the specimens visually, there are some expansions on the surfaces owing to the result of rapid heating at the beginning. If the specimens experience too high a temperature, it will result in low strength development due to the increased microcracks and pores. The results in Figure 2-7 show that temperature of 80°C or above is unfavorable to the strength development of the mortar specimens.

For comparison, the average powers during the 45-minute microwave process of Cases I and IV are 412 and 403 watts, respectively. It is clear that Case IV requires slightly less microwave energy than Case I; therefore, Case IV is the optimal case for microwave process of mortar with feedback temperature control and process with constant power level.

It is therefore important to highlight the findings from these *mortar* cases as follows:

Table 2.2: Results of the effect of heating rate on the compressive strength development (at 4.5 hours and 7 days) of 0.50 w/c mortar specimens under microwave curing for Cases I, II, II, IV, and V

Case #	W/C ratio by Wt before MCWC	Microwave Curing - MCWC				Normal Curing - NC	
		4.5 hours		7 days		7 days	
		Compr. Strength (psi)	NC 7-day Comp. Str. (%)	Compr. Strength (psi)	NC 7-day Comp. Str. (%)	Compr. Strength (psi)	NC 7-day Comp. Str. (%)
I	0.50	1874.5	30.0	4077.9	65.3	6242.5	100
II	0.50	709.7	11.1	5708.4	89.5	6380.3	100
III	0.50	1364.7	21.1	4583.7	71.0	6458.2	100
IV	0.50	1857.5	27.3	4808.8	70.7	6805.9	100
V	0.50	1374.6	21.2	2666.7	41.2	6468.8	100

- By allowing the appropriate time (in this experiment, around 30 minutes) for specimens to cure after reaching the second peak, high strength at early time can be obtained.
- The strength development can be interrupted enormously if the rate of heating is too high and if the internal temperature of specimen during the microwave heating is above 80°C.

2.4.2 Concrete specimens

For regular concrete, (i) the effect of heating rate (with temperature probe), (ii) the process with discrete power (with temperature probe), and (iii) the effect of temperature probe are investigated.

Effect of heating rate (with temperature probe)

To bring the findings from mortar to concrete, the feedback temperature control at 80°C for 45 minutes with "Max@412W" is employed (Case TCC1). Other cases (TCC2, TCC3 and TCC5). are also carried out for comparison. It is desirable to use "Max@412W" for Case TCC1 of concrete instead of "Max@800W" as Case IV of mortar because with "Max@800W", the maximum power is actually at 1200 watts which is believed to be too high for concrete microwave processing.

Case TCC2 is the process with constant power at 412 watts for 45 minutes while Case TCC3 uses the same power history obtained from Case TCC1 but reverse it before use (see Figure 2-9). Actually, the

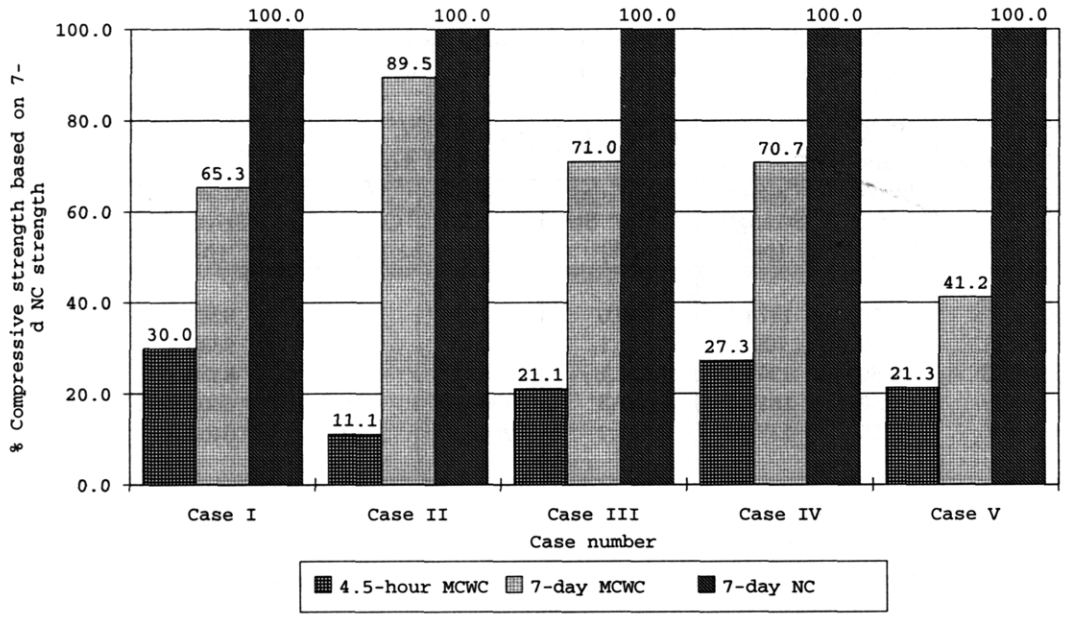

Figure 2-8: Results of the effect of heating rate on the compressive strength development (at 4.5 hours and 7 days) of 0.50 w/c mortar specimens under microwave curing for Cases I, II, III, IV, and V

average power during 45 minutes of microwave processing for Case TCC3 which is 321 watts is a little lower than that of Case TCC1 which is 336 watts because of the inaccuracy of the scale factor at the high power of the analog output for microwave power which is used to control microwave power. (Note: with the output data stored in an output file in the computer, the analog output device will convert it to analog format and send the signal to control the microwave power level.)

Case TCC5 uses the feedback temperature control at 85°C for 45 minutes with "Max@1200W" allowing higher rate of heating. The power histories for these cases are shown in Figure 2-9. Since the temperature probe has been used in all of these cases, the temperature histories during and after microwave heating can be plotted as illustrated in Figure 2-10.

In Table 2.3 and Figure 2-11, it is obvious that the result of Case TCC1 is better than those of Cases TCC3, and TCC5 but slightly better than that of Case TCC2. Its early (4.5 hours) and later (7 days) strength of microwave-cured specimens are as high as 59.1% and 94.9%, respectively, based on the 7-days strength of the normally cured specimens while those of Case TCC2 are 62.5% and 87.1%.

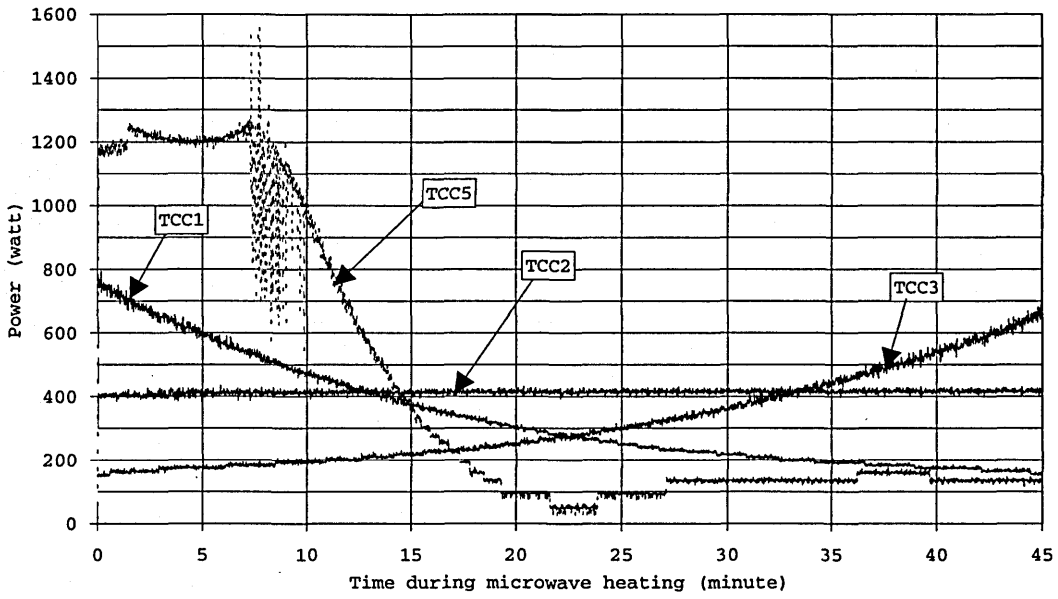

Figure 2-9: Power history plots for Cases TCC1, TCC2, TCC3, and TCC5 of 0.40 w/c microwave-cured concrete specimens (Time in x-axis = time during microwave processing)

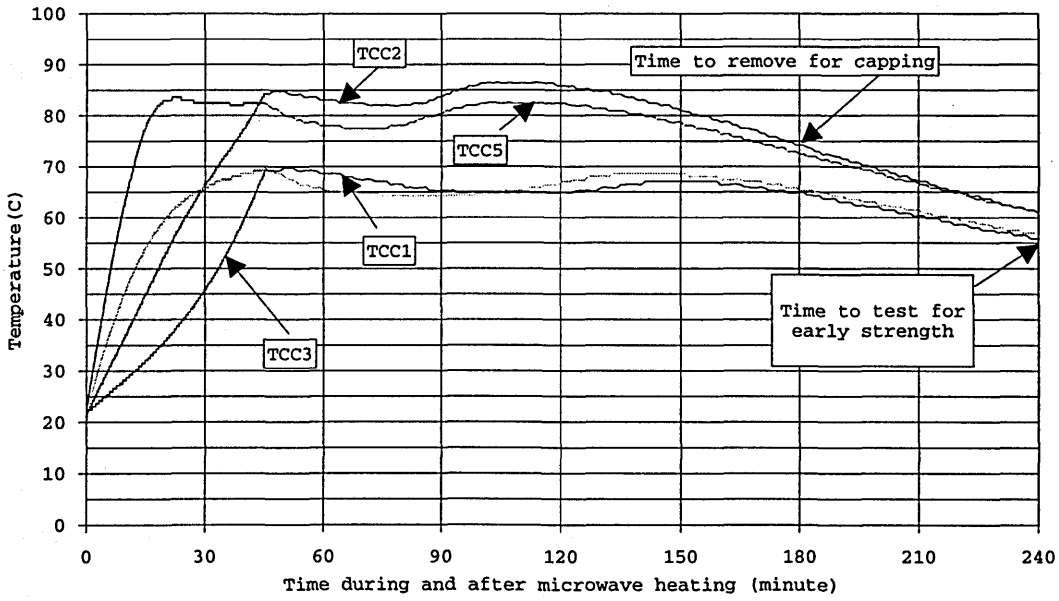

Figure 2-10: Temperature history plots for Cases TCC1, TCC2, TCC3, and TCC5 of 0.40 w/c microwave-cured concrete specimens (Time in x-axis = time during and after microwave processing)

Table 2.3: Results of the effect of heating rate on the compressive strength development of Cases TCC1, TCC2, TCC3, and TCC5

Case #	W/C ratio by Wt before MCWC	W/C ratio by Wt after MCWC	Microwave Curing - MCWC				Normal Curing - NC	
			4.5 hours		7 days		7 days	
			Compr. Str. (psi)	NC 7-day Comp. Str. (%)	Compr. Str. (psi)	NC 7-day Comp. Str. (%)	Compr. Str. (psi)	NC 7-day Comp. Str. (%)
TCC1	0.40	0.382	4083.2	59.1	6558.4	94.9	6911.0	100
TCC2	0.40	0.380	4272.4	62.5	5952.4	87.1	6833.2	100
TCC3	0.40	0.383	3785.5	52.9	6083.3	85.1	7149.6	100
TCC5	0.40	0.376	3532.1	50.4	4461.6	63.7	7006.4	100

Comparing Case TCC2 to Case TCC3 in Figure 2-10, it is clear that the heating rate of Case TCC2 is higher than that of Case TCC3. However, their later strength are the same while their early strength are different. The early strength of Case TCC2 is a little higher than that of Case TCC3 because the second peak of Case TCC2 occurs about 45 minutes before that of Case TCC3. Based on the 7-days normal-cured strength, the later strength development of Case TCC3 (from 52.9% at 4.5 hours to 85.1% at 7 days) is actually higher than that of Case TCC2 (from 62.5% at 4.5 hours to 87.1% at 7 days). This is because the effect of the excessive rate of heating of Case TCC2 leads to slower development of later strength. Figure 2-12 shows the strength development of Cases TCC1, TCC2, TCC3, and TCC5 compared to the strength development of 0.40 w/c normal-cured concrete.

For Case TCC5, the heating rate is too high that high early strength is obtained owing to the effect of accelerated cement hydration, but the later strength is impaired enormously due to the effect of the increased porosity and microcracks.

For comparison, the average powers during 45 minutes of microwave processing for Cases TCC1, TCC2, TCC3, and TCC5 are 336, 414, 321, and 419 watts, respectively. It is apparent that Case TCC1 requires about 20% less energy than Case TCC2 to obtain similar strength performance; therefore, Cases TCC1 is actually better than Case TCC2.

In conclusion, with economic and strength development considerations, Case TCC1 is considered to be

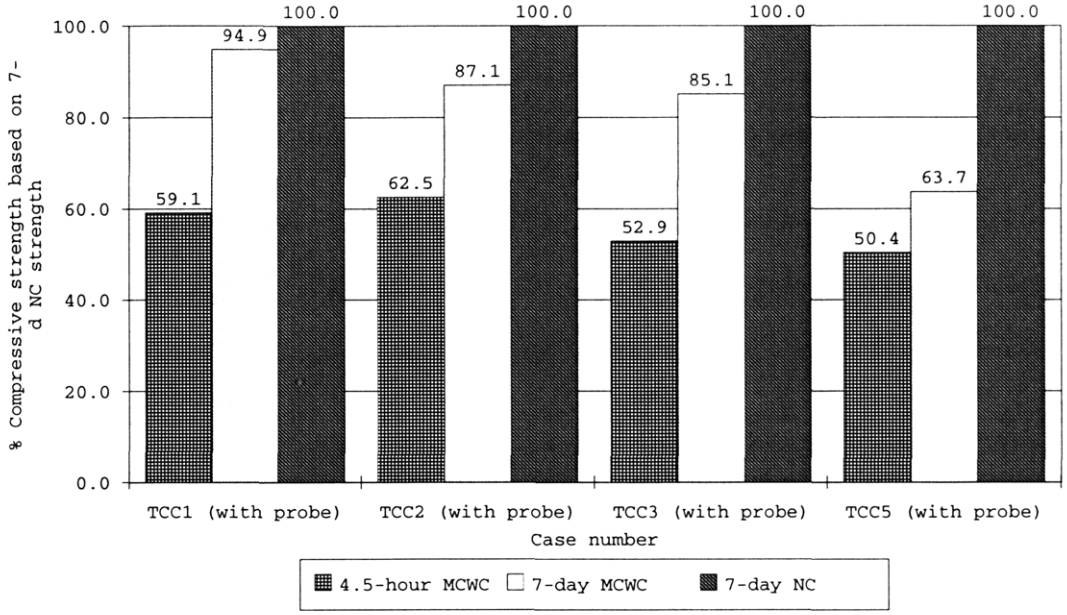

Figure 2-11: Results of the effect of heating rate on the compressive strength development of Cases TCC1, TCC2, TCC3 and TCC5

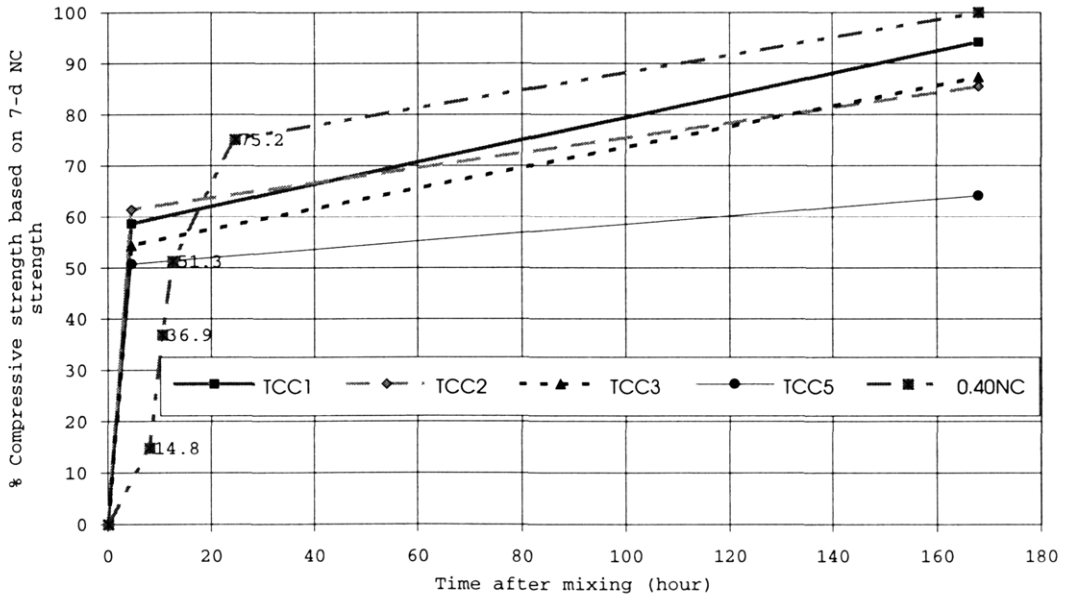

Figure 2-12: Compressive strength development of Cases TCC1, TCC2, TCC3, TCC5 and 0.40 w/c normal-cured concrete

the optimal case for microwave process with feedback temperature control and process with constant power levels.

Process with discrete power (with temperature probe)

After the optimal process is obtained from Case TCC1, process with discrete power levels obtained from discretization of continuous power history of Case TCC1 is investigated to simulate the power in the low cost kitchen microwave oven which is turned on and off for a different fractions of time to provide various discrete power levels.

The microwave heating patterns of Case TCC6 are (i) 800W(5M), standing for heating at 800 watts for 5 minutes, (ii) 412W(10M), (iii) 300W(10M), and (iv) 200W(20M). For TCC7, the microwave heating patterns are 675-550-450-350-300-250-200-150-100 watts for the heating duration of 5 minutes each. Figure 2-13 compares the power history of the optimal case (Case TCC1) to those of the discrete power cases (Cases TCC6 and TCC7). The average powers during 45 minutes of microwave process for Cases TCC1, TCC6, and TCC7 are 336, 338, and 337 watts, respectively. The difference in rate of heating among those cases can be seen from Figure 2-14 which shows the temperature histories during and after microwave processing. It is clear that the heating rate of Case TCC6 at the first 10 minutes is higher than those of Cases TCC1 and TCC7 and the second peaks of Cases TCC6 and TCC1 occur at the same time but before that of Case TCC7.

From the results in Table 2.4 and Figure 2-15, the strength both at early and later age of Cases TCC6 and TCC7 are comparable. Although the early strength of Case TCC1 is a little higher than those of both discrete power cases, Cases TCC6 and TCC7 are considered to simulate Case TCC1 well enough.

Effect of temperature probe

Since the temperature probe can reflect some microwave energy and affect the microwave process, to study the effect of temperature probe on the strength development, Case TCC16 (same power history as Case TCC6) and Case TCC8 (same power history as Case TCC7) are performed without the probes and compared with Case TCC6 and Case TCC7, respectively.

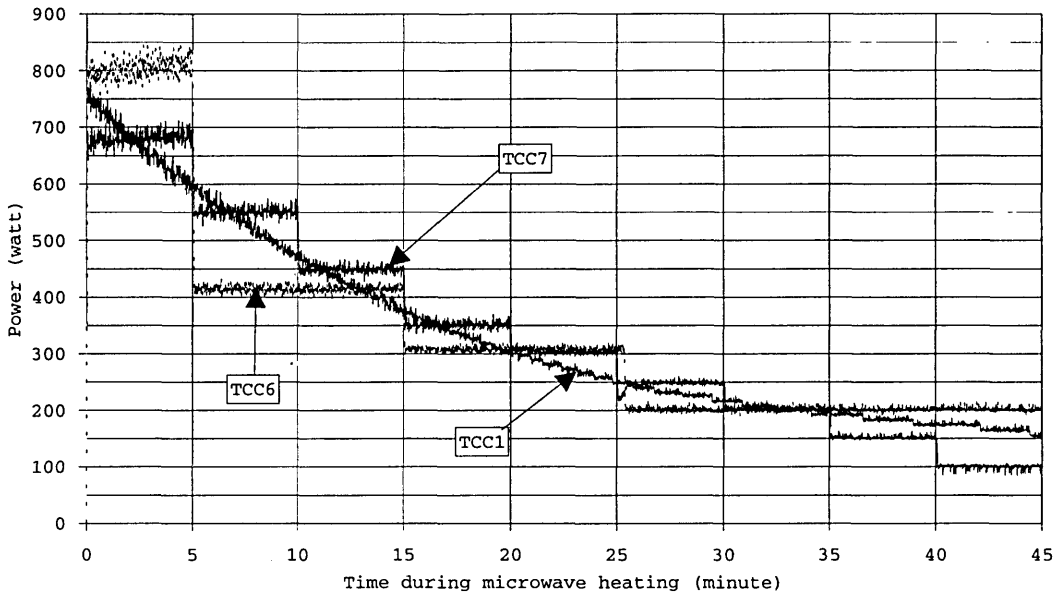

Figure 2-13: Power history plots for Cases TCC1, TCC6 and TCC7 of 0.40 w/c microwave-cured concrete specimens (Time in x-axis = time during microwave processing)

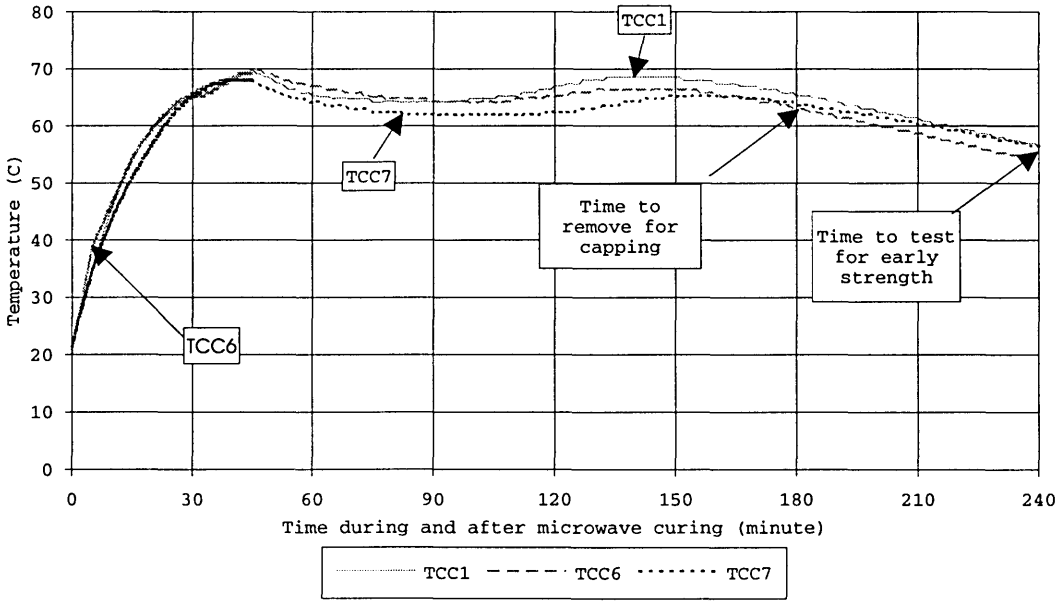

Figure 2-14: Temperature history plots for Cases TCC1, TCC6 and TCC7 of 0.40 w/c microwave-cured concrete specimens (Time in x-axis = time during and after microwave processing)

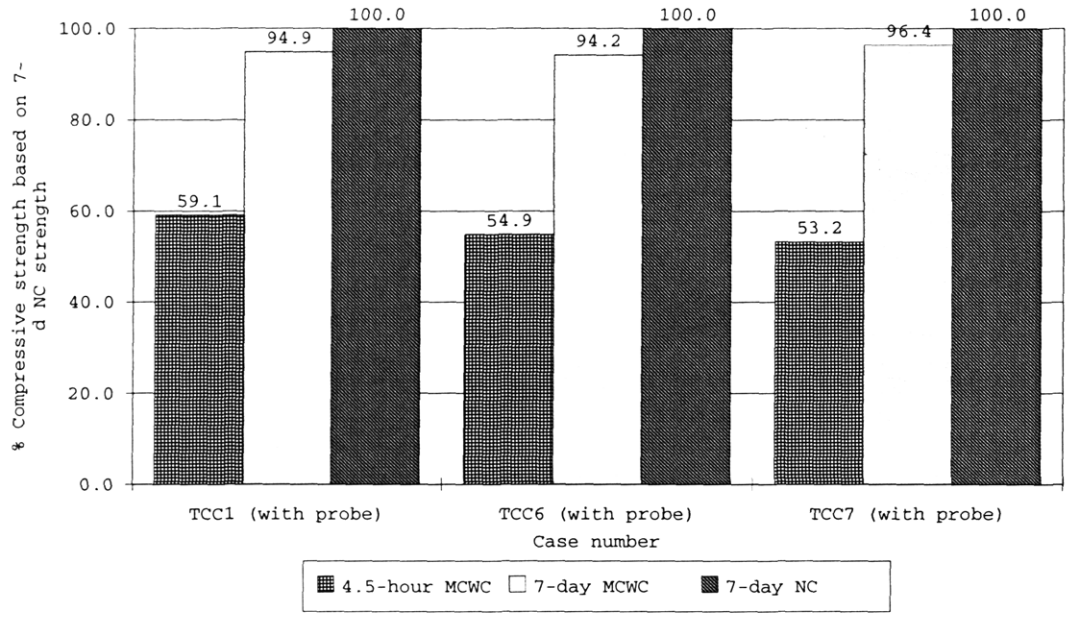

Figure 2-15: Results of the effect of discrete power levels on the compressive strength development of Cases TCC1, TCC6, and TCC7

Table 2.5 and Figures 2-16(a) and (b) show the effects of temperature probe on the strength development by considering Cases TCC16 versus TCC6 and Cases TCC8 versus TCC7, respectively. It is obvious that the early and later strength of Cases TCC16 and TCC8 are increased significantly because the heating is more uniform when the probes are not used.

To conclude, for the discrete power cases TCC6 and TCC7 without the probes (standing for Cases TCC16 and TCC8), results are slightly better than that of Case TCC1 where the probe is used.

2.4.3 Concrete specimens with superplasticizer

The results show that microwave curing can provide high early and later strength for low w/c ratio. Superplasticizer, called a high range water-reducer, is introduced into the mix to increase workability while using low w/c ratio. Therefore, fresh concrete with low w/c (such as 0.35 and 0.325) and superplasticizer is cured with microwave energy and then tested for the strength development. First, the effect of superplasticizer (with temperature probe) is studied. Secondly, process with discrete power is performed. Then, the optimal

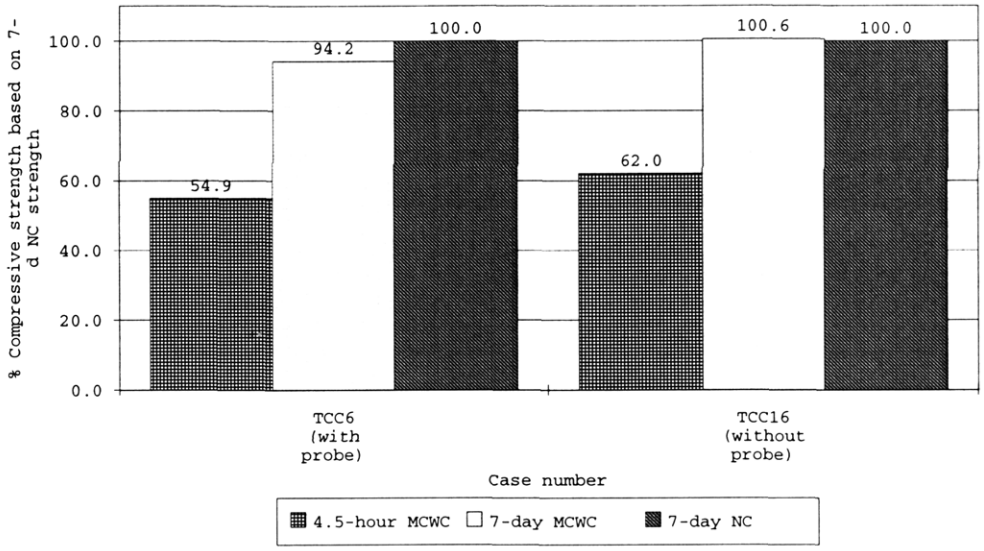

(a) Case TCC6 versus Case TCC16

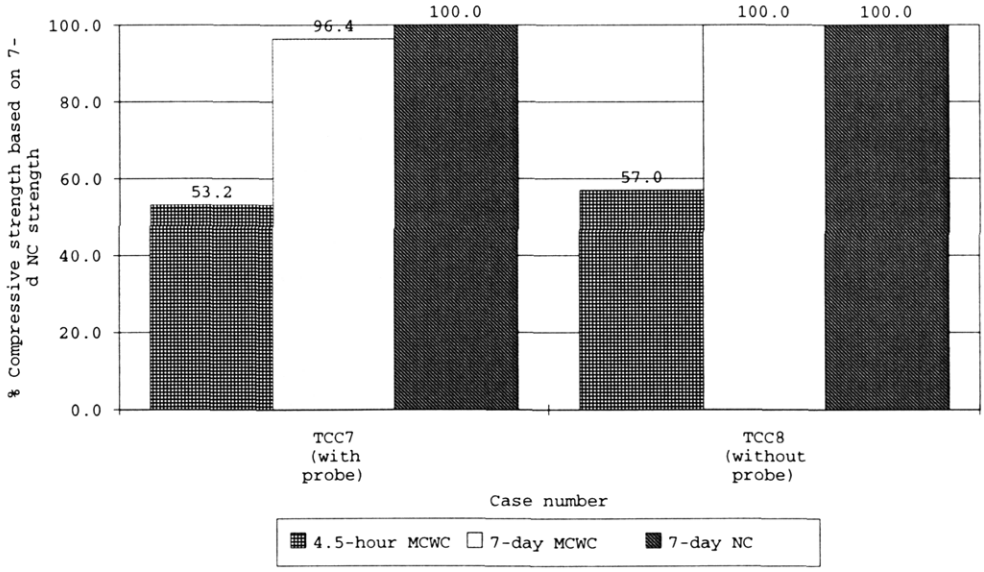

(b) Case TCC7 versus Case TCC8

Figure 2-16: Results of the effect of temperature probe on the compressive strength development

Table 2.4: Results of the effect of discrete power levels on the compressive strength development of Cases TCC1, TCC6, and TCC7

Case #	W/C ratio by Wt before MCWC	W/C ratio by Wt after MCWC	Microwave Curing - MCWC				Normal Curing - NC	
			4.5 hours		7 days		7 days	
			Compr. Str. (psi)	NC 7-day Comp. Str. (%)	Compr. Str. (psi)	NC 7-day Comp. Str. (%)	Compr. Str. (psi)	NC 7-day Comp. Str. (%)
TCC1	0.40	0.382	4083.2	59.1	6558.4	94.9	6911.0	100
TCC6	0.40	0.381	3792.6	54.9	6507.7	94.2	6912.0	100
TCC7	0.40	0.381	3659.4	53.2	6627.9	96.4	6873.1	100

Table 2.5: Results of the effect of temperature probe on the compressive strength development of concrete under microwave curing

Case #	W/C ratio by Wt before MCWC	W/C ratio by Wt after MCWC	Microwave Curing - MCWC				Normal Curing - NC	
			4.5 hours		7 days		7 days	
			Compr. Str. (psi)	NC 7-day Comp. Str. (%)	Compr. Str. (psi)	NC 7-day Comp. Str. (%)	Compr. Str. (psi)	NC 7-day Comp. Str. (%)
TCC6	0.40	0.381	3792.6	54.9	6507.7	94.2	6912.0	100
TCC16	0.40	0.381	4281.9	62.0	6953.3	100.6	6910.9	100
TCC7	0.40	0.381	3659.4	53.2	6627.9	96.4	6873.1	100
TCC8	0.40	0.381	4011.9	57.0	7035.8	100.0	7037.0	100

case is determined. Finally, the conclusion on the effect of water/cement ratio is obtained.

Effect of superplasticizer (with temperature probe)

Using the same temperature control process as in Case TCC1 (0.40 w/c without superplasticizer), Case TCC9 (0.35 w/c with superplasticizer) is processed and tested for strength. As a result, the power history of Case TCC9 is the same as that of Case TCC1. The results from Table 2.6 and Figure 2-17 illustrate that higher strength at both early and later age can be obtained with the use of low w/c with superplasticizer.

In Figure 2-18, it is apparent that the temperature histories during the microwave heating of Cases TCC1 and TCC9 are the same. However, the second acceleration peak of Case TCC9 occurs about 30 minutes after

Table 2.6: Results of the effect of superplasticizer on the compressive strength development of Cases TCC9 compared with Case TCC1

Case #	W/C ratio by Wt before MCWC	W/C ratio by Wt after MCWC	Microwave Curing - MCWC				Normal Curing - NC	
			4.5 hours		7 days		7 days	
			Compr. Str. (psi)	NC 7-day Comp. Str. (%)	Compr. Str. (psi)	NC 7-day Comp. Str. (%)	Compr. Str. (psi)	NC 7-day Comp. Str. (%)
TCC1	0.40	0.382	4083.2	59.1	6558.4	94.9	6911.0	100
TCC9	0.35	0.333	4653.2	58.1	7337.0	91.5	8014.4	100

that of Case TCC1 due to the effect of superplasticizer. The same effect can be seen in the normal curing condition. With the same 0.40 w/c normal-cured concrete, the second peak of the case with superplasticizer occurs about 30 minutes after that of the case without superplasticizer (Figure 2-19).

Despite the delay of the second acceleration period, the early strength of Case TCC9 is still high because its second peak occurs about 20 minutes before the time to remove specimens for capping.

Process with discrete power

As shown previously, Cases TCC1 and TCC9 experience the same power and temperature histories during the microwave heating. The same discrete power heating patterns used in the regular concrete from Cases TCC6 and TCC7 can be used for concrete with superplasticizer.

Since superplasticizer delays rising of the second peak, to accelerate the early strength development by shifting the second peak to occur earlier, applying high heating rate at the beginning as Case TCC6 is preferred. It is reminded that the heating rate of Case TCC6 at the first 10 minutes is higher than those of Cases TCC1 and TCC7 while the second peaks of Cases TCC6 and TCC1 occur at the same time but before that of Case TCC7. Moreover, it is believed that in the regular concrete and concrete with superplasticizer, the second peak of Case TCC6 without using the probe certainly occurs before that of Cases TCC1 with the probe and TCC7 without the probe.

Therefore, it is speculated that for concrete with superplasticizer, case simulating the discrete power of

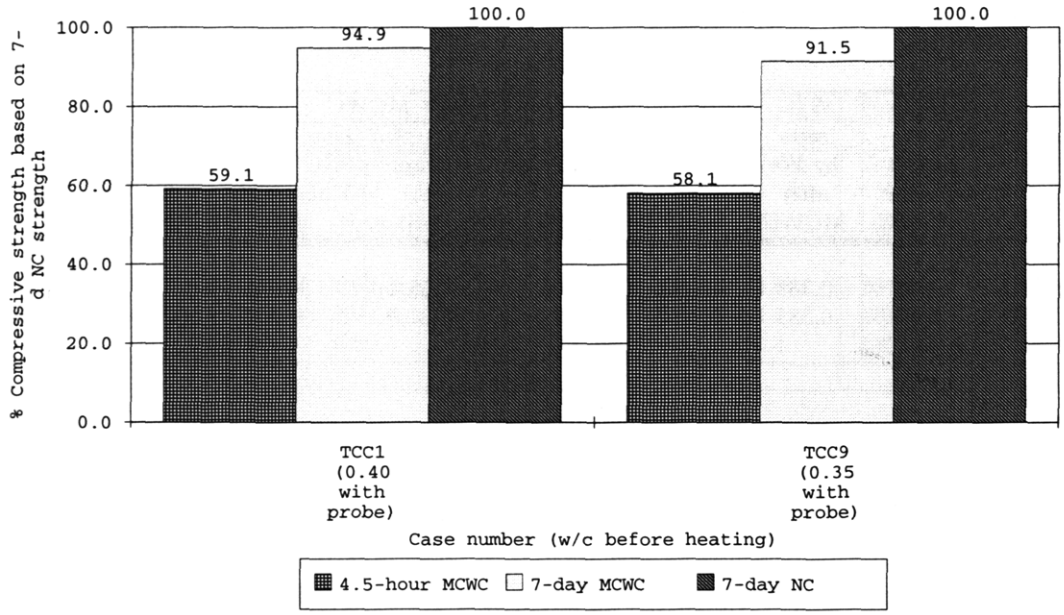

Figure 2-17: Results of the effect of superplasticizer on the compressive strength development of Case TCC9 compared with Case TCC1

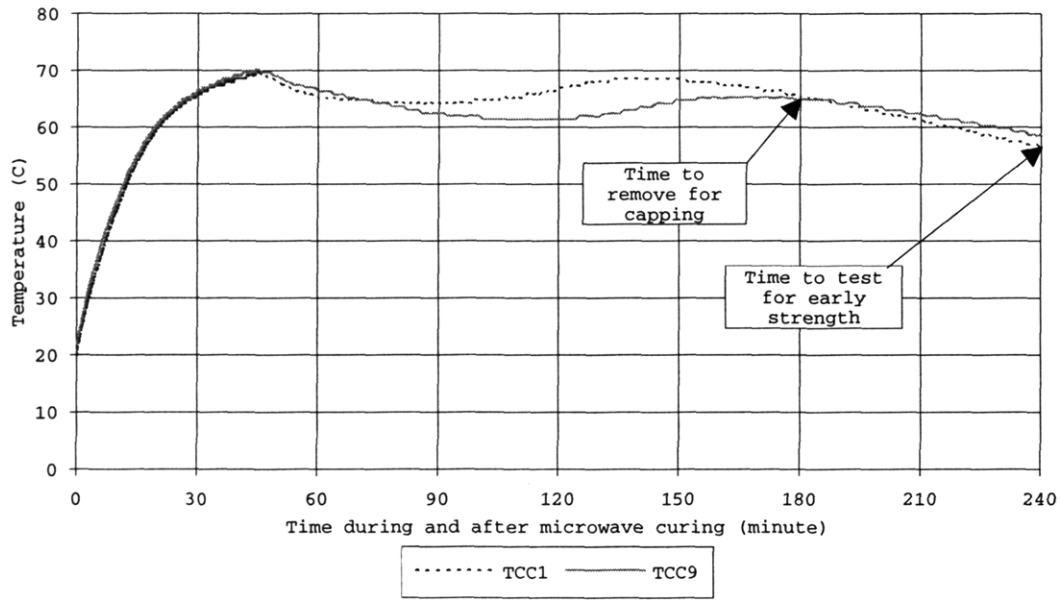

Figure 2-18: Temperature history plots for Cases TCC1 and TCC9 (Time in x-axis = time during and after microwave processing)

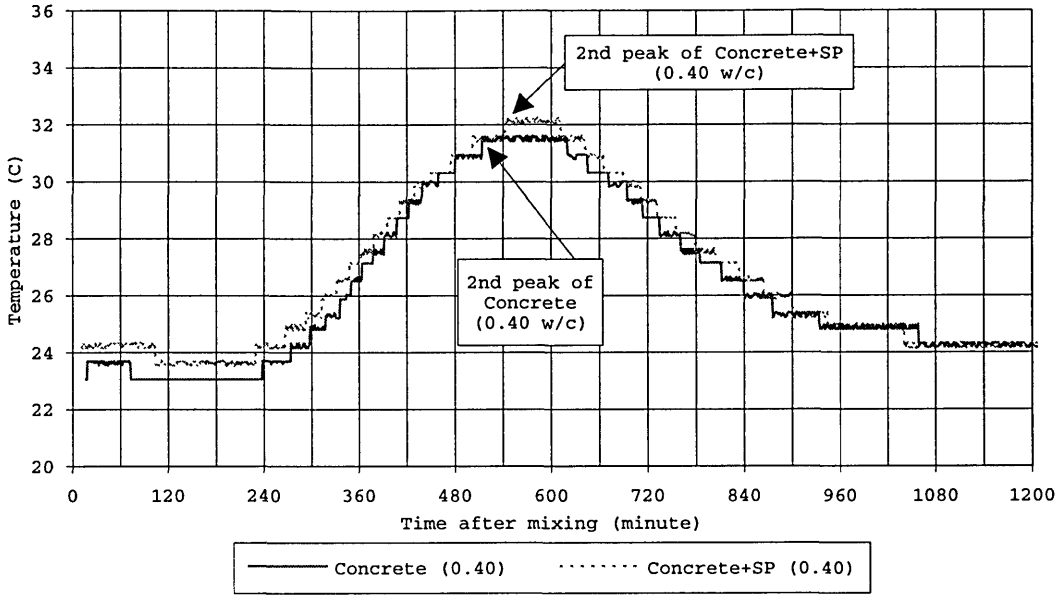

Figure 2-19: Comparison of the temperature history plots for normal curing case in the presence and absence of superplasticizer (Time in x-axis = time after water is mixed with the cement and aggregates)

Case TCC6 but without the probe will achieve better strength development than Case TCC9 with the probe and case simulating the power of Case TCC7 without the probe.

In the experiment, Case TCC12 (same power history as Case TCC7) and Case TCC13 (same power history as Case TCC6) are performed and compared to Case TCC9 (with a probe). As expected, the results in Table 2.7 and Figure 2-20 show that Case TCC13 not only gives the best early strength development but also later strength development. For Case TCC12, its early strength is much lower than that of Case TCC13. It is believed that the second peak of Case TCC12 occurs closer to the removal time than that of Case TCC13. In conclusion, Case TCC13 gives better results.

Optimal case

To further improve the early strength development, lower w/c is used while it is already known that the discrete power of Case TCC6 (with no probe) gives the optimal result. In the experiment, Case TCC10 (same power history as Case TCC7–lower heating rate) and Case TCC14 (same power history as Case

Table 2.7: Results of the effect of discrete power levels on the compressive strength development of Cases TCC9, TCC12, and TCC13

Case #	W/C ratio by Wt before MCWC	W/C ratio by Wt after MCWC	Microwave Curing - MCWC				Normal Curing - NC	
			4.5 hours		7 days		7 days	
			Compr. Str. (psi)	NC 7-day Comp. Str. (%)	Compr. Str. (psi)	NC 7-day Comp. Str. (%)	Compr. Str. (psi)	NC 7-day Comp. Str. (%)
TCC9	0.35	0.333	4653.2	58.1	7337.0	91.5	8014.4	100
TCC12	0.35	0.332	4165.6	54.5	7064.5	92.4	7645.6	100
TCC13	0.35	0.335	4705.1	61.4	8028.4	104.8	7662.2	100

TCC6–higher heating rate) with the same w/c ratio of 0.325 are performed and compared. The results in Table 2.8 and Figure 2-21 show that Case TCC14 gives higher strength at early and later age than Case TCC10.

Table 2.8: Results of the effect of heating rate on the compressive strength development of Cases TCC10 and TCC14

Case #	W/C ratio by Wt before MCWC	W/C ratio by Wt after MCWC	Microwave Curing - MCWC				Normal Curing - NC	
			4.5 hours		7 days		7 days	
			Compr. Str. (psi)	NC 7-day Comp. Str. (%)	Compr. Str. (psi)	NC 7-day Comp. Str. (%)	Compr. Str. (psi)	NC 7-day Comp. Str. (%)
TCC10	0.325	0.311	4422.1	51.7	8350.3	97.6	8551.4	100
TCC14	0.325	0.311	5128.8	61.6	8259.0	99.2	8322.2	100

Therefore, with use of the power history of Case TCC6, Case TCC14 (0.325 w/c concrete with 4 grams of superplasticizer admixture per 1 lb. of cement) is found to be the *best* case for microwave process with discrete power acting on concrete consisting of superplasticizer admixture. It can also be concluded that high heating rate at the beginning is preferred when superplasticizer is used because the superplasticizer delays the second acceleration period resulting in low early strength development.

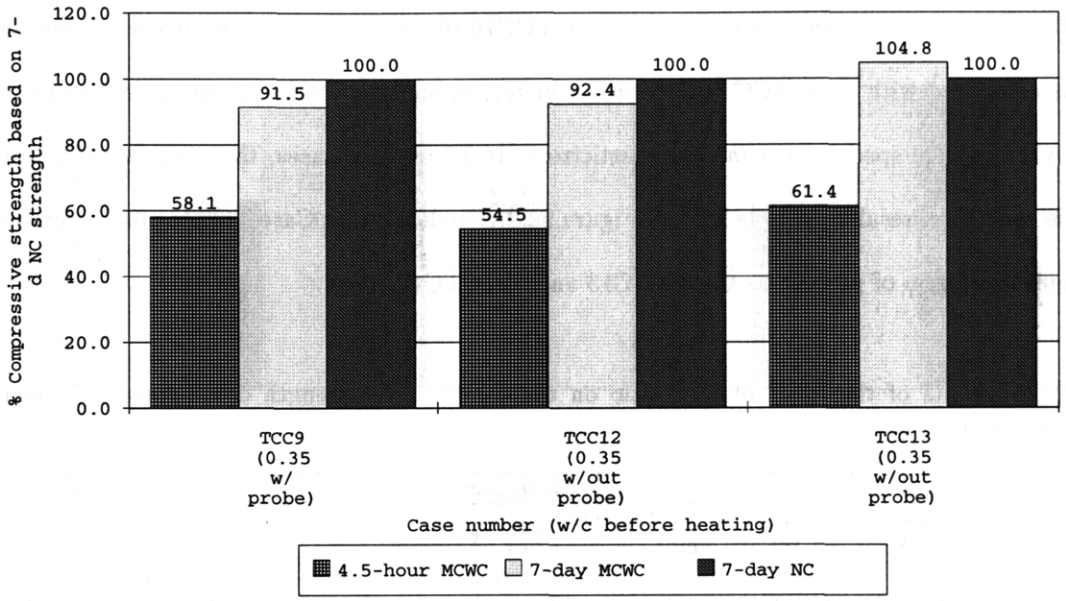

Figure 2-20: Results of the effect of discrete power levels on the compressive strength development of Cases TCC9, TCC12, and TCC13

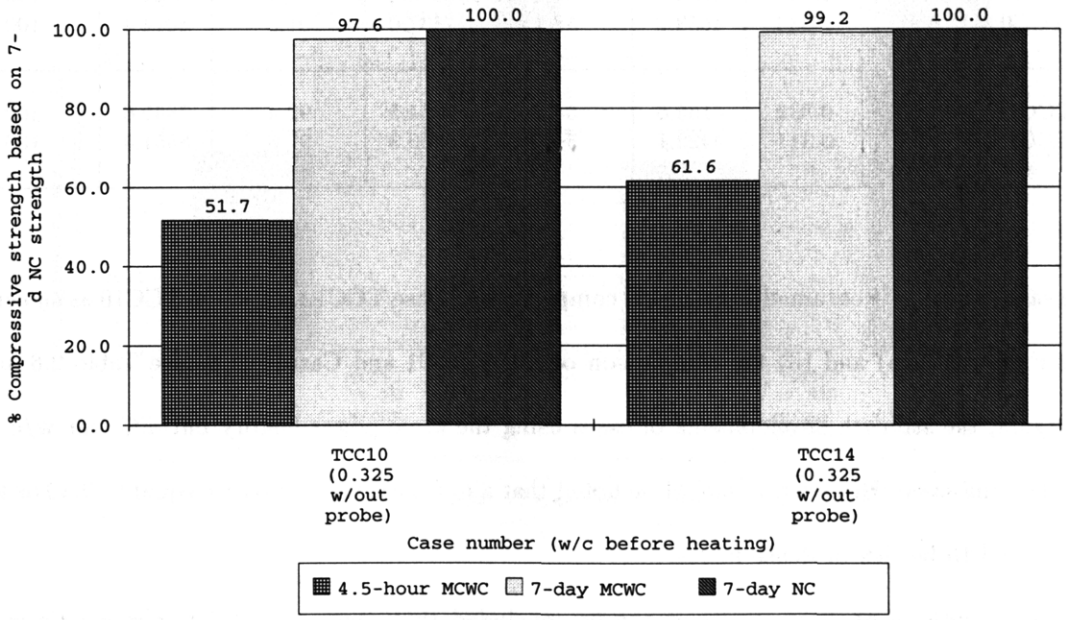

Figure 2-21: Results of the effect of heating rate on the compressive strength development of Cases TCC10 and TCC14

Effect of water/cement ratio

To further investigate the effect of w/c ratio, Case TCC16 (0.40 w/c concrete specimens *without* superplasticizer) is compared with Case TCC13 (0.35 w/c concrete specimens *with* superplasticizer) and Case TCC14 (0.325 w/c concrete specimens *with* superplasticizer). In all of these cases, the same power history as Case TCC6 is used. The results in Table 2.9 and Figure 2-22(a) indicate that Case TCC16 obtains similar strength development in term of percent as Case TCC13 and Case TCC14.

Table 2.9: Results of the effect of w/c ratio on the compressive strength development of concrete under microwave curing

Case #	W/C ratio by Wt before MCWC	W/C ratio by Wt after MCWC	Microwave Curing - MCWC				Normal Curing - NC	
			4.5 hours		7 days		7 days	
			Compr. Str. (psi)	NC 7-day Comp. Str. (%)	Compr. Str. (psi)	NC 7-day Comp. Str. (%)	Compr. Str. (psi)	NC 7-day Comp. Str. (%)
TCC16	0.40	0.381	4281.9	62.0	6953.3	100.6	6910.9	100
TCC13	0.35	0.335	4705.1	61.4	8028.4	104.8	7662.2	100
TCC14	0.325	0.311	5128.8	61.6	8259.0	99.2	8322.2	100
TCC1	0.40	0.382	4083.2	59.1	6558.4	94.9	6911.0	100
TCC9	0.35	0.333	4653.2	58.1	7337.0	91.5	8014.4	100
TCC12	0.35	0.332	4165.6	54.5	7064.5	92.4	7645.6	100
TCC10	0.325	0.311	4422.1	51.7	8350.3	97.6	8551.4	100

The same results are obtained from (i) the comparison of Case TCC12 and Case TCC10 as shown in Table 2.9 and Figure 2-22(b) and (ii) the comparison of Case TCC1 and Case TCC9 (see Table 2.6 and Figure 2-17). Again, the strength developments of cases using the same power history but different w/c ratios are more or less the same. However, it should be noted that all of these w/c ratios are equal to 0.40 or less which are considered to be rich or dense mixes.

Therefore, with all of these results, it can be concluded that concrete with lower w/c ratio responds to microwave curing well. And it seems that use of superplasticizer does not cause any significant increase or decrease in the percent gain of the strength. One plausible explanation for this is that concrete with dense mix

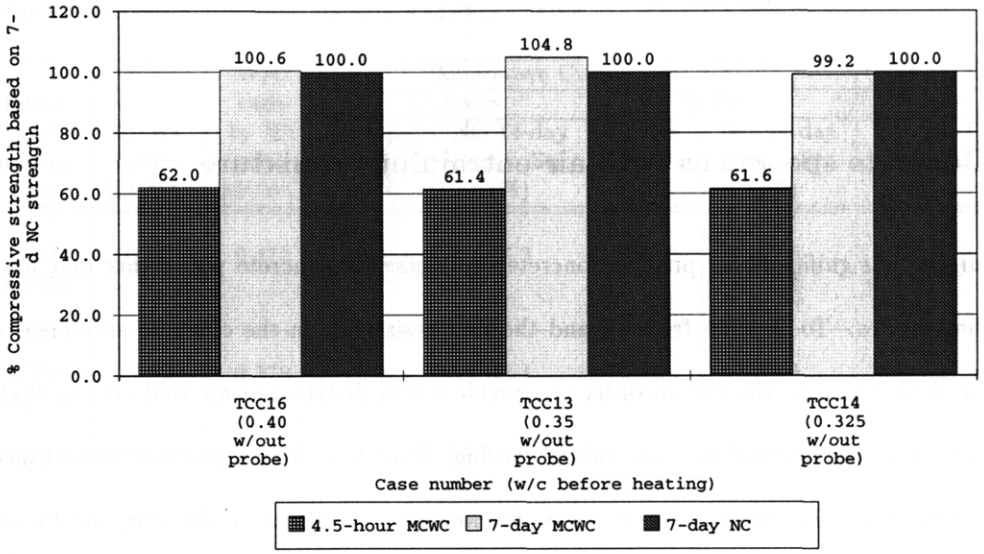

(a) Case TCC16 versus Case TCC13 and TCC14

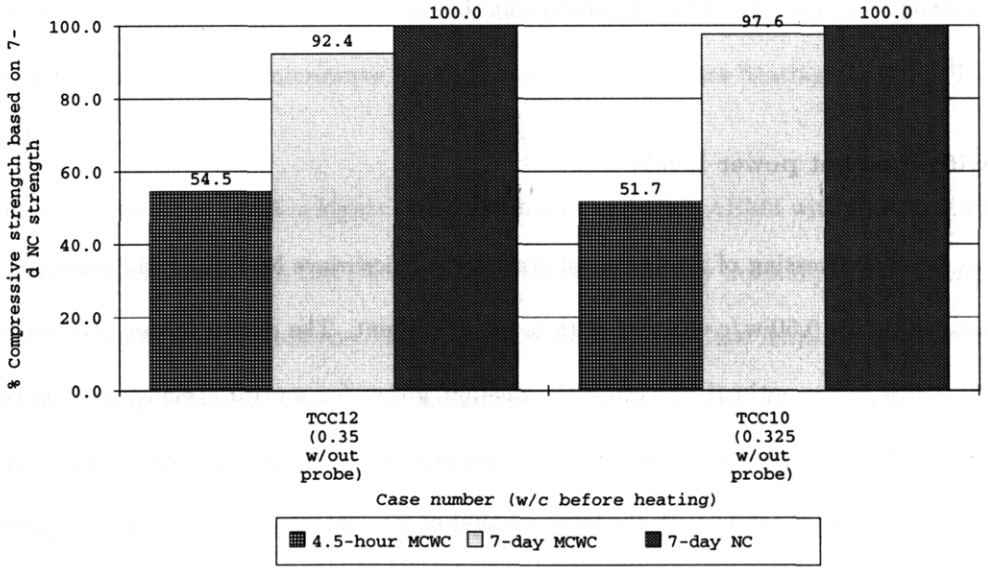

(b) Case TCC12 versus Case TCC10

Figure 2-22: Results of the effect of w/c ratio on the compressive strength development

can counter the differential expansion during the application of microwave energy better so the development of pores and microcracks is minimized.

2.4.4 Concrete specimens with air-entraining admixture

Air entrainment is significant for precast concrete products and concrete pavements that may be exposed to freeze-thaw cycles. To develop freezing and thawing resistance in the concrete specimen, air-entraining admixture will be added to the mix in order to provide a well distributed air-void system that allows water movement to relieve the internal pressure due to freezing. Therefore, it is of practical importance to study the effect of microwave on the compressive strength development as well as the freezing and thawing resistance of the air-entrained concrete. In this chapter, only the effect of microwave on the compressive strength development will be presented. The parameters to be investigated are power levels and the amount of air-entrainment (or % air content). Results of freeze-thaw durability of the air-entrained concrete under microwave curing will be reported in the subsequent chapter.

Process with constant power levels

For constant power processing of air-entrained concrete, a microwave heating of 412 watts for 45 minutes is used in Case AEM2 for 0.50 w/c concrete with 5.4% air content. The reason to use "412 watts-45 minutes" heating is that this is the optimal process with constant power for mortar specimens. The results of Case AEM2 in Table 2.10 and Figure 2-23 show that very low early and later strength are obtained. An explanation is that excessive microwave power with the large amount of air content in Case AEM2 can cause major pores and microcracks in the specimens due to the greater expansion of air.

Thus, microwave heating of 375 watts for 45 minutes is used in Case AEM4 for 0.50 w/c concrete with the same 5.4% air content as that of Case AEM2 in order to obtain higher early and later strength. As expected, Case AEM4 gains higher early and later strength than Case AEM2.

Table 2.10: Results of the effect of heating rate on the compressive strength development of Cases AEM2 and AEM4 for air-entrained concrete under microwave curing

Case # (%air)	Power and heating time	W/C ratio by Wt before MCWC	W/C ratio by Wt after MCWC	Microwave Curing - MCWC				Normal Curing - NC	
				4.5 hours		14 days		14 days	
				Compr. Str. (psi)	NC 14-day Comp. Str. (%)	Compr. Str. (psi)	NC 14-day Comp. Str. (%)	Compr. Str. (psi)	NC 14-day Comp. Str. (%)
AEM2 (5.4%)	412W &45M	0.50	0.472	1305.1	25.3	2092.0	40.6	5153.1	100
AEM4 (5.4%)	375W &45M	0.50	0.378	1718.9	32.1	3764.9	70.3	5352.9	100

Effect of the amount of air content

There are two different water/cement ratios investigated for the effect of the amount of air content: 0.50 and 0.38 w/c. For 0.50 w/c, Case AEM4 is compared with Case AEM5 while Case AEM3 is compared with Case AEM6 for 0.38 w/c. All cases are heated at a constant power of 375 watts because it is determined from the previous section to be a good microwave heating power for 45 minutes heating duration. The results are shown in Table 2.11.

With 0.50 w/c, Case AEM5 with a higher 7.5% air content and Case AEM4 with a lower 5.4% air content gain early strength at the same rate (30.1% and 32.1% based on 14-day normally cured strength for Cases AEM5 and AEM4, respectively). However, the strength at later age of Case AEM5 is much less than that of Case AEM4 (see Figure 2-24(a)). This is due to the effect of greater expansion of air when the microwave energy is applied to the concrete specimens: the specimens with larger amount of air voids tend to experience more severe microcracking than those with lower amount of air voids leading to lower development of later strength.

For the lower w/c of 0.38, Cases AEM3 and AEM6 gain early and later strength at the same rate (see Figure 2-24(b)). The explanation is that the dense mix of low w/c ratio tends to counter the expansion of the air voids better so that the strength development for cases with a difference of air void contents will not

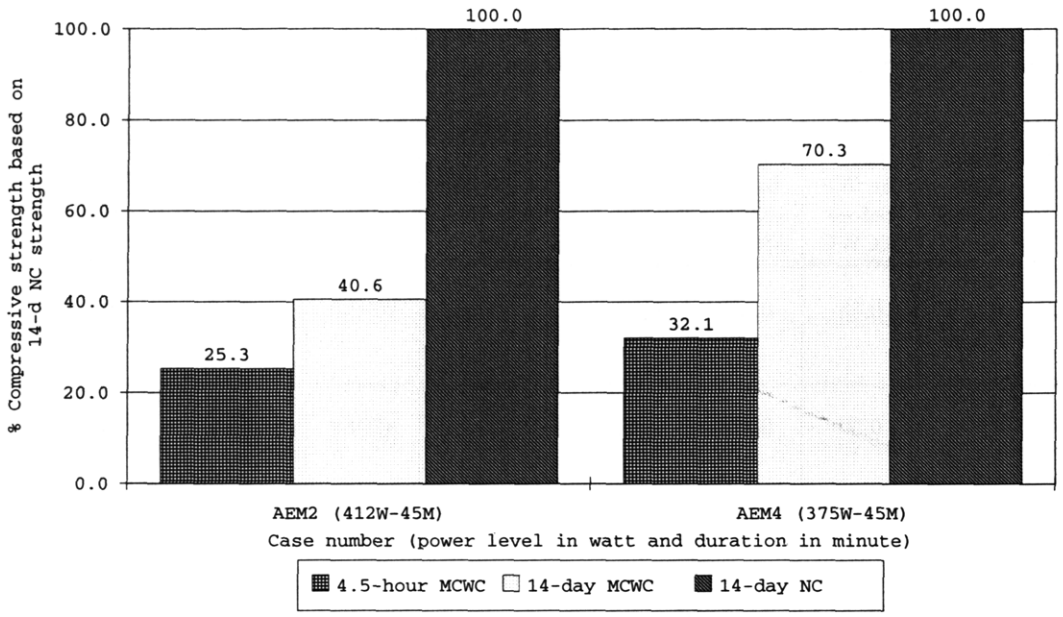

Figure 2-23: Results of the effect of heating rate on the compressive strength development of Cases AEM2 and AEM4 for air-entrained concrete

be significantly different.

2.5 Additional Test

2.5.1 Splitting tensile strength

The splitting tensile strength are measured because (1) same type of microwave-cured specimen used for compression can be used and (2) it is believed that the splitting tensile strength is closer to true tensile strength of concrete than the modulus of rupture obtained from flexural test [32].

Since Case TCC8 gives high early and later strength, its power history is used for Case TCC15 to measure the splitting tensile strength of microwave-cured concrete compared with that of normally cured concrete. The results in Table 2.12 show that the microwave-cured concrete can gain not only high compressive strength but also high splitting tensile strength both at early and later time.

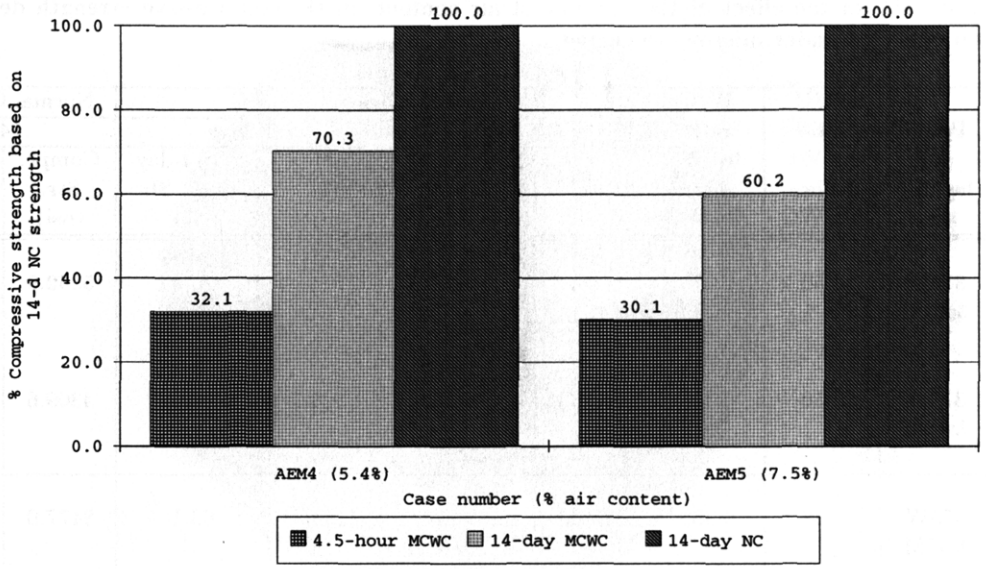

(a) Case AEM4 versus Case AEM5

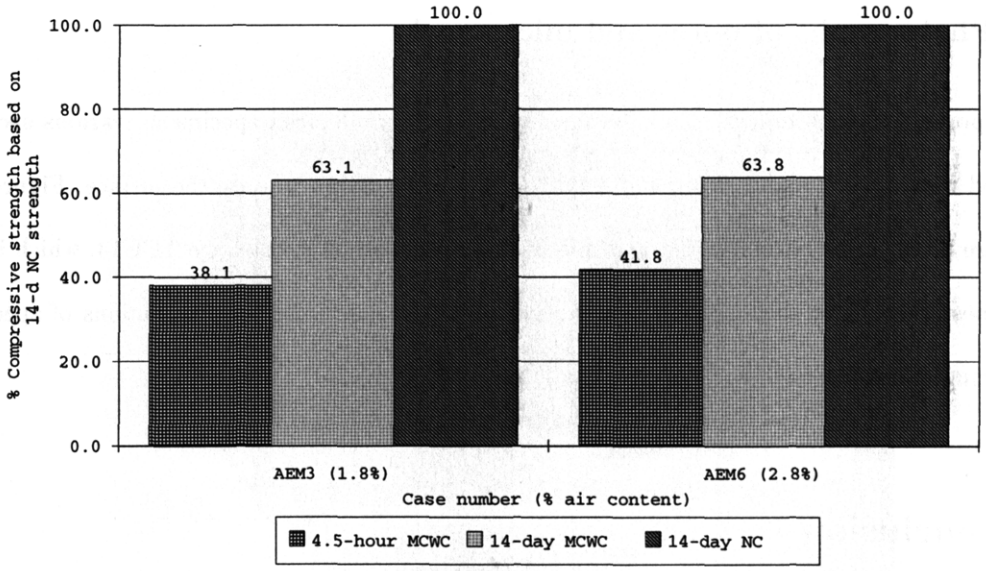

(b) Case AEM3 versus Case AEM6

Figure 2-24: Results of the effect of the amount of air content on the compressive strength development of air-entrained concrete

Table 2.11: Results of the effect of the amount of air content on the compressive strength development of air-entrained concrete under microwave curing

Case # (%air)	Power and heating time	W/C ratio by Wt before MCWC	W/C ratio by Wt after MCWC	Microwave Curing - MCWC				Normal Curing - NC	
				4.5 hours		14 days		14 days	
				Compr. Str. (psi)	NC 14-day Comp. Str. (%)	Compr. Str. (psi)	NC 14-day Comp. Str. (%)	Compr. Str. (psi)	NC 14-day Comp. Str. (%)
AEM4 (5.4%)	375W &45M	0.50	0.378	1718.9	32.1	3764.9	70.3	5352.9	100
AEM5 (7.5%)	375W &45M	0.50	0.477	1296.8	30.1	2596.0	60.2	4309.6	100
AEM3 (1.8%)	375W &45M	0.38	0.365	3118.3	38.1	5161.3	63.1	8177.0	100
AEM6 (2.8%)	375W &45M	0.38	0.367	3102.9	41.8	4734.0	63.8	7422.8	100

2.5.2 Photographs of pores and microcracks

To reveal pores and microcracks of microwave-cured and normal-cured specimens, various sections are cut and painted with a black paint. Then white zinc oxide powder is spread onto the surface. Figure 2-25(a) and (b) compare pictures for normal-cured and microwave-cured specimens of Case TCC14, which is determined to be the best case. It is clear that there is no visible difference in the surface sections of specimens under normal curing and microwave curing.

2.6 Conclusion

In conclusion, the significant findings are as followings:

- Feedback temperature control at 80°C for 45 minutes microwave curing process with "Max@412W" is used as a guideline to obtain optimal process for concrete.

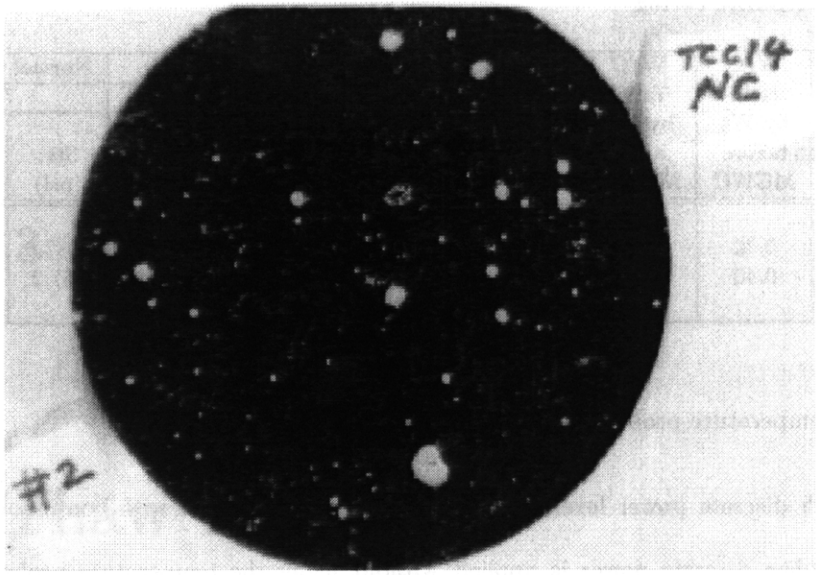

(a) For normal curing

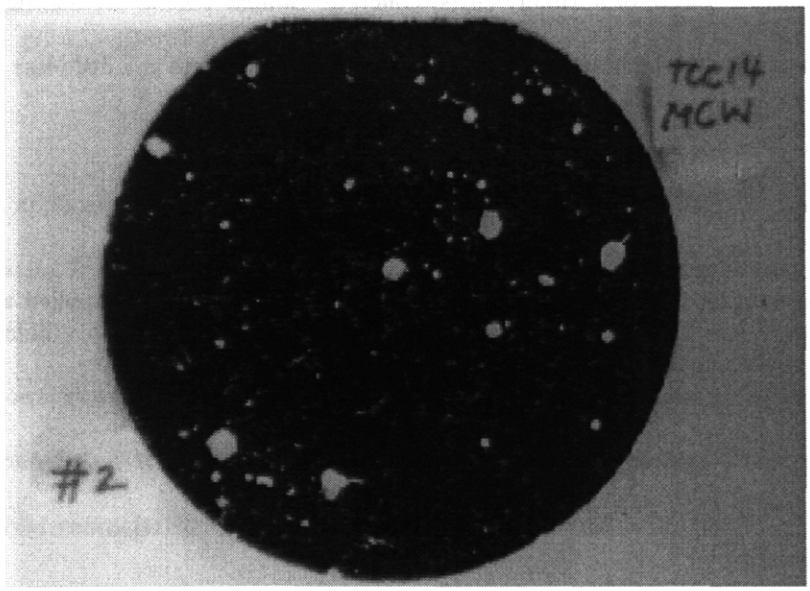

(b) For microwave curing

Figure 2-25: Pictures showing pores and microcracks in concrete specimens of Case TCC14 (0.325 w/c)

Table 2.12: Comparison of compressive strength development and splitting tensile strength development of concrete under microwave curing

Case #	W/C ratio by Wt before MCWC	W/C ratio by Wt after MCWC	Microwave Curing - MCWC				Normal Curing - NC	
			4.5 hours		7 days		7 days	
			Str. (psi)	NC 7-day Str. (%)	Str. (psi)	NC 7-day Str. (%)	Str. (psi)	NC 7-day Str. (%)
TCC8	0.40	0.381	4011.9	57.0	7035.8	100.0	7037.0	100
TCC15	0.40	0.382	327.6	58.8	492.4	88.4	557.2	100

- Using the temperature probe can reduce the early and later strength.
- Process with discrete power levels simulates the optimal process with continuous power levels well. Moreover, when discrete power is applied without using the temperature probe, the discrete power process gives better results than the continuous power process.
- High early compressive strength of microwave-cured concrete is obtained while its later strength is the same as the later strength of normally cured concrete. Similar results are obtained for splitting tensile strength except that the later strength of microwave-cured concrete is a little less than that of normally cured concrete.
- Concrete with a lower w/c ratio responds to microwave curing well.
- For microwave curing process, a relatively high heating power should be applied at the beginning while low heating power should be used at the end.

Chapter 3

Freeze-Thaw Durability

3.1 Introduction

One of the potential applications of microwave curing technique is in concrete pavement repair. In the winter, the pavements are facing frost attack. It is therefore of significance to study the effect of microwave energy on the freeze-thaw durability of air-entrained concrete. The resistance to freezing and thawing of air-entrained concrete under microwave curing is investigated in accordance with the requirements of Procedure A of ASTM C 666-92, and compared to that of air-entrained concrete under normal curing. Their compressive strength at 14 days and air-void characteristics are also measured and compared.

In this chapter, (i) background of freeze-thaw durability, (ii) experimental program, (iii) results of compressive strength test, freeze-thaw resistance test, and air-void characteristics test, (iv) discussion, and (v) conclusion are presented.

3.2 Background

3.2.1 Frost damage of hardened concrete

The physical properties of concrete, such as its permeability, degree of saturation, absorption of water, extensibility and strength, and the size of pores and other voids determine its resistance to frost attack. These pores and voids include capillary cavities (0.010 to 5μm), gel pores (< 0.01μm), entrained air bubbles (50 to 1000μm), entrapped voids (1 to 3 mm), fissures or cracks, and etc. Freezable water exists in the capillary cavities. At very low temperature, ice can easily form in them. However, practically, there is no formation of ice in the gel pores because their sizes are so small that the water is held rigidly and its freezing temperature is below -78°C (see Figure 3-1) [32]. When ice forms in pores with over about 85% saturation, the volume expansion can cause damage to the structure of the paste [32]. By adding air-entraining admixture into the mix, air bubbles with the size of 0.002 to 0.04 in. (0.05 to 1 mm) are incorporated into the concrete to relieve pressure due to ice formation during frost action. Like entrained air bubbles, the entrapped air voids (due to poor compaction) and fissures or cracks will also help resisting the frost attack instead.

Two forms of frost damage that can occur are (1) internal cracking and (2) surface scaling. Internal cracking, the most dominant form of frost attack, can be detected by length change, pulse velocity, and relative dynamic modulus of elasticity. Scaling, the surface deterioration, is easy to be detected by visually examining or by weight loss.

Internal cracking

The internal cracking of concrete can occur when dilating pressure during frost attack is greater than its tensile strength. Two sources of dilating pressure are (1) hydraulic pressure due to freezing of water in the capillary cavities and (2) diffusion of water caused by osmotic pressure [32].

When ice forms in the capillary cavities, the increasing volume of ice by about 9% at the freezing point (see Figure 3-2) will cause the excess water to be driven out of the cavities resulting in hydraulic pressure. The developed hydraulic pressure depends on the resistance to fluid flow of the concrete which is determined

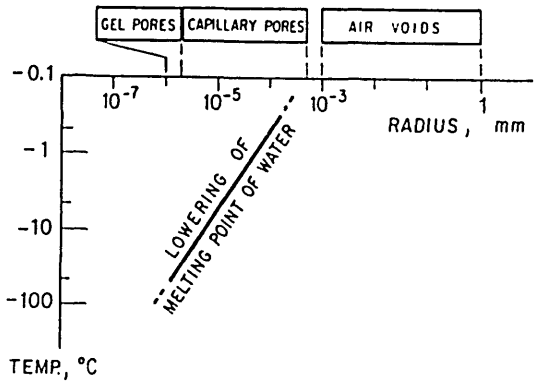

Figure 3-1: The relationship between size of pores in concrete and melting temperature of water- -The melting temperature is the equilibrium temperature between pore water and bulk ice. It depends on the pore dimensions and the physicochemical properties of the inner pore surface. In general, the freezing temperature is lower than the melting temperature. Therefore, the freezing temperature of the gel pores (mentioned in the text) is actually lower than the melting temperature shown here. [Harnik et al., 1980]

by (1) the spacing factor, which is the maximum distance from the periphery of bubbles to the interior of cement paste in concrete, and (2) the permeability of the paste between the freezing cavities and the air bubbles [32]. Because of the differences in entropy of newly formed ice and water in gel pores, thermodynamic disequilibrium is resulted. To balance this disequilibrium, the gel water in a high energy state will migrate to the capillary cavities containing ice, which is at a lower energy location. Consequently, this migration of water leads to a growth of ice, internal pressure, and finally the internal cracking expansion of the concrete unless excess capillary water can escape to air bubbles by diffusing through unfrozen pores.

Another source of expansion of the concrete is due to the diffusion of water caused by osmotic pressure leading to the growth of many small bodies of ice [32]. In general, solutions in capillary cavities are not pure water; they are water containing several soluble substances, for example, alkalies, chlorides, free lime (CaO) and calcium hydroxide. Therefore, their freezing temperatures are lower than that of pure water. Osmotic pressure can occur when pure water is frozen after it separates from the soluble substances leading to an increase of local concentration of solutions. So the diffusion of water can take place when there are

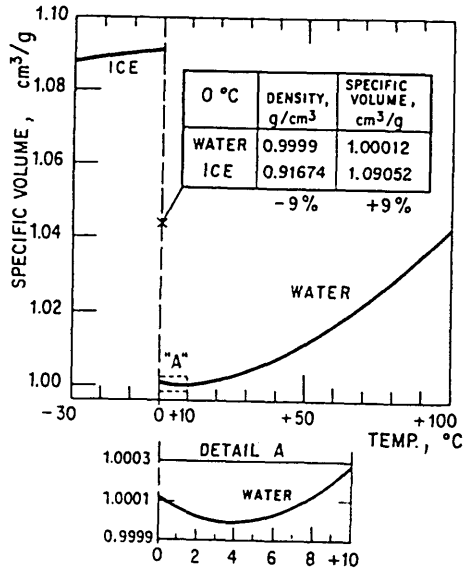

Figure 3-2: The specific volume of water and ice as a function of temperature [Harnik et al., 1980]

differences in the local concentrations between capillary cavities. This mechanism is very significant in frost attack because in the case that concrete is in direct contact with water, water can travel through the concrete by osmotic pressure resulting in an increase of the moisture content which leads to severe frost damage eventually.

Surface scaling

Scaling can occur under two different conditions. First, it may occur when the dilating pressure in concrete due to freeze-thaw cycles is greater than its tensile strength so the surface scaling will occur first and then followed by complete disintegration beginning from the exposed surface through its depth [32]. Second, it can occur independently owing to the effect of finishing process which reduces the air content at the surface area leading to higher disruptive forces during freezing [40]. Also, since the surface is generally more saturated with water, surface scaling can be significant.

3.2.2 Factors controlling frost resistance of hardened concrete

It is believed that under normal curing condition, the freeze-thaw resistance of concrete depends on several factors as shown below:

1) Entrained air-void characteristics

2) Water/cement ratio

3) Saturation condition

4) Tensile strength

Entrained air-void characteristics

According to ASTM C 457-90, Standard test method for Microscopical Determination of Parameters of the Air-Void System in Hardened Concrete, the characteristics of the air voids of hardened concrete such as the air content, average chord length, specific surface, void frequency and spacing factor can be determined. It is however stated that the spacing factor is the most important indicator of the freeze-thaw resistance of concrete. The spacing factor is significant because in order to relieve the internal pressure and expansion from freezing of the water by diffusion of water from capillary cavities to the entrained bubbles, the distance between paste and bubbles should not be too large. It is recommended by ASTM C 457-90 that the maximum spacing factor be equal to 0.008 in. (or 0.20 mm) for moderate exposure, lower than 0.008 in. for severe exposure, and larger than 0.008 in. for mild exposure. In general, the spacing factor for air-entrained concrete designed in accordance with ACI 201.2R and ACI 211.1 should be in the range of 0.004 to 0.008 inch (0.10 to 0.20 mm) [4].

Although the ASTM C 457-90 recommended the maximum spacing factor of concrete exposed to freezing and thawing cycles to be equal to 0.008 in. (or 0.20 mm) for good resistance to frost action, the results by several authors have shown that concrete with spacing factor much larger than the limit value can have adequate frost resistance. The results by Pigeon et al. [37], have shown that the critical spacing factors for 0.50 w/(c+s) silica fume concrete and 0.50 w/c normal concrete are 0.01 and 0.02 in. (0.25 and 0.50 mm), respectively. High critical spacing factor values are consistent with the results from the previous work by

Pigeon et al. [36]. Moreover, additional work by Pigeon et al. [38] has shown that the critical spacing factors of 0.30 w/(c+s) silica fume concrete and 0.30 w/c normal concrete are 0.012 and 0.016 in. (0.30 and 0.40 mm).

In addition, the work by Carette and Malhotra [8] shows that the spacing factors of silica fume concrete could not be used as the indicator of their freeze-thaw durability since these values do not correlate well with the durability factors. Aïtcin and Vezina [1] compare the freeze-thaw resistances and air-void characteristics of concrete with and without silica fume. Even though both concrete have the same spacing factor value of 0.005 in. (0.126 mm), it is found that the durability factor of the silica fume concrete (at 83) is higher than that of normal concrete (at 68) because the permeability of the former is lower due to the lower value of its percent absorption. Finally, the work by Foy et al. [12] shows that the 0.25 w/c normal concrete has the critical spacing factor of 0.028 in. (0.70 mm) which is much higher than the limiting value of 0.008 in. (0.20 mm) suggested by ASTM C 457-90.

To summarize, the maximum spacing factor value of 0.008 in. (0.20 mm) as recommended by ASTM C 457-90 cannot be used as the indicator of the frost resistance of the concrete. However, it can be used in comparative study in order to explain the performance of concrete subject to freeze-thaw cycles.

Water/cement ratio

In general, concrete with high w/c ratio has high permeability because there are insufficient hydration products to fill all the pores. Thus, concrete with high w/c needs to have a suitable air-void spacing factor to ensure frost resistance. For low w/c concrete, it is believed that it has good freeze-thaw durability because it will create only small capillary cavities and will reduce the amount of freezable water. In addition, since the strength of the low w/c paste is higher that that of high w/c paste, it is obvious that the low w/c paste can resist higher hydraulic pressure during freezing resulting in good frost resistance. However, some researcher like Litvan [24] believed that lower spacing factor is needed for low w/c concrete because the low permeability of the paste could cause difficulty in the movement of water towards air voids during freezing which could cause disruption of the paste.

The results by Foy et al. [12] have shown that the 0.25 w/c normal concrete without any dosage of air-entraining admixture can have the durability factor in a range of 84 to 102 after 300 cycles of freezing and thawing in the water. Their spacing factors are in a range of 0.023 to 0.030 in. (0.590 to 0.758 mm). For concrete with various dosages of air-entraining admixture, all of their durability factors are over 100 whereas their spacing factors are below 0.028 in. (0.70 mm). However, the work by Khalil et al. [19] on freeze-thaw durability of non-air-entrained high strength concretes containing superplasticizers concluded that air entrainment should be used in all mixes subjected to freeze-thaw cycles no matter what w/c is used.

In summary, it seems that low w/c concrete with addition of air-entraining admixture will ensure good frost resistance because it has a reduced amount of freezable water, an adequate air-void system, and a stronger paste. However, the limiting value of the spacing factor of 0.008 in. (0.20 mm) appears to be no longer suitable.

Saturation condition

It is generally known that dry concrete will not be damaged by the frost attack as much as concrete with high degree of saturation. The role of the saturation condition of concrete is very significant to its frost resistance because water is the main cause of expansion when concrete is exposed to very low temperature. The degree of saturation of concrete mainly depends on its permeability and its ability to absorb water. In wet condition, low permeability concrete does not absorb water as much as concrete with high permeability; therefore, a better durability to frost attack will be obtained in concrete with low permeability. In addition, concrete with high percent absorption of water tends to be damaged from the internal cracking more than concrete with low percent absorption of water. To summarize, the more the saturation condition of concrete is, the more severe the frost damage will be.

Tensile strength

Tensile strength is one of the factors affecting deterioration in concrete subject to frost attack. As the dilating pressure in concrete caused by frost action is built up and becomes greater than its tensile strength, surface

scaling and internal cracking can begin and complete disintegration will follow ultimately.

3.2.3 Calculation of durability factor of concrete

According to ASTM C666-92, Test Method for Resistance of Concrete to Rapid Freezing and Thawing, the calculation of durability factor (D.F.) is as follows:

$$D.F. = \frac{P * N}{M}$$

where P = relative dynamic modulus of elasticity at N cycles in percent,

N = numbers of cycles at termination of the test where its relative dynamic modulus of elasticity reaches 60% of the initial modulus or the total number of cycles reaches 300, whichever occurs first,

and M = numbers of cycles at specified termination.

The relative dynamic modulus of elasticity after c cycles can be calculated from

$$P_c = \left(\frac{n_1}{n}\right)^2 * 100$$

where P_c = relative dynamic modulus of elasticity after c cycles in percent,

n_1 = fundamental transverse frequency at 0 cycle,

and n = fundamental transverse frequency after c cycles.

It is noted that the calculation of relative dynamic modulus of elasticity is based on the assumption that the weight and dimension of the specimens are the same throughout the test [6]. This assumption is adequate if the results from this test are mainly for qualitative comparison.

3.3 Experimental Program

For concrete with air-entraining admixture, nine 3-inch by 8-inch and two 3-inch by 11-inch specimens are casted in each batch. Five 3-inch by 8-inch specimens are cured with the microwave energy while the rests are cured normally. Three out of five microwave-cured specimens and two 3-inch by 8-inch normal-cured specimens are tested for compressive strength at 14 days. The rests are subject to the test for resistance to freezing and thawing.

Specimens, which are frozen and thawed in water as explained in Procedure A of ASTM C 666-92, are weighed and measured for fundamental transverse frequency which is used to compute the relative dynamic modulus of elasticity after specific numbers of freeze-thaw cycles. In our experiment, each cycle takes about 7 hours and each specimen is subjected to freeze-thaw cycles until its relative dynamic modulus of elasticity reaches 60% of its initial modulus or the number of total cycles reaches 300, whichever occurs first.

To obtain the fundamental transverse frequency, the specimen is supported so that it may vibrate freely in the transverse mode. The signal pickup device is attached to the top surface and near the end of the specimen and held firmly with a hand. Bad contact of the signal pickup device to the surface results in no fundamental frequency and no meaningful data. Using a small hammer as an impactor, the top surface of the other end of the specimen is struck lightly. The amplitude versus frequency is recorded by the spectrum analyzer. The fundamental transverse frequency of the specimen, which is the frequency with the highest amplitude on the display is recorded. Figure 3-3 shows a picture of (1) HP 3582A Spectrum Analyzer used to receive the signals upon the impact in order to provide the display of amplitude versus frequency and (2) 4102 current source and signal pickup device by DYTAAN used to pick up the signals from the impact, and (3) a small hammer (impactor) used to strike the surface of specimen to provide the impact.

To determine the air content of freshly mixed concrete, ASTM C 231-91b, Standard test method for air content of freshly mixed concrete by the pressure method, is followed. The air meter type B, supplied by Forney, Inc., according to ASTM C 231 is used. It is composed of a measuring bowl and a cover assembly (see Figure 3-4). The basic operational design of this meter is based on the principle of Boyle's law which gives the relationship between the volume of air and the applied pressure at a constant temperature. A known

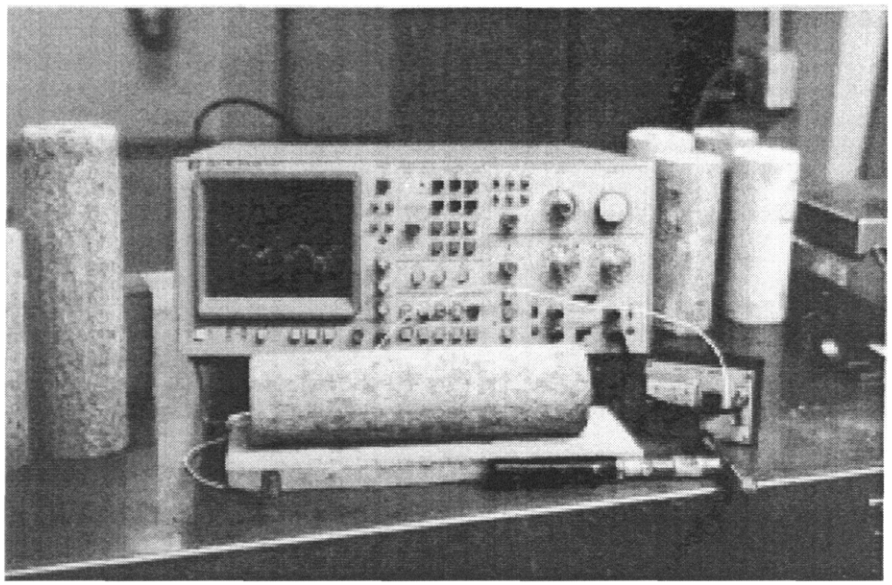

Figure 3-3: Picture of the set-up for fundamental frequency measurement: HP 3582A Spectrum Analyzer, 4102 current source by DYTAAN, and a small hammer

volume of air at a predetermined pressure in an air chamber, located on the cover assembly of the meter, will be equalized with the unknown volume of air in fresh concrete, contained in the measuring bowl which is the bottom part of the meter. The percent air content can be easily read off from the dial of the pressure gauge which is calibrated in term of percent air content for the pressure at the equilibrium point. According to ASTM C 231, the range of pressure from 7.5 to 30.0 psi (51 to 207 kPa) has been used satisfactorily.

To determine the characteristics of the air voids of hardened concrete such as the air content, average chord length, specific surface, void frequency and spacing factor, *longitudinal* sections of the specimens are cut, polished, and examined in accordance with the requirements of Procedure B, the modified point-count method, of ASTM C 457-90. This procedure consists of determination of compositions of concrete sample by examining each point on its surface at a regular grid system to see whether it falls in an air void, cement paste, or aggregate (see Figure 3-5(a)). The data collected are (1) the horizontal (East-West) distance between each point as the examination moves along the horizontal axis, (2) the total number of stops (or points), (3) the number of stops in air voids, (4) the number of stops in cement paste, and (5) the total number of air voids intersected by line of traverse during the horizontal translation. From these data, various parameters of

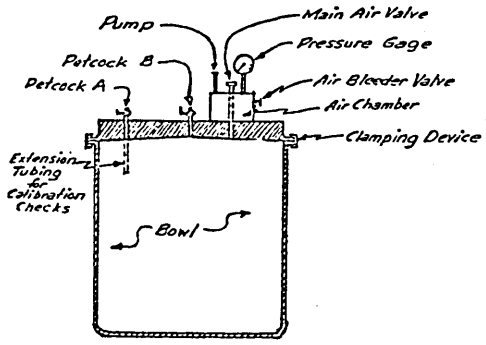

Figure 3-4: Schematic diagram of Type B air meter according to ASTM C 231-91b

the air-void system of hardened concrete can be computed. The definitions of these parameters are shown graphically in Figure 3-5(b).

For better understanding, some definitions of these parameters will also be explained here. The average chord length is the average of the length that passes through a void. With the procedure B of ASTM C 457, the average chord length is calculated by dividing the product of the number of stops in air and the horizontal distance between each stop with the total number of voids intersected by the line of traverse. This calculated value is however an approximation. To be correct, it should be calculated by dividing the total length formed by transection of the voids with the total number of voids intersected by the line of traverse, which is absolutely correct for the calculation shown in Procedure A (the linear-traverse method) of ASTM C 457. The summary of this procedure will not be described here. For specific surface, by definition it is the surface area of the air voids divided by their volume. According to ASTM C 457, the specific surface inversely relates to the average chord length. Therefore, the result of either specific surface or average chord length will be presented. And, it is important to note that the lower the average chord length, the higher the specific surface, and the smaller the size of the air void.

To limit the uncertainty of the results, ASTM C 457 requires, for the maximum size of aggregate of 0.375 in. (9.5 mm), (1) the minimum length of traverse for examination to be 75 in. (1905 mm), (2) the

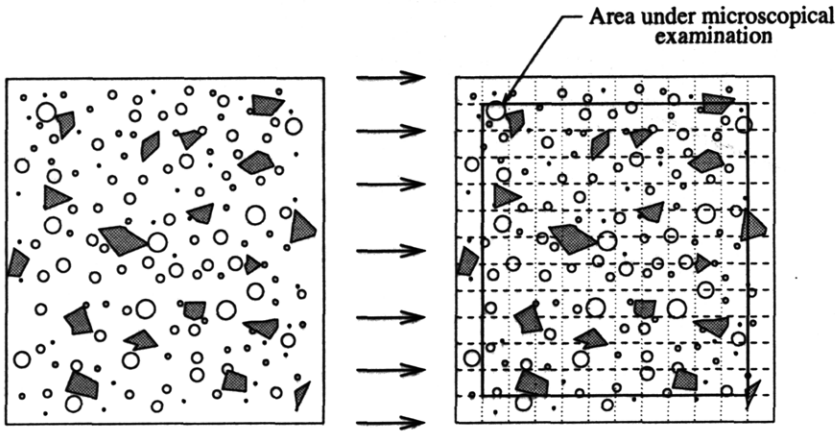

(a) A regular grid system

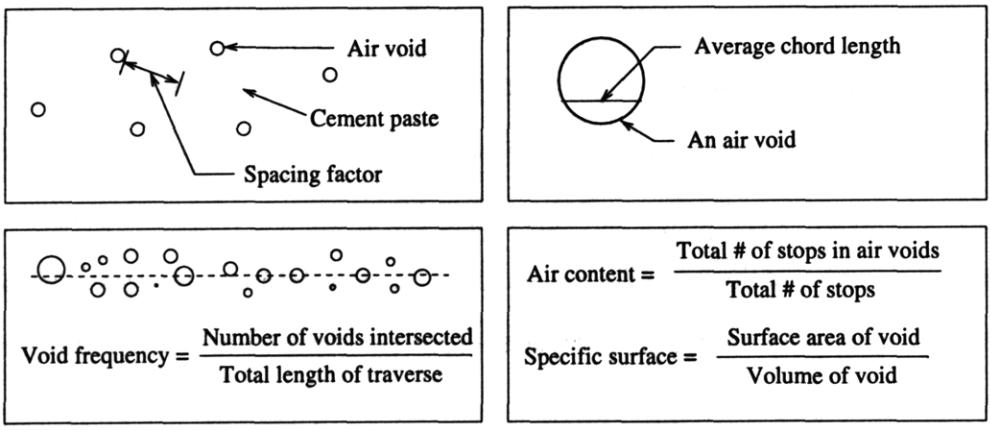

(b) Definitions of various parameters

Figure 3-5: Procedure B, the modified point-count method, of ASTM C 457-90

minimum area to be traversed for examination to be 9 in^2 (58 cm^2), and (3) the minimum number of points for examination to be 1125 points. In our experiment, the maximum size of aggregate is 0.371 in. (or 9.4 mm) and these requirements are met. The length of traverse for each set of specimen is 94.5 in. (2400 mm) while the examined area is 9.3 $in.^2$ (60 cm^2) and the number of total stops is 1200.

3.4 Results

In this experiment, fresh air-entrained concrete to be cured with microwave energy is heated with a constant power at 375 watts for 45 minutes. Fives cases to be tested for compressive strength, freeze-thaw durability, and air-void characteristics are as follows:

- Case D-1 or NAEM2-D: 0.40 w/c with 0% air content concrete
- Case D-2 or AEM5-D: 0.50 w/c with 7.5% air content concrete
- Case D-3 or AEM4-D: 0.50 w/c with 5.4% air content concrete
- Case D-4 or AEM3-D: 0.38 w/c with 1.8% air content concrete
- Case D-5 or AEM6-D: 0.38 w/c with 2.8% air content concrete

The results are reported in three parts: compressive strength result, freeze-thaw test result, and air-void characteristics result.

3.4.1 Compressive strength result

Table 3.1 shows, for five cases, the compressive strength results at 14 days of concrete under microwave and normal curing while Figure 3-6 shows their 14-day percent compressive strength of concrete under microwave curing based on those of normal-cured concrete.

As expected, for the normal curing results, concrete with low w/c and low air content (i.e., Case D-1 with 0.40 w/c and 0% air content) has the highest compressive strength at 14 days followed by the strength of Case D-4 (0.38 w/c with 1.8% air content), D-5 (0.38 w/c with 2.8%), D-3 (0.50 w/c with 5.4%), and

Table 3.1: Results of the effect of microwave energy (375 Watts for 45 minutes) on the compressive strength development of Cases D-1, D-2, D-3, D-4, and D-5

Case #	%air	W/C ratio by Wt before MCWC	W/C ratio by Wt after MCWC	Microwave Curing-MCWC 14 days		Normal Curing-NC 14 days		Size (inch×inch)
				Compr. Str. (psi)	NC 14-day Comp. Str. (%)	Compr. Str. (psi)	NC 14-day Comp. Str. (%)	
D-1 (NAEM2-D)	0	0.40	0.385	6862.8	86.9	7897.6	100	3×8
D-2 (AEM5-D)	7.5	0.50	0.477	2720.5	62.8	4335.2	100	3×8&3×11
D-3 (AEM4-D)	5.4	0.50	0.478	4127.4	77.0	5360.0	100	3×8&3×11
D-4 (AEM3-D)	1.8	0.38	0.367	4978.1	63.3	7867.6	100	3×8&3×11
D-5 (AEM6-D)	2.8	0.38	0.367	4807.9	67.3	7147.4	100	3×8&3×11

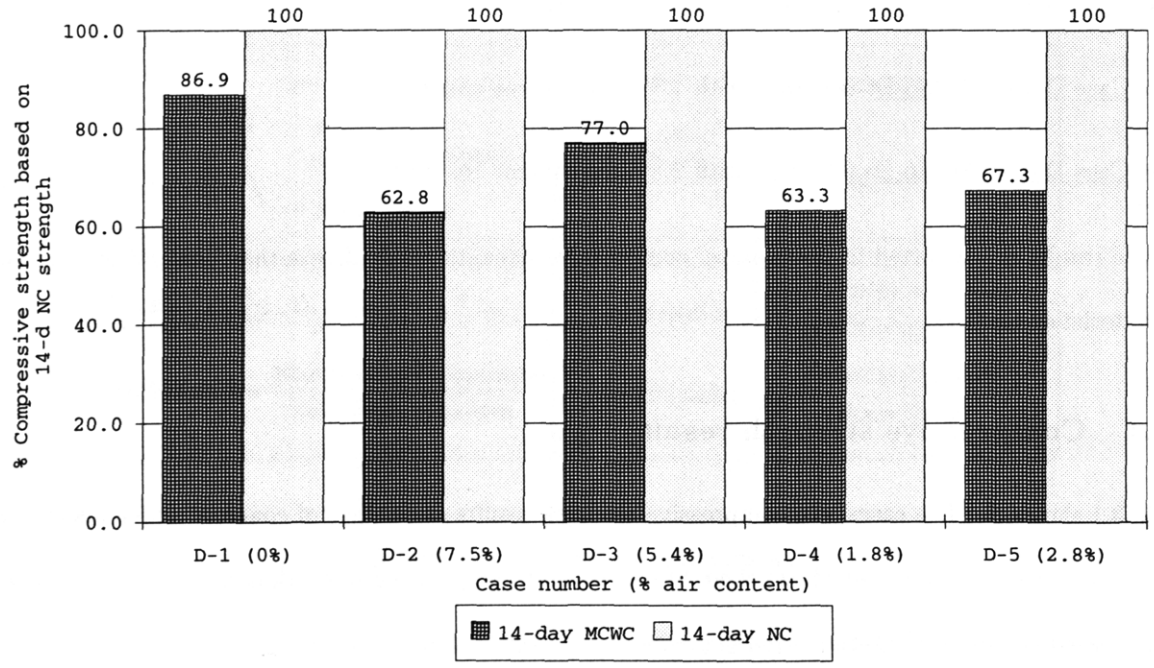

Figure 3-6: Results of the effect of microwave energy on the compressive strength development of Cases D-1, D-2, D-3, D-4 and D-5

D-2 (0.50 w/c with 7.5%). This is due to the result of the introduction of entrained air voids into the paste causing the reduced strength. The more the percent entrained air content in the cement paste is, the less its strength will be.

For the microwave curing results, the decreasing order of the strength at 14 days, for five cases of microwave-cured concrete, is as follows: Cases D-1, D-4, D-5, D-3 and D-2. It is noted that in addition to the effect of the entrained air voids that causes reduced strength, microwave can also reduce the strength by causing expansion of air and cracking in the concrete. The specimens with larger amount of air content tend to experience more microcracks than those with lower amount of air content due to the effect of greater expansion of air when the microwave energy is applied to the concrete specimens (see Figure 3-7). Therefore, the larger the air content, the lower the strength.

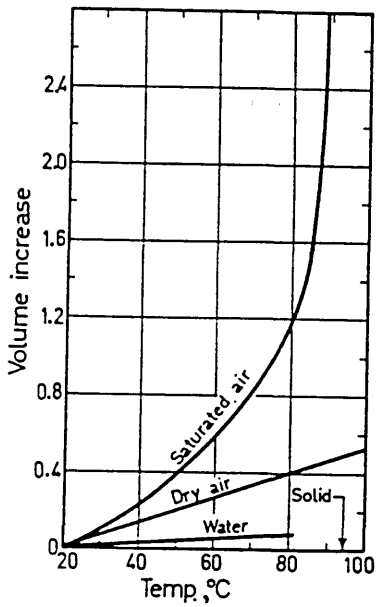

Figure 3-7: Relative thermal expansion of water and air relative to that of solids [Soroka, 1979] (from Alexanderson, J., "Strength Loses in Heat Cured Concrete," *Proc. Swedish Cement Concrete Research Institute,* 43, 1972.)

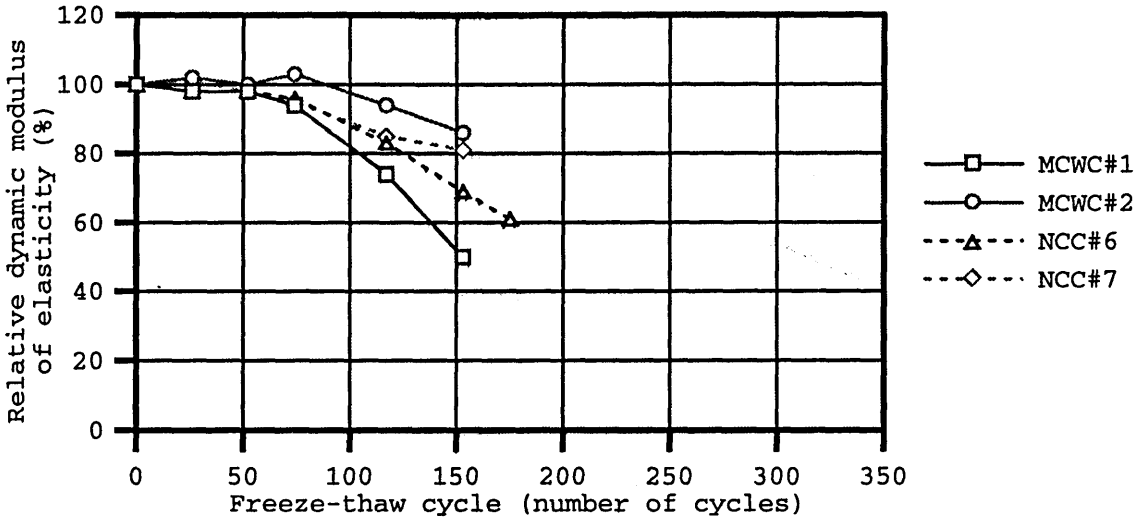

Figure 3-8: Relative dynamic modulus of elasticity versus freeze-thaw cycles for Case D-1 (MCWC = microwave-cured concrete and NCC = normal-cured concrete)

3.4.2 Freeze-thaw test result

The durability factor results are summarized in Table 3.2. In addition, Figures 3-8 through 3-12 show the relationship between relative dynamic modulus of elasticity and freeze-thaw cycles while Figures 3-13 through 3-17 show the graphs of loss of mass versus freeze-thaw cycles.

As shown in Figures 3-8 through 3-12, Case D-1 with 0% air content suffers from the frost attack the most while the other cases survive the frost action after approximately 300 repeated freeze-thaw cycles except that the durability factor of microwave-cured concrete for Case D-3 is 88 which is marginally satisfactory, It is noted that the passing scale of the durability factor according to ASTM C 494-90 is 80. However, some industrial company (e.g. W.R. Grace & Co.) set it to 90. According to Neville [32], the durability factor is used only for comparison and the value of 60 is satisfactory whereas there is no established criteria.

Figure 3-18(a) and (b) show photographs of test specimens of Case D-1 under microwave and normal curing after the end of test. Surface scaling is very severe for both types of specimens. In Figure 3-19(a) and (b), the photograph of microwave-cured specimen of Case D-3 is compared with that of normal-cured

Table 3.2: Freeze-thaw test results: durability factor for Cases D-1, D-2, D-3, D-4, and D-5 (MCWC = microwave-cured concrete and NCC = normal-cured concrete)

Case# & initial W/C	Specimen type and #	Length (inch)	Air Content fresh concrete (%)	Durability Factor for each	Durability Factor average
D-1	MCWC #1	7.94	0	26	35
(NAEM2-D)	MCWC #2	8.09	0	44	
0.40					
	NCC #6	8.06	0	36	39
	NCC #7	7.78	0	41	
D-2	MCWC #1	7.91	7.5	107	105
(AEM5-D)	MCWC #2	8.06	7.5	103	
0.50					
	NCC #6	8.00	7.5	105	109
	NCC #7	7.81	7.5	112	
	NCC #10	11.03	7.5	112	110
	NCC #11	11.00	7.5	108	
D-3	MCWC #1	7.88	5.4	84	88
(AEM4-D)	MCWC #2	8.00	5.4	93	
0.50					
	NCC #6	7.94	5.4	108	107
	NCC #7	7.75	5.4	106	
	NCC #10	11.00	5.4	107	105
	NCC #11	10.97	5.4	103	
D-4	MCWC #4	7.94	1.8	107	108
(AEM3-D)	MCWC #5	8.09	1.8	109	
0.38					
	NCC #6	8.06	1.8	103	102
	NCC #7	7.78	1.8	100	
	NCC #10	11.00	1.8	102	101
	NCC #11	11.00	1.8	99	
D-5	MCWC #3	8	2.8	112	114
(AEM6-D)	MCWC #4	8	2.8	115	
0.38					
	NCC #8	8	2.8	105	104
	NCC #9	8	2.8	103	
	NCC #11	11	2.8	105	105

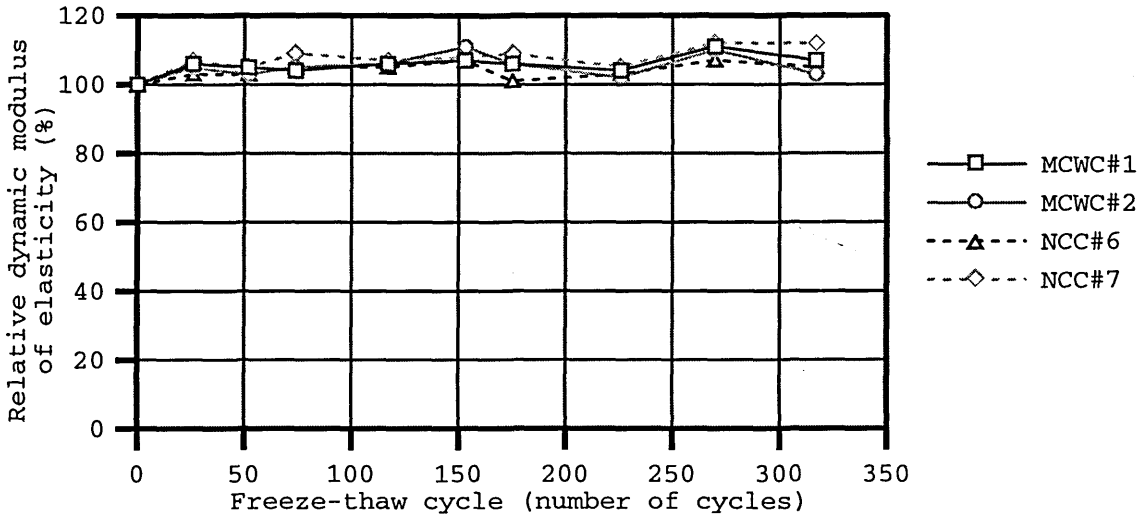

Figure 3-9: Relative dynamic modulus of elasticity versus freeze-thaw cycles for Case D-2 (MCWC = microwave-cured concrete and NCC = normal-cured concrete)

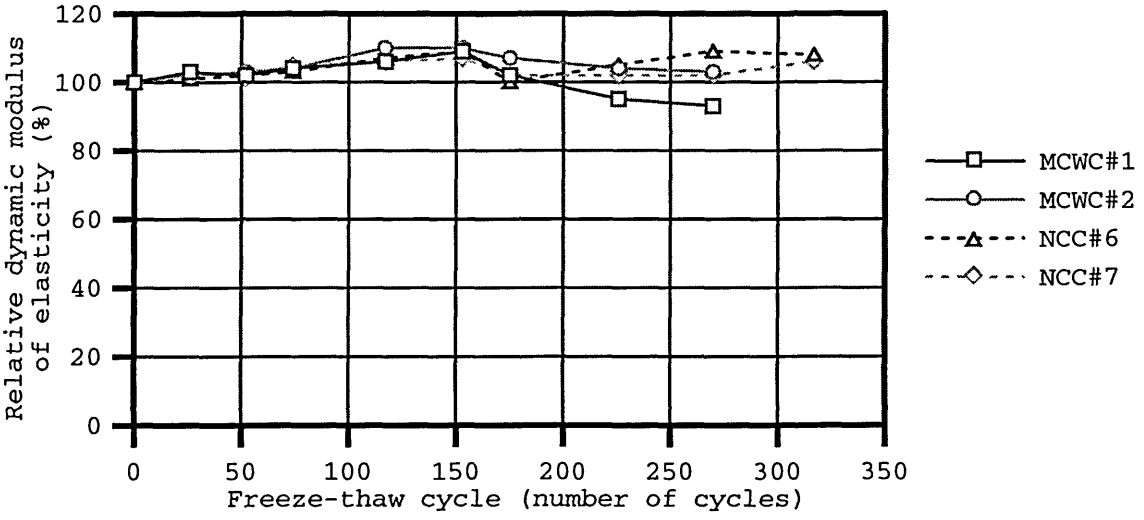

Figure 3-10: Relative dynamic modulus of elasticity versus freeze-thaw cycles for Case D-3 (MCWC = microwave-cured concrete and NCC = normal-cured concrete)

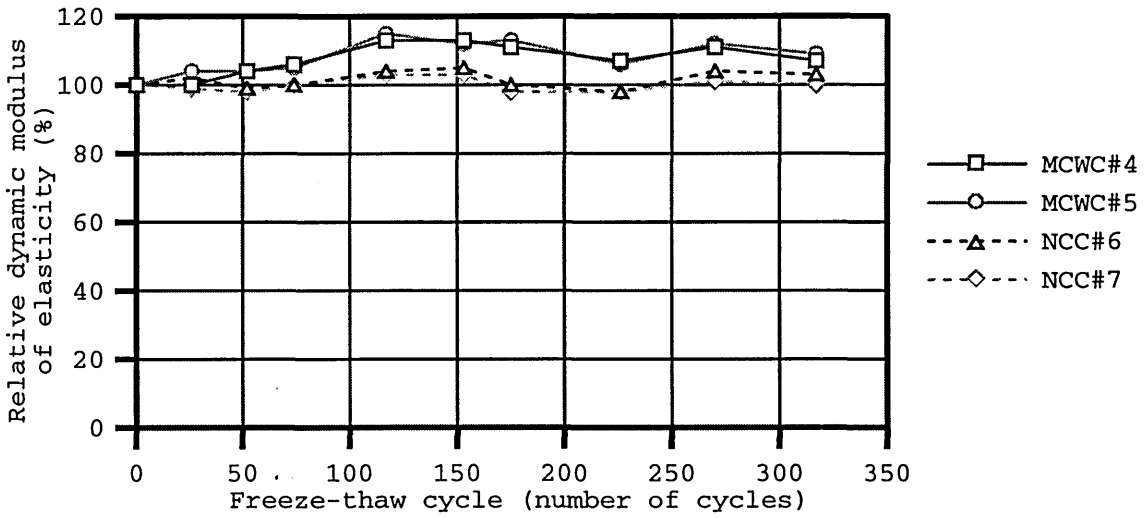

Figure 3-11: Relative dynamic modulus of elasticity versus freeze-thaw cycles for Case D-4 (MCWC = microwave-cured concrete and NCC = normal-cured concrete)

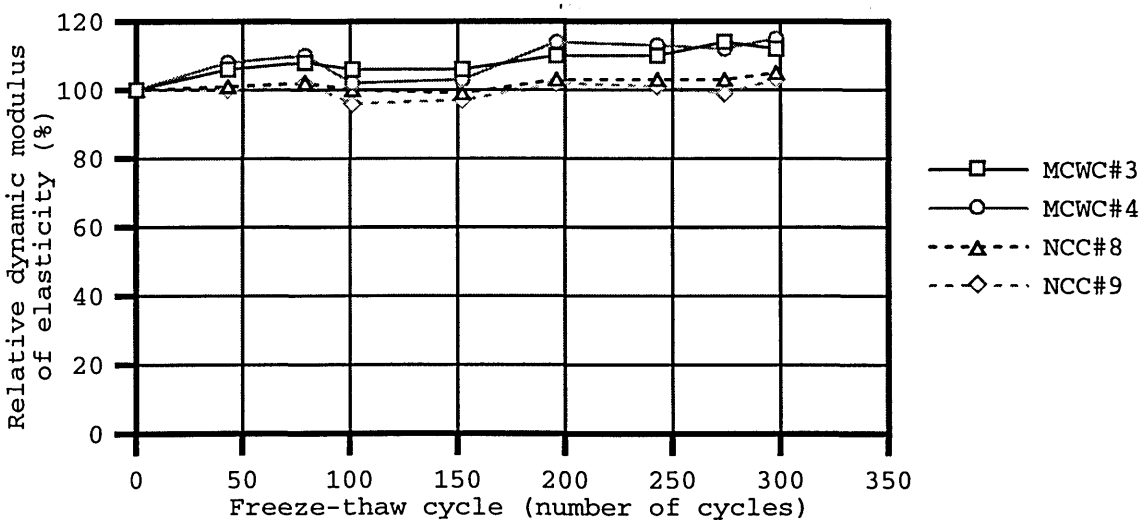

Figure 3-12: Relative dynamic modulus of elasticity versus freeze-thaw cycles for Case D-5 (MCWC = microwave-cured concrete and NCC = normal-cured concrete)

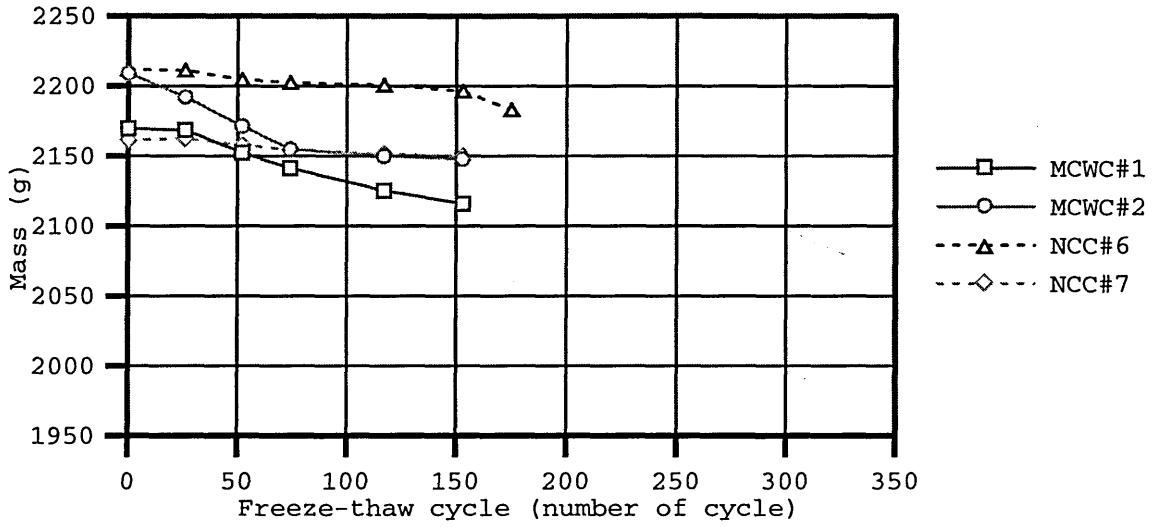

Figure 3-13: Loss of mass versus freeze-thaw cycles for Case D-1 (MCWC = microwave-cured concrete and NCC = normal-cured concrete)

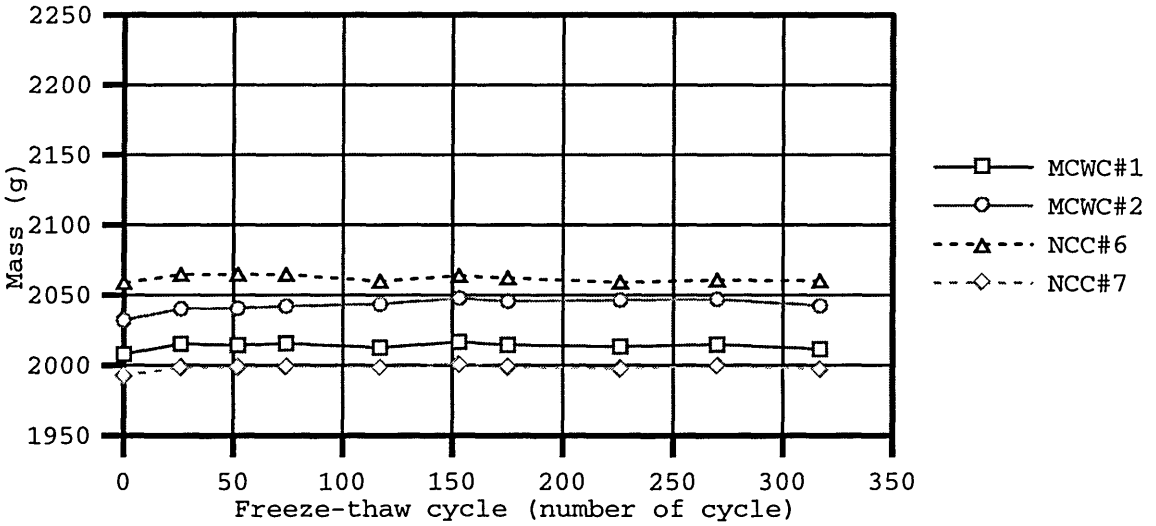

Figure 3-14: Loss of mass versus freeze-thaw cycles for Case D-2 (MCWC = microwave-cured concrete and NCC = normal-cured concrete)

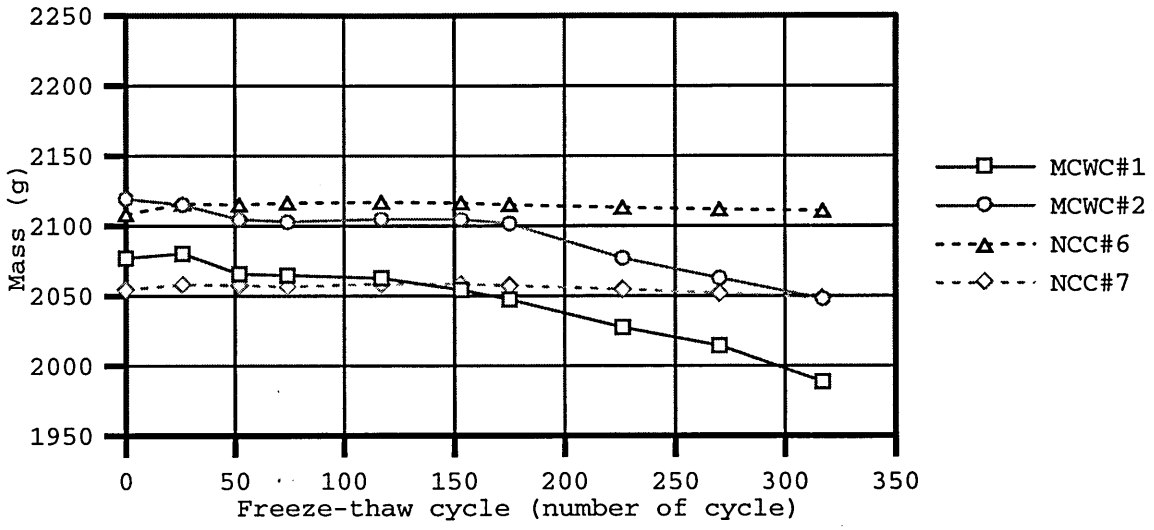

Figure 3-15: Loss of mass versus freeze-thaw cycles for Case D-3 (MCWC = microwave-cured concrete and NCC = normal-cured concrete)

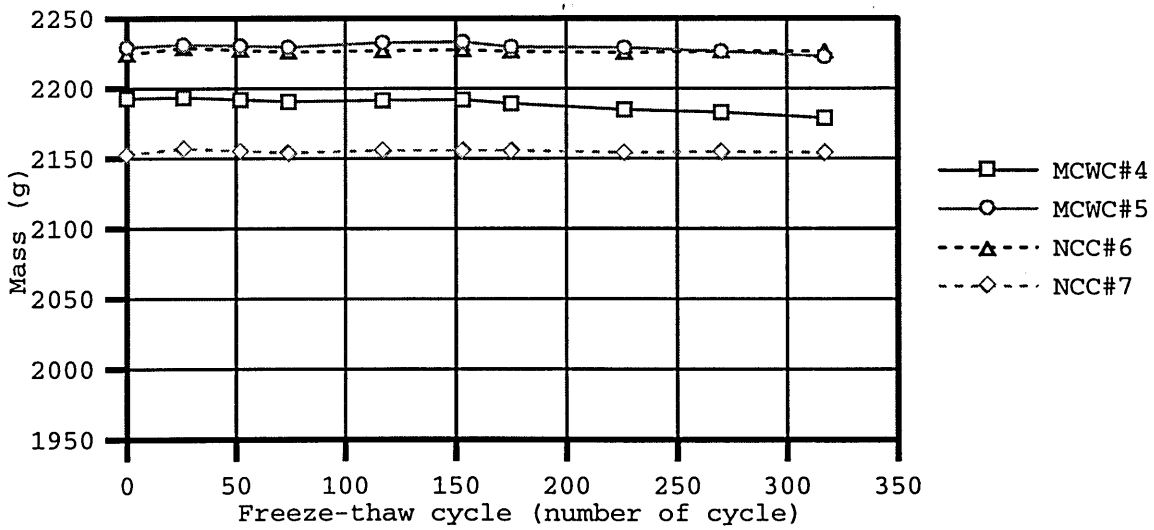

Figure 3-16: Loss of mass versus freeze-thaw cycles for Case D-4 (MCWC = microwave-cured concrete and NCC = normal-cured concrete)

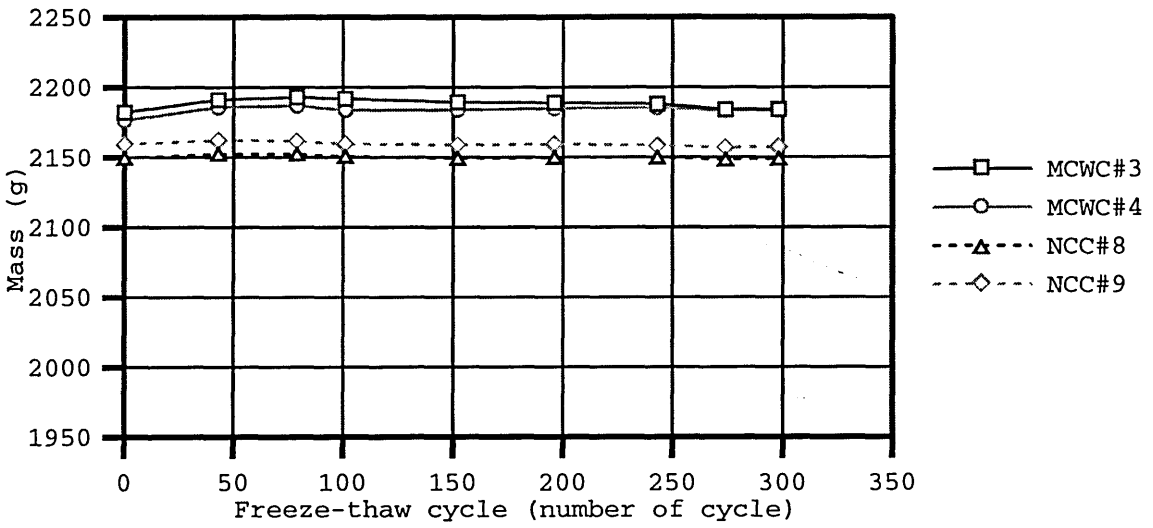

Figure 3-17: Loss of mass versus freeze-thaw cycles for Case D-5 (MCWC = microwave-cured concrete and NCC = normal-cured concrete)

specimen. It is clear that scaling of microwave-cured specimen, for Case D-3, is more severe than that of normal-cured specimen but slightly less severe than that of specimens of Case D-1. The degree of scaling can be directly identified from the results of the mass change in Figures 3-13 through 3-17.

3.4.3 Air-void characteristics result

According to the durability factor results reported in Table 3.2, besides the results of non-entrained specimens in Case D-1, the microwave-cured specimens of Case D-3 exhibit the lowest durability factor which is less than that of the specimens under normal curing from the same mix. It is therefore of importance to further investigate and compare the air-void characteristics, especially the spacing factor, of specimens under microwave and normal curing of Case D-3 in order to explain their results from the freeze-thaw resistance test. Additional air-void characteristics of Cases D-2 and D-5 are also obtained for comparison.

Table 3.3 shows the results of the air-void characteristics of hardened concrete of Cases D-2, D-3, and D-5. Their spacing factors vary from 0.0071 to 0.0155 in. (0.181 to 0.393 mm). In addition to the results

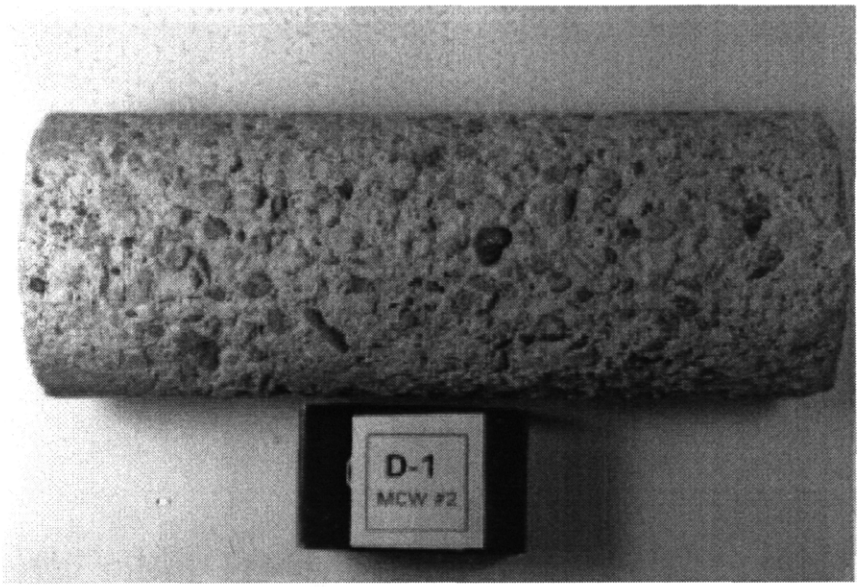

(a) Microwave-cured specimen

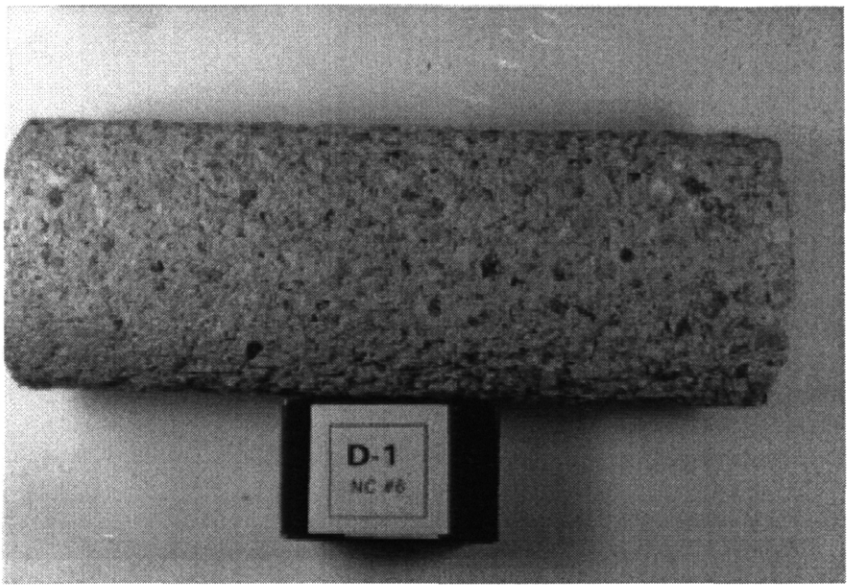

(b) Normal-cured specimen

Figure 3-18: Photographs of test specimens of Case D-1 at the end of freeze-thaw resistance test

(a) Microwave-cured specimen

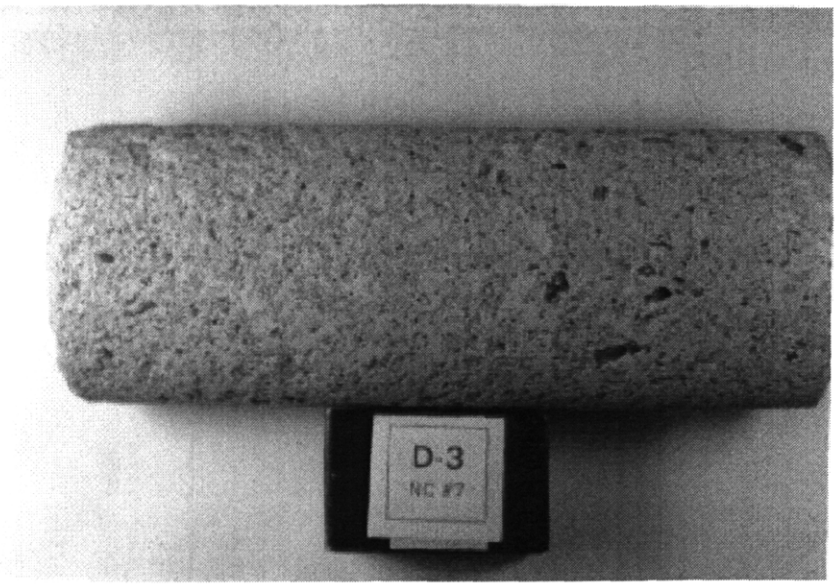

(b) Normal-cured specimen

Figure 3-19: Photographs of test specimens of Case D-3 at the end of freeze-thaw resistance test

Table 3.3: Air-void characteristics of hardened concrete

Specimen #	Description	Air Content		Specific surface (per mm)	Spacing factor (mm)
		fresh concrete (%)	hardened concrete (%)		
D-2#2	0.50 w/c - MCWC	7.5	9.5	21.60	0.197
D-2#6	0.50 w/c - NCC	7.5	7.9	25.18	0.181
D-3#2	0.50 w/c - MCWC	5.4	5.2	19.32	0.301
D-3#6	0.50 w/c - NCC	5.4	3.7	26.59	0.239
D-5#4	0.38 w/c - MCWC	2.8	5.7	13.62	0.393
D-5#9	0.38 w/c - NCC	2.8	3.7	23.95	0.266

of the spacing factor, the results of air content in the hardened concrete can be meaningful. For Cases D-2, D-3, and D-5, it is found that the air contents of hardened microwave-cured concrete are approximately 1.5 to 2% higher than those of normal-cured concrete.

3.5 Discussion

There are three major areas of discussions on the results shown previously: I) effect of microwave energy on freeze-thaw durability, II) use of data from loss of mass as the indicator of freeze-thaw durability, and III) effect of the length difference of the specimens on freeze-thaw durability.

3.5.1 Effect of microwave energy on freeze-thaw durability

In addition to reducing the amount of freezable water in fresh concrete cured with microwave energy, it is believed that during microwave application, microwave not only can cause small air voids to coalesce into larger voids but also can cause air voids to expand and become a little larger due to the effect of greater thermal expansion coefficient of air compared to those of water and other concrete constituents (see Figure 3-7). As a result of coalescence of small air voids, the spacing factor of microwave-cured concrete becomes larger while the size of air voids is greater, which well relates to the smaller value of specific surface. Moreover, the effect of expansion of air voids under microwave curing results in the increase of percent air content of hardened microwave-cured concrete as well as the larger size of air voids. Cracks can also be formed if

pressure due to expansion is increased and exceeded the resistance of the paste. The effect of microwave on several air-void characteristics of air-entrained concrete shown in Table 3.3 agrees well with the proposed explanation. It indicates that the spacing factor and the percent air content of microwave-cured concrete are larger than those of normal-cured concrete while the specific surface of the former is lower than that of the latter.

To summarize, the significant factors affecting the freeze-thaw durability of concrete cured with microwave energy are as follows:

1) Reduced freezable water

2) Increased spacing factor

3) Increased air content (related to decreased specific surface and increased size of air voids)

4) Increased formation of cracks

It is believed that the effect of these factors on the durability significantly depends on the amount of air content and the w/c ratio before the application of microwave energy. However, it is important to point out that the amount of air content relates well to the w/c. The lower the w/c ratio, the lower the amount of air content. This is due to the stiff paste of concrete with low w/c. Therefore, the effect of microwave energy on freeze-thaw durability will be mainly discussed in two different cases of w/c ratio: low w/c case and high w/c case. In addition, the comparison of some of the results between low and high w/c will be discussed.

Before the discussion between these two cases begins, it is important to note that non-air-entrained concrete from both normal curing and microwave curing need an adequate air-void system to resist frost attack as shown by the freeze-thaw resistance test result of Case D-1. For the results of air-entrained concrete, for low w/c of Cases D-4 and D-5, it appears that the microwave-cured specimens obtain a little *higher* durability factor than the normal-cured specimens; on the other hand, for high w/c cases, the microwave-cured specimens of Cases D-2 and D-3 exhibit a little *lower* durability factor than the normal-cured specimens.

Low water/cement case

For low w/c of Cases D-4 and D-5, the durability factors for concrete specimens under normal and microwave curing are above 100 which means that the specimens can actually increase their maturity during the repeated freeze-thaw cycles instead of being damaged by frost attack. The ability to resist frost attack of low w/c normal-cured concrete is probably due to the effect of low freezable water in addition to the contributions of an adequate air-void system.

For concrete under microwave curing, its good freeze-thaw durability is mostly contributed by reduced freezable water, increased air content, and increased formation of cracks or voids, caused by the application of microwave energy. Since the initial amount of w/c is already low, when microwave energy is applied, some of the water will be dried out resulting in even lower w/c and lower freezable water. As already known, the lower the freezable water, the less the frost action, and therefore the higher the frost resistance. For the effect of increased air content, it is believed that its freeze-thaw resistance is likely to be improved rather than deteriorated although it has been known from the principle of freeze-thaw resistance that it is not the total percent air content that provides freeze-thaw resistance but the spacing factor. However, the freeze-thaw durability result from Table 3.2 and the air-void characteristics result from Table 3.3 show that the spacing factor is not important to freeze-thaw resistance of low w/c concrete under microwave curing. It is clear that the increased spacing factor of microwave-cured low w/c concrete has no significant effect on freeze-thaw durability even though the spacing factor is a lot higher than that of normal-cured concrete.

Moreover, it is believed that during microwave application, since the cement paste of low w/c concrete is stiff, microwave will cause some formation of cracks and also cause the air voids to link to one another and form continued channels of voids. By doing these, the freeze-thaw durability is improved. These explanations are strongly supported by an observation of cracks and continued channels of pores, which mostly appear along the aggregate interfaces, on the polished surfaces of the hardened microwave-cured specimens. For comparison, Figures 3-20(a) and (b) show photographs of the actual surfaces, which are cut and polished, of the microwave-cured concrete and normal-cured concrete of Case D-5, respectively. It is clear that the continued channel of pores along the aggregate interface can be seen in the former while the latter shows only

small air voids which are apart from one another. For better illustration, the drawings of the air-void system for low w/c concrete under normal curing versus microwave curing are compared and shown in Figure 3-21.

To summarize, for microwave-cured low w/c concrete, the reduced freezable water, increased air content, and increased formation of cracks seem to be the most dominant factors to resist frost attack. These factors are believed to be the causes for microwave-cured specimen to obtain a little higher durability factor than the normal-cured specimen.

High water/cement case

In contrast to the freeze-thaw durability results of concrete with low w/c, the durability factors of the microwave-cured specimens of high w/c of Cases D-2 and D-3 are lower than those of the normal-cured specimens, especially that of microwave-cured specimens of Case D-3. The freeze-thaw durability of high w/c normal-cured concrete is believed to be controlled mostly by an adequate air-void system with sufficient air content and low spacing factor which is important for high permeability paste.

For high w/c microwave-cured concrete, it is believed that its freeze-thaw resistance depends mainly on the adequate air-void system or the adequate spacing factor and increased air content while the roles of other factors such as the reduced freezable water and increased formation of cracks are not so distinct. A plausible explanation is that the freezable water of high w/c concrete is still considered to be high after microwave curing compared to that of low w/c concrete. There is also less formation of cracks because of the ease of movement of air voids and water and less resistance of the high permeable paste during microwave application. For the effect of microwave on spacing factor, it is believed that microwave can cause small air voids to coalesce together and become larger during the initial stage of microwave curing, resulting in bigger voids (and possibly higher air content) and larger spacing factor, which can be detrimental to the frost resistance. For the increased air content, it is still believed that it has positive effect on the freeze-thaw resistance. To compare, Figure 3-22(a) and (b) show photographs of the actual surfaces, which are cut and polished, of the microwave-cured concrete and normal-cured concrete of Case D-2, respectively. It is seen that their surfaces look similar and contain no continued pores and cracks. To better understand how

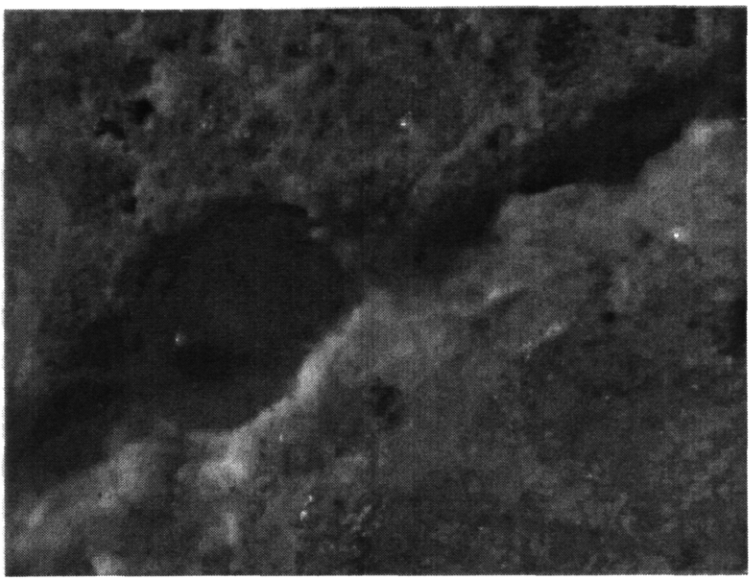

(a) Microwave-cured specimen from D-5#4

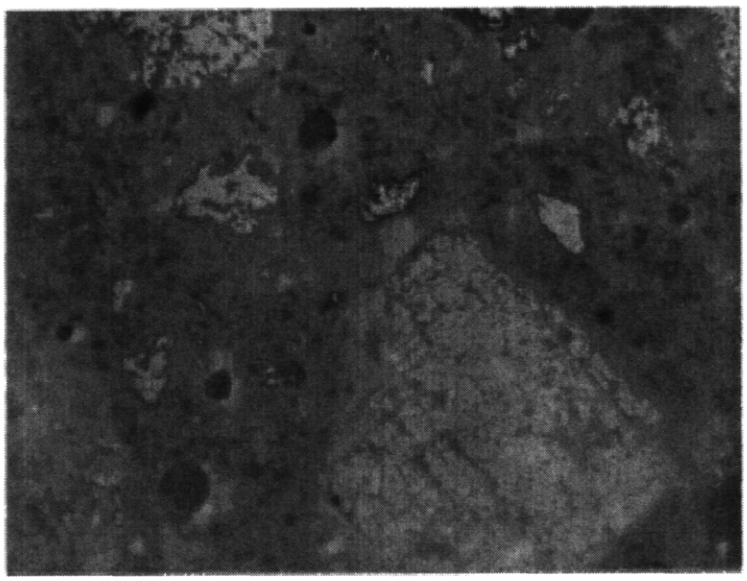

(b) Normal-cured specimen from D-5#9

Figure 3-20: Photographs of surfaces of low w/c specimens of Case D-5 at a magnification of 50x

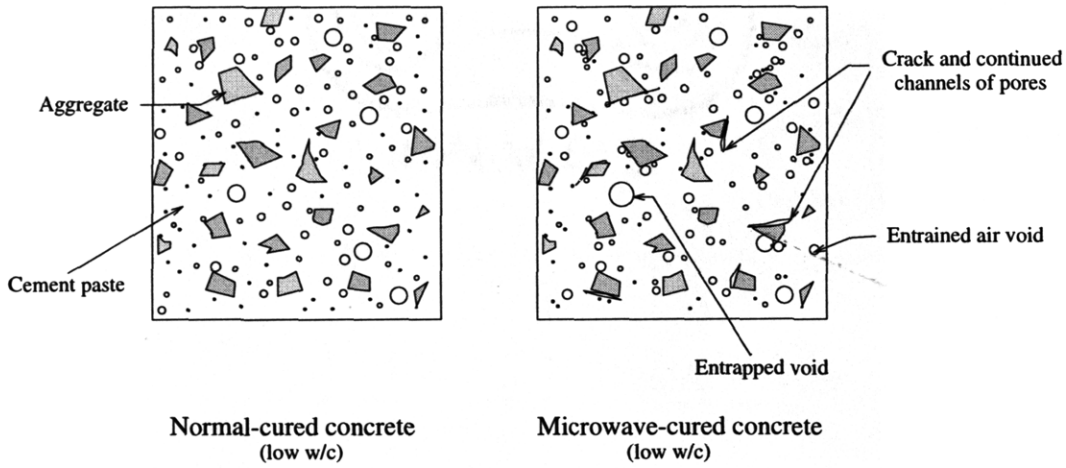

Figure 3-21: Drawing of air-void system of low w/c air-entrained concrete under normal curing versus microwave curing

microwave affects the air-void system of concrete, the drawing of the air-void system for high w/c concrete under microwave curing is compared to that of normal curing (see Figure 3-23).

To see the effect of spacing factor on the durability, Case D-3#2 representing microwave-cured concrete is compared to Case D-3#6 representing normal-cured concrete and it is found that the spacing factor value of the former is higher than that of the latter while the durability factor of the former is lower than that of the latter. Since there is more freezable water in high w/c paste, the need for lower spacing factor or adequate air-void system is important in order to allow the pressure to be relieved in a proper manner during freezing. If the spacing factor is not small enough, concrete will deteriorate more as it continues to be exposed to freeze-thaw cycles.

In summary, the spacing factor becomes the most dominant factor to resist frost attack for microwave-cured high w/c concrete and it is believed to be the only cause for microwave-cured specimen to obtain a lower durability factor than the normal-cured specimen.

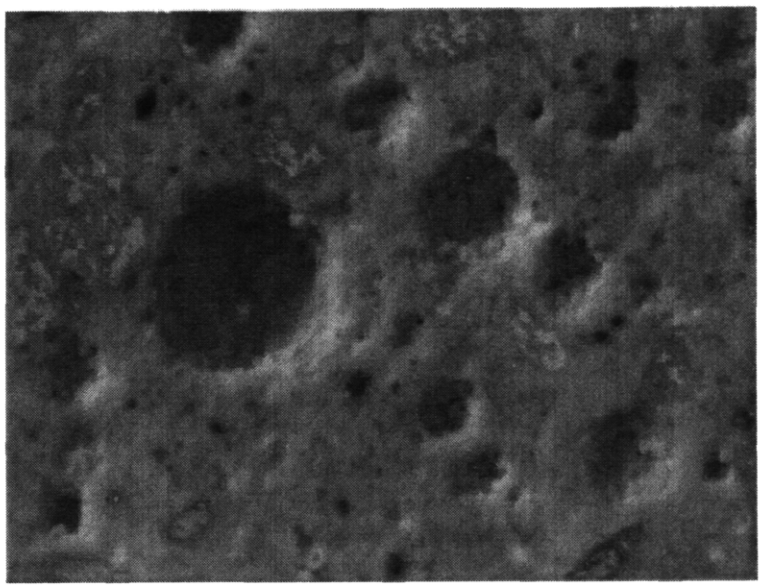

(a) Microwave-cured specimen from D-2#2

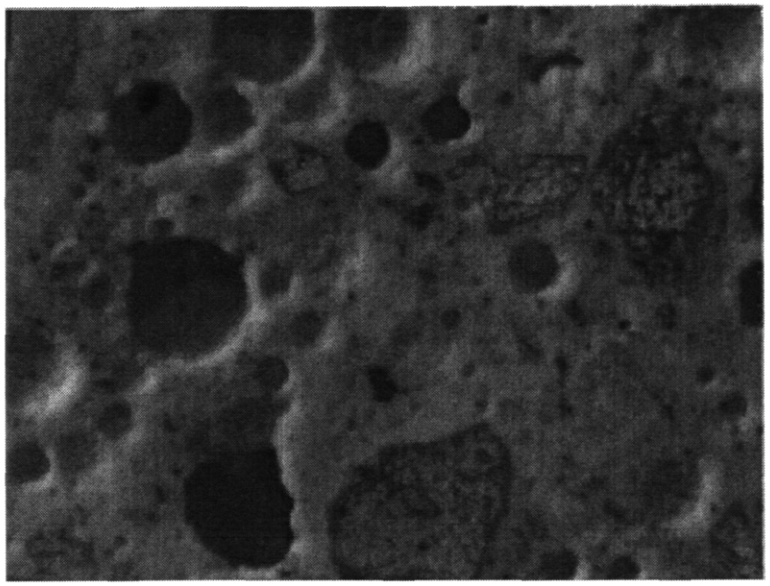

(b) Normal-cured specimen from D-2#6

Figure 3-22: Photographs of surfaces of high w/c specimens of Case D-2 at a magnification of 50x

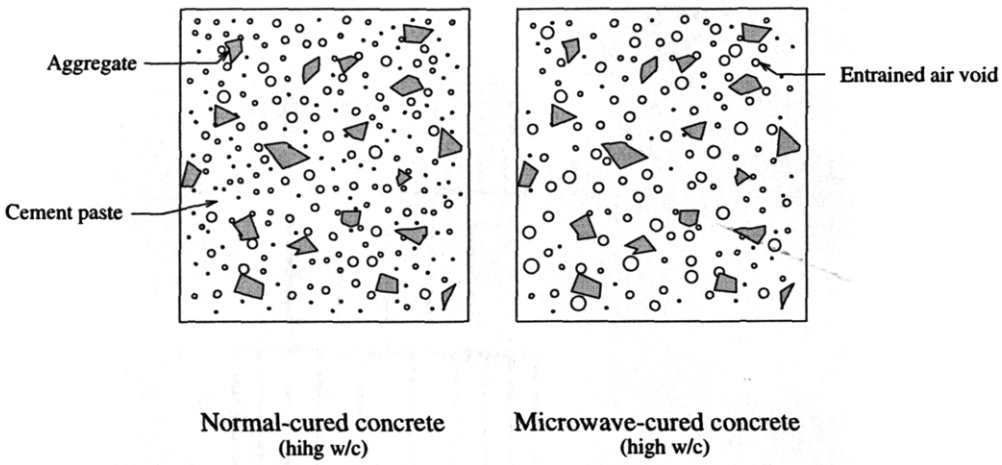

Figure 3-23: Drawing of air-void system of high w/c air-entrained concrete under normal curing versus microwave curing

Summary

As shown in Tables 3.2 and 3.3, it can be summarized that the effect of denser mix gives higher freeze-thaw durability than the effect of better air-void system (i.e., smaller spacing factor). This is supported by the comparison between the freeze-thaw resistance result of the denser mix of Case D-5#4 and that of the better air-void system of Case D-3#2. This is mainly because the effect of less freezable water in Case D-5#4 is more important to freeze-thaw resistance than the effect of lower spacing factor in Case D-3#2.

3.5.2 Use of data from loss of mass as the indicator of freeze-thaw durability

In general, loss of mass during freeze-thaw cycles in water is mainly due to surface scaling, but it can be more severe if internal cracking of concrete occurs simultaneously. Figures 3-13 through 3-17 show the relationship between loss of mass and freeze-thaw cycles.

Comparing the results of the mass loss as shown in Figures 3-13 through 3-17 to the results of the relative dynamic modulus of elasticity in Table 3.2, the relationship between the decrease of the relative dynamic modulus of elasticity and the loss of mass can be established. It is quite clear that loss of mass of the sample

correlates well to the decrease of the relative dynamic modulus of elasticity of concrete. Therefore, the significant loss of weight of the concrete can be used as an extra indicator of frost damage in the experiment.

3.5.3 Effect of the length difference of the specimens on freeze-thaw durability

Since the height of the microwave oven limits the size of the specimen under microwave curing, 3-inch by 8-inch cylinder is used rather than 3-inch by 11-inch cylinder which is the minimum size of cylinder required by the ASTM C 666-92. Therefore, to study the effect of the length difference on the durability factor of the normal-cured specimen, two 3-inch by 11-inch normal-cured specimens from Cases D-2, D-3, and D-4, and one specimen from Case D-5, are compared against the 3-inch by 8-inch normal-cured specimens from each case. It can be concluded from Table 3.2 that there is no significant difference in durability factor among 3 by 8 and 3 by 11 specimens of any case. Also, their mass changes are about the same as shown in Figures 3-13 through 3-17.

3.6 Conclusion

In conclusion, the significant findings are as follows:

- In normal curing, the frost resistance of low w/c concrete is proved to be better because of its low permeability and low amount of freezable water while that of high w/c concrete is mainly due to the smaller spacing factor and the higher air content.

- The microwave-cured air-entrained concrete need an adequate air-void system, similar to the normal-cured air-entrained concrete.

- In microwave curing, the freeze-thaw resistance of specimens with low w/c with a relatively low air content is the same as (or even better than) that of specimens with high w/c and high air content. In other words, the effect of denser mix gives higher freeze-thaw durability than the effect of better air-void system (i.e., smaller spacing system).

- For high w/c concrete, microwave can cause small air voids to coalesce together and become larger during the initial stage of microwave curing, resulting in bigger voids and larger spacing factor, which can be detrimental to the frost resistance. On the other hand, for microwave-cured low w/c concrete, the reduced freezable water, increased air content, and increased formation of cracks and voids help resisting frost attack.

- Use of spacing factor as an indicator for freeze-thaw resistance is ambiguous. The spacing factor is only useful for comparative study in concrete with high w/c with large amount of air content.

- In our experiments, loss of weight of the sample correlates well with decrease of the relative dynamic modulus of elasticity of concrete. Therefore, like the relative dynamic modulus of elasticity, it can be used as an indicator of frost damage in the concrete.

- Length of the sample (3 by 8 inch versus 3 by 11 inch) has no significant effect on the freeze-thaw resistance.

Chapter 4

Complex Permittivity Measurement of Concrete

4.1 Introduction

Because concrete is a non-magnetic material, its electromagnetic properties are fully characterized by its complex permittivity. The real part of the permittivity is a measure of how much energy from an external electric field is stored while the imaginary part represents how lossy the material is due to the external electric field [7]. Once the concrete is placed inside the cavity and the microwave power is turned on, the electric and magnetic fields will penetrate into its interior and part of the microwave energy will be coupled to the material and dissipated as heat. Therefore, the complex permittivity which is frequency dependent is essential in this microwave heating problem.

Since the state of concrete is changing continuously over time due to the reaction of water and cement, the complex permittivity also changes. To include the evolution of complex permittivity as well as the additional heat from microwave energy to establish the actual evolution of permittivity of heated concrete at microwave frequency, the traditional maturity concept is employed. The maturity concept is widely used in predicting

the strength of concrete from its thermal history and its current state for safe removal of formwork in concrete construction.

Maturity concept simply states that concrete of the same composition with equal maturity will have the equal strength no matter how different their actual temperature-time histories are [41]. However, it does not take the influence of early temperature into consideration and since the early temperature can affect the long term strength tremendously, some adjustment is needed [50].

In this work, the maturity concept is used to establish the permittivity evolution of heated concrete. Firstly, the complex permittivity of concrete during the heating period has to be determined and the transmission line method is selected for the measurement. Secondly, the average temperature is monitored and recorded continuously throughout the heating period. Several heating conditions are applied in order to find the most representative permittivity-maturity relationship for microwave heating. Once the relationship is found and the thermal history is known, maturity can be computed and its corresponding complex permittivity will be determined.

This chapter includes (i) permittivity of concrete, (ii) theory for the permittivity measurement, (iii) measurement setup and procedure, (iv) permittivity results of water, normal-cured concrete and concrete cured under several temperature histories, (v) permittivity-maturity relation of heated concrete, (vi) suggestion, and (vii) conclusion.

4.2 Permittivity of Concrete

For concrete whose permeability is close to free space permeability ($\mu_o = 4\pi \times 10^{-7}$ henry/meter), its electromagnetic properties are fully characterized by its complex permittivity, ϵ, which can be defined as:

$$\epsilon = \epsilon' + i\epsilon''$$

where ϵ' = the real part of the complex permittivity of material, and

ϵ'' = the imaginary part of the complex permittivity of material.

By dividing the above equation by the permittivity in free space ($\epsilon_o = 8.85 \times 10^{-12}$ farad/meter), the relative complex permittivity, ϵ_r, can be obtained as follows:

$$\epsilon_r = \epsilon'_r + i\epsilon''_r$$

where ϵ'_r = the real part of relative complex permittivity or *dielectric constant, and*

ϵ''_r = the imaginary part of relative complex permittivity or *loss factor.*

The imaginary part of complex permittivity, representing the loss in the material, is the main reason for the microwave energy to couple the material and cause thermal dissipation during microwave heating. Typically, in most materials, all losses are due to either the conductivity (ionic conduction) or the friction among polarized molecules (dipole rotation) or both [33]. Further reviews on loss mechanisms could be found in [33], [28], and [49].

In many references, the loss tangent ($\tan \delta$) is mentioned in place of loss factor and it is defined as follows:

$$\tan \delta = \frac{\epsilon''_r}{\epsilon'_r}$$

4.3 Theory for the Measurement Method

Fresh concrete, composed of water, aggregates, and cement, is a high loss material (i.e., large imaginary part of permittivity). To measure its complex permittivity with accuracy, the transmission line method, which is suitable for the measurement of both permittivity (ϵ) and permeability (μ) of absorptive materials, with the use of simple fixtures, is selected [14]. With this method, large sample volume is used in order to obtain appropriate and average dielectric property of a heterogeneous material such as concrete. It involves placing a rectangular-shaped concrete sample (liquid or solid state) inside a transmission line (waveguide section) backed with a metallic plate. A signal is then launched from the Network analyzer at the frequency of 2.45 GHz to the sample. The receiver will then detect the reflected signals from the sample. To compute the complex permittivity of a material at each state with accuracy, two samples with different optimal lengths

are prepared and the magnitudes of their corresponding reflection coefficients are used in the appropriate formula. It is noted that only the magnitude of reflection coefficient is used because the phase value is quite sensitive and not reliable.

The optimum length is chosen in such a way that the relative magnitude of reflected signal is closed to 1.0 due to that fact that the magnitude error for reflected signal increases when its magnitude approaches 0 and decreases when approaching 1 [14]. Therefore, if the permittivity of the material under test is generally known, the plot of magnitude of reflected signal versus length will help to identify the optimum lengths to be used in the measurement. However, the selected length should not be too small to handle. For example, the permittivity of 25°C water at 3 GHz is known to be $(76.7+12.0i)$ [9]; by plotting out the reflected value versus thickness, it is easy to identify the range of optimum length. From Figure 4-1, the ranges of the optimum length are (i) 0.60-0.80 cm and (ii) 1.3-1.5 cm, for example.

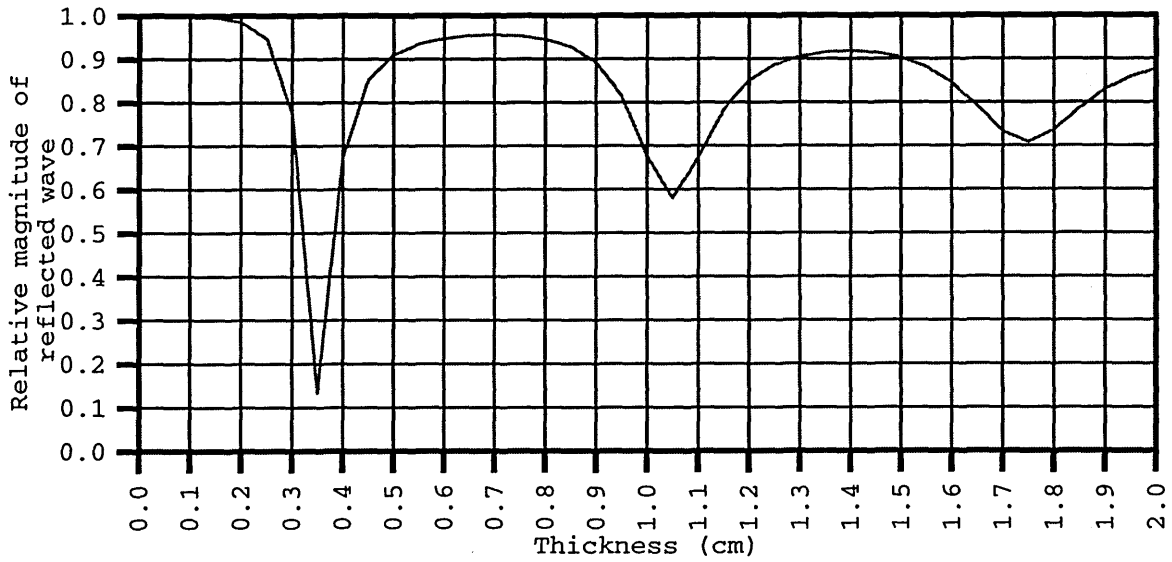

Figure 4-1: Relation between thickness of 25°C water with $(76.7 + 12.0i)$ backed with a metal plate and its relative magnitude of reflection coefficient

The formula to compute the reflected valued can be obtained by applying the field theory to solve the problem of a two-layered media in rectangular waveguide. By applying the appropriate boundary conditions,

the reflection coefficient, R, can be expressed as follows: (see Appendix I for derivation)

$$R = \frac{R_{01} + R_{12}e^{i2k_{1z}(d1-d0)}}{1 + R_{01}R_{12}e^{i2k_{1z}(d1-d0)}} e^{i2k_z d_0} \tag{4.1}$$

where $k_x = \frac{\pi}{a}$,

$k_{0z} = \sqrt{w^2\mu_0\epsilon_0 - {k_x}^2} = \sqrt{\left(\frac{2\pi f_o}{c}\right)^2 \mu_{r0}\epsilon_{r0} - \left(\frac{\pi}{a}\right)^2}$,

$k_{1z} = \sqrt{w^2\mu_1\epsilon_1 - {k_x}^2} = \sqrt{\left(\frac{2\pi f_o}{c}\right)^2 \mu_{r1}\epsilon_{r1} - \left(\frac{\pi}{a}\right)^2}$,

R_{01} = reflection coefficient for wave propagating from region 0 to 1,

$= \frac{1-p_{01}}{1+p_{01}} = -R_{10}$,

$p_{01} = \frac{\mu_0 k_{1z}}{\mu_1 k_{0z}} = \frac{1}{p_{10}}$,

R_{12} = reflection coefficient for wave propagating from region 1 to 2,

f_o = the measurement frequency (2.45 GHz),

c = speed of light (3×10^8 meter/sec),

a = width of the rectangular waveguide (10.922 cm for WR 430),

ϵ_{r0} = the relative complex permittivity for region 0 (air)

ϵ_{r1} = the relative complex permittivity for region 1 (material under test or MUT),

μ_{r0} = the relative complex permeability for region 0

μ_{r1} = the relative complex permeability for region 1

d_0 = z-axis coordinate for region 0,

d_1 = z-axis coordinate for region 1, and

$i = \sqrt{-1}$.

This measurement technique uses the perfect conductor as the second layer. As a result, R_{12} is set to -1. Thus, the reflection coefficient formula when short is connected, R_S, is given by (where d_0 is set to zero)

$$R_S = \frac{R_{01} - e^{i2k_{1z}(d1)}}{1 - R_{01}e^{i2k_{1z}(d1)}} \tag{4.2}$$

After two reflection coefficients are obtained, method of trial and error is used to solve for the relative complex permittivity by limiting the percent error between the magnitude of calculated and measured reflected values of each optimal-length specimen to be within a certain range (for example 0.05%-0.5%). An example of this calculation is given in Appendix II.

4.4 Measurement

In this section, the measurement set-up is briefly described and followed by the experimental procedure.

4.4.1 Measurement set-up

A typical transmission line set-up makes up of

1. A HP 8510 network analyzer system consisting of
    - a signal source or the sweeper to provide the stimulus
    - the test set providing the signal separation and the receiver input stage
    - the vector network analyzer including signal processor and display (see Figure 4-2)

Figure 4-2: HP 8510 vector network analyzer

2. A waveguide(WR-430)-to-coaxial adapter (see Figure 4-3)

3. Two WR-430 waveguide sections (5.461 cm width x 10.922 cm height or 2.15 inch x 4.30 inch) to ensure the ability to contain any solid or liquid material (each for an optimum length)

4. A metallic plate

Figure 4-3: An example of waveguide-to-coaxial adapter

4.4.2 Measurement procedure

The measurement procedure for computing the permittivity of any high loss materials can be listed as follows:

1. Perform S_{22}[1] 1-port calibration with the 3.5mm coaxial interface calibration kit supplied by Hewlett-Packard to eliminate the systematic measurement errors, which is stable and repeatable, due to the imperfections of the system. Random errors such as noise and temperature, which cannot be avoided in the calibration, have to be minimized in order to obtain reliable measured data by (i) obtaining good measurement practices and (ii) minimizing physical movement of the test port cables and the fixture after calibration [7]. It is noted that the calibration is done with the 3.5mm coaxial interface calibration kit supplied by Hewlett-Packard instead of the WR-430 waveguide calibration kit following the procedures in [15] because the reflection coefficients obtained from the latter calibration kit are not satisfactory.

[1] defined as the relative magnitude of reflected signal measured at port #2 while a signal is originally launched from the same port.

2. Connect the 3.5mm coaxial to the waveguide-to-coaxial adapter.

3. Insert sample material with the optimum length into the waveguide section and closed the waveguide end with the metallic plate (see Figure 4-4). In case of liquid or wet material, lossless clear plastic tape will be used to confine material within the waveguide section.

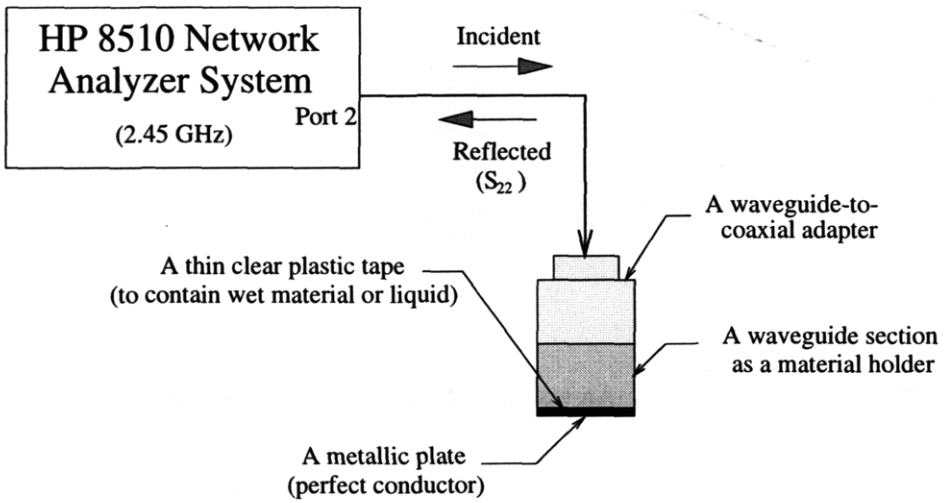

Figure 4-4: A setup to measure reflection coefficient when a metallic plate is at the end of waveguide

4. Connect the material waveguide section to the waveguide-to-coaxial adapter and then connect the adapter to the cable of test set which is connected to the network analyzer.

5. Measure the scattering parameters (i.e., the reflected signal or S_{22}). The source from the network analyzer system will launch a signal at a defined frequency of 2.45 GHz to the material under test (MUT). The receiver tuned to that frequency will detect the reflected signal from the material. The network analyzer system will then process the measured data and display the magnitude and phase. Since the phase value is not so accurate, only magnitude of reflected value will be used to compute the permittivity of MUT.

6. Measure another reflected value with another optimum length.

7. Use these two reflected values to compute for the real and imaginary parts of permittivity of MUT.

4.5 Results

To check the validity of the described method, the permittivity of water at room temperature is measured and compared with the published value by Von Hippel[9]. In addition, the permittivities of normal-cured fresh concrete at several ages after mixing are measured to ensure that the values are reasonable when compared to the permittivities of hardened concrete measured by Rhim[39] using probe technique. Then the required measurements of fresh concrete cured under several heating conditions are performed.

4.5.1 Water

By limiting the percent error between the magnitude of calculated and measured reflected values to be within 0.05% for each optimum length, reasonable result can be obtained. Table 4.1 shows average permittivity of room-temperature water measured and computed at approximately 0.68- and 0.73-cm thicknesses. Its permittivity of $(79.8 + 11.5i)$ is close to the reported value of $(76.7 + 12.0i)$ for 25°C water at 3 GHz in [9].

Table 4.1: Result of measured permittivity of room temperature water at 2.45 GHz

Material	dielectric constant	loss factor
water at room temperature	79.8	11.5

4.5.2 Fresh concrete cured normally

For concrete in general, the optimum length should be in the range of 1.7 to 2.0 cm based on the reflection coefficient calculation with use of permittivity value of $(11.3 + 1.64i)$ reported by Rhim[39]. Therefore, in this experiment, the approximated lengths of 1.7 cm and 1.9 cm are chosen to be used.

Figures 4-5 and 4-6 show the measured dielectric constant and loss factor of both 0.45 and 0.50 w/c concrete at ages between 0.5 to 24 hours, respectively. It is noted that since the uncertainty in permittivity

measurement of heterogeneous material is higher than that of homogeneous material, the percent error between the magnitude of calculated and measured reflected values for the former is set to be higher than that of the latter. For concrete, the percent error is set to be between 0.1-0.5% and it is found that the computed complex permittivities are reasonable and fall within the expected range.

4.5.3 Fresh concrete cured under different temperature histories

In order to compute the power dissipated inside fresh concrete during microwave heating, the actual evolution of permittivity in heated concrete has to be determined first. The evolution of permittivity of concrete, even under normal curing, is complex. By applying the microwave energy, more complication arises. This is because the evolution involves several parameters such as composition of concrete, heat of cement hydration, microwave power dissipation, water evaporation due to heat, and thermal properties of concrete. To simplify the problem, it is assumed that the change of permittivity of concrete depends only on the maturity of concrete. This assumption is similar to the assumption made in the maturity concept used widely in concrete construction to predict the strength of hardening concrete for safe formwork removal. However, there will not be one unique curve representing all kinds of concrete cured under different temperature histories. This is due to the drawback of maturity concept, which is the neglecting of the influence of early age temperature on the degree of hydration which can greatly affect concrete properties including strength and permittivity.

To obtain the permittivity-maturity relation of heated concrete, fresh concrete *after 30 minutes of mixing with water* will be cured under several temperature histories and its average interior temperature will be monitored and recorded throughout the measurement. It is assumed that heating is uniform since the specimen is relatively thin and small. Each measurement will take about 1-1.5 minute to obtain the reflection coefficient. To complete the data curve, the specimen will be taken out of the curing chamber at about 10-minute intervals and will then be returned to the chamber until reaching 45 minutes of curing. By using the maturity concept, the permittivity-maturity relation of heated concrete can be obtained and will be described in the next section.

Since it is generally known that the maturity equation is not suitable for concrete initially cured at different temperature [50], the reported results here will be arranged into two groups: low and high temperature range.

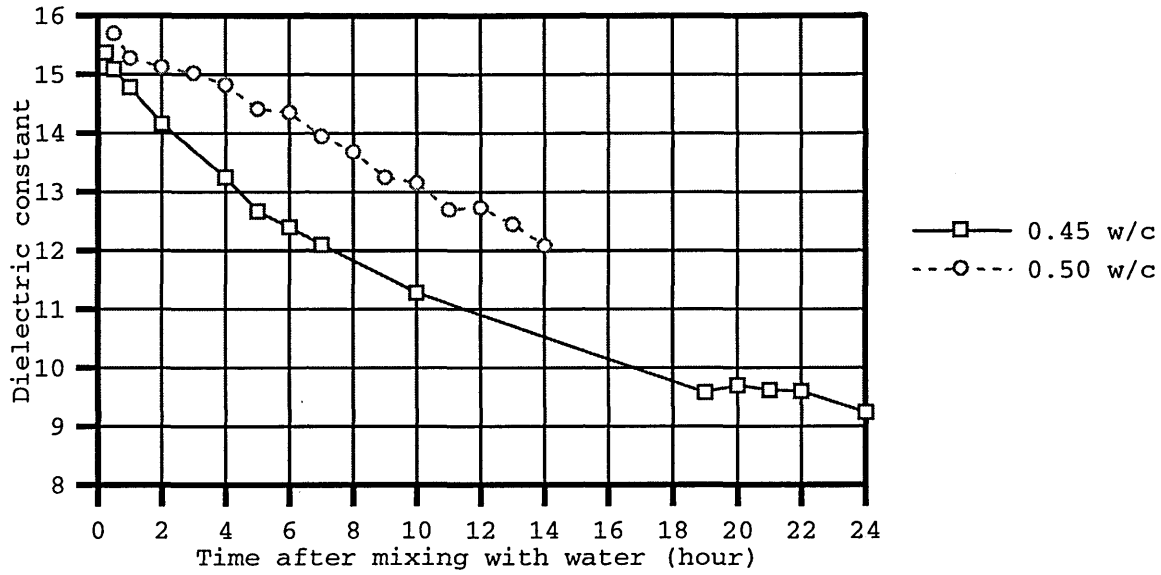

Figure 4-5: Plots of dielectric constant vs time after mixing of 0.45 and 0.50 w/c concrete cured normally

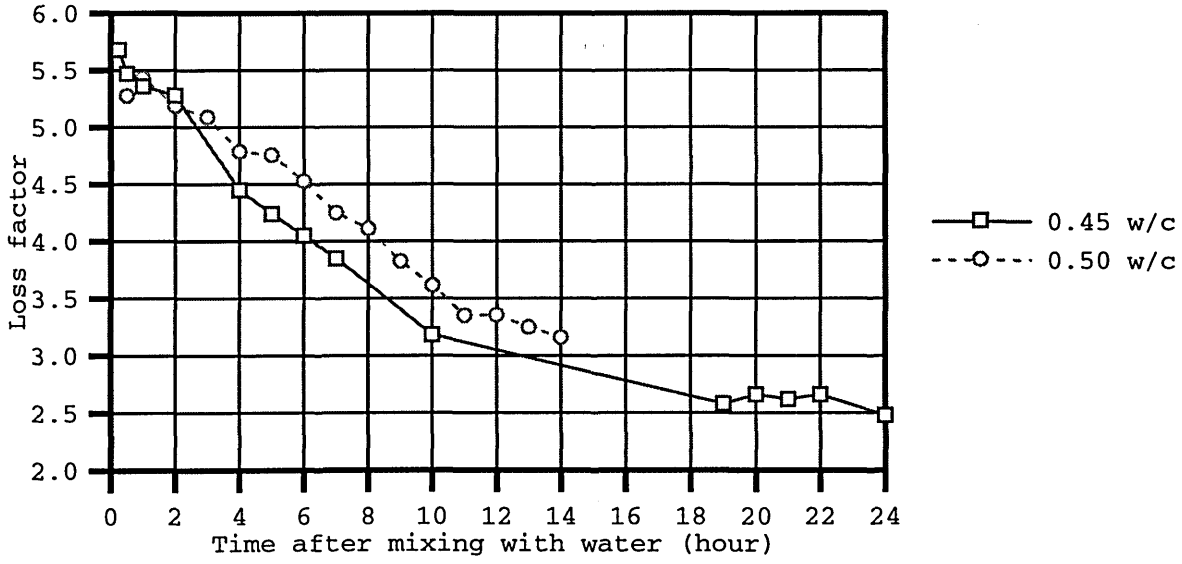

Figure 4-6: Plots of loss factor vs time after mixing of 0.45 and 0.50 w/c concrete cured normally

Low temperature range

Concrete with 0.50 w/c initially cured under 30 to 50°C for 45 minutes in this case is classified to be in the low temperature range. Its temperature histories in the first 45 minutes in the curing chamber are shown in Figure 4-7 and Figure 4-8 shows its thermal histories after 30 minutes of mixing with water for a 10-hour period. The plots of measured dielectric constant and loss factor versus time are shown respectively in Figures 4-9 and 4-10.

High temperature range

High temperature range includes 45-minute heating of 0.50 w/c concrete in the chamber whose temperature lies in between 70 to 140°C. Figure 4-11 illustrates its several measured temperature histories. The corresponding dielectric constant and loss factor results are shown in Figures 4-12 and 4-13, respectively. It is noted that the loss factor results vary a bit due to the fact that concrete is a non-homogeneous material whose properties vary and are not as consistent as those of a homogeneous material. However, the general trends are obtained and seem to be reasonable.

4.6 Permittivity-Maturity Relation of Heated Concrete

As mentioned before, maturity concept is used here to obtain the evolution of permittivity of concrete cured under different temperature histories even though it does not account for the effect of early age temperature on the degree of hydration which greatly influence properties such as strength and permittivity. It is used because it makes the derivation of permittivity evolution rule of heated concrete less complicated. However, some adjustment is needed. Fresh concrete under different initial curing temperature ranges will have their own well defined permittivity-maturity curves instead of having just one curve for all initial curing temperatures. In this work, permittivity-maturity curves are obtained for low and high ranges of initial curing temperatures.

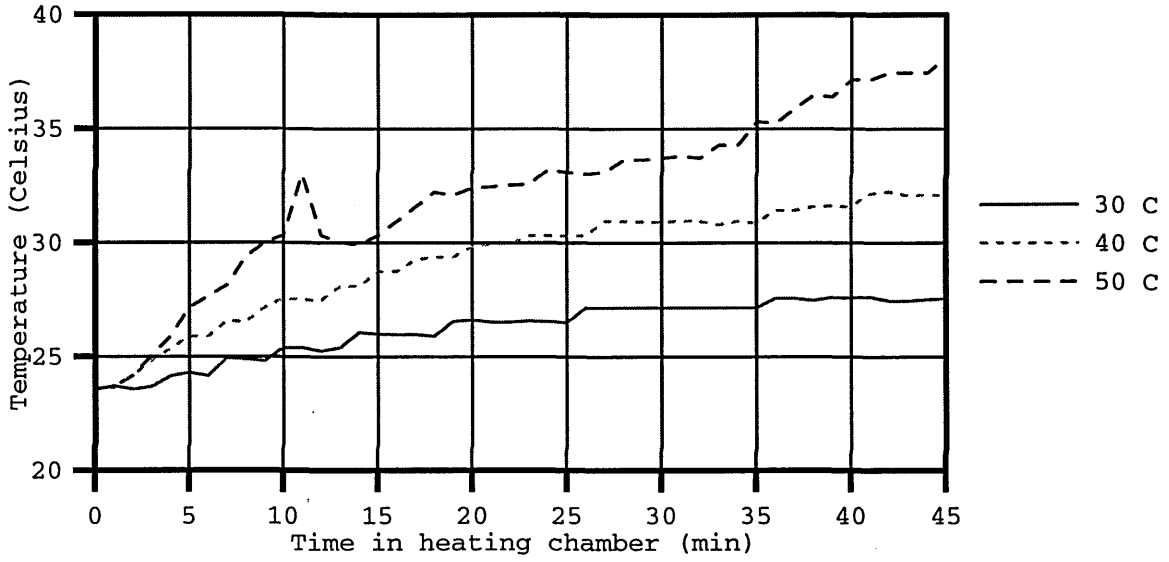

Figure 4-7: Plots of temperature vs time in the first 45 minutes in curing chamber of 0.50 w/c concrete cured under low range temperature history

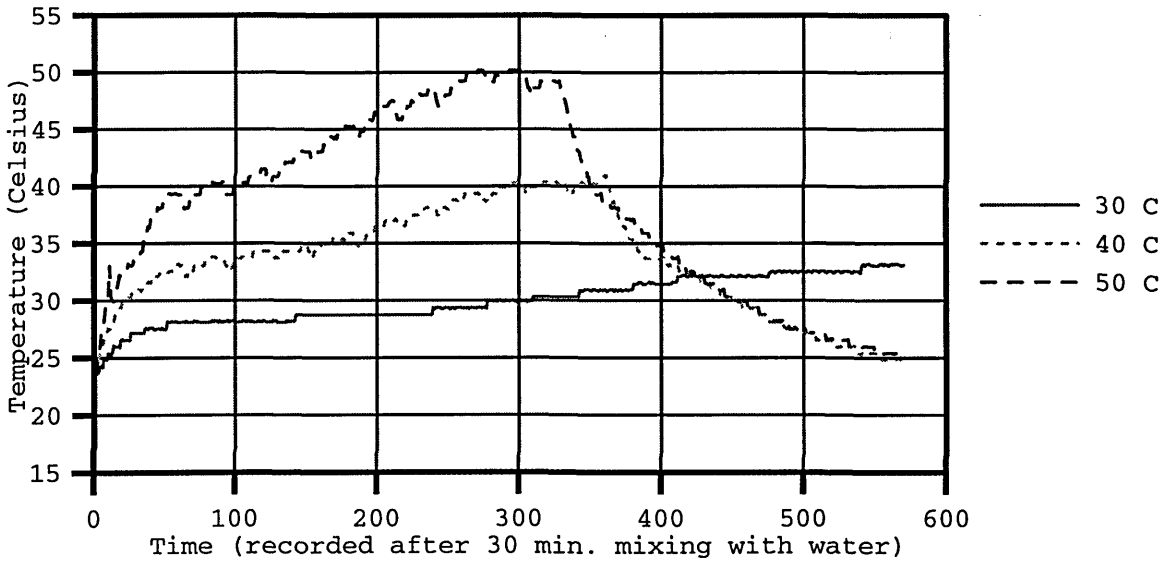

Figure 4-8: Plots of temperature vs time after 30 minutes mixing with water of 0.50 w/c concrete cured under low range temperature history

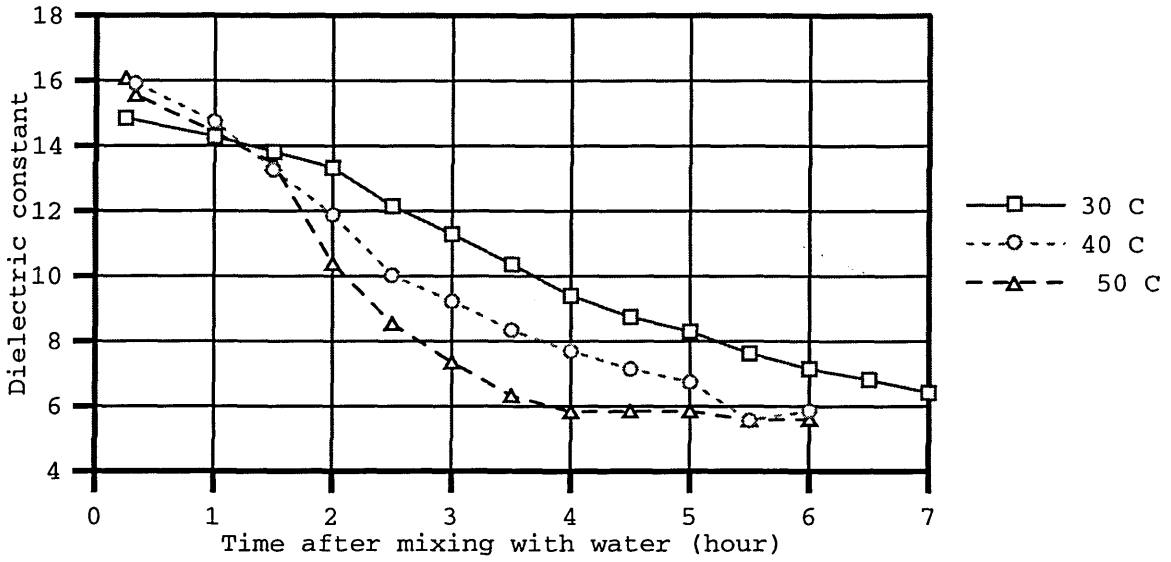

Figure 4-9: Plots of dielectric constant vs time after mixing of 0.50 w/c concrete cured under low range temperature history

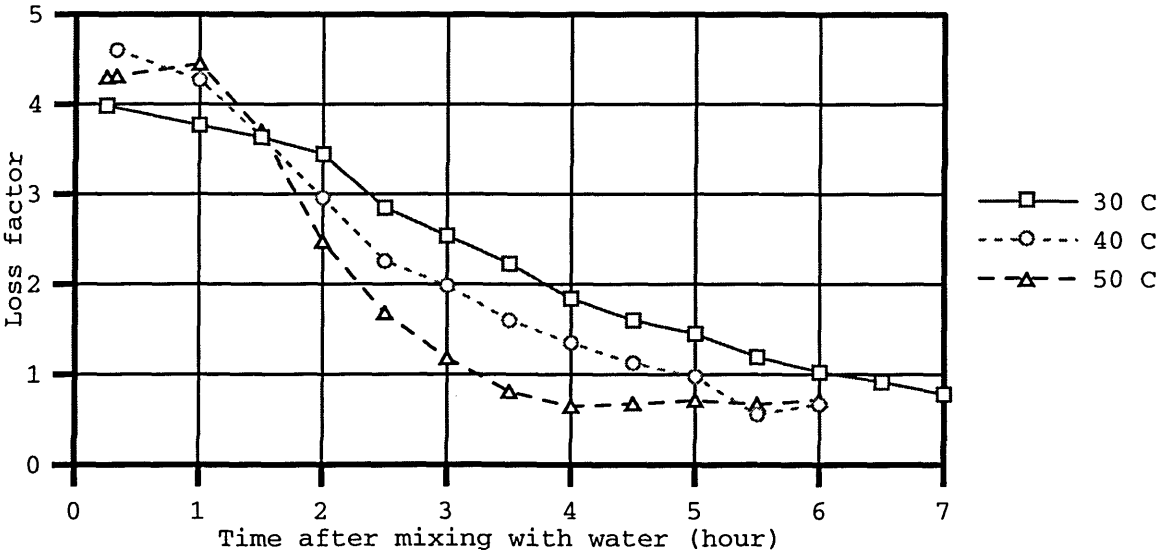

Figure 4-10: Plots of loss factor vs time after mixing of 0.50 w/c concrete cured under low range temperature history

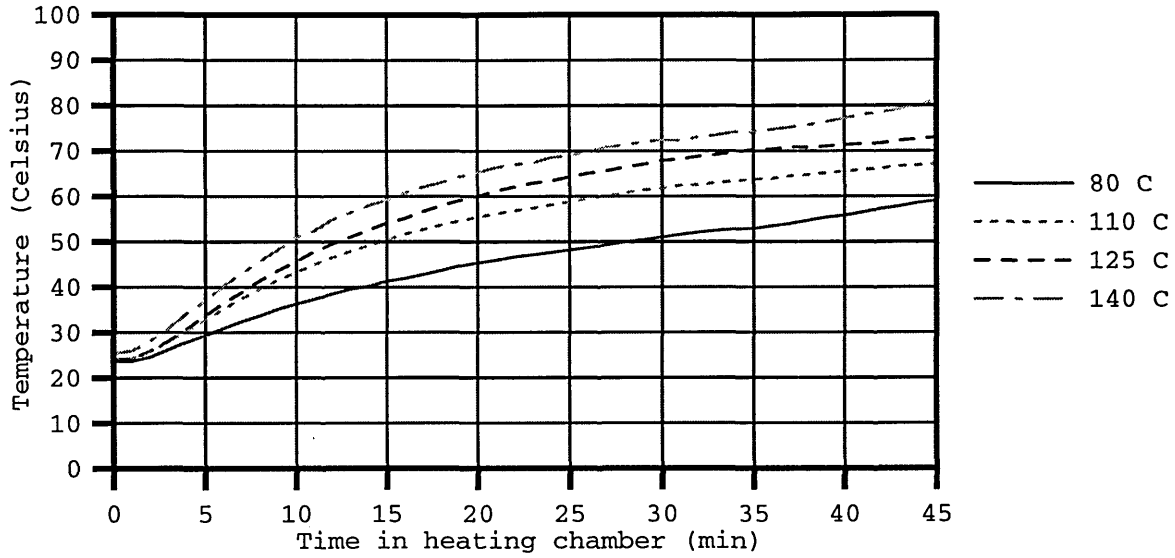

Figure 4-11: Plots of temperature vs time after mixing of 0.50 w/c concrete cured under high-range temperature history

To compute for maturity, the following equation introduced by [26, 34, 41] is used

$$M = \int_0^t (T - T_o)dt$$

where M = maturity at age t minute (unit in °C Minute),

T = temperature of concrete (°C), and

T_o = datum temperature (°C).

It is noted that T_o, or datum temperature (originally selected as the temperature when there is no gain in strength), should be set to the initial temperature. However, it is set to zero in this work for simplicity and due to the fact that all fresh concrete specimens have the same initial temperatures.

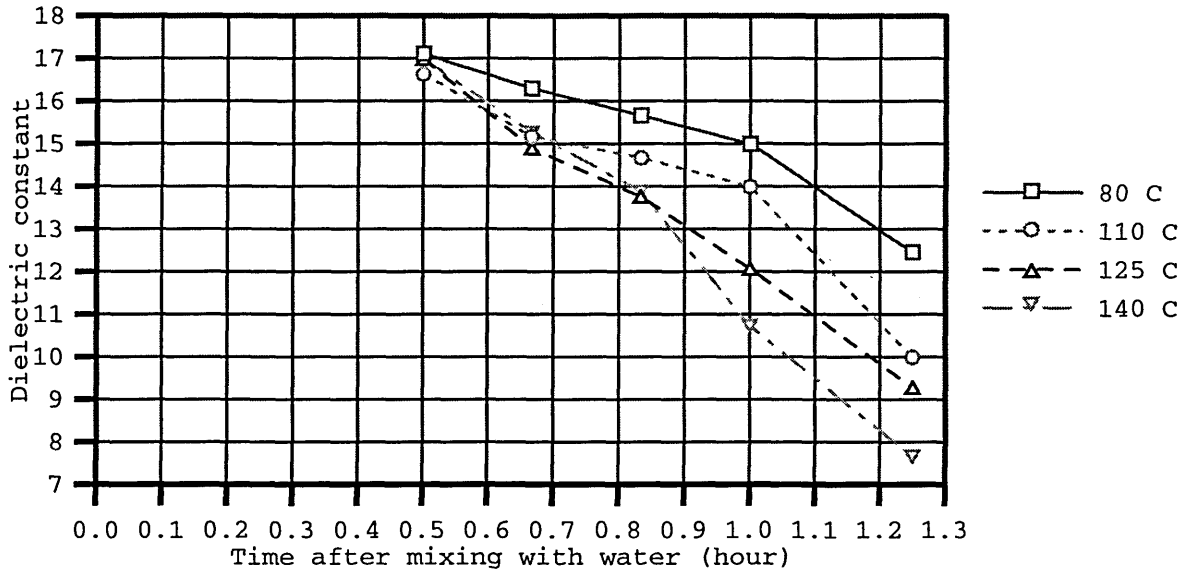

Figure 4-12: Plots of dielectric constant vs time after mixing of 0.50 w/c concrete cured under high-range temperature history

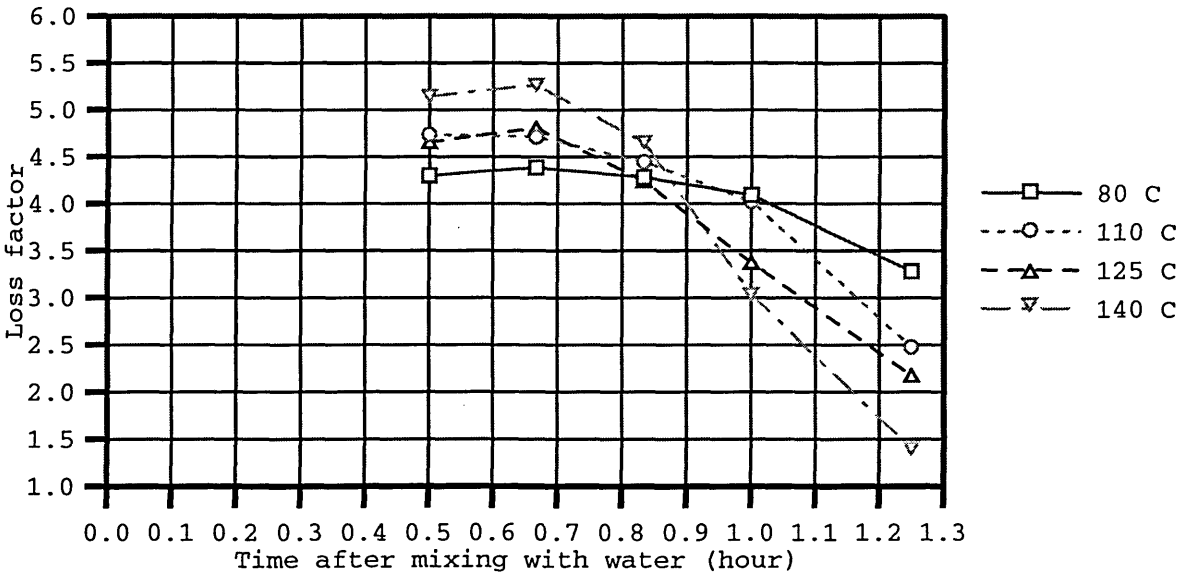

Figure 4-13: Plots of loss factor vs time after mixing of 0.50 w/c concrete cured under high-range temperature history

4.6.1 Low temperature range

Using the measured temperature history and the complex permittivity, the complex permittivity-maturity relations are shown in Figures 4-14 and 4-15. It is clear that there seems to be a consistent trend of permittivity vs maturity for temperature in this range. However, the average complex permittivity-maturity relation will not be calculated here since this temperature range is not in the interested range of temperature for microwave curing. This result is useful to prove that there will not be just a single curve to represent the permittivity-maturity relation for concrete cured at different temperature ranges.

4.6.2 High temperature range

For the high temperature range which is representative of microwave curing in the interested range of temperature, Figures 4-16 and 4-17 show its complex permittivity-maturity relation. Again, there is an apparent trend for permittivity-maturity relationship of concrete heated within the range of temperature. To summarize, the complex permittivity-maturity relation can be approximated with the following experimentally-fitted expressions.

For dielectric-maturity relation,

$$\epsilon'_r = (\text{-}0.00288 \times M) + 16.81 \text{ ; for any } M\ (^{\circ}C \cdot Min)$$

and for loss factor-maturity relation,

$$\epsilon''_r = \begin{cases} 4.71 & \text{; for } 0 \leq M \leq 540\ (^{\circ}C \cdot Min) \\ (-0.00132 \times M) + 5.42 & \text{; for } 540 < M < 3000\ (^{\circ}C \cdot Min) \end{cases}$$

4.7 Suggestion

4.7.1 Measurement with only one optimum length

If the perfectly matched load of rectangular waveguide is available, the complex permittivity measurement can be done with only one optimum length of material. However, two reflected signals are still needed: one

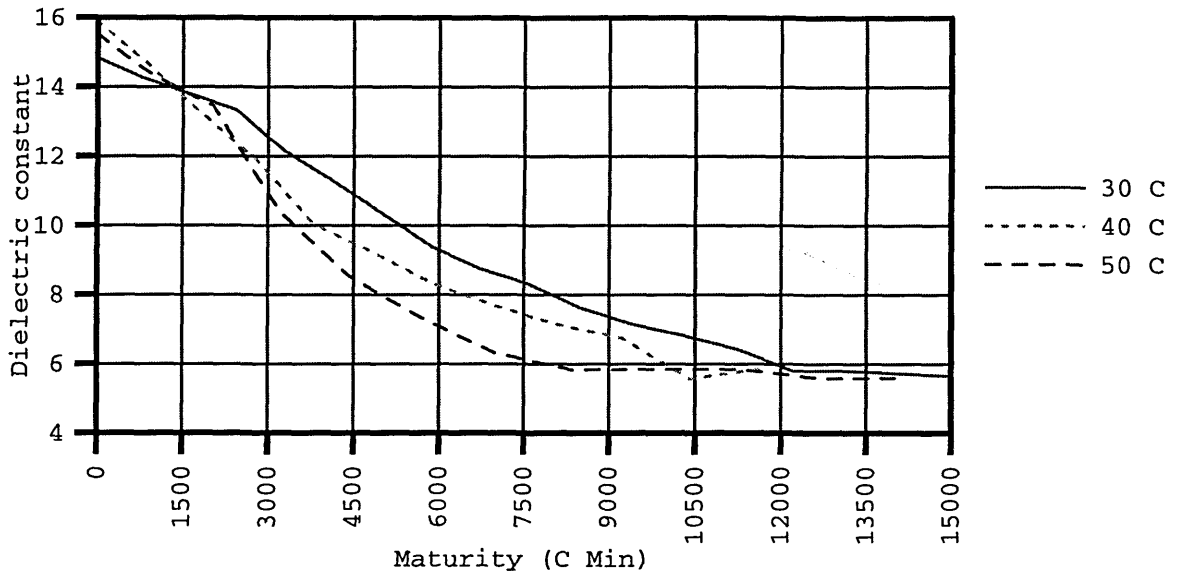

Figure 4-14: Permittivity (real part)-maturity relation of 0.50 w/c concrete cured under low-range temperature history

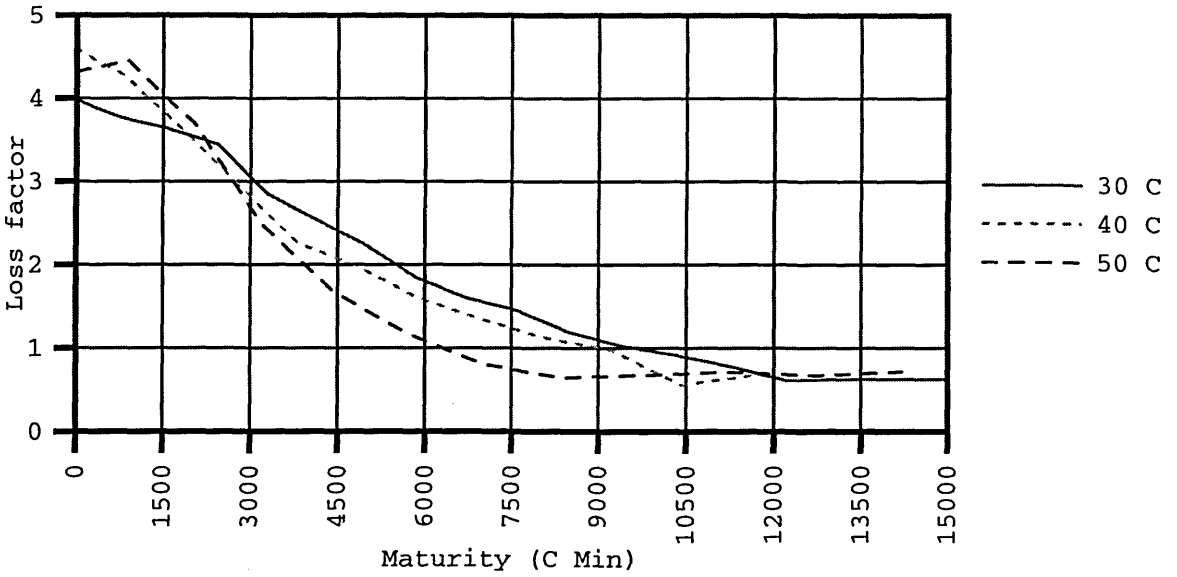

Figure 4-15: Permittivity (imaginary part)-maturity relation of 0.50 w/c concrete cured under low-range temperature history

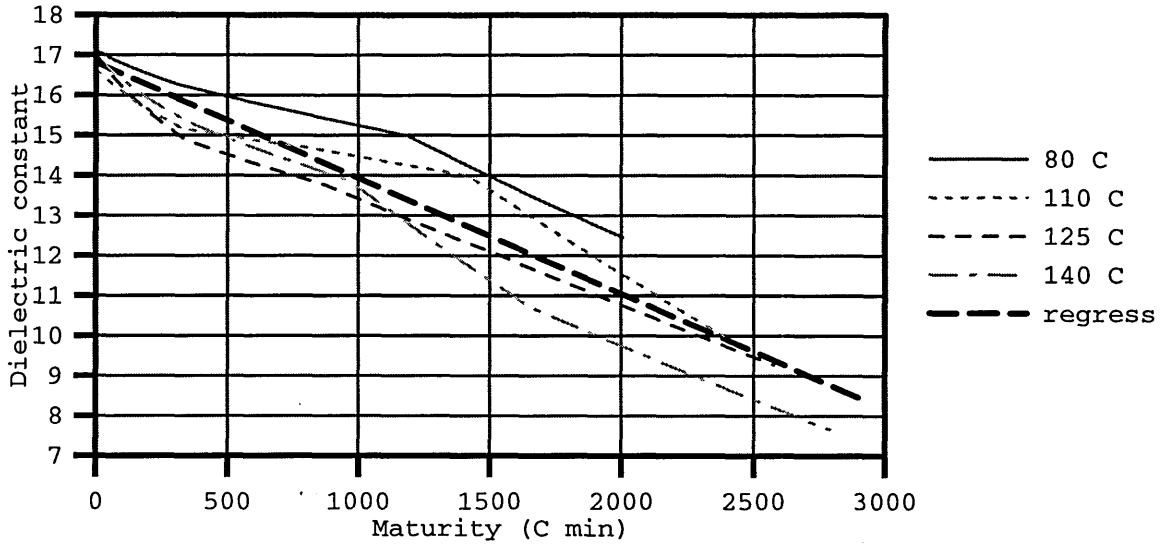

Figure 4-16: Permittivity (real part)-maturity relation of 0.50 w/c concrete cured under high-range temperature history

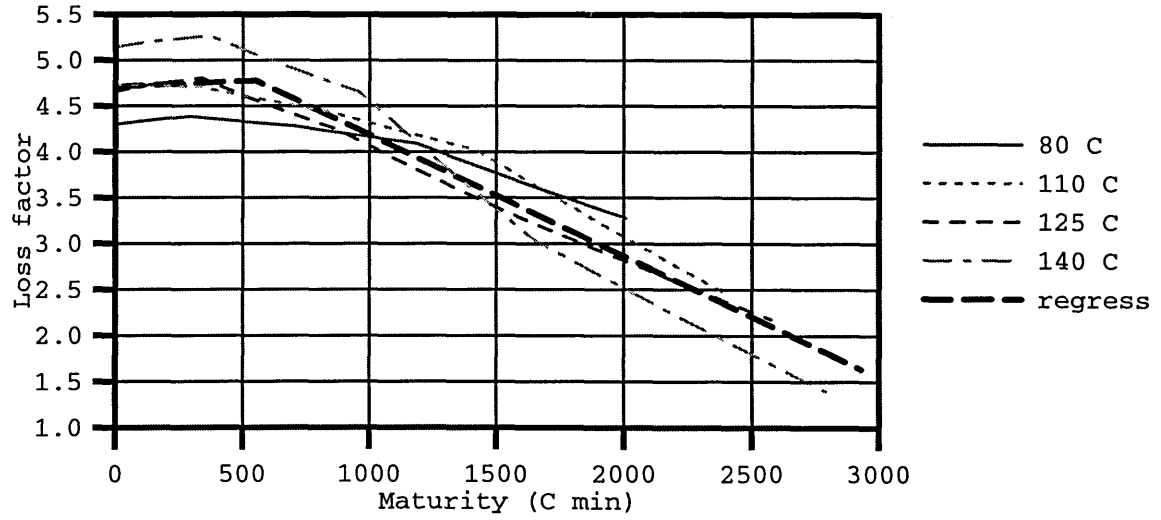

Figure 4-17: Permittivity (imaginary part)-maturity relation of 0.50 w/c concrete cured under high-range temperature history

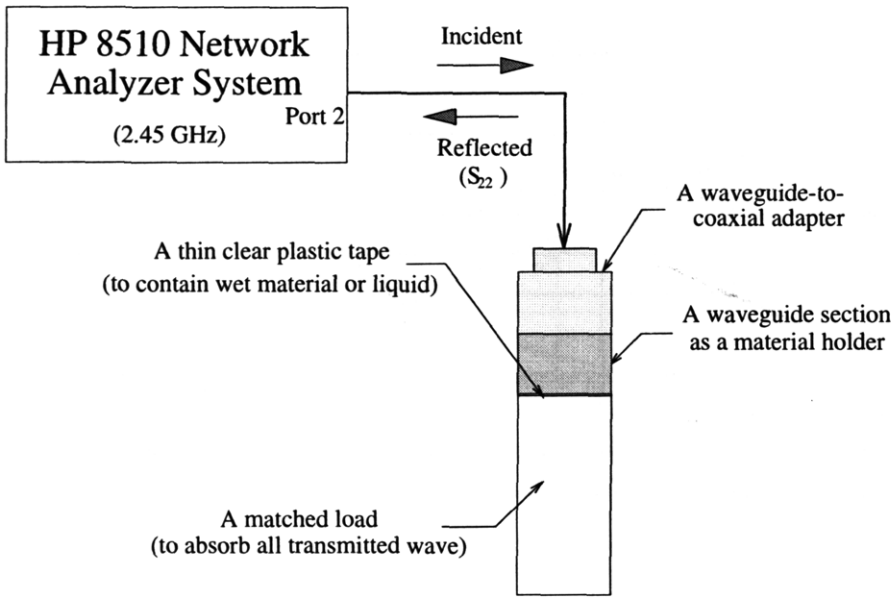

Figure 4-18: A setup to measure reflection coefficient when matched load is at the end of waveguide

from the waveguide with a short end and the other one from the waveguide connected to the load at its end. The equation for reflection coefficient when load is connected, R_L, (adapted from equation (4.1) but $R_{12} = R_{10} = -R_{01}$ and $d_0 = 0$) can then be written as follows:

$$R_L = \frac{R_{01} - R_{01}e^{i2k_{1z}(d1)}}{1 - R_{01}R_{01}e^{i2k_{1z}(d1)}}$$

By using the above equation along with the equation (4.2) for the waveguide with short end, the complex permittivity of the material can be computed in the same way as before. Moreover, it is noted that if the load is not perfectly matched, there will be some error in the measured value and of course the result will not be so accurate.

4.8 Conclusion

Based on the results in this work, it can be concluded that the complex permittivity-maturity relation of concrete cured under different temperature histories can be roughly established with the use of maturity concept, although different maturity relation are required for different temperature ranges.

4.9 Appendix I. - Two-Layered Medium in Rectangular Waveguide

This derivation of reflection coefficient for a two-layered medium inside the rectangular waveguide is based on the derivation of the reflection coefficient of a plane wave incident on a layered medium using field theory described in [20].

For region l of layered medium inside the rectangular waveguide (see Figure 4-19(a)), the field components of TE_{10} wave propagating in $-\hat{z}$ direction can be written as

$$E_{yl} = \left(A_l e^{ik_{lz}z} + B_l e^{-ik_{lz}z}\right)\left(e^{ik_x x} - e^{-ik_x x}\right) \tag{4.3}$$

$$H_{xl} = \frac{1}{iw\mu_l}\left(-\frac{\partial}{\partial z}E_{yl}\right) = \frac{k_{lz}}{w\mu_l}\left(-A_l e^{ik_{lz}z} + B_l e^{-ik_{lz}z}\right)\left(e^{ik_x x} - e^{-ik_x x}\right) \tag{4.4}$$

$$H_{zl} = \frac{1}{iw\mu_l}\left(+\frac{\partial}{\partial x}E_{yl}\right) = \frac{k_x}{w\mu_l}\left(A_l e^{ik_{lz}z} + B_l e^{-ik_{lz}z}\right)\left(e^{ik_x x} - e^{-ik_x x}\right) \tag{4.5}$$

where A_l = amplitude of total waves propagating in $+\hat{z}$ axis, and

B_l = amplitude of total waves propagating in $-\hat{z}$ axis

It is noted that in region 0 where $l = 0$,

$$A_0 = RE_0 \quad \text{and} \quad B_0 = E_0$$

while in transmitted region t where $l = t$,

$$A_t = 0 \quad \text{and} \quad B_t = TE_0$$

where R and T represent reflection and transmission coefficients, respectively.

By applying appropriate boundary conditions between each layer, A_l and B_l can be expressed in the form of neighboring A_{l+1} and B_{l+1}. At $z = -d_l$, tangential electric (E_y) and magnetic (H_x) fields are continuous, we therefore obtain

$$\left(A_l e^{-ik_{lz}d_l} + B_l e^{ik_{lz}d_l}\right) = \left(A_{l+1}e^{-ik_{(l+1)z}d_l} + B_{l+1}e^{ik_{(l+1)z}d_l}\right) \tag{4.6}$$

$$\frac{k_{lz}}{w\mu_l}\left(-A_l e^{-ik_{lz}d_l} + B_l e^{ik_{lz}d_l}\right) = \frac{k_{(l+1)z}}{w\mu_{(l+1)}}\left(-A_{l+1}e^{-ik_{(l+1)z}d_l} + B_{l+1}e^{ik_{(l+1)z}d_l}\right) \tag{4.7}$$

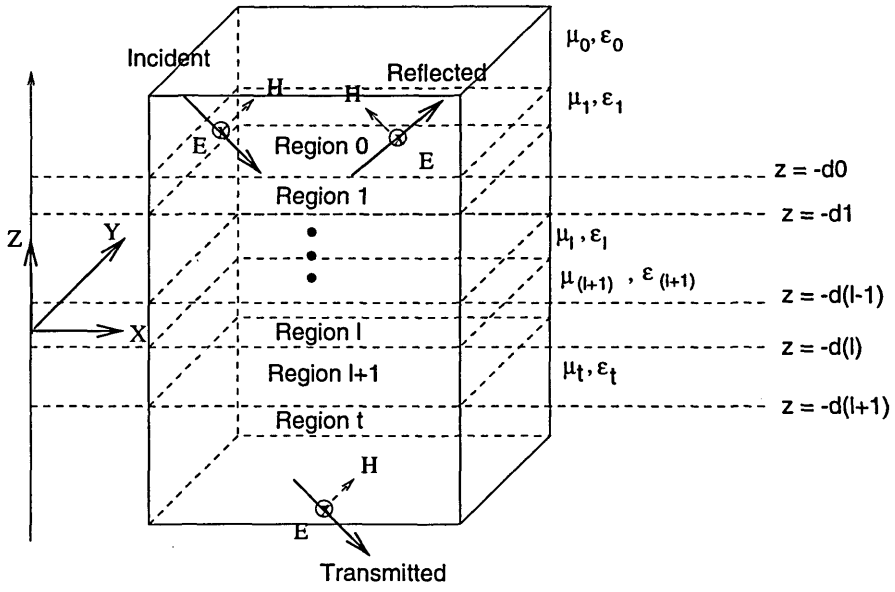

(a) layered medium

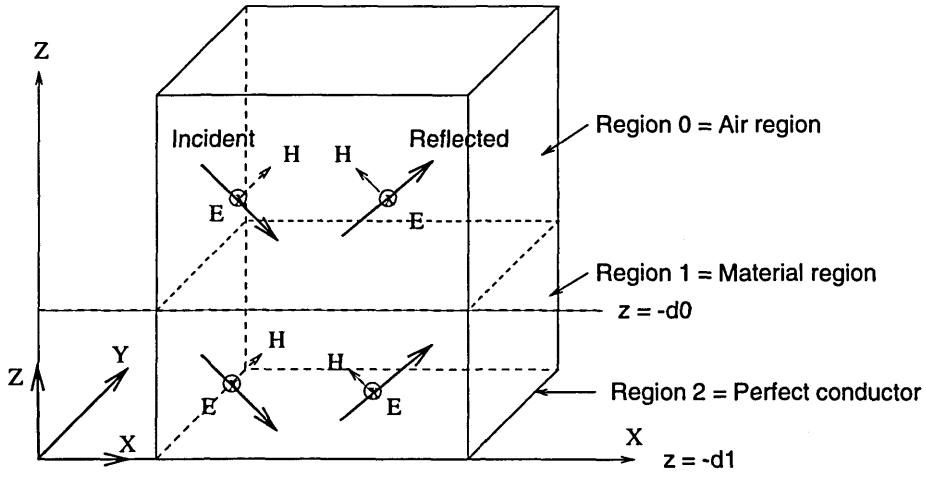

(b) two-layered medium

Figure 4-19: Reflection and Transmission of TE wave in a layered medium inside the rectangular waveguide

By solving equations (4.6) and (4.7), we obtain [20]

$$\frac{A_l}{B_l} = \frac{e^{i2k_{lz}d_l}}{R_{l(l+1)}} + \frac{\left[1-\left(1/R_{l(l+1)}^2\right)\right]e^{i2(k_{(l+1)z}+k_{lz})d_l}}{\left[1/R_{l(l+1)}\right]e^{i2(k_{(l+1)z})d_l}+(A_{l+1}/B_{l+1})} \tag{4.8}$$

where $R_{l(l+1)} = \frac{1-p_{l(l+1)}}{1+p_{l(l+1)}} = -R_{(l+1)l}$

$p_{l(l+1)} = \frac{\mu_l k_{(l+1)z}}{\mu_{(l+1)}k_{lz}} = \frac{1}{p_{(l+1)l}}$

Therefore, the closed-form solution of reflection coefficient, R, due to a layered medium can be found from equation (4.8) since $R = \frac{A_0}{B_0}$ which is expressed in $\frac{A_1}{B_1}$ term and $\frac{A_1}{B_1}$ can be expressed in $\frac{A_2}{B_2}$ term and so on until the transmitted region, where $\frac{A_t}{B_t} = 0$, is reached. It is noted that this solution is identical to the solution of reflection coefficient when a plane wave is incident on a layered medium (see the complete solution in [20]).

Again, by solving equations (4.6) and (4.7), we are able to write $A_{(l+1)}$ and $B_{(l+1)}$ in terms of A_l and B_l which will be useful when solutions of field components in region l are found and field components in region $(l+1)$ layer are yet to be determined.

$$A_{(l+1)} = \frac{1}{2}\left(1+p_{(l+1)l}\right)\left(A_l e^{-ik_{lz}d_l} + R_{(l+1)l}B_l e^{ik_{lz}d_l}\right)e^{ik_{(l+1)z}d_l}$$

$$B_{(l+1)} = \frac{1}{2}\left(1+p_{(l+1)l}\right)\left(R_{(l+1)l}A_l e^{-ik_{lz}d_l} + B_l e^{ik_{lz}d_l}\right)e^{-ik_{(l+1)z}d_l}$$

But only a two-layered medium inside the rectangular waveguide (see Figure 4-19(b)) is considered in this work, its reflected coefficient can therefore be simply expressed as [20]

$$R = \frac{R_{01}+R_{12}e^{i2k_{1z}(d1-d0)}}{1+R_{01}R_{12}e^{i2k_{1z}(d1-d0)}}e^{i2k_z d_0}$$

4.10 Appendix II. - An Example of Permittivity Calculation

To understand the complex permittivity calculation used in this work better, an example of permittivity calculation of water is described in details. According to Figure 4-1, two measurements are done at the optimum length of 0.68- and 0.73-cm.

At 2.45 GHz, the measured relative magnitudes of reflected signals for room-temperature water at approximately 0.68- and 0.73-cm thicknesses are 0.960 and 0.958, respectively. Using equation (4.2), we will have

$$S_{22}^1 = \frac{R_{01} - e^{i2k_{1z}(0.0068)}}{1 - R_{01}e^{i2k_{1z}(0.0068)}} = \text{relative reflected signal for optimum length of 0.0068 m}$$

$$S_{22}^2 = \frac{R_{01} - e^{i2k_{1z}(0.0073)}}{1 - R_{01}e^{i2k_{1z}(0.0073)}} = \text{relative reflected signal for optimum length of 0.0073 m}$$

Substitute R_{01} with $\left(\frac{1-\frac{k_{1z}}{k_{0z}}}{1+\frac{k_{1z}}{k_{0z}}}\right)$, we obtain

$$S_{22}^1 = \frac{\left(\frac{1-\frac{k_{1z}}{k_{0z}}}{1+\frac{k_{1z}}{k_{0z}}}\right) - e^{i2k_{1z}(0.0068)}}{1 - \left(\frac{1-\frac{k_{1z}}{k_{0z}}}{1+\frac{k_{1z}}{k_{0z}}}\right) e^{i2k_{1z}(0.0068)}}$$

$$S_{22}^2 = \frac{\left(\frac{1-\frac{k_{1z}}{k_{0z}}}{1+\frac{k_{1z}}{k_{0z}}}\right) - e^{i2k_{1z}(0.0073)}}{1 - \left(\frac{1-\frac{k_{1z}}{k_{0z}}}{1+\frac{k_{1z}}{k_{0z}}}\right) e^{i2k_{1z}(0.0073)}}$$

Moreover, by substituting k_{0z} with $\sqrt{\left(\frac{2\pi f_o}{c}\right)^2 \mu_{r0}\epsilon_{r0} - \left(\frac{\pi}{a}\right)^2}$ and k_{1z} with $\sqrt{\left(\frac{2\pi f_o}{c}\right)^2 \mu_{r1}\epsilon_{r1} - \left(\frac{\pi}{a}\right)^2}$, the following equations can be obtained.

$$S_{22}^1 = \frac{\left(\frac{1-\frac{\sqrt{\left(\frac{2\pi f_o}{c}\right)^2 \mu_{r1}\epsilon_{r1} - \left(\frac{\pi}{a}\right)^2}}{\sqrt{\left(\frac{2\pi f_o}{c}\right)^2 \mu_{r0}\epsilon_{r0} - \left(\frac{\pi}{a}\right)^2}}}{1+\frac{\sqrt{\left(\frac{2\pi f_o}{c}\right)^2 \mu_{r1}\epsilon_{r1} - \left(\frac{\pi}{a}\right)^2}}{\sqrt{\left(\frac{2\pi f_o}{c}\right)^2 \mu_{r0}\epsilon_{r0} - \left(\frac{\pi}{a}\right)^2}}}\right) - e^{i2\sqrt{\left(\frac{2\pi f_o}{c}\right)^2 \mu_{r1}\epsilon_{r1} - \left(\frac{\pi}{a}\right)^2}(0.0068)}}{1 - \left(\frac{1-\frac{\sqrt{\left(\frac{2\pi f_o}{c}\right)^2 \mu_{r1}\epsilon_{r1} - \left(\frac{\pi}{a}\right)^2}}{\sqrt{\left(\frac{2\pi f_o}{c}\right)^2 \mu_{r0}\epsilon_{r0} - \left(\frac{\pi}{a}\right)^2}}}{1+\frac{\sqrt{\left(\frac{2\pi f_o}{c}\right)^2 \mu_{r1}\epsilon_{r1} - \left(\frac{\pi}{a}\right)^2}}{\sqrt{\left(\frac{2\pi f_o}{c}\right)^2 \mu_{r0}\epsilon_{r0} - \left(\frac{\pi}{a}\right)^2}}}\right) e^{i2\sqrt{\left(\frac{2\pi f_o}{c}\right)^2 \mu_{r1}\epsilon_{r1} - \left(\frac{\pi}{a}\right)^2}(0.0068)}} \quad (4.9)$$

$$S_{22}^2 = \frac{\left(\frac{1-\frac{\sqrt{\left(\frac{2\pi f_o}{c}\right)^2 \mu_{r1}\epsilon_{r1} - \left(\frac{\pi}{a}\right)^2}}{\sqrt{\left(\frac{2\pi f_o}{c}\right)^2 \mu_{r0}\epsilon_{r0} - \left(\frac{\pi}{a}\right)^2}}}{1+\frac{\sqrt{\left(\frac{2\pi f_o}{c}\right)^2 \mu_{r1}\epsilon_{r1} - \left(\frac{\pi}{a}\right)^2}}{\sqrt{\left(\frac{2\pi f_o}{c}\right)^2 \mu_{r0}\epsilon_{r0} - \left(\frac{\pi}{a}\right)^2}}} \right) - e^{i2\sqrt{\left(\frac{2\pi f_o}{c}\right)^2 \mu_{r1}\epsilon_{r1} - \left(\frac{\pi}{a}\right)^2}(0.0073)}}{1 - \left(\frac{1-\frac{\sqrt{\left(\frac{2\pi f_o}{c}\right)^2 \mu_{r1}\epsilon_{r1} - \left(\frac{\pi}{a}\right)^2}}{\sqrt{\left(\frac{2\pi f_o}{c}\right)^2 \mu_{r0}\epsilon_{r0} - \left(\frac{\pi}{a}\right)^2}}}{1+\frac{\sqrt{\left(\frac{2\pi f_o}{c}\right)^2 \mu_{r1}\epsilon_{r1} - \left(\frac{\pi}{a}\right)^2}}{\sqrt{\left(\frac{2\pi f_o}{c}\right)^2 \mu_{r0}\epsilon_{r0} - \left(\frac{\pi}{a}\right)^2}}} \right) e^{i2\sqrt{\left(\frac{2\pi f_o}{c}\right)^2 \mu_{r1}\epsilon_{r1} - \left(\frac{\pi}{a}\right)^2}(0.0073)}} \tag{4.10}$$

where f_o = the measurement frequency = 2.45 GHz,

c = speed of light = 3×10^8 meter/sec,

a = width of the rectangular waveguide = 0.10922 m for WR 430,

ϵ_{r0} = the relative complex permittivity for region 0 (air) = 1.0 ,

ϵ_{r1} = the relative complex permittivity for region 1 (material under test),

$= \epsilon'_{r1} + i\epsilon''_{r1}$,

μ_{r0} = the relative complex permeability for region 0 (air) = 1.0,

μ_{r1} = the relative complex permeability for region 1 (non-magnetic) = 1.0.

The method of trial and error is used to determine the relative complex permittivity of material under test. By sweeping the values of ϵ_{r1} both real(ϵ'_{r1}) and imaginary(ϵ''_{r1}) parts in equations (4.9) and (4.10), two corresponding relative magnitudes of reflected signals can be obtained and then compared with the measured values of 0.960 and 0.958, respectively. If the percent differences of both comparison (one for each optimal length) are less than 0.05, the relative complex permittivity of material under test can be found.

In this example, the real part of permittivity is swept from 1 to 90 and from 0 to 20 for the imaginary part. And by comparing the computed magnitude value of S_{22}^1 to 0.960 (from measurement) and that of S_{22}^2 to 0.958 (from measurement) within 0.05% allowed difference, the average complex permittivity of (79.8+11.5i) is obtained.

Chapter 5

Power Dissipation Model

5.1 Introduction

Because of its ease of implementation and flexibility, the Finite-Difference Time-Domain technique (FDTD) is used to solve electric and magnetic fields in Maxwell's equations to compute power dissipation during microwave heating of dielectric material. In this chapter, the Maxwell's equations governing the electromagnetic problems, the FDTD algorithm, treatment of free space and dielectric material, treatment of boundary conditions, treatment of excitation source, calculation of dissipated power, and verification of model will be presented in order.

5.2 Maxwell's Equations

Maxwell's equations are fundamental to the electromagnetic wave theory. Composed of Faraday's induction law, Ampere's circuit law and Gauss' laws for magnetic and electric fields, they are valid for all time at everywhere in space and can be written in time-dependent three-dimensional differential forms for an isotropic and homogeneous non-magnetic conducting material in source free region,

$$\nabla \times \overline{E} = -\frac{\partial}{\partial t}\overline{B} \tag{5.1}$$

$$\nabla \times \overline{H} = \frac{\partial}{\partial t}\overline{D} + \sigma\overline{E} \tag{5.2}$$

$$\nabla \cdot \overline{D} = 0 \tag{5.3}$$

$$\nabla \cdot \overline{B} = 0 \tag{5.4}$$

where $\overline{E}$ = electric field strength (volt/m),

$\overline{H}$ = magnetic field strength (ampere/m) ,

$\overline{D}$ = electric displacement (coulomb/m^2),

$\overline{B}$ = magnetic flux density (weber/m^2), and

σ = conductivity (mho/m)

To solve for $\overline{E}(\overline{r},t)$, $\overline{H}(\overline{r},t)$, $\overline{D}(\overline{r},t)$, and $\overline{B}(\overline{r},t)$, the constitutive relations which depend on electric and magnetic properties of material are necessary and can be written as

$$\overline{D} = \epsilon\overline{E} = \epsilon_r\epsilon_o\overline{E} \tag{5.5}$$

$$\overline{B} = \mu\overline{H} = \mu_r\mu_o\overline{H} \tag{5.6}$$

where ϵ = permittivity (farad/m), and

μ = permeability (henry/m)

From (5.1) and (5.6), in rectangular coordinate system, we have

$$\begin{aligned}\nabla \times \overline{E} &= \hat{x}\left(\frac{\partial}{\partial y}E_z - \frac{\partial}{\partial z}E_y\right) + \hat{y}\left(\frac{\partial}{\partial z}E_x - \frac{\partial}{\partial x}E_z\right) + \hat{z}\left(\frac{\partial}{\partial x}E_y - \frac{\partial}{\partial y}E_x\right) \\ &= -\mu_r\mu_o\frac{\partial}{\partial t}\left(\hat{x}H_x + \hat{y}H_y + \hat{z}H_z\right)\end{aligned}$$

Therefore, for $\hat{x}$ field component,

$$\left(\frac{\partial}{\partial y}E_z - \frac{\partial}{\partial z}E_y\right) = -\mu_r\mu_o\frac{\partial}{\partial t}(H_x)$$

which can be rearranged to

$$\frac{\partial}{\partial t}H_x = \frac{1}{\mu_r\mu_o}\left[\frac{\partial}{\partial z}E_y - \frac{\partial}{\partial y}E_z\right] \tag{5.7}$$

Similarly, for $\hat{y}$ and $\hat{z}$ field components, we have

$$\frac{\partial}{\partial t}H_y = \frac{1}{\mu_r\mu_o}\left[\frac{\partial}{\partial x}E_z - \frac{\partial}{\partial z}E_x\right] \tag{5.8}$$

$$\frac{\partial}{\partial t}H_z = \frac{1}{\mu_r\mu_o}\left[\frac{\partial}{\partial y}E_x - \frac{\partial}{\partial x}E_y\right] \tag{5.9}$$

Similar approach is applied for (5.2) and (5.5), we obtain

$$\frac{\partial}{\partial t}E_x = \frac{1}{\epsilon_r\epsilon_o}\left[\frac{\partial}{\partial y}H_z - \frac{\partial}{\partial z}H_y - \sigma E_x\right] \tag{5.10}$$

$$\frac{\partial}{\partial t}E_y = \frac{1}{\epsilon_r\epsilon_o}\left[\frac{\partial}{\partial z}H_x - \frac{\partial}{\partial x}H_z - \sigma E_y\right] \tag{5.11}$$

$$\frac{\partial}{\partial t}E_z = \frac{1}{\epsilon_r\epsilon_o}\left[\frac{\partial}{\partial x}H_y - \frac{\partial}{\partial y}H_x - \sigma E_z\right] \tag{5.12}$$

5.3 FDTD Algorithm

In FDTD technique, Maxwell's equations in differential form will be solved using center difference approximation both in space and time. The calculated electric and magnetic fields are positioned on a mesh first introduced by Yee [53] (see Figure 5-1). The mesh allows one to employ center difference to space derivative of Maxwell's curl equations and also to implement Faraday's law and Ampere's law [46].

In FDTD calculation, time-stepping algorithm is used. First, all of the field values in the computational domain are initialized to be zero. Then, the electric and magnetic fields will be computed alternately at every

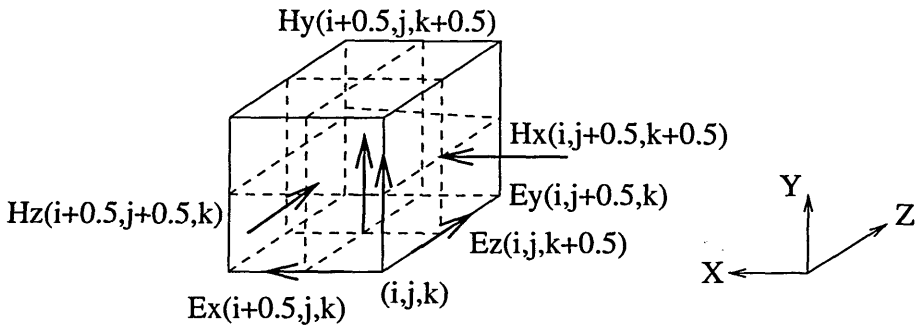

Figure 5-1: Field components of a unit cell in rectangular coordinate

half time step. In this algorithm, the electric field will be determined first. Field calculation will continue until sinusoidal steady state is reached or time expires.

The following notation used in Yee's mesh as shown in Figure 5-1 will be used in the finite difference equations throughout this chapter. For any function of space and time,

$$F^n(i,j,k) = F(i\Delta x, j\Delta y, k\Delta z, n\Delta t)$$

Now, let's review the algorithm of center difference approximation which will be applied to the partial derivatives of space and time in Maxwell's curl equations. Then we will discuss how to choose the space and time increments.

5.3.1 Center difference

From Figure 5-2, for a function $f_{(x)}$, forward, backward and center difference algorithms can be used to approximate the value of derivative of $f_{(x)}$, $f'_{(x)}$. For very small Δ, using forward difference

$$f'_{(x)} \approx \frac{f_{(x+\frac{\Delta}{2})} - f_{(x)}}{\Delta/2}$$

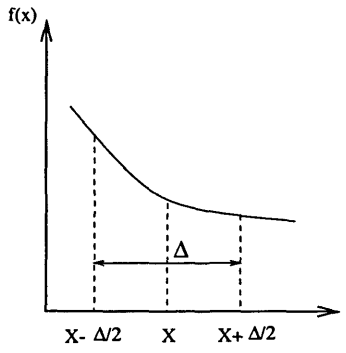

Figure 5-2: Finite difference plot

and for backward difference

$$f'_{(x)} \approx \frac{f_{(x)} - f_{(x-\frac{\Delta}{2})}}{\Delta/2}$$

and the average of both forward and backward difference algorithm gives

$$f'_{(x)} \approx \frac{f_{(x+\frac{\Delta}{2})} - f_{(x-\frac{\Delta}{2})}}{\Delta} \tag{5.13}$$

which is the center difference algorithm.

To determine the level of accuracy of finite-difference using center difference approximation, Taylor's expansion is used as follows:

$$f_{(x+\frac{\Delta}{2})} = f_{(x)} + \frac{\Delta}{2}f'_{(x)} + \frac{1}{2}(\frac{\Delta}{2})^2 f''_{(x)} + \frac{1}{6}(\frac{\Delta}{2})^3 f'''_{(x)} + ... \tag{5.14}$$

$$f_{(x-\frac{\Delta}{2})} = f_{(x)} - \frac{\Delta}{2}f'_{(x)} + \frac{1}{2}(\frac{\Delta}{2})^2 f''_{(x)} - \frac{1}{6}(\frac{\Delta}{2})^3 f'''_{(x)} + ... \tag{5.15}$$

Subtract equation (5.15) from (5.14) resulting

$$f_{(x+\frac{\Delta}{2})} - f_{(x-\frac{\Delta}{2})} = \Delta f'_{(x)} + \frac{1}{3}(\frac{\Delta}{2})^3 f'''_{(x)} + ...$$

and after rearranging, we obtain

$$f'_{(x)} = \frac{f_{(x+\frac{\Delta}{2})} - f_{(x-\frac{\Delta}{2})}}{\Delta} + \overbrace{\bigcirc(\Delta)^2 + ...}^{error\ terms}$$

which is similar to equation (5.13) except that there are some additional terms which will be discarded and therefore cause the center difference approximation to have an *error of second-order* for both time and space discretization.

5.3.2 Choices of space and time increment

Choices of space and time increment determine the stability and accuracy of the field calculation [48]. It is suggested that grid size be a small fraction ($\sim \frac{1}{10}$ to $\frac{1}{20}$) of either the smallest wavelength in the problem or the smallest dimension of the scattering object so that calculated field values cannot change significantly in one space increment and the generated mesh well represents the object [48]. Also, use of fine-enough gridding helps minimizing the numerical dispersion which can lead to physically invalid results [46]. In this model,

$$\Delta x = \Delta y = \Delta z = \Delta$$

To satisfy the stability condition of time-stepping algorithm derived in [48], the condition of Δt for a three-dimensional case must be

$$\begin{aligned} \Delta t &\leq \frac{1}{C_{max}} \left(\frac{1}{(\Delta x)^2} + \frac{1}{(\Delta y)^2} + \frac{1}{(\Delta z)^2} \right)^{-\frac{1}{2}} \\ &\leq \frac{\Delta}{C_{max}\sqrt{3}} \end{aligned} \tag{5.16}$$

where C_{max} = the maximum wave velocity in the model.

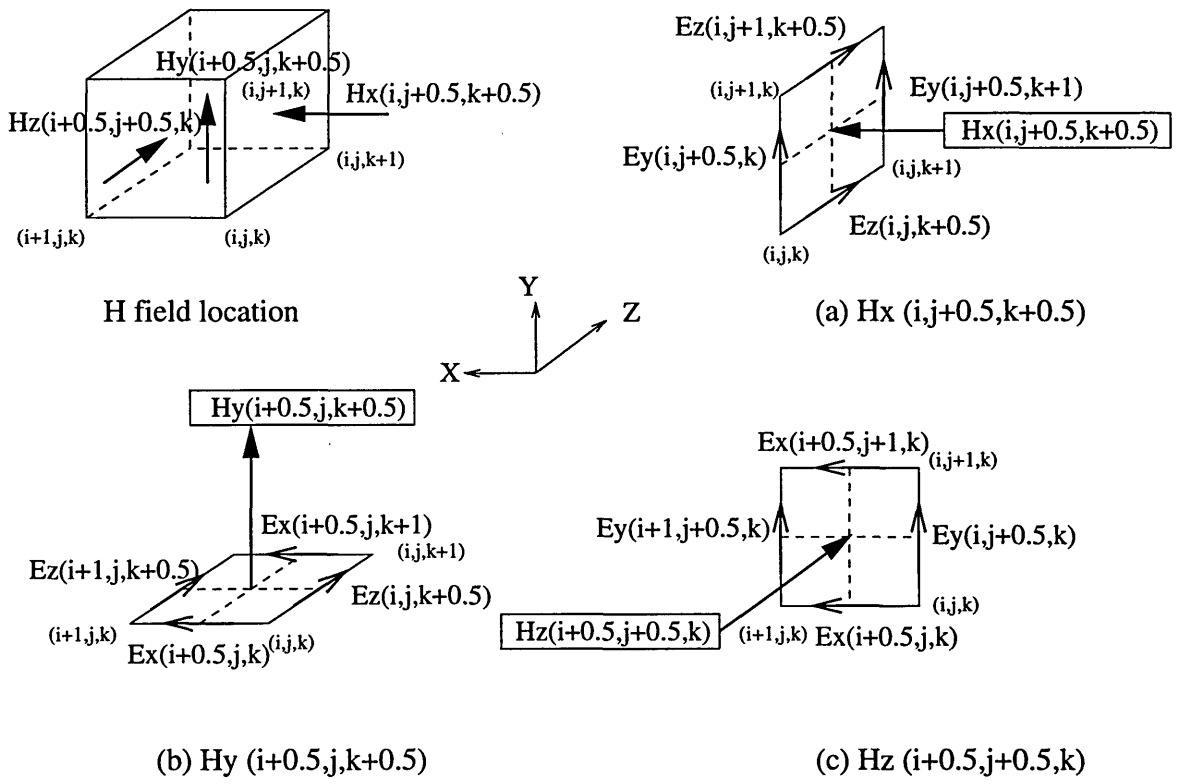

Figure 5-3: Location of field components used to compute magnetic field in FDTD

5.4 Treatment of Free Space and Dielectric Material

In this section, the finite difference equations for free space ($\epsilon_r = 1 + 0i$) and dielectric material are obtained by applying center difference to Maxwell's equations.

Referring to equation (5.7), for example, the center difference approximations is applied to its partial derivatives to determine $H_x^{(n)}(i, j+\frac{1}{2}, k+\frac{1}{2})$ with related $E_y^{(n)}$ and $E_z^{(n)}$ (see Figure 5-3(a)),

$$\frac{\partial}{\partial t}H_x = \frac{H_x^{(n+\frac{1}{2})}(i, j+\frac{1}{2}, k+\frac{1}{2}) - H_x^{(n-\frac{1}{2})}(i, j+\frac{1}{2}, k+\frac{1}{2})}{\Delta t} \tag{5.17}$$

$$\frac{\partial}{\partial z}E_y = \frac{E_y^{(n)}(i, j+\frac{1}{2}, k+1) - E_y^{(n)}(i, j+\frac{1}{2}, k)}{\Delta z} \tag{5.18}$$

$$\frac{\partial}{\partial y}E_z = \frac{E_z^{(n)}(i, j+1, k+\frac{1}{2}) - E_z^{(n)}(i, j, k+\frac{1}{2})}{\Delta y} \tag{5.19}$$

Substituting $\frac{\partial}{\partial t}H_x$, $\frac{\partial}{\partial z}E_y$, and $\frac{\partial}{\partial y}E_z$ from equations (5.17), (5.18), and (5.19), respectively back into its

original equation (5.7) results in the finite-difference equation (where $\Delta x = \Delta y = \Delta z = \Delta$) used to compute $H_x^{(n+\frac{1}{2})}(i, j+\frac{1}{2}, k+\frac{1}{2})$,

$$H_x^{(n+\frac{1}{2})}(i,j+\frac{1}{2},k+\frac{1}{2}) = H_x^{(n-\frac{1}{2})}(i,j+\frac{1}{2},k+\frac{1}{2}) + \frac{\Delta t}{\Delta \mu_r \mu_o}\left[E_y^{(n)}(i,j+\frac{1}{2},k+1) - E_y^{(n)}(i,j+\frac{1}{2},k) + E_z^{(n)}(i,j,k+\frac{1}{2}) - E_z^{(n)}(i,j+1,k+\frac{1}{2})\right] \quad (5.20)$$

Similarly, $H_y^{(n+\frac{1}{2})}(i+\frac{1}{2}, j, k+\frac{1}{2})$ and $H_z^{(n+\frac{1}{2})}(i+\frac{1}{2}, j+\frac{1}{2}, k)$ can be obtained from equations (5.8) and (5.9), respectively (see Figure 5-3(b) and (c) for related field locations),

$$H_y^{(n+\frac{1}{2})}(i+\frac{1}{2},j,k+\frac{1}{2}) = H_y^{(n-\frac{1}{2})}(i+\frac{1}{2},j,k+\frac{1}{2}) + \frac{\Delta t}{\Delta \mu_r \mu_o}\left[E_z^{(n)}(i+1,j,k+\frac{1}{2}) - E_z^{(n)}(i,j,k+\frac{1}{2}) + E_x^{(n)}(i+\frac{1}{2},j,k) - E_x^{(n)}(i+\frac{1}{2},j,k+1)\right] \quad (5.21)$$

$$H_z^{(n+\frac{1}{2})}(i+\frac{1}{2},j+\frac{1}{2},k) = H_z^{(n-\frac{1}{2})}(i+\frac{1}{2},j+\frac{1}{2},k) + \frac{\Delta t}{\Delta \mu_r \mu_o}\left[E_x^{(n)}(i+\frac{1}{2},j+1,k) - E_x^{(n)}(i+\frac{1}{2},j,k) + E_y^{(n)}(i,j+\frac{1}{2},k) - E_y^{(n)}(i+1,j+\frac{1}{2},k)\right] \quad (5.22)$$

Next, the finite-difference equations for electric fields will be obtained by applying the center difference approximation to each derivative of equation(5.12), for instance,

$$\begin{aligned}
\frac{\partial}{\partial t}E_z &= \frac{E_z^{(n+1)}(i,j,k+\frac{1}{2}) - E_z^{(n)}(i,j,k+\frac{1}{2})}{\Delta t} \\
\frac{\partial}{\partial x}H_y &= \frac{H_y^{(n+\frac{1}{2})}(i+\frac{1}{2},j,k+\frac{1}{2}) - H_y^{(n+\frac{1}{2})}(i-\frac{1}{2},j,k+\frac{1}{2})}{\Delta x} \\
\frac{\partial}{\partial y}H_x &= \frac{H_x^{(n+\frac{1}{2})}(i,j+\frac{1}{2},k+\frac{1}{2}) - H_x^{(n+\frac{1}{2})}(i,j-\frac{1}{2},k+\frac{1}{2})}{\Delta y} \\
\sigma E_z &= \sigma\left[\frac{E_z^{(n+1)}(i,j,k+\frac{1}{2}) + E_z^{(n)}(i,j,k+\frac{1}{2})}{2}\right]
\end{aligned}$$

and then substitute $\frac{\partial}{\partial t}E_z$, $\frac{\partial}{\partial x}H_y$, $\frac{\partial}{\partial y}H_x$, and σE_z from above back to equation (5.12) (see Figure 5-4(c)),

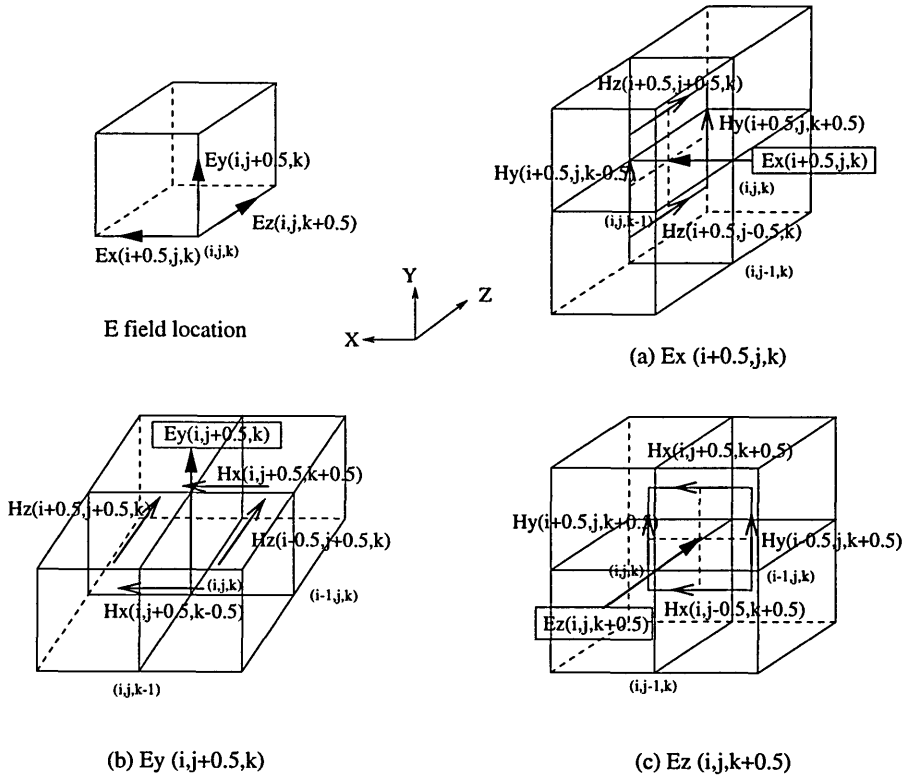

Figure 5-4: Location of field components used to compute electric field in FDTD

yielding

$$E_z^{(n+1)}(i,j,k+\frac{1}{2}) = \left[\frac{1-\frac{\sigma\Delta t}{2\epsilon_r\epsilon_o}}{1+\frac{\sigma\Delta t}{2\epsilon_r\epsilon_o}}\right] E_z^{(n)}(i,j,k+\frac{1}{2}) + \left[\frac{\frac{\Delta t}{\Delta\mu_r\mu_o}}{1+\frac{\sigma\Delta t}{2\epsilon_r\epsilon_o}}\right] \times \{H_y^{(n+\frac{1}{2})}(i+\frac{1}{2},j,k+\frac{1}{2}) - H_y^{(n+\frac{1}{2})}(i-\frac{1}{2},j,k+\frac{1}{2}) + H_x^{(n+\frac{1}{2})}(i,j-\frac{1}{2},k+\frac{1}{2}) - H_x^{(n+\frac{1}{2})}(i,j+\frac{1}{2},k+\frac{1}{2})\} \quad (5.23)$$

Again, $E_y^{(n+1)}(i,j+\frac{1}{2},k)$ and $E_x^{(n+1)}(i+\frac{1}{2},j,k)$ can be obtained in similar manner from equations (5.11) and (5.10), respectively (see Figure 5-4(b) and (a) for related field locations).

$$E_y^{(n+1)}(i,j+\frac{1}{2},k) = \left[\frac{1-\frac{\sigma\Delta t}{2\epsilon_r\epsilon_o}}{1+\frac{\sigma\Delta t}{2\epsilon_r\epsilon_o}}\right] E_y^{(n)}(i,j+\frac{1}{2},k) + \left[\frac{\frac{\Delta t}{\Delta\mu_r\mu_o}}{1+\frac{\sigma\Delta t}{2\epsilon_r\epsilon_o}}\right] \times \{H_x^{(n+\frac{1}{2})}(i,j+\frac{1}{2},k+\frac{1}{2}) - H_x^{(n+\frac{1}{2})}(i,j+\frac{1}{2},k-\frac{1}{2}) + H_z^{(n+\frac{1}{2})}(i-\frac{1}{2},j+\frac{1}{2},k) - H_z^{(n+\frac{1}{2})}(i+\frac{1}{2},j+\frac{1}{2},k)\} \quad (5.24)$$

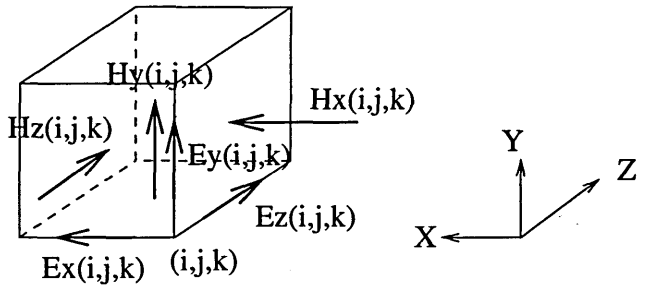

Figure 5-5: Field assignment for implementation

$$E_x^{(n+1)}(i+\frac{1}{2},j,k) = \left[\frac{1-\frac{\sigma\Delta t}{2\epsilon_r\epsilon_o}}{1+\frac{\sigma\Delta t}{2\epsilon_r\epsilon_o}}\right] E_x^{(n)}(i+\frac{1}{2},j,k) + \left[\frac{\frac{\Delta t}{\Delta\mu_r\mu_o}}{1+\frac{\sigma\Delta t}{2\epsilon_r\epsilon_o}}\right] \times \{H_z^{(n+\frac{1}{2})}(i+\frac{1}{2},j+\frac{1}{2},k) - H_z^{(n+\frac{1}{2})}(i+\frac{1}{2},j-\frac{1}{2},k) + H_y^{(n+\frac{1}{2})}(i+\frac{1}{2},j,k-\frac{1}{2}) - H_y^{(n+\frac{1}{2})}(i+\frac{1}{2},j,k+\frac{1}{2})\} \quad (5.25)$$

5.4.1 Implementation

To implement the above finite-difference equations, several changes in grid notation have been made. For example, at (i,j,k) unit cell, $H_x(i,j+\frac{1}{2},k+\frac{1}{2})$, $H_y(i+\frac{1}{2},j,k+\frac{1}{2})$,and $H_z(i+\frac{1}{2},j+\frac{1}{2},k)$ are assigned to be $H_x(i,j,k)$, $H_y(i,j,k)$ and $H_z(i,j,k)$, respectively while for electric field values, $E_x(i+\frac{1}{2},j,k)$, $E_y(i,j+\frac{1}{2},k)$,and $E_z(i,j,k+\frac{1}{2})$ are assigned to be $E_x(i,j,k)$, $E_y(i,j,k)$ and $E_z(i,j,k)$ (compare Figure 5-5 to Figure 5-1).

Therefore, equations (5.20), (5.21), (5.22), (5.23), (5.24), and (5.25) become

$$H_x^{(n+\frac{1}{2})}(i,j,k) = H_x^{(n-\frac{1}{2})}(i,j,k) + \frac{\Delta t}{\Delta\mu_r\mu_o}\left[E_y^{(n)}(i,j,k+1) - E_y^{(n)}(i,j,k) + E_z^{(n)}(i,j,k) - E_z^{(n)}(i,j+1,k)\right] \quad (5.26)$$

$$H_y^{(n+\frac{1}{2})}(i,j,k) = H_y^{(n-\frac{1}{2})}(i,j,k) + \frac{\Delta t}{\Delta\mu_r\mu_o}\left[E_z^{(n)}(i+1,j,k) - E_z^{(n)}(i,j,k) + E_x^{(n)}(i,j,k) - E_x^{(n)}(i,j,k+1)\right] \quad (5.27)$$

$$H_z^{(n+\frac{1}{2})}(i,j,k) = H_z^{(n-\frac{1}{2})}(i,j,k) + \frac{\Delta t}{\Delta \mu_r \mu_o}\left[E_x^{(n)}(i,j+1,k) - E_x^{(n)}(i,j,k) + E_y^{(n)}(i,j,k) - E_y^{(n)}(i+1,j,k)\right] \quad (5.28)$$

$$E_z^{(n+1)}(i,j,k) = \left[\frac{1-\frac{\sigma\Delta t}{2\epsilon_r\epsilon_o}}{1+\frac{\sigma\Delta t}{2\epsilon_r\epsilon_o}}\right] E_z^{(n)}(i,j,k) + \left[\frac{\frac{\Delta t}{\Delta\mu_r\mu_o}}{1+\frac{\sigma\Delta t}{2\epsilon_r\epsilon_o}}\right] \times \{H_y^{(n+\frac{1}{2})}(i,j,k) - H_y^{(n+\frac{1}{2})}(i-1,j,k) + H_x^{(n+\frac{1}{2})}(i,j-1,k) - H_x^{(n+\frac{1}{2})}(i,j,k)\} \quad (5.29)$$

$$E_y^{(n+1)}(i,j,k) = \left[\frac{1-\frac{\sigma\Delta t}{2\epsilon_r\epsilon_o}}{1+\frac{\sigma\Delta t}{2\epsilon_r\epsilon_o}}\right] E_y^{(n)}(i,j,k) + \left[\frac{\frac{\Delta t}{\Delta\mu_r\mu_o}}{1+\frac{\sigma\Delta t}{2\epsilon_r\epsilon_o}}\right] \times \{H_x^{(n+\frac{1}{2})}(i,j,k) - H_x^{(n+\frac{1}{2})}(i,j,k-1) + H_z^{(n+\frac{1}{2})}(i-1,j,k) - H_z^{(n+\frac{1}{2})}(i,j,k)\} \quad (5.30)$$

$$E_x^{(n+1)}(i,j,k) = \left[\frac{1-\frac{\sigma\Delta t}{2\epsilon_r\epsilon_o}}{1+\frac{\sigma\Delta t}{2\epsilon_r\epsilon_o}}\right] E_x^{(n)}(i,j,k) + \left[\frac{\frac{\Delta t}{\Delta\mu_r\mu_o}}{1+\frac{\sigma\Delta t}{2\epsilon_r\epsilon_o}}\right] \times \{H_z^{(n+\frac{1}{2})}(i,j,k) - H_z^{(n+\frac{1}{2})}(i,j-1,k) + H_y^{(n+\frac{1}{2})}(i,j,k-1) - H_y^{(n+\frac{1}{2})}(i,j,k)\} \quad (5.31)$$

5.5 Treatment of Boundary Conditions

Several types of boundary conditions are involved in our numerical modeling: (1) perfect electric conductor at metallic walls of the cavity and waveguide, (2) interfaces between dielectric materials, (3) absorbing boundary condition to simulate unbounded space, and (4) boundary condition at the excitation port.

5.5.1 At metallic wall

At surface of metallic wall of cavity and waveguide which is assumed to be made of perfect electric conductor, it is generally known that the tangential electric field and normal magnetic field vanish.

$$\hat{n} \times \overline{E} = 0$$

$$\hat{n} \cdot \overline{H} = 0$$

Thus, $E_{tangential}$ and H_{normal} will be simply set to zero at the metallic surface.

5.5.2 At interface of dielectric materials

Because the material properties (i.e., complex dielectric permittivity) in each unit cell can be different at any time, the finite-difference equations to calculate electric fields at dielectric interface have to be treated carefully. Using integral form of equation (5.2) to calculate $\overline{E}$,

$$\begin{aligned}\oint_C \overline{H} \cdot d\overline{S} &= \int_{S_1+S_2+S_3+S_4} \left(\frac{\partial}{\partial t}\overline{D} + \sigma\overline{E}\right) \cdot d\overline{a} \\ &= \int_{S_1} \left(\epsilon_{r1}\epsilon_o \frac{\partial}{\partial t}\overline{E} + \sigma_1\overline{E}\right) \cdot d\overline{a} + \int_{S_2} \left(\epsilon_{r2}\epsilon_o \frac{\partial}{\partial t}\overline{E} + \sigma_2\overline{E}\right) \cdot d\overline{a} + \\ &\quad \int_{S_3} \left(\epsilon_{r3}\epsilon_o \frac{\partial}{\partial t}\overline{E} + \sigma_3\overline{E}\right) \cdot d\overline{a} + \int_{S_4} \left(\epsilon_{r4}\epsilon_o \frac{\partial}{\partial t}\overline{E} + \sigma_4\overline{E}\right) \cdot d\overline{a} \end{aligned} \tag{5.32}$$

By applying Stoke's theorem,

$$\oint_C \overline{H} \cdot d\overline{S} = \int_S (\nabla \times \overline{H}) \cdot d\overline{a} \tag{5.33}$$

to integral form of equation (5.32) in order to obtain its differential form. We obtain, E_z (Figure 5-6), for instance,

$$\left[\frac{\partial}{\partial x}H_y - \frac{\partial}{\partial y}H_x\right] = \left(\frac{\epsilon_{r1}+\epsilon_{r2}+\epsilon_{r3}+\epsilon_{r4}}{4}\right)\epsilon_o \frac{\partial}{\partial t}E_z + \left(\frac{\sigma_1+\sigma_2+\sigma_3+\sigma_4}{4}\right)E_z \tag{5.34}$$

It is clear that equation (5.34) is similar to equation (5.12) except that the material property is averaged along the interface in the former. Similar equations for E_x and E_y can then be obtained.

It should be noted that the permeability is equal to 1 everywhere in the model since only non-magnetic material are considered. Therefore, the equations used to compute magnetic field components remain the same.

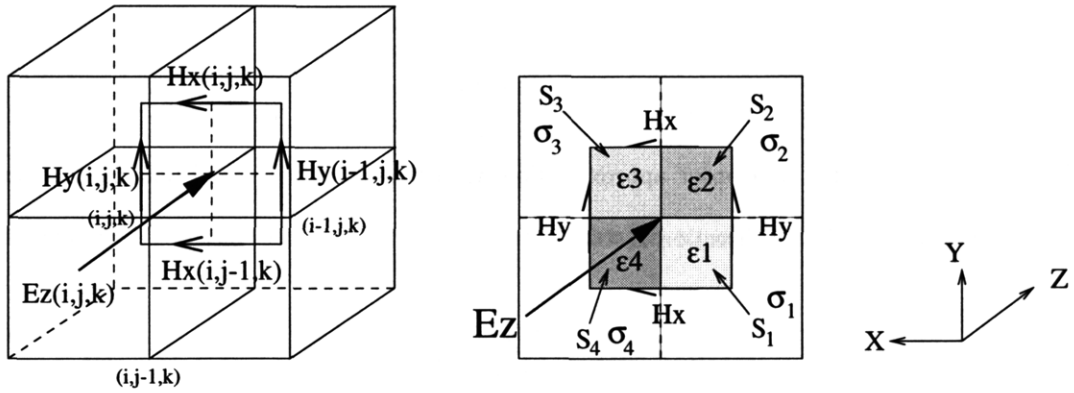

Figure 5-6: Interface between unit cells to compute E_z

5.5.3 At unbounded space

To be able to simulate the open or unbounded space at one end of excited waveguide, in our problem, the absorbing boundary condition (ABC) is needed to be employed. The outstanding characteristic of ABC is to make the computational domain finite so that the unbounded space can be simulated [11, 31]. Since there is only one unbounded space behind the waveguide in this problem and for simplicity, the first-order approximation ABC derived by Engquist and Majda [11] is employed rather than its second-order approximation ABC.

Because of the nature of Yee's grid notation, the calculation of magnetic field requires the neighboring electric field values which are in the same unit cell while to compute the electric field, the magnetic field values at the near unit cell must be known. With this knowledge, the first-order approximation ABC will be applied only to tangential electric field or the electric field at the boundary. And since TE_{10} wave is dominant in the waveguide problem, there will be only one tangential electric field needed to be taken care of. For example, assuming the width of waveguide is along the x-axis and TE_{10} wave is propagating in $\pm\hat{z}$ direction, only the field components of E_y, H_x, and H_z will exist inside the waveguide. Therefore, ABC will be implemented on E_y field component only.

In this section, two examples of ABC's implementation are illustrated: (1) reflected TE_{10} wave propagating in $-\hat{z}$ direction and (2) reflected TE_{10} wave propagating in $+\hat{z}$ direction.

Reflected TE_{10} wave propagating in $-\hat{z}$ direction

The differential equation for first-order approximation absorbing boundary condition used when reflected TE_{10} wave is propagating in $-\hat{z}$ direction is

$$\left(\frac{\partial}{\partial z} - \frac{1}{C}\frac{\partial}{\partial t}\right) E_y = 0 \tag{5.35}$$

Engquist and Majda, and Mur illustrated how to derive the above equation in [11, 31]. Another way to explain their derivations is that the first-order equation is derived from factoring of partial differential operator for three-dimensional one-way wave equation with use of one-term Taylor series approximation [47].

Using linear interpolation in both space and time for each component of the above differential equation along with center difference approximation, we obtain

$$\begin{aligned}\frac{\partial}{\partial z}E_y^{n+\frac{1}{2}}(i,j+\frac{1}{2},k+\frac{1}{2}) &= \frac{E_y^{(n+\frac{1}{2})}(i,j+\frac{1}{2},k+1) - E_y^{(n+\frac{1}{2})}(i,j+\frac{1}{2},k)}{\Delta} \\ &= \frac{1}{\Delta}[(\frac{E_y^{(n+1)}(i,j+\frac{1}{2},k+1)+E_y^{(n)}(i,j+\frac{1}{2},k+1)}{2}) - (\frac{E_y^{(n+1)}(i,j+\frac{1}{2},k)+E_y^{(n)}(i,j+\frac{1}{2},k)}{2})]\end{aligned}$$

$$\begin{aligned}\frac{\partial}{\partial t}E_y^{n+\frac{1}{2}}(i,j+\frac{1}{2},k+\frac{1}{2}) &= \frac{E_y^{(n+1)}(i,j+\frac{1}{2},k+\frac{1}{2}) - E_y^{(n)}(i,j+\frac{1}{2},k+\frac{1}{2})}{\Delta t} \\ &= \frac{1}{\Delta t}[(\frac{E_y^{(n+1)}(i,j+\frac{1}{2},k+1)+E_y^{(n+1)}(i,j+\frac{1}{2},k)}{2}) - (\frac{E_y^{(n)}(i,j+\frac{1}{2},k+1)+E_y^{(n)}(i,j+\frac{1}{2},k)}{2})]\end{aligned}$$

Substituting $\frac{\partial}{\partial z}E_y^{n+\frac{1}{2}}(i,j+\frac{1}{2},k+\frac{1}{2})$ and $\frac{\partial}{\partial t}E_y^{n+\frac{1}{2}}(i,j+\frac{1}{2},k+\frac{1}{2})$ from above equations to equation (5.35) yields

$$E_y^{(n+1)}(i,j+\frac{1}{2},k) = E_y^{(n)}(i,j+\frac{1}{2},k+1) + \left(\frac{C\Delta t-\Delta}{C\Delta t+\Delta}\right)\left[E_y^{(n+1)}(i,j+\frac{1}{2},k+1) - E_y^{(n)}(i,j+\frac{1}{2},k)\right] \tag{5.36}$$

If reflected wave is to be absorbed at plane $z = 0$, for example, by substituting k with 0, the absorbing

boundary condition obtained from equation (5.36) simply becomes,

$$E_y^{(n+1)}(i,j+\frac{1}{2},0) = E_y^{(n)}(i,j+\frac{1}{2},1) + \left(\frac{C\Delta t - \Delta}{C\Delta t + \Delta}\right)\left[E_y^{(n+1)}(i,j+\frac{1}{2},1) - E_y^{(n)}(i,j+\frac{1}{2},0)\right] \quad (5.37)$$

Implementation To implement the ABC from above example, equation (5.37) will become

$$E_y^{(n+1)}(i,j,0) = E_y^{(n)}(i,j,1) + \left(\frac{C\Delta t - \Delta}{C\Delta t + \Delta}\right)\left[E_y^{(n+1)}(i,j,1) - E_y^{(n)}(i,j,0)\right]$$

Reflected TE_{10} wave propagating in $+\hat{z}$ direction

The similar first-order approximation boundary equation to absorb the reflected TE_{10} wave propagating in $+\hat{z}$ direction is

$$\left(\frac{\partial}{\partial z} + \frac{1}{C}\frac{\partial}{\partial t}\right) E_y = 0 \quad (5.38)$$

Similar procedure as described in previous section applies to this case, yielding

$$E_y^{(n+1)}(i,j+\frac{1}{2},k) = E_y^{(n)}(i,j+\frac{1}{2},k+1) + \left(\frac{C\Delta t + \Delta}{C\Delta t - \Delta}\right)\left[E_y^{(n+1)}(i,j+\frac{1}{2},k+1) - E_y^{(n)}(i,j+\frac{1}{2},k)\right] \quad (5.39)$$

For example, if reflected wave is needed to be absorbed at the end of waveguide at plane $z = p$, by substituting k with $(p-1)$ (since there is no $(p+1)$ plane), the absorbing boundary condition from equation (5.39) is rearranged and yields

$$E_y^{(n+1)}(i,j+\frac{1}{2},p) = E_y^{(n)}(i,j+\frac{1}{2},p-1) + \left(\frac{C\Delta t - \Delta}{C\Delta t + \Delta}\right)\left[E_y^{(n+1)}(i,j+\frac{1}{2},p-1) - E_y^{(n)}(i,j+\frac{1}{2},p)\right] \quad (5.40)$$

Implementation Again, to implement the ABC from above example, equation (5.40) becomes

$$E_y^{(n+1)}(i,j,p) = E_y^{(n)}(i,j,p-1) + \left(\frac{C\Delta t - \Delta}{C\Delta t + \Delta}\right)\left[E_y^{(n+1)}(i,j,p-1) - E_y^{(n)}(i,j,p)\right]$$

5.5.4 At excitation port

In numerical model, the computational domain is divided into two regions: total and scattering field. The total field is defined as

$$\text{total field} \quad = \quad \text{scattering field} \quad + \quad \text{incident wave}$$

The incident wave basically is an incoming wave which is excited inside the computational domain and propagates into the total field region which is the area of interest. The main purpose to have the scattering field excluded from the total field is to be able to include the incident wave into the model. Therefore, the computation of E and H fields at the boundary between scattering and total field must be performed carefully.

As examples for better understanding, treatments of boundary condition at excitation port for incoming wave excited in the waveguide coming in $\pm\hat{z}$ direction are illustrated as followings. And it should be noted that the notation used in these examples is for implementation purpose only.

Incoming TE_{10} wave propagating in $+\hat{z}$ direction (For implementation)

For incoming wave traveling in $+\hat{z}$ direction, the finite-difference equations in the vicinity of the excitation port from equations (5.26) and (5.30) are modified while those from equations (5.27), (5.28), (5.29), and (5.31) remain the same. And if the excitation port is at plane $z = k$, the modified finite-difference equations of the unit cells around the excitation port are (see Figure 5-7):

$$H_{x_{scat}}^{(n+\frac{1}{2})}(i,j,k-1) = H_{x_{scat}}^{(n-\frac{1}{2})}(i,j,k-1) + \frac{\Delta t}{\Delta\mu_r\mu_o}\times$$

$$\Big[\underbrace{\underbrace{(E_{y_{total}}^{(n)}(i,j,k)}_{total\ field} - \underbrace{E_{y_{inc}}^{(n)}(i,j,k))}_{incident\ wave} - E_{y_{scat}}^{(n)}(i,j,k-1) + E_{z_{scat}}^{(n)}(i,j,k-1) - E_{z_{scat}}^{(n)}(i,j+1,k-1)}_{Scattering\ Field}\Big] \quad (5.41)$$

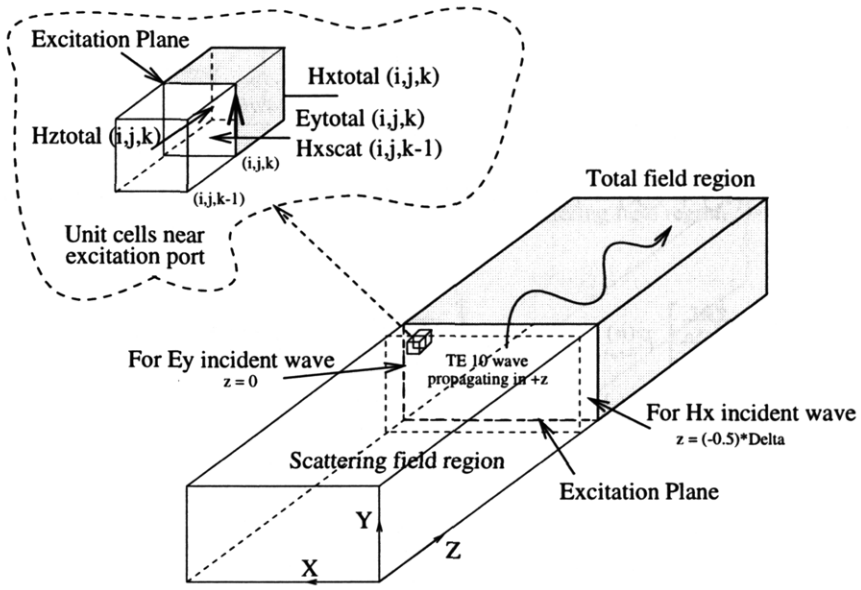

Figure 5-7: Details at excitation port when TE_{10} wave is propagating in $+\hat{z}$ direction

$$E_{y_{total}}^{(n+1)}(i,j,k) = \left[\frac{1-\frac{\sigma\Delta t}{2\epsilon_r\epsilon_o}}{1+\frac{\sigma\Delta t}{2\epsilon_r\epsilon_o}}\right] E_{y_{total}}^{(n)}(i,j,k) + \left[\frac{\frac{\Delta t}{\Delta\mu_r\mu_o}}{1+\frac{\sigma\Delta t}{2\epsilon_r\epsilon_o}}\right] \times \{H_{x_{total}}^{(n+\frac{1}{2})}(i,j,k)$$
$$\underbrace{- \left(\underbrace{H_{x_{scat}}^{(n+\frac{1}{2})}(i,j,k-1)}_{scattering\ field} + \underbrace{H_{x_{inc}}^{(n+\frac{1}{2})}(i,j,k-1)}_{incident\ wave} \right)}_{Total\ Field} + H_{z_{total}}^{(n+\frac{1}{2})}(i-1,j,k) - H_{z_{total}}^{(n+\frac{1}{2})}(i,j,k)\} \quad (5.42)$$

where $H_{x_{inc}}^{(n+\frac{1}{2})}(i,j,k-1)$ and $E_{y_{inc}}^{(n)}(i,j,k)$ are the field components of TE_{10} incident wave which will be discussed in the next section. It is noted that $H_{x_{inc}}^{(n+\frac{1}{2})}(i,j,k-1)$ is added to $H_{x_{scat}}^{(n+\frac{1}{2})}(i,j,k-1)$ in order to use $H_{x_{total}}^{(n+\frac{1}{2})}(i,j,k-1)$ component in the equation. For similar reason, $E_{y_{total}}^{(n)}(i,j,k)$ is subtracted by $E_{y_{inc}}^{(n)}(i,j,k)$ in order to be compatible with other scattering components in the equation.

For the other field components, the finite-difference equations (5.27), (5.28), (5.29), and (5.31) remain the same as followings:

$$H_{y_{scat}}^{(n+\frac{1}{2})}(i,j,k-1) = H_{y_{scat}}^{(n-\frac{1}{2})}(i,j,k-1) + \frac{\Delta t}{\Delta\mu_r\mu_o} \times$$

$$\left[E^{(n)}_{z_{scat}}(i+1,j,k-1) - E^{(n)}_{z_{scat}}(i,j,k-1) + E^{(n)}_{x_{scat}}(i,j,k-1) - (E^{(n)}_{x_{total}}(i,j,k) - \underbrace{E^{(n)}_{x_{inc}}(i,j,k)}_{no\ E_{x_{inc}}}) \right]$$

$$H^{(n+\frac{1}{2})}_{z_{total}}(i,j,k) = H^{(n-\frac{1}{2})}_{z_{total}}(i,j,k) + \frac{\Delta t}{\Delta\mu_r\mu_o}\left[E^{(n)}_{x_{total}}(i,j+1,k) - E^{(n)}_{x_{total}}(i,j,k) + E^{(n)}_{y_{total}}(i,j,k) - E^{(n)}_{y_{total}}(i+1,j,k)\right]$$

$$E^{(n+1)}_{z_{total}}(i,j,k) = \left[\frac{1-\frac{\sigma\Delta t}{2\epsilon_r\epsilon_o}}{1+\frac{\sigma\Delta t}{2\epsilon_r\epsilon_o}}\right] E^{(n)}_{z_{total}}(i,j,k) + \left[\frac{\frac{\Delta t}{\Delta\mu_r\mu_o}}{1+\frac{\sigma\Delta t}{2\epsilon_r\epsilon_o}}\right] \times \{H^{(n+\frac{1}{2})}_{y_{total}}(i,j,k) - H^{(n+\frac{1}{2})}_{y_{total}}(i-1,j,k) + H^{(n+\frac{1}{2})}_{x_{total}}(i,j-1,k) - H^{(n+\frac{1}{2})}_{x_{total}}(i,j,k)\}$$

$$E^{(n+1)}_{x_{total}}(i,j,k) = \left[\frac{1-\frac{\sigma\Delta t}{2\epsilon_r\epsilon_o}}{1+\frac{\sigma\Delta t}{2\epsilon_r\epsilon_o}}\right] E^{(n)}_{x_{total}}(i,j,k) + \left[\frac{\frac{\Delta t}{\Delta\mu_r\mu_o}}{1+\frac{\sigma\Delta t}{2\epsilon_r\epsilon_o}}\right] \times \{H^{(n+\frac{1}{2})}_{z_{total}}(i,j,k) - H^{(n+\frac{1}{2})}_{z_{total}}(i,j-1,k) + (H^{(n+\frac{1}{2})}_{y_{scat}}(i,j,k-1) + \underbrace{H^{(n+\frac{1}{2})}_{y_{inc}}(i,j,k-1)}_{=0\ because\ no\ H_{y_{inc}}}) - H^{(n+\frac{1}{2})}_{y_{total}}(i,j,k)\}$$

And it should be noted that there will be no $H_{z_{inc}}$ included in the finite-difference equations at the excitation plane although H_z component exists in TE_{10} wave.

Incoming TE_{10} wave propagating in $-\hat{z}$ direction (For implementation)

For incoming wave traveling in $-\hat{z}$ direction and the excitation port is at plane $z = k$, the modified finite-difference equations in the vicinity of the excitation port are only different in signs of incident wave compared to those of the previous section (see Figure 5-8). For similar reason as in above case, the finite-difference equations (5.27), (5.28), (5.29), and (5.31) for the other field components remain unchanged.

$$H^{(n+\frac{1}{2})}_{x_{scat}}(i,j,k) = H^{(n-\frac{1}{2})}_{x_{scat}}(i,j,k) + \frac{\Delta t}{\Delta\mu_r\mu_o}\times \left[E^{(n)}_{y_{scat}}(i,j,k+1) - \underbrace{(\underbrace{E^{(n)}_{y_{total}}(i,j,k)}_{total\ field} - \underbrace{E^{(n)}_{y_{inc}}(i,j,k)}_{incident\ wave})}_{scattering\ field} + E^{(n)}_{z_{scat}}(i,j,k) - E^{(n)}_{z_{scat}}(i,j+1,k) \right] \quad (5.43)$$

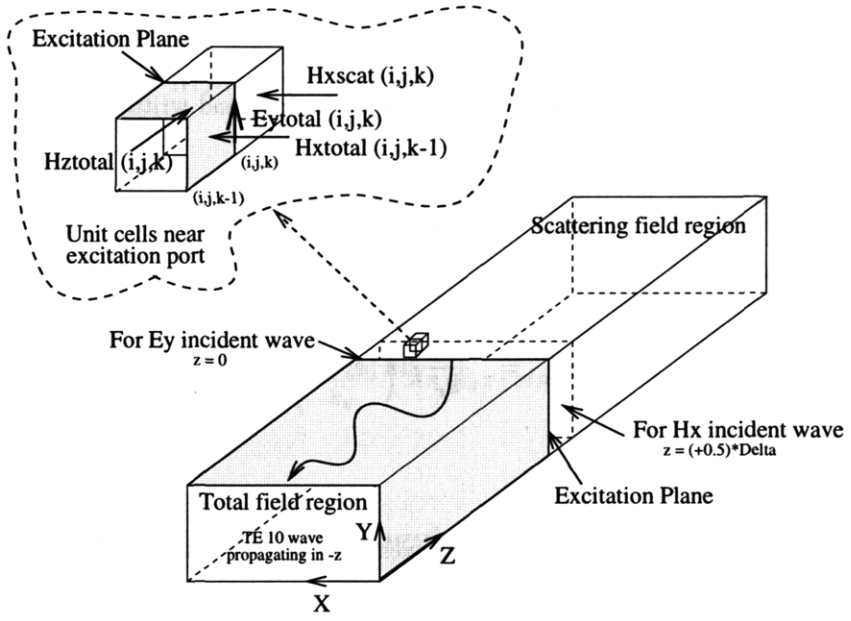

Figure 5-8: Details at excitation port when TE_{10} wave is propagating in $-\hat{z}$ direction

$$E_{y_{total}}^{(n+1)}(i,j,k) = \left[\frac{1-\frac{\sigma\Delta t}{2\epsilon_r\epsilon_o}}{1+\frac{\sigma\Delta t}{2\epsilon_r\epsilon_o}}\right] E_{y_{total}}^{(n)}(i,j,k) + \left[\frac{\frac{\Delta t}{\Delta\mu_r\mu_o}}{1+\frac{\sigma\Delta t}{2\epsilon_r\epsilon_o}}\right] \times \overbrace{\{\overbrace{(H_{x_{scat}}^{(n+\frac{1}{2})}(i,j,k)}^{scattering\ field} + \overbrace{H_{x_{inc}}^{(n+\frac{1}{2})}(i,j,k))}^{incident\ wave}}^{Total\ Field}$$
$$-H_{x_{total}}^{(n+\frac{1}{2})}(i,j,k-1) + H_{z_{total}}^{(n+\frac{1}{2})}(i-1,j,k) - H_{z_{total}}^{(n+\frac{1}{2})}(i,j,k)\} \quad (5.44)$$

where $H_{x_{inc}}^{(n+\frac{1}{2})}(i,j,k)$ and $E_{y_{inc}}^{(n)}(i,j,k)$ are the field components of TE_{10} incident wave.

5.6 Treatment of Excitation Source

Since TE_{10} mode is the fundamental mode or the dominant mode in rectangular waveguide, it is assumed that only TE_{10} mode is excited in the air-filled waveguide. In this section, the field components of TE_{10} wave propagating in $\pm\hat{z}$ directions are illustrated as well as the formula for each excited field component used in implementation.

5.6.1 TE_{10} mode in air-filled rectangular waveguide propagating in $+\hat{z}$ direction

For guided waves propagating in $+\hat{z}$ direction (see Figure 5-7), the time-harmonic field components of TE_{10} wave existing inside the rectangular waveguide can be easily obtained and written as [20]

$$H_z(\overline{r}) = cos\,(k_x x)\, e^{ik_z z} \tag{5.45}$$

$$H_x(\overline{r}) = \frac{-ik_z}{k_x} sin\,(k_x x)\, e^{ik_z z} \tag{5.46}$$

$$E_y(\overline{r}) = \frac{iw\mu}{k_x} sin\,(k_x x)\, e^{ik_z z} \tag{5.47}$$

where $k_x = \frac{\pi}{a}$,

$k_z = \sqrt{w^2\mu_o\epsilon_o - {k_x}^2}$ = real component (for air-filled waveguide), and

a = width of rectangular waveguide along x-axis

To obtain the time-space field components, e^{-iwt} will be multiplied to the time-harmonic field components and take the real part as shown below.

$$\overline{E}(\overline{r},t) = Re\left\{\overline{E}(\overline{r})e^{-iwt}\right\}$$

Therefore, the equations (5.45),(5.46) and (5.47) can be rewritten in time-space relation as followings:

$$H_z(\overline{r},t) = cos\,(k_x x)\, cos\,(k_z z - wt) \tag{5.48}$$

$$H_x(\overline{r},t) = \left(\frac{k_z}{k_x}\right) sin\,(k_x x)\, sin\,(k_z z - wt) \tag{5.49}$$

$$E_y(\overline{r},t) = \left(\frac{-w\mu_o}{k_x}\right) sin\,(k_x x)\, sin\,(k_z z - wt) \tag{5.50}$$

Implementation

Let the excitation plane be at plane $z = 0$, the implementation for $H_{x_{inc}}$ and $E_{y_{inc}}$ of the incident wave can be illustrated below.

For $H_{x_{inc}}^{(n+\frac{1}{2})}(i,j,k-1)$ from equation (5.42), the value of z is assigned to equal $(-\frac{1}{2}\Delta)$ in the equation

(5.49) (see Figure 5-7), resulting

$$H_{x_{inc}}^{(n+\frac{1}{2})}(i,j,k-1) = \left(\frac{k_z}{k_x}\right) sin\,(k_x x)\, sin\left(k_z(-\frac{1}{2}\Delta) - wt\right)$$

while for $E_{y_{inc}}^{(n)}(i,j,k)$ from equation (5.41), z is set to equal $(0 * \Delta)$ in the equation (5.50) (see Figure 5-7) and we will have

$$E_{y_{inc}}^{(n)}(i,j,k) = \left(\frac{-w\mu_o}{k_x}\right) sin\,(k_x x)\, sin\,(k_z(0 * \Delta) - wt)$$

5.6.2 TE_{10} mode in air-filled rectangular waveguide propagating in $-\hat{z}$ direction

To obtain time-space field components for TE_{10} wave propagating in $-\hat{z}$ direction (see Figure 5-8), similar steps as shown in the previous section are applied so the field components of TE_{10} wave can be shown below.

$$\begin{aligned} H_z(\overline{r},t) &= cos\,(k_x x)\, cos\,(k_z z + wt) \\ H_x(\overline{r},t) &= \left(\frac{k_z}{k_x}\right) sin\,(k_x x)\, sin\,(k_z z + wt) \\ E_y(\overline{r},t) &= \left(\frac{w\mu_o}{k_x}\right) sin\,(k_x x)\, sin\,(k_z z + wt) \end{aligned}$$

Implementation

Again, let the excitation plane is located at plane $z = 0$, the field component of $H_{x_{inc}}^{(n+\frac{1}{2})}(i,j,k)$ from equation (5.44) and $E_{y_{inc}}^{(n)}(i,j,k)$ from equation (5.43)to be implemented are (see Figure 5-8)

$$\begin{aligned} H_{x_{inc}}^{(n+\frac{1}{2})}(i,j,k) &= \left(\frac{k_z}{k_x}\right) sin\,(k_x x)\, sin\left(k_z(\frac{1}{2}\Delta) + wt\right) \\ E_{y_{inc}}^{(n)}(i,j,k) &= \left(\frac{w\mu_o}{k_x}\right) sin\,(k_x x)\, sin\,(k_z(0 * \Delta) + wt) \end{aligned}$$

5.7 Calculation of Dissipated Power

5.7.1 Review of Poynting's theorem

From vector identity, $\nabla \cdot (\overline{A} \times \overline{B}) = \overline{B} \cdot (\nabla \times \overline{A}) - \overline{A} \cdot (\nabla \times \overline{B})$, we will have,

$$\nabla \cdot (\overline{E} \times \overline{H}) = \overline{H} \cdot (\nabla \times \overline{E}) - \overline{E} \cdot (\nabla \times \overline{H}) \tag{5.51}$$

From equations (5.1) and (5.2), equation (5.51) becomes

$$\nabla \cdot (\overline{E} \times \overline{H}) = \overline{H} \cdot (-\frac{\partial}{\partial t}\overline{B}) - \overline{E} \cdot (\frac{\partial}{\partial t}\overline{D} + \sigma\overline{E})$$

Since $\overline{B} = \mu\overline{H}$ and $\overline{D} = \epsilon\overline{E}$, the above equation becomes

$$-\nabla \cdot (\overline{E} \times \overline{H}) = \sigma\overline{E}^2 + \left(\mu\overline{H} \cdot (\frac{\partial}{\partial t}\overline{H}) + \epsilon\overline{E} \cdot \frac{\partial}{\partial t}\overline{E}\right) \tag{5.52}$$

Equation (5.52) is the differential form of Poynting's theorem. And by integrating over a volume V bounded by the closed surface S, equation (5.52) becomes,

$$\int_V -\nabla \cdot (\overline{E} \times \overline{H})\, dV = \int_V \sigma\overline{E}^2 dV + \int_V \left(\mu\overline{H} \cdot (\frac{\partial}{\partial t}\overline{H}) + \epsilon\overline{E} \cdot \frac{\partial}{\partial t}\overline{E}\right) dV$$

which is the integral form of Poynting's theorem. And by using Gauss' theorem or divergence theorem (which is a mathematical form different from Gauss' law which is a physical law stating that total $\overline{D}$ flux leaving a closed surface is the total charge inside the surface [43]) which states that

$$\int_V dV\, (\nabla \cdot \overline{A}) = \int_S dS\, (\hat{n} \cdot \overline{A})$$

where $\hat{n}$ is a unit vector whose direction is outward normal to the surface S. We will obtain

$$-\int_S \hat{n}\cdot(\overline{E}\times\overline{H})dS = \int_V \sigma\overline{E}^2 dV + \int_V \left(\mu\overline{H}\cdot(\frac{\partial}{\partial t}\overline{H}) + \epsilon\overline{E}\cdot\frac{\partial}{\partial t}\overline{E}\right)dV$$

And for linear and isotropic medium, we obtain

$$-\int_S \hat{n}\cdot(\overline{E}\times\overline{H})\,dS = \int_V \sigma\overline{E}^2 dV + \int_V \left(\frac{1}{2}\mu\cdot(\frac{\partial}{\partial t}\overline{H}^2) + \frac{1}{2}\epsilon\cdot\frac{\partial}{\partial t}\overline{E}^2\right)dV \tag{5.53}$$

The left term of equation (5.53) is the net inward flux of the Poynting vector, $\overline{S} = \overline{E}\times\overline{H}$, into the volume V. For the right hand side part, its first term is the power dissipated as heat while the second term represents the total electromagnetic energy stored in the volume V. Therefore, the power dissipated inside the volume, P, can be written as

$$P = \int_V \left(\sigma\overline{E}^2\right)dV$$

And for conductivity medium, the power dissipation equation is

$$P = \int_V \left(w\epsilon_o\epsilon_r''\overline{E}^2\right)dV$$

Since the electric field values vary sinusoidally with time, the time average power dissipated inside the volume, $< P >$, can be computed from

$$< P > = \frac{1}{2}w\epsilon_o\epsilon_r''\int_V \left(\overline{E}_{max}\right)^2 dV \tag{5.54}$$

where $(\overline{E}_{max})^2 = (E_{x_{max}})^2 + (E_{y_{max}})^2 + (E_{z_{max}})^2$

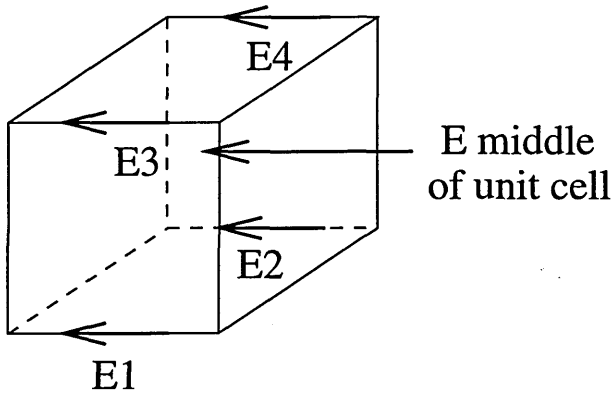

Figure 5-9: A component of E field in a unit cell

5.7.2 Finite difference equations for power dissipation equation

According to the nature of Yee's lattice, each unit cell is composed of four values of each electric field vector component along the boundaries (see Figure 5-9). To compute time average dissipated power for each cell, the maximum values of each electric field value on the boundaries for each cell over a full cycle must be identified first. Then linear interpolation is used to obtain the electric field in the middle of the cell. Therefore, $(E_{x_{max}})^2$, $(E_{y_{max}})^2$, and $(E_{z_{max}})^2$ for each unit cell at (i,j,k) used to calculate time average dissipated power can be obtained from the following equations:

$$\left(E^{n+1}_{x_{max}}(i,j,k)\right)^2 = \frac{1}{16}\times$$
$$\left[E^{n+1}_{x_{max}}(i+\frac{1}{2},j,k)+E^{n+1}_{x_{max}}(i+\frac{1}{2},j+1,k)+E^{n+1}_{x_{max}}(i+\frac{1}{2},j+1,k+1)+E^{n+1}_{x_{max}}(i+\frac{1}{2},j,k+1)\right]^2$$
$$\left(E^{n+1}_{y_{max}}(i,j,k)\right)^2 = \frac{1}{16}\times$$
$$\left[E^{n+1}_{y_{max}}(i,j+\frac{1}{2},k)+E^{n+1}_{y_{max}}(i,j+\frac{1}{2},k+1)+E^{n+1}_{y_{max}}(i+1,j+\frac{1}{2},k)+E^{n+1}_{y_{max}}(i+1,j+\frac{1}{2},k+1)\right]^2$$
$$\left(E^{n+1}_{z_{max}}(i,j,k)\right)^2 = \frac{1}{16}\times$$
$$\left[E^{n+1}_{z_{max}}(i,j,k+\frac{1}{2})+E^{n+1}_{z_{max}}(i,j+1,k+\frac{1}{2})+E^{n+1}_{z_{max}}(i+1,j,k+\frac{1}{2})+E^{n+1}_{z_{max}}(i+1,j+1,k+\frac{1}{2})\right]^2$$

And equation (5.54) to calculate the time average power dissipation for each element (unit in watts) becomes

$$< P^{n+1}(i,j,k) > = \frac{\Delta^3}{2} w\epsilon_o\epsilon_r'' \left[\left(E_{x_{max}}^{n+1}(i,j,k)\right)^2 + \left(E_{y_{max}}^{n+1}(i,j,k)\right)^2 + \left(E_{z_{max}}^{n+1}(i,j,k)\right)^2 \right] \quad (5.55)$$

where $\Delta = \Delta x = \Delta y = \Delta z =$ grid size in the model.

Implementation

In our numerical model, the following equations are employed instead of those shown above while the equation (5.55) to calculate the time average power dissipation remains the same.

$$\left(E_{x_{max}}^{n+1}(i,j,k)\right)^2 = \frac{1}{16}\left[E_{x_{max}}^{n+1}(i,j,k) + E_{x_{max}}^{n+1}(i,j,k+1) + E_{x_{max}}^{n+1}(i,j+1,k) + E_{x_{max}}^{n+1}(i,j+1,k+1)\right]^2$$

$$\left(E_{y_{max}}^{n+1}(i,j,k)\right)^2 = \frac{1}{16}\left[E_{y_{max}}^{n+1}(i,j,k) + E_{y_{max}}^{n+1}(i+1,j,k) + E_{y_{max}}^{n+1}(i,j,k+1) + E_{y_{max}}^{n+1}(i+1,j,k+1)\right]^2$$

$$\left(E_{z_{max}}^{n+1}(i,j,k)\right)^2 = \frac{1}{16}\left[E_{z_{max}}^{n+1}(i,j,k) + E_{z_{max}}^{n+1}(i+1,j,k) + E_{z_{max}}^{n+1}(i,j+1,k) + E_{z_{max}}^{n+1}(i+1,j+1,k)\right]^2$$

5.7.3 Steady-state dissipated power calculation

In this work, the excitation source generates sinusoidal waveform to the microwave cavity to heat the dielectric material. To obtain steady state dissipated power distribution in the material, the summation of calculated power at all layers in the dielectric material over a full cycle of the incident wave will be plotted against time step so that we can check when the steady state has been reached. As shown in Figure 5-10, the steady states for several materials are reached after approximately 6000 time steps. Therefore, after 6000 time steps, the maximum electric field values will be obtained from each element of heated material over a full cycle and used to compute the steady-state time average dissipated power.

5.8 Verification of the Power Dissipation Model

To check the developed FDTD algorithm used to analyze the absorbed power distribution, the values of calculated field and power density are compared with either the analytical solution or the available results

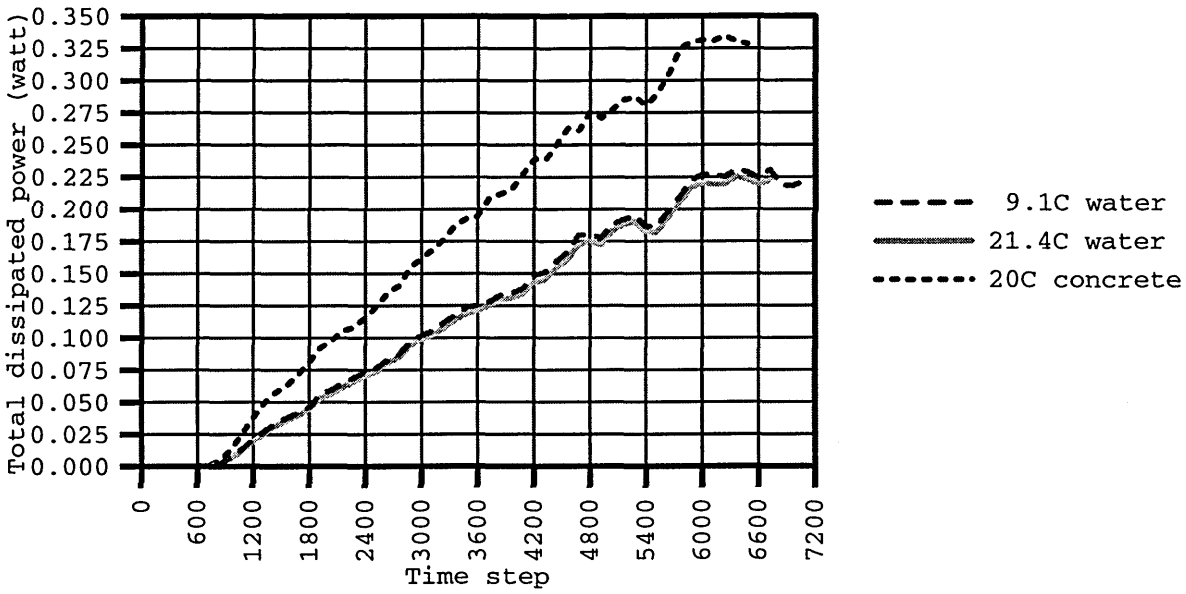

Figure 5-10: Example plots of total dissipated power versus time step for several materials

from other related papers. The analytical solution can be found in the appendix at the end of this chapter.

5.8.1 Field value comparison

Calculation of field values for two simple examples are performed and compared with the analytical solutions. The problem is to compute the existing field values in the rectangular waveguide filled with air and some lossy material (see Figure 5-11). One of the ends of waveguide is connected with metallic plate while the other is opened to free space. It is assumed that the TE_{10} wave propagating in $-\hat{z}$ direction is excited at 2.45 GHz at plane $z = 0.20$ m where the specified field is

$$H_x = sin(\frac{\pi x}{a})$$

where a = width of rectangular waveguide

Two interested points (where results are to be obtained) are at (0.05,0.025,0.05) and (0.05,0.025,0.15). First, the simplest case is considered when there is no lossy material in the waveguide. Then, the waveguide is

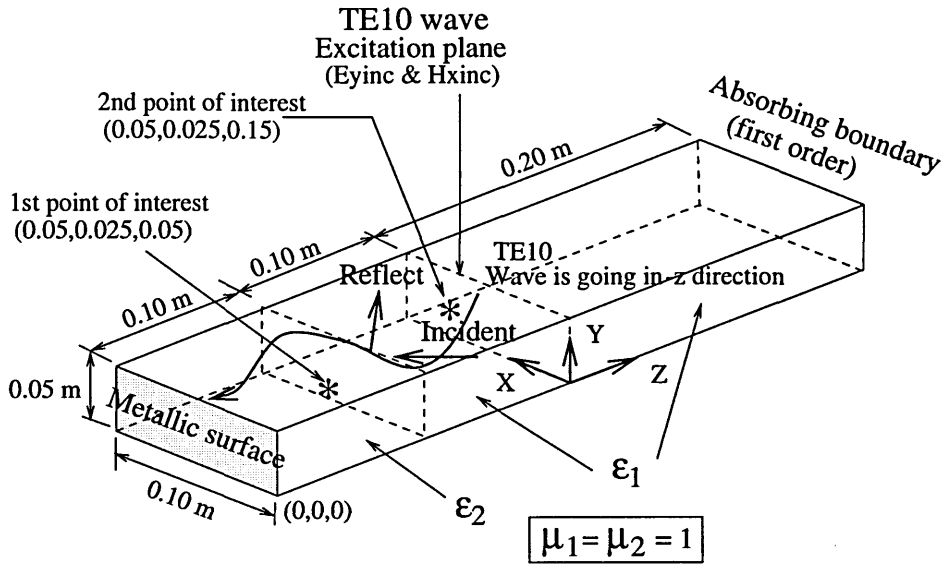

Figure 5-11: Rectangular waveguide problem with excited TE_{10} wave

partially filled with a lossy material.

Example 1: TE_{10} wave in air-filled rectangular waveguide

Figures 5-12, 5-13 and 5-14 compare the E_y, H_x, and H_z results obtained from the FDTD model to the analytical results at two locations of interest ((0.05,0.025,0.05) and (0.05,0.025,0.15)) in air-filled rectangular waveguide excited with TE_{10} wave. In this example, the space increment, which is equal to 0.01 m, is about (1/12.25) of the smallest wavelength in the model while the time increment, 6.803E-12 second, is about (1/60) of the period of incident wave excited at 2.45 GHz. And $\epsilon_1 = \epsilon_2 = 1.0$ for air in both regions. The other parameters can be seen from Figure 5-11.

It is obvious that the field calculations from the model are matched well with the analytical results (in the appendix).

Example 2: TE_{10} wave in two-layered medium-filled rectangular waveguide

In this example, ϵ_1 is set to 1.0 for air in region 1 while ϵ_2 is assigned to $(2 + 0.5i)$ for dielectric material in region 2. The rest of the parameters are kept the same as those in the previous example. Figures 5-15,

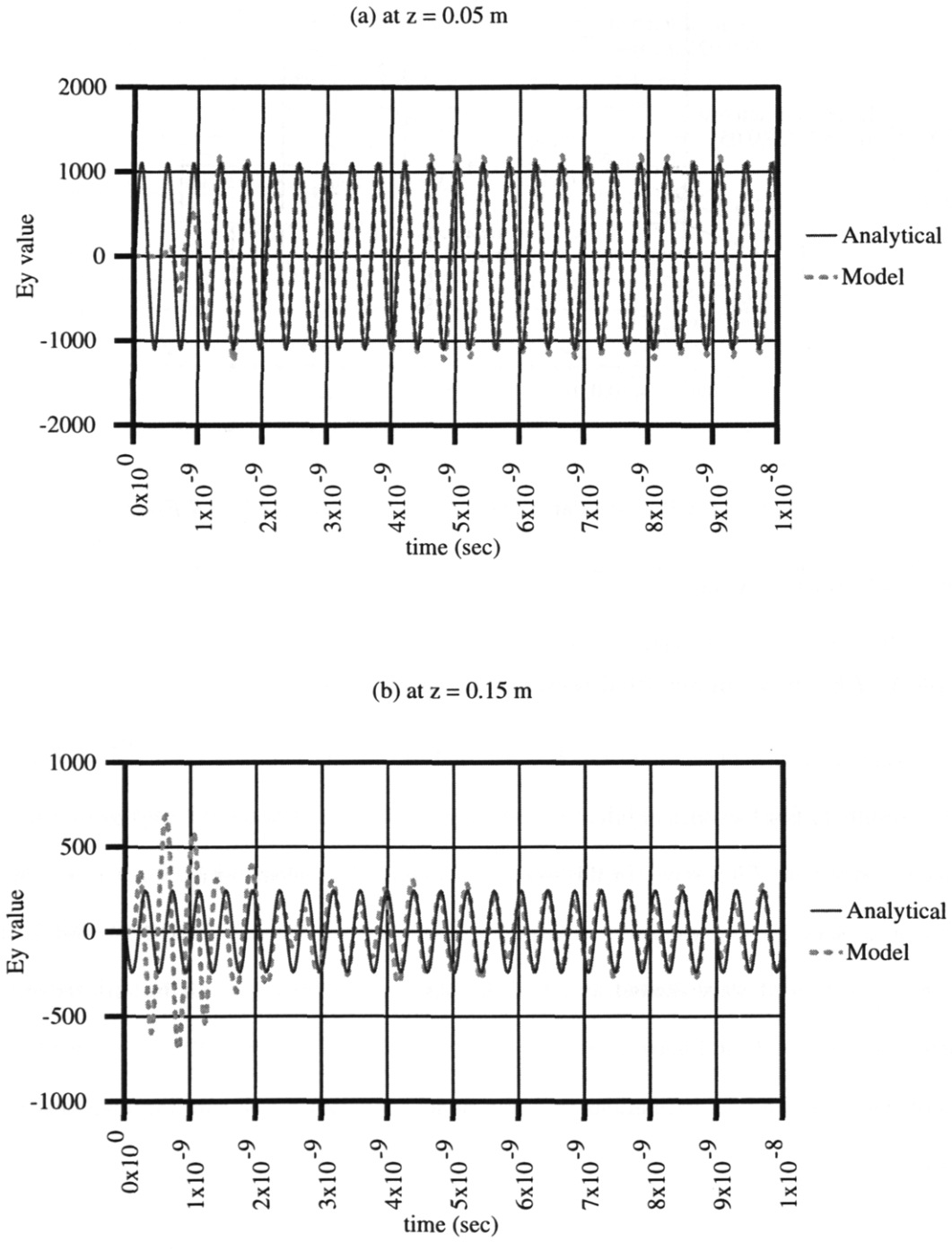

Figure 5-12: Comparison of Ey values from analytical solution and numerical modeling in air-filled rectangular waveguide (unit of E is volt/meter)

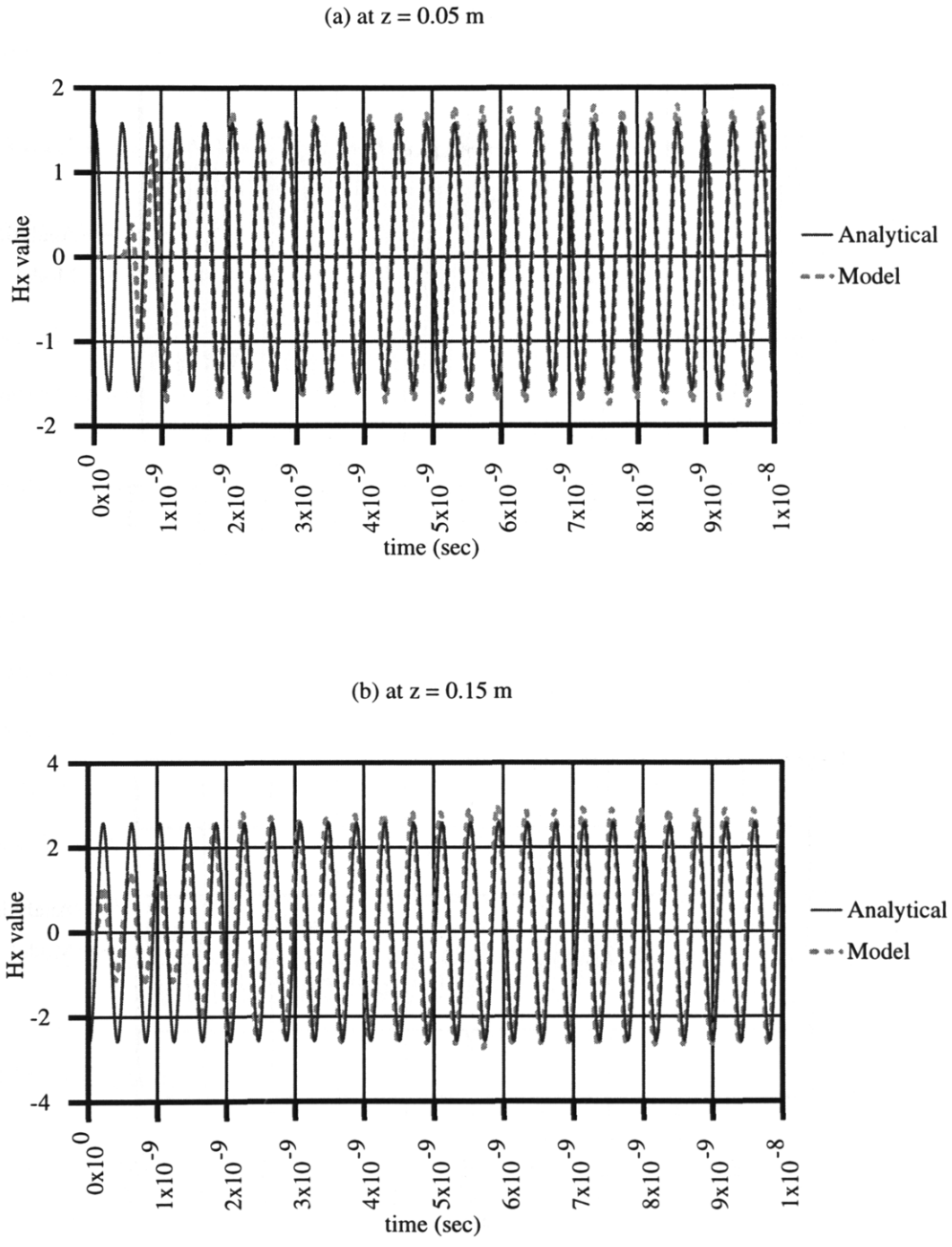

Figure 5-13: Comparison of Hx values from analytical solution and numerical modeling in air-filled rectangular waveguide (unit of H is ampere/meter)

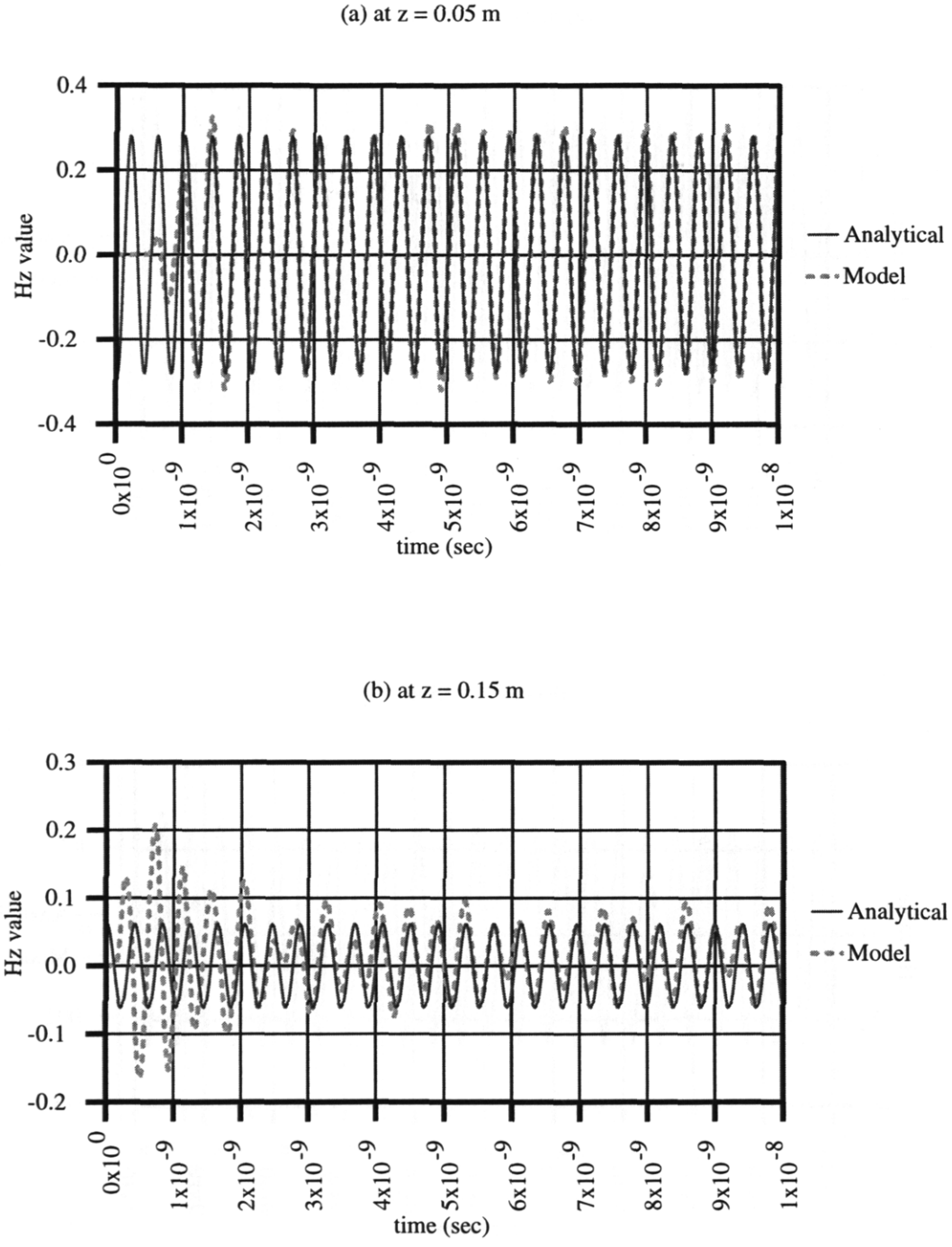

Figure 5-14: Comparison of Hz values from analytical solution and numerical modeling in air-filled rectangular waveguide (unit of H is ampere/meter)

5-16 and 5-17 compare the results obtained from the FDTD model to the analytical results (in the appendix) at two locations of interest ((0.05,0.025,0.05) and (0.05,0.025,0.15)). Again, the field calculations from the model agree well with the analytical solutions.

5.8.2 Dissipated power distribution comparison

In this section, the computed dissipated power distribution from the model is compared to the available results by Liu et. al. [25]. As shown in Figure 5-18, a simple cavity is composed of a rectangular waveguide unit connected to top of main cavity. The incident TE_{10} wave is excited at a plane inside the waveguide in order to introduce wave to the cavity where the dielectric material exists.

Example 3: Rectangular cavity with a lossy material

The lossy material under this comparison is a 11.47x11.47x1.72 cm rectangular block material whose permittivity is $(2 + 0.5i)$. Its dissipated power is computed when material is either at 1.72 or 4.587 cm from top of cavity as shown in Figures 5-19 and 5-20, respectively.

The results, in Figures 5-19 and 5-20, are compared with the results by Liu et. al. [25] as shown in Figures 5-21 and 5-22. It is noted that Figures 5-19 and 5-20 show plots of steady-state dissipated power distribution for each layer and all layers of material while for the plots in Figures 5-21 and 5-22, Liu et. al. [25] did not mention which layer is used to plot the dissipated power. However, after carefully comparison, the plots of middle layer of material is found to match well with the plots in Liu et. al.

5.9 Conclusion

The Finite-Difference Time-Domain technique is an integral part of the power dissipation model. The model is used to determine the steady-state dissipated power which is useful in simulation of microwave heating. A computer algorithm for this model has been developed and tested. Plots of field values and dissipated power distribution agree well with analytical solutions and available results.

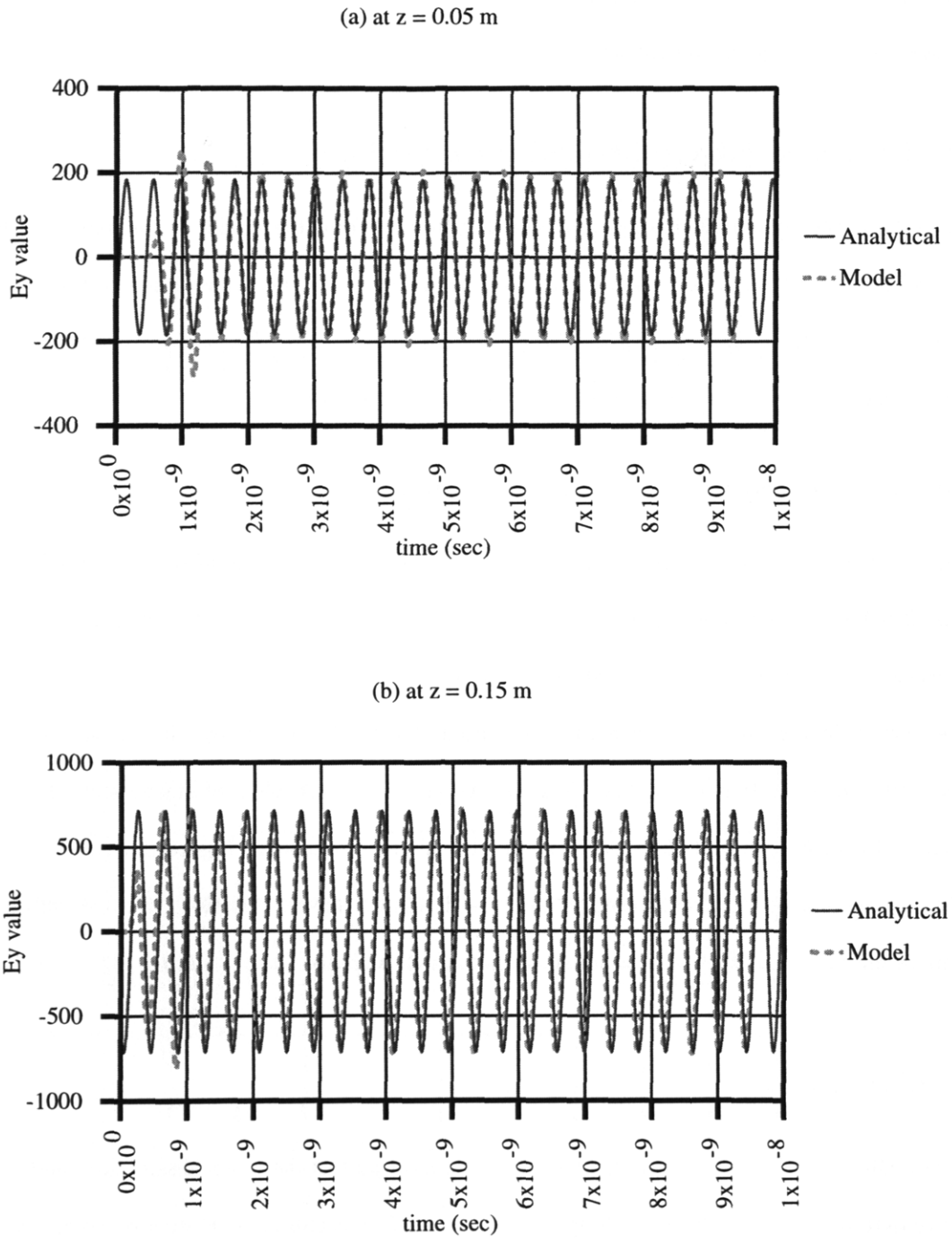

Figure 5-15: Comparison of Ey values from analytical solution and numerical modeling in two-layered medium-filled rectangular waveguide (unit of E is volt/meter)

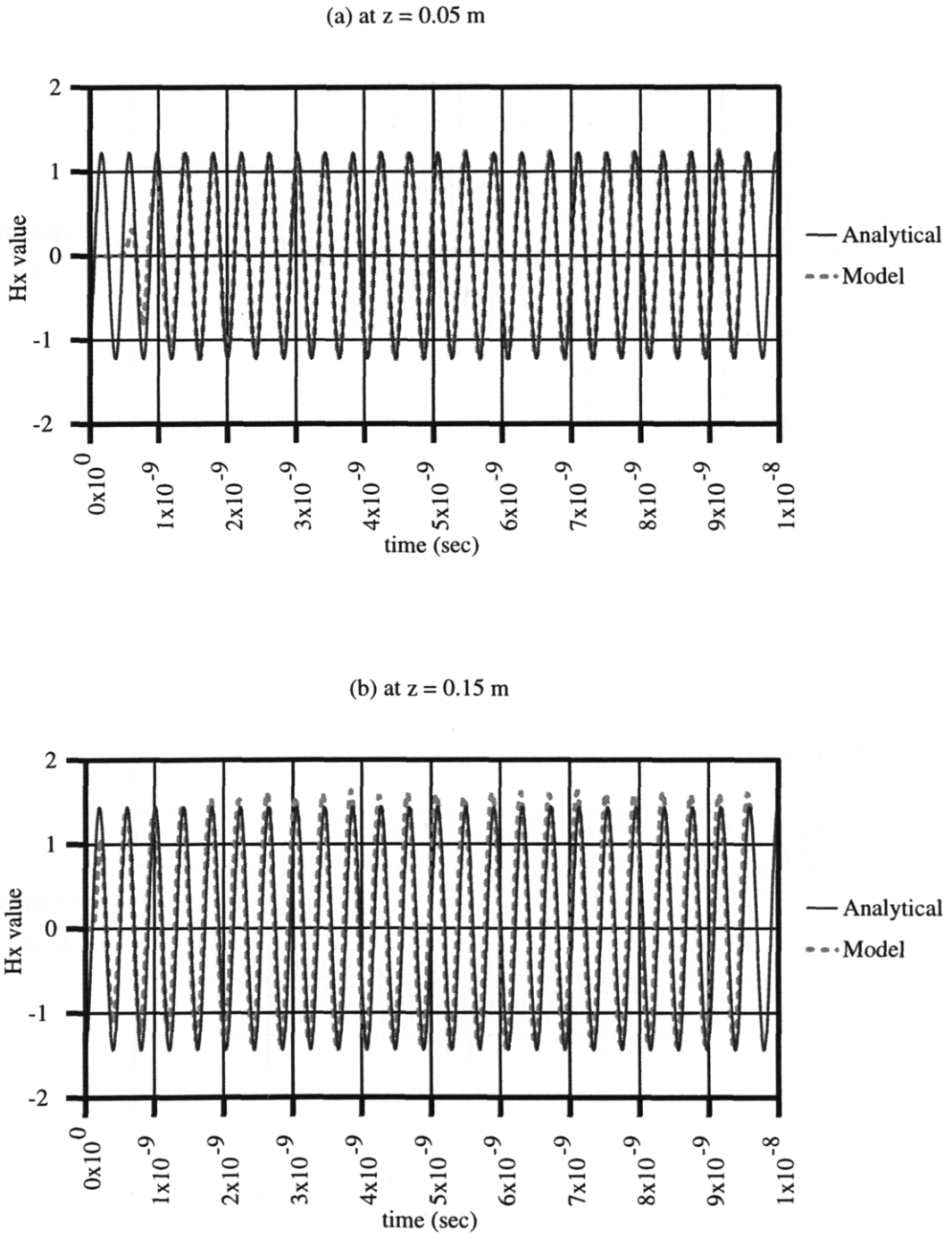

Figure 5-16: Comparison of Hx values from analytical solution and numerical modeling in two-layered medium-filled rectangular waveguide (unit of H is ampere/meter)

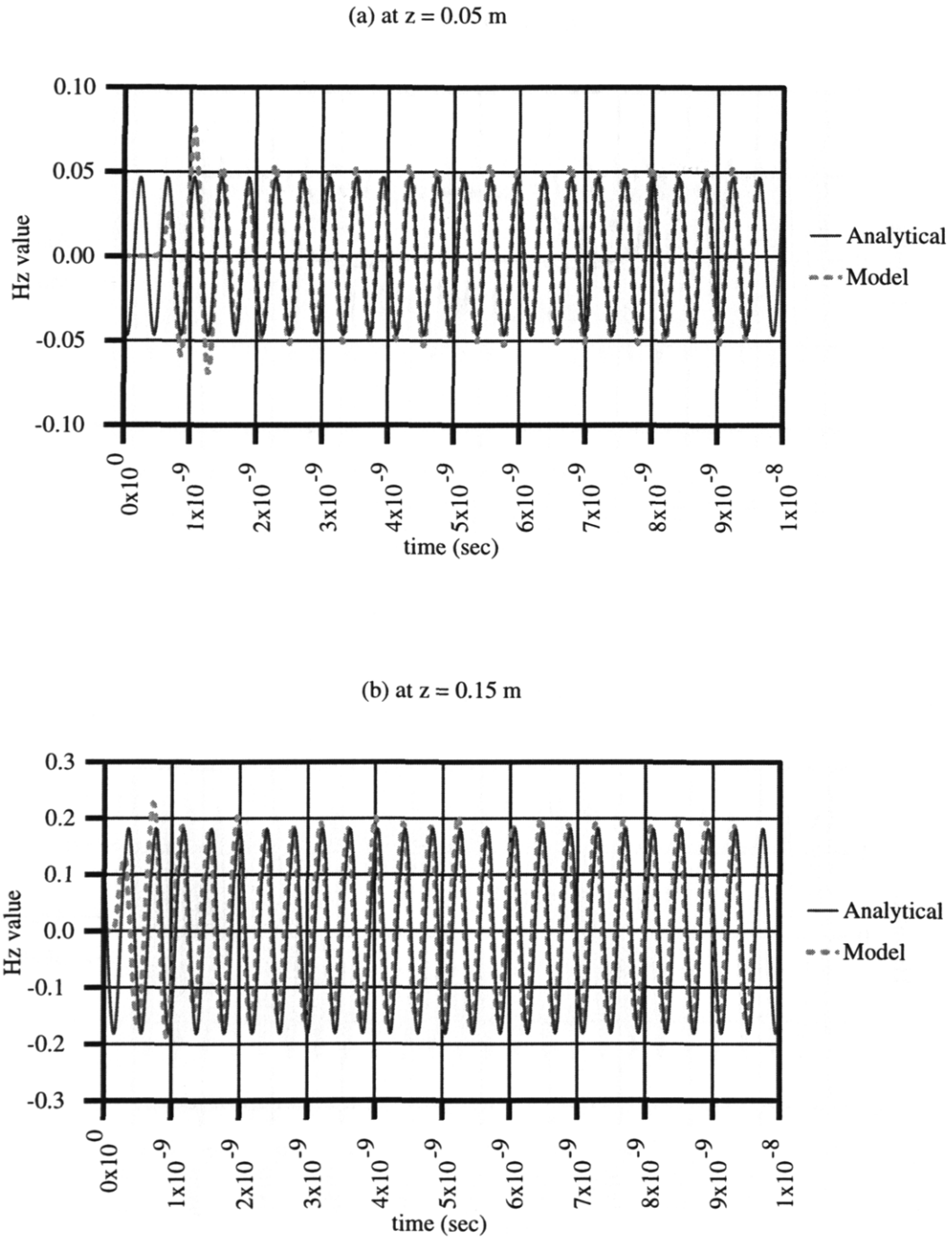

Figure 5-17: Comparison of Hz values from analytical solution and numerical modeling in two-layered medium-filled rectangular waveguide (unit of H is ampere/meter)

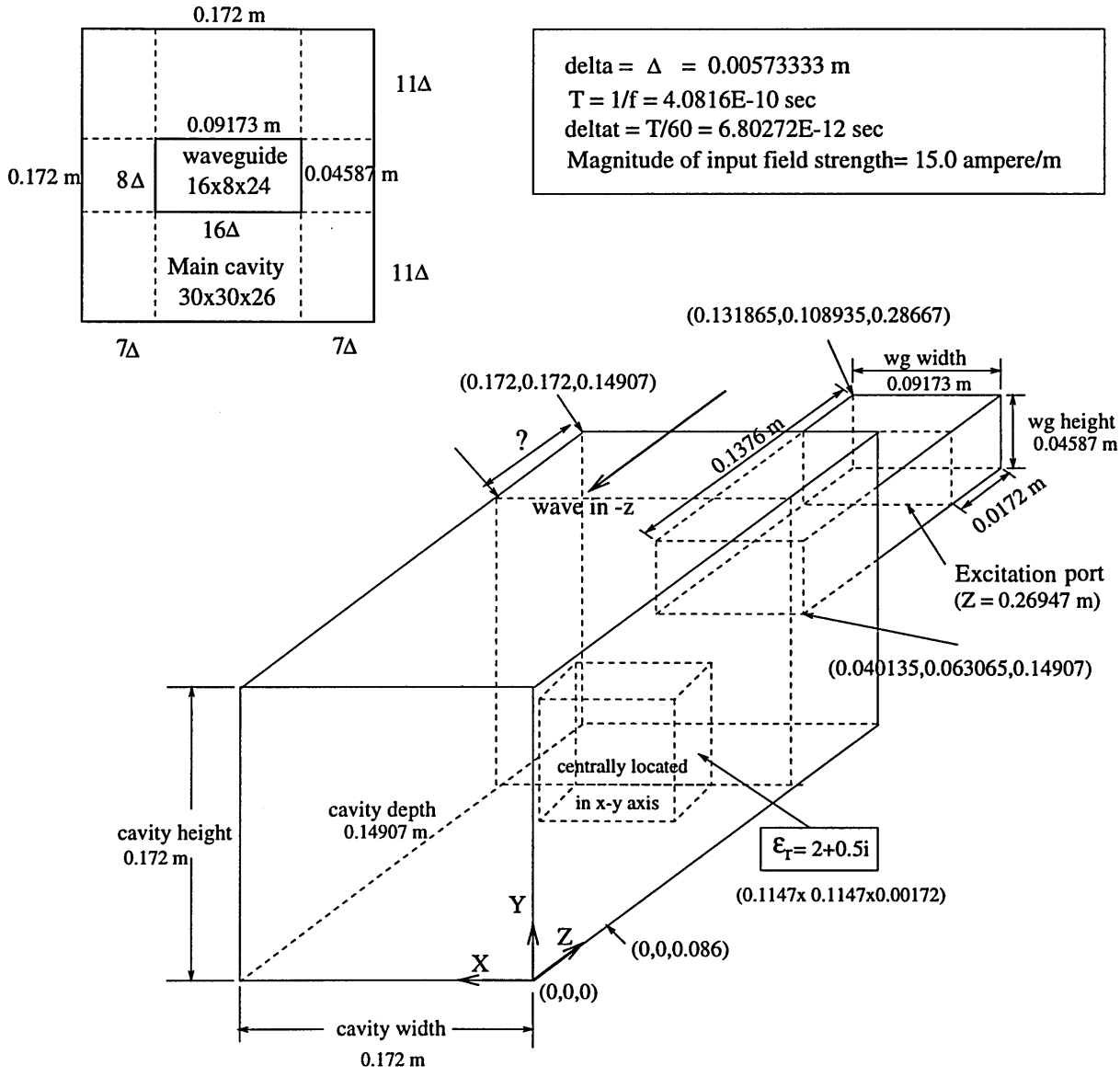

Figure 5-18: Rectangular cavity problem (loaded with dielectric material) with excited TE_{10} in the rectangular waveguide

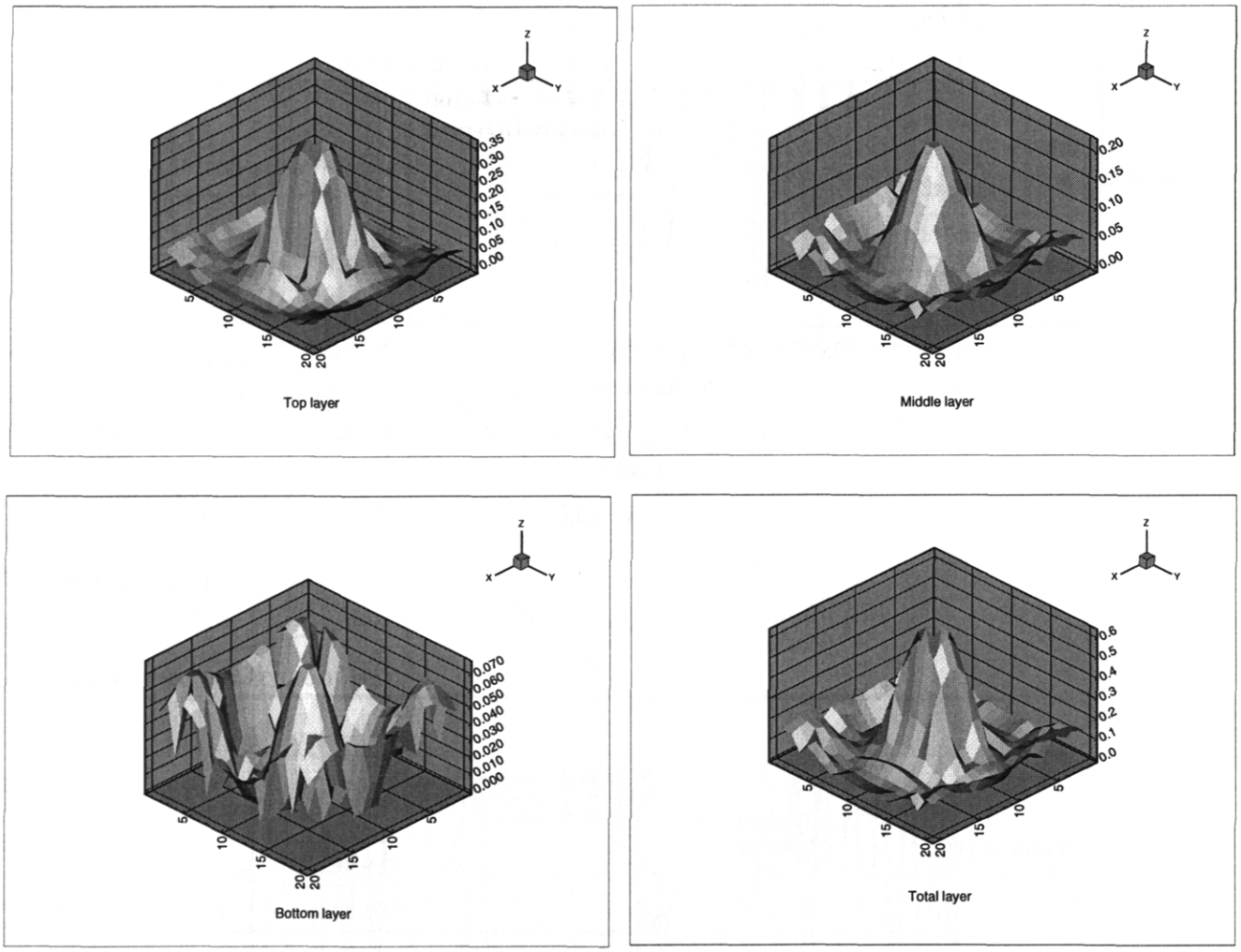

Figure 5-19: Steady-state dissipated power distribution for each layer of a block of $(2 + 0.5i)$ material in a rectangular cavity (material is 1.72 cm from top of cavity and unit of power on z-axis is in watt)

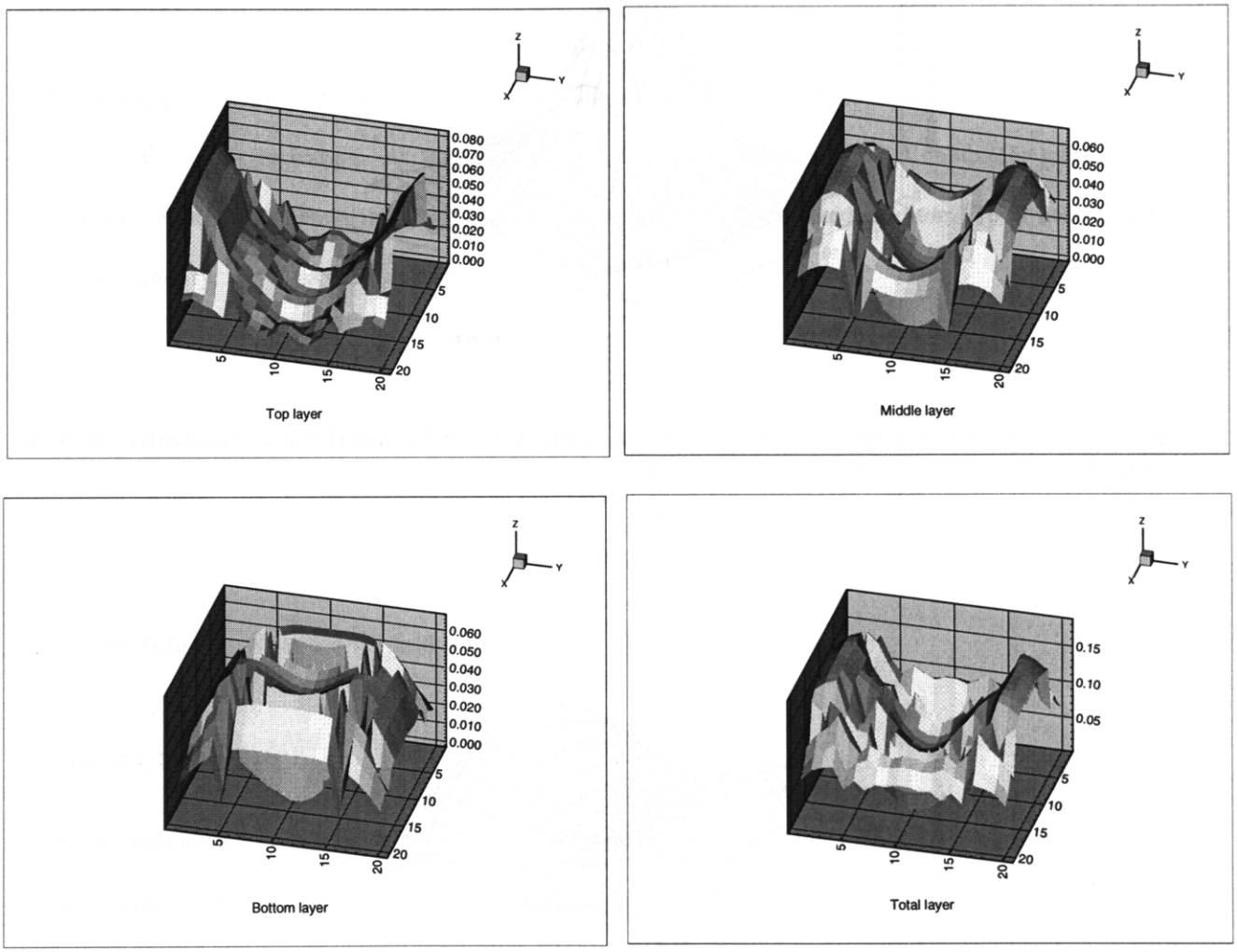

Figure 5-20: Steady-state dissipated power distribution for each layer of a block of $(2 + 0.5i)$ material in a rectangular cavity (material is 4.587 cm from top of cavity and unit of power on z-axis is in watt)

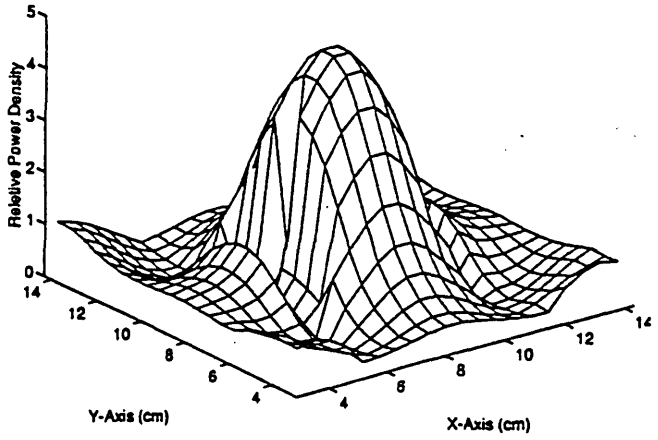

Figure 5-21: FDTD results for dissipated power of a block of $(2 + 0.5i)$ material in a rectangular cavity by Liu et. al. (material is 1.72 cm from top of cavity)

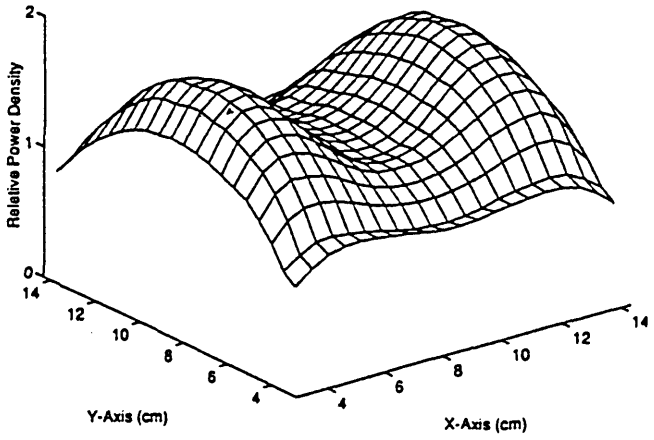

Figure 5-22: FDTD results for dissipated power of a block of $(2 + 0.5i)$ material in a rectangular cavity by Liu et. al. (material is 4.587 cm from top of cavity)

5.10 Appendix I. - Two-Layered Medium in Rectangular Waveguide

5.10.1 Problem description

The rectangular waveguide filled with air and some lossy material is excited at 2.45 GHz and only TE_{10} mode exists in this excitation. At the bottom, it is terminated with the perfect conductor while the top is left open. Figure 5-23 shows the rectangular waveguide with a two-layered medium. Total field is specified at the boundary, $z = c$, as followings:

$$H_x = H_0 sin(\frac{\pi x}{a}) \tag{5.56}$$

where H_0 = the strength of the magnetic field = 1.0 ampere/m , and

a = width of rectangular waveguide

Question: What are the field components in regions 0 and 1?

5.10.2 Solution

Let us consider a two-layered medium inside the rectangular waveguide with perfect conductor at region 2 (see Figure 4-19(b) and refer to Appendix I of Chapter 4). The field components for TE_{10} wave in region 0 and 1 can be written as (from equations (4.3), (4.4) and (4.5))

For region 0:

$$E_{y0} = \left(A_0 e^{ik_{0z}z} + B_0 e^{-ik_{0z}z}\right)\left(e^{ik_x x} - e^{-ik_x x}\right) \tag{5.57}$$

$$H_{x0} = \frac{1}{iw\mu_0}\left(-\frac{\partial}{\partial z}E_{y0}\right) = \frac{k_{0z}}{w\mu_0}\left(-A_0 e^{ik_{0z}z} + B_0 e^{-ik_{0z}z}\right)\left(e^{ik_x x} - e^{-ik_x x}\right) \tag{5.58}$$

$$H_{z0} = \frac{1}{iw\mu_0}\left(+\frac{\partial}{\partial x}E_{y0}\right) = \frac{k_x}{w\mu_0}\left(A_0 e^{ik_{0z}z} + B_0 e^{-ik_{0z}z}\right)\left(e^{ik_x x} + e^{-ik_x x}\right) \tag{5.59}$$

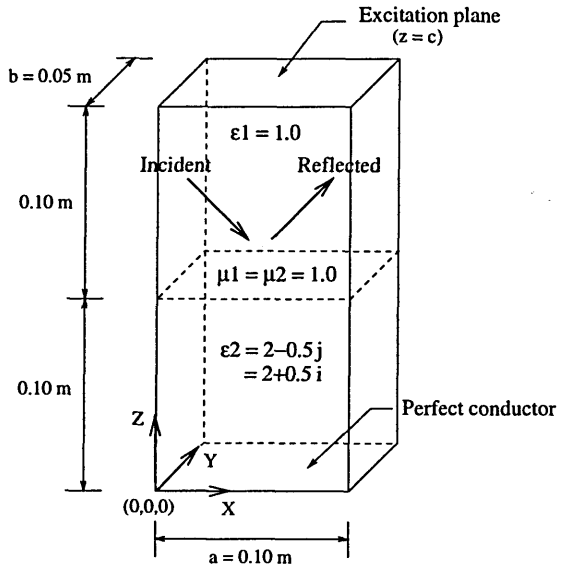

Figure 5-23: Layered medium in rectangular waveguide

and for region 1:

$$E_{y1} = \left(A_1 e^{ik_{1z}z} + B_1 e^{-ik_{1z}z}\right)\left(e^{ik_x x} - e^{-ik_x x}\right) \tag{5.60}$$

$$H_{x1} = \frac{k_{1z}}{w\mu_1}\left(-A_1 e^{ik_{1z}z} + B_1 e^{-ik_{1z}z}\right)\left(e^{ik_x x} - e^{-ik_x x}\right) \tag{5.61}$$

$$H_{z1} = \frac{k_x}{w\mu_1}\left(A_1 e^{ik_{1z}z} + B_1 e^{-ik_{1z}z}\right)\left(e^{ik_x x} + e^{-ik_x x}\right) \tag{5.62}$$

where $k_x = \frac{\pi}{a}$,

$k_{0z} = \sqrt{w^2\mu_0\epsilon_0 - {k_x}^2}$,

$k_{1z} = \sqrt{w^2\mu_1\epsilon_1 - {k_x}^2}$,

$A_0 = RE_0$,

$B_0 = E_0$, magnitude of electric field strength,

$R = \frac{R_{01}+R_{12}e^{i2k_{1z}(d1-d0)}}{1+R_{01}R_{12}e^{i2k_{1z}(d1-d0)}} e^{i2k_z d_0}$,

$R_{01} = \frac{1-p_{01}}{1+p_{01}} = -R_{10}$,

$$
\begin{aligned}
p_{01} &= \tfrac{\mu_0 k_{1z}}{\mu_1 k_{0z}} = \tfrac{1}{p_{10}}, \\
R_{12} &= -1 \text{ when perfect conductor is at region 2} \\
A_1 &= \tfrac{1}{2}\left(1+p_{10}\right)\left(A_0 e^{-ik_{0z}d_0} + R_{10}B_0 e^{ik_{0z}d_0}\right) e^{ik_{1z}d_0}, \text{ and} \\
B_1 &= \tfrac{1}{2}\left(1+p_{10}\right)\left(R_{10}A_0 e^{-ik_{0z}d_0} + B_0 e^{ik_{0z}d_0}\right) e^{-ik_{1z}d_0}
\end{aligned}
$$

To solve the problem, $H_{x0} = H_0 sin(\frac{\pi x}{a})$ is specified at the boundary (z=c) in region 0. Therefore,

$$
\begin{aligned}
H_0 sin(\frac{\pi x}{a}) &= \frac{k_{0z}}{w\mu_0}\left(-A_0 e^{ik_{0z}c} + B_0 e^{-ik_{0z}c}\right)\left(e^{ik_x x} - e^{-ik_x x}\right) \\
\frac{H_0}{2i}\left(e^{ik_x x} - e^{-ik_x x}\right) &= \frac{k_{0z}E_0}{w\mu_0}\left(-Re^{ik_{0z}c} + e^{-ik_{0z}c}\right)\left(e^{ik_x x} - e^{-ik_x x}\right) \\
E_0 &= \frac{w\mu_0 \overbrace{H_0}^{1}}{2ik_{0z}\left(-Re^{ik_{0z}c} + e^{-ik_{0z}c}\right)} \\
E_0 &= \frac{w\mu_0}{2ik_{0z}\left(-Re^{ik_{0z}c} + e^{-ik_{0z}c}\right)}
\end{aligned}
$$

Thus, the field components, E_{y0}, H_{x0}, and H_{z0}, in regions 0 can be determined by substituting A_0 and B_0 in term of E_0 (from above equation) as shown in equations (5.57), (5.58), and (5.59). Similarly, E_{y1}, H_{x1}, and H_{z1}, as shown in equations (5.60), (5.61), and (5.62), respectively, can also be determined.

Chapter 6

Heat Transfer Model

6.1 Introduction

After the steady-state dissipated power is determined, the heat transfer model is used to compute the temperature distribution during the microwave heating. By using the same finite-difference scheme as in the previous section, the original mesh generated in the power dissipation model is applicable to the heat transfer model but their time steps are different significantly. For example, the time step of the power dissipation model is in an order of picosecond (10^{-12}) while that of the heat transfer model is in an order of 1 second.

In this chapter, the transient heat diffusion, the effect of cylindrical-shaped material in the model, the verification of model as well as the stability analysis are included.

6.2 Transient Heat Diffusion

The transient heat diffusion equation for inhomogeneous and stationary solid medium is given as

$$\frac{\partial}{\partial t}\left(\rho c_p T\right) = -(\nabla \cdot Q) + F$$

if medium is uniform, i.e., ρ and c_p are constants,

$$\rho c_p \frac{\partial}{\partial t}(T) = -(\nabla \cdot Q) + F \tag{6.1}$$

where ρ = density of material (kg/m^3),

c_p= specific heat (joule/(kg °C)),

Q= rate of heat flow conducted through a unit area (watt/m^2), and

F= rate of heat source per unit volume (watt/m^3)

In microwave curing, temperature rise in fresh concrete are mainly due to heat absorbed from microwave energy and convective heat lost to the surroundings. Heat generated from cement hydration is assumed to be not so significant. Therefore, rate of heat source per unit volume includes only (i) rate of generated heat due to microwave power absorption per unit volume (F_{abs}) and (ii) rate of convective heat loss per unit volume (F_{cvec}).

Thus, equation (6.1) becomes

$$\frac{\partial T}{\partial t} = \frac{1}{\rho c_p} \times \{-(\nabla \cdot Q) + F_{abs} - F_{cvec}\} \tag{6.2}$$

6.2.1 Rate of generated heat due to microwave power absorption

Rate of heat due to power absorption per unit volume (F_{abs}) can be simply written as

$$F_{abs} = \frac{P}{V}$$

where P = absorbed power obtained from the power dissipation model (watt), and

V = volume (m^3)

6.2.2 Rate of convective heat loss

Convection loss depends on the exposed surface area, the air flow over the exposed area, and the temperature between the surface and the air. Therefore, rate of heat loss due to convection per unit volume (F_{cvec}) can be expressed as

$$F_{cvec} = \frac{h_{cv} A(T_s - T_a)}{V}$$

where h_{cv} = heat transfer coefficient (watt/(m^2 K)),

A = surface area (m^2),

T_s = temperature at surface area (K), and

T_a = temperature of the surrounding air (K)

Note that the convective term is only required for elements at the exposed surface. It can be set to zero for all internal elements.

Since the convection heat transfer coefficient for air in natural convection is reported to be 5-25 watt/(m^2 K) [17] and free convection is encountered in microwave curing, the heat transfer coefficient used in this work is therefore assumed to be 25 watt/(m^2 K).

6.2.3 Implementation

The explicit finite-difference scheme is used to represent the heat diffusion equation. If the grid sizes in x, y, and z axis are equal ($\Delta x = \Delta y = \Delta z = \Delta$), to compute the temperature of element (i,j,k) at the next time step, $T^{n+1}(i,j,k)$ from equation (6.2) can be expressed as

$$T^{n+1}(i,j,k) = T^n(i,j,k) + \frac{\Delta t}{\rho(i,j,k)c_p(i,j,k)} \times \{-(\nabla \cdot Q^n(i,j,k)) + F^n_{abs}(i,j,k) - F^n_{cvec}(i,j,k)\}$$

where $F^n_{abs}(i,j,k) = \frac{P^n(i,j,k)}{\Delta^3}$,

$F^n_{cvec}(i,j,k) = \frac{h_{cv}A(i,j,k)(T^n(i,j,k)-T_a(i,j,k))}{\Delta^3}$ (at elements near exposed surface only),

and $(\nabla \cdot Q^n(i,j,k))$ is the net flow of Q out of a small unit cube cell divided by the cube volume. For example, consider a vector Q having only $\hat{x}$ component and refer to Figure 6-1, the following can be obtained.

$$\begin{aligned} \hat{x}(\nabla \cdot Q) &= \frac{(Q_{xl}\Delta y\Delta z - Q_{xr}\Delta y\Delta z)}{\Delta x\Delta y\Delta z} \\ &= \frac{(Q_{xl} - Q_{xr})}{\Delta} \end{aligned}$$

Therefore, for three dimensions, $(\nabla \cdot Q)$ can be written as (notation is shown in Figure 6-1)

$$\begin{aligned} (\nabla \cdot Q) &= \frac{(Q_{xl} - Q_{xr})}{\Delta x} + \frac{(Q_{yt} - Q_{yb})}{\Delta y} + \frac{(Q_{zf} - Q_{zn})}{\Delta z} \\ -(\nabla \cdot Q) &= \frac{(Q_{xr} - Q_{xl})}{\Delta x} + \frac{(Q_{yb} - Q_{yt})}{\Delta y} + \frac{(Q_{zn} - Q_{zf})}{\Delta z} \end{aligned}$$

where each component of Q, which depends on thermal conductivity and temperature gradient according to Fourier's law of heat, can be written as

$$\begin{aligned} Q_{xr} &= -K_{xr}\frac{[T(i,j,k) - T(i-1,j,k)]}{\Delta x} \\ Q_{xl} &= -K_{xl}\frac{[T(i+1,j,k) - T(i,j,k)]}{\Delta x} \\ Q_{yb} &= -K_{yb}\frac{[T(i,j,k) - T(i,j-1,k)]}{\Delta y} \\ Q_{yt} &= -K_{yt}\frac{[T(i,j+1,k) - T(i,j,k)]}{\Delta y} \\ Q_{zn} &= -K_{zn}\frac{[T(i,j,k) - T(i,j,k-1)]}{\Delta z} \\ Q_{zf} &= -K_{zf}\frac{[T(i,j,k+1) - T(i,j,k)]}{\Delta z} \end{aligned}$$

where K_{xr}, K_{xl}, K_{yb}, K_{yt}, K_{zn}, and K_{zf} can be determined from averaging the thermal conductivities over the adjacent cells as follows:

$$K_{xr} = \frac{1}{2}[K_c(i,j,k) + K_c(i-1,j,k)]$$

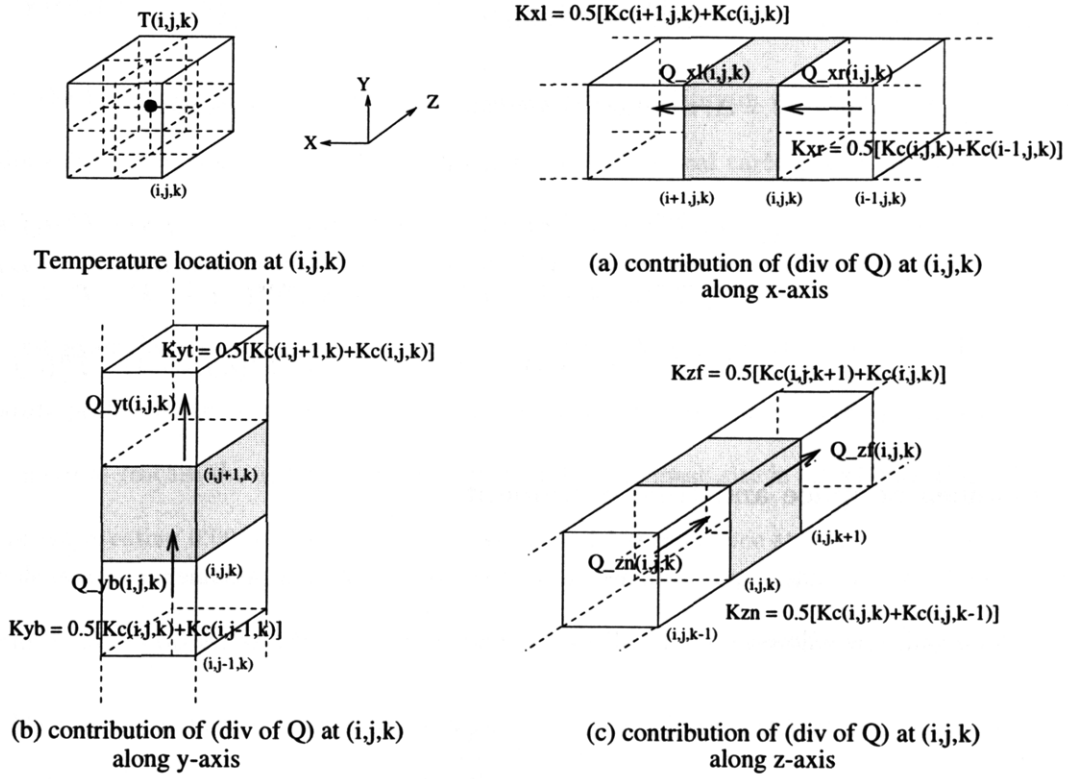

Figure 6-1: Notation used in implementation of heat flow

$$
\begin{aligned}
K_{xl} &= \frac{1}{2}[K_c(i+1,j,k) + K_c(i,j,k)] \\
K_{yb} &= \frac{1}{2}[K_c(i,j,k) + K_c(i,j-1,k)] \\
K_{yt} &= \frac{1}{2}[K_c(i,j+1,k) + K_c(i,j,k)] \\
K_{zn} &= \frac{1}{2}[K_c(i,j,k) + K_c(i,j,k-1)] \\
K_{zf} &= \frac{1}{2}[K_c(i,j,k+1) + K_c(i,j,k)]
\end{aligned}
$$

where $K_c(i,j,k)$ is thermal conductivity of material at unit cell (i,j,k)

And by allowing $\Delta x = \Delta y = \Delta z = \Delta$, equation to compute $-(\nabla \cdot Q^n(i,j,k))$ becomes

$$
\begin{aligned}
-(\nabla \cdot Q^n(i,j,k)) &= \frac{1}{(\Delta)^2}\{K_{xl}[T^n(i+1,j,k) - T^n(i,j,k)] + K_{xr}[T^n(i-1,j,k) - T^n(i,j,k)]\} \\
&+ \frac{1}{(\Delta)^2}\{K_{yt}[T^n(i,j+1,k) - T^n(i,j,k)] + K_{yb}[T^n(i,j-1,k) - T^n(i,j,k)]\} \\
&+ \frac{1}{(\Delta)^2}\{K_{zf}[T^n(i,j,k+1) - T^n(i,j,k)] + K_{zn}[T^n(i,j,k-1) - T^n(i,j,k)]\} \quad (6.3)
\end{aligned}
$$

6.2.4 Choices of space and time increment

The choice of grid size and time step is obtained from the stability criterion (assume no source) shown in the appendix section and is as follows:

$$\Delta t \leq \frac{\Delta^2}{6\alpha}$$

where $\alpha = \frac{K_c}{\rho c_p}$ = thermal diffusivity

6.3 Effect of Cylindrical Shape of Material in Numerical Model

For heat transfer problem, the heat due to convection related to heat transfer coefficient can be significant. And because in the numerical modeling using Cartesian coordinate system, the cylindrical-shaped material cannot be modeled exactly but will be modeled in a staircase manner. Therefore, the effective heat transfer

coefficient has to be computed and used in heat diffusion equation.

If the original heat transfer coefficient is used, the heat due to convection will not be correct. The effective heat transfer coefficient is therefore computed locally based on the ratio of the circumference length of the real cylinder and the length around the surface of the staircase model. By doing this, the contribution of convective heat will be more reasonable.

6.4 Verification of the Heat Transfer Model

To verify the heat transfer model, an example of reaching equilibrium and two examples of temperature calculations during the cooling process of rectangular and cylindrical carbon steel are illustrated.

Example 1: A thin slab of water-like material (no heat loss to surroundings)

In this first example, the convective heat loss is neglected. A thin water-like material slab with an initial temperature profile as shown in Figure 6-2 is left to return to equilibrium. As shown in Figure 6-2, it is clear that the material reaches the equilibrium after 60 seconds. The mesh size is 5x5x1 with the 0.001 m grid size (therefore representing 0.005x0.005x0.001 m material) and 1-second time step is used.

Example 2: A rectangular block of steel bar (including heat loss to surroundings)

The problem is to compute the temperature after 10 minutes in the center of the 150°C rectangular plain carbon steel cooling in the air. The surrounding temperature is 35°C and the average heat transfer coefficient during the cooling process is 600 watt/(m^2 °C). Figure 6-3 shows the complete details of this problem.

From the approximation using the chart method (infinite-slab method) available in general heat transfer text book such as in [42], the temperature in the middle of the steel bar after 10 minutes is about 42.4°C or 315.5 K while the result from the numerical model gives 41.2°C or 314.4 K. The small difference of temperatures is probably due to the inaccuracy in reading the values off the available chart in the chart method. To conclude, the value from the model is satisfactory. The time step is 0.25 second and the space increment is 0.005 meter.

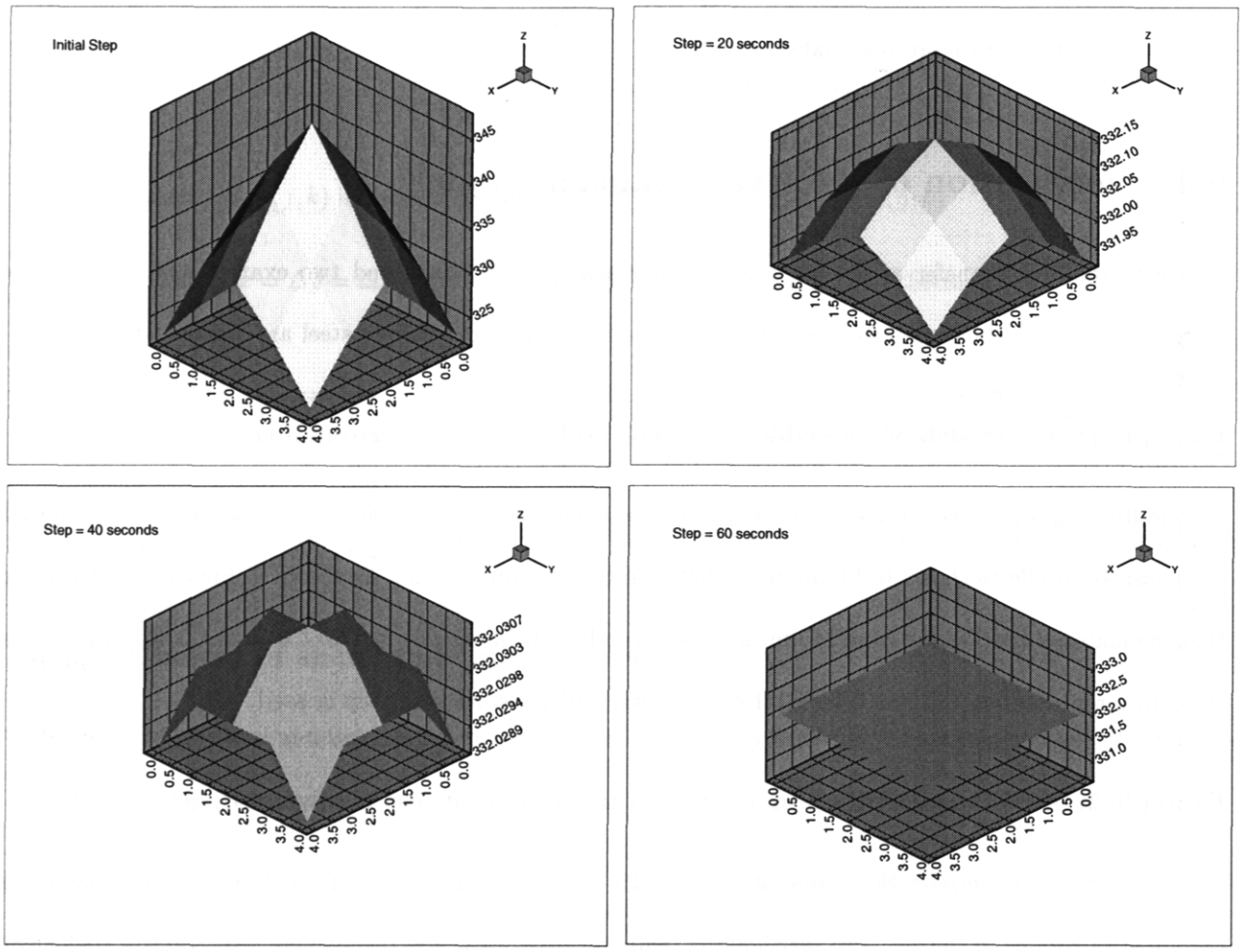

Figure 6-2: Temperature distribution within a thin slab made of water-like material excluding heat loss to surroundings (temperature on z-axis in Kelvin)

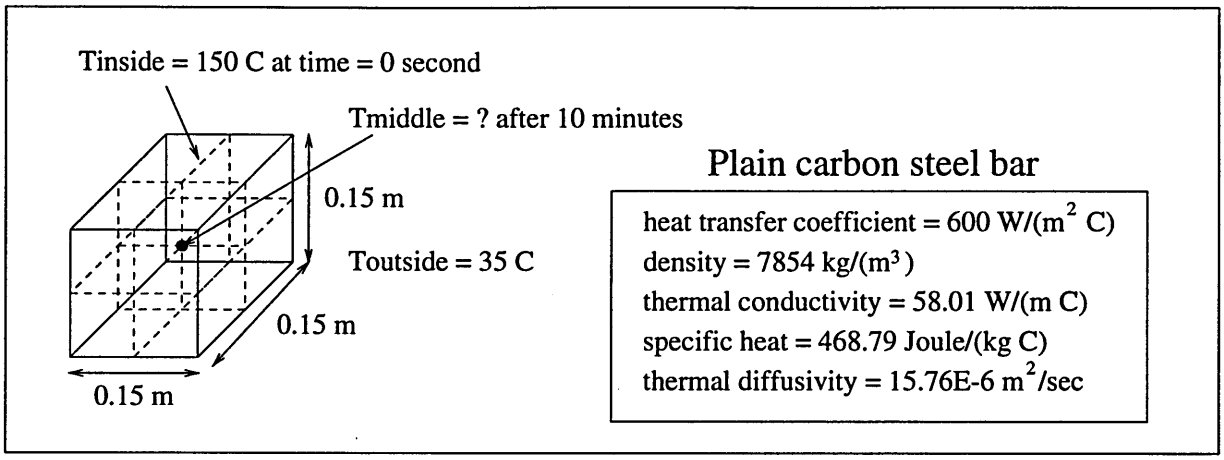

Figure 6-3: Problem description for cooling process of rectangular steel bar

Example 3: A cylindrical shape of steel bar (including heat loss to surroundings)

This problem is similar to the previous problem except that the material is a cylinder and there is an insulation at one end where temperature will be computed after 5 minutes of cooling. Figure 6-4 shows the description of this example.

Again, by comparing the temperature obtained from an approximation using the chart method with that from the numerical model, there is negligible difference between them. The temperatures of both methods are 84.2°C or 357.3 K. The time step is 0.25 second and the space increment is 0.005 meter.

6.5 Conclusion

The heat transfer model is developed, verified and ready to be combined with the power dissipation model in order to form the complete numerical model of the microwave heating.

It is noted that the time increment for heat transfer model is much larger than that for power dissipation model which will help saving computation time tremendously during temperature computation.

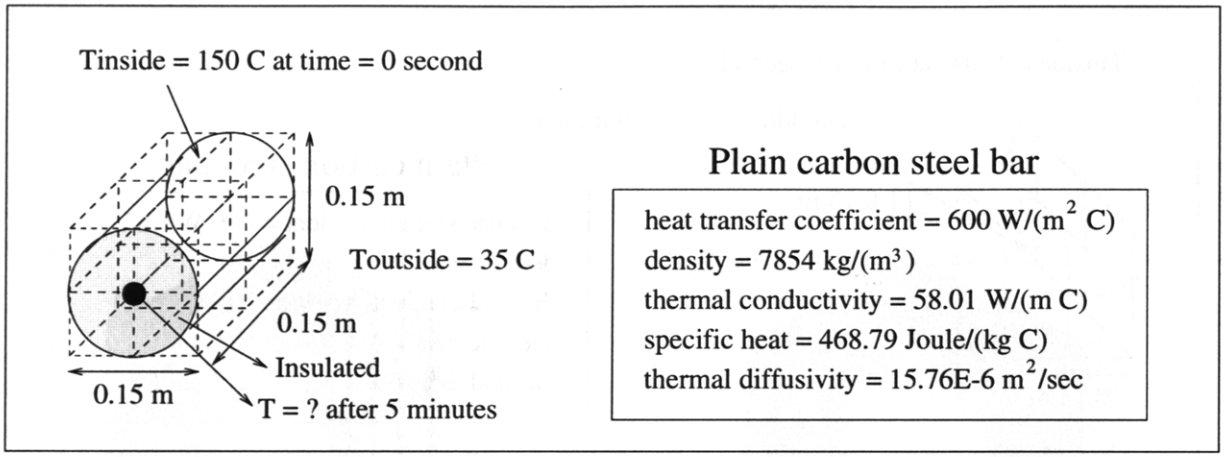

Figure 6-4: Problem description for cooling process of cylindrical steel bar with one end insulated

6.6 Appendix I. - Stability Analysis

This derivation is based on von Neumann stability analysis which is limited to linear equation and pure initial value problem (with periodic initial data) but in practice it is still valuable beyond this limitation [30].

Since we know that

$$\frac{\partial}{\partial t}(\rho c_p T) = -(\nabla \cdot Q) + F$$

and according to Fourier's law,

$$Q = -K_c \nabla T$$

and if medium is uniform, i.e., K_c (thermal conductivity), ρ and c_p are constants, we obtain

$$\begin{aligned} \rho c_p \frac{\partial T}{\partial t} &= (\nabla \cdot K_c \nabla T) + F \\ \frac{\partial T}{\partial t} &= \frac{K_c}{\rho c_p}(\nabla^2 T) + \frac{F}{\rho c_p} \\ \frac{\partial T}{\partial t} &= \alpha(\nabla^2 T) + \frac{F}{\rho c_p} \end{aligned}$$

where $\alpha = \frac{K_c}{\rho c_p}$ = thermal diffusivity

To simplify the derivation, we assume no source. Thus the three-dimension heat diffusion equation becomes

$$\begin{aligned}\frac{\partial T}{\partial t} &= \alpha(\nabla^2 T) \\ &= \alpha\left(\frac{\partial^2}{\partial x^2}T + \frac{\partial^2}{\partial y^2}T + \frac{\partial^2}{\partial z^2}T\right)\end{aligned}$$

By applying the center difference, we get

$$\frac{T_j^{n+1} - T_j^n}{\Delta t} = \alpha\left[\frac{(T_{j+1}^n - 2T_j^n + T_{j-1}^n)}{(\Delta x)^2} + \frac{(T_{j+1}^n - 2T_j^n + T_{j-1}^n)}{(\Delta y)^2} + \frac{(T_{j+1}^n - 2T_j^n + T_{j-1}^n)}{(\Delta z)^2}\right] \quad (6.4)$$

Assuming that S is the exact solution of the above difference equation and $S + \delta$ is the numerical solution where δ is the error due to numerical method including roundoff. If $S + \delta$ is substituted into equation (6.4), the following will be obtained

$$\begin{aligned}\frac{(S+\delta)_j^{n+1} - (S+\delta)_j^n}{\Delta t} = & \quad \alpha\left(\frac{(S+\delta)_{j+1}^n - 2(S+\delta)_j^n + (S+\delta)_{j-1}^n}{(\Delta x)^2}\right) \\ & + \alpha\left(\frac{(S+\delta)_{j+1}^n - 2(S+\delta)_j^n + (S+\delta)_{j-1}^n}{(\Delta y)^2}\right) \\ & + \alpha\left(\frac{(S+\delta)_{j+1}^n - 2(S+\delta)_j^n + (S+\delta)_{j-1}^n}{(\Delta z)^2}\right)\end{aligned}$$

and because of definition from equation (6.4), we obtain

$$\begin{aligned}\frac{(\delta)_j^{n+1} - (\delta)_j^n}{\Delta t} = & \quad \alpha\left(\frac{(\delta)_{j+1}^n - 2(\delta)_j^n + (\delta)_{j-1}^n}{(\Delta x)^2}\right) \\ & + \alpha\left(\frac{(\delta)_{j+1}^n - 2(\delta)_j^n + (\delta)_{j-1}^n}{(\Delta y)^2}\right) \\ & + \alpha\left(\frac{(\delta)_{j+1}^n - 2(\delta)_j^n + (\delta)_{j-1}^n}{(\Delta z)^2}\right) \quad (6.5)\end{aligned}$$

The general solutions of the error $\delta(t)$ and $\delta(t + \Delta t)$ for equation (6.5) used to study stability analysis of

difference scheme for three dimensions are shown below [30].

$$\delta(x,y,z,t) = e^{at}e^{i\beta x}e^{i\gamma y}e^{i\eta z} \tag{6.6}$$

$$\delta(x,y,z,t+\Delta t) = e^{a(t+\Delta t)}e^{i\beta x}e^{i\gamma y}e^{i\eta z} \tag{6.7}$$

where a = real or complex number,

β = wave number in x direction,

γ = wave number in y direction, and

η = wave number in z direction.

Let's introduce the amplification factor or $|G|$ which is defined as

$$|G| = \frac{\delta(x,y,z,t+\Delta t)}{\delta(x,y,z,t)} \tag{6.8}$$

Now substitute equations (6.6) and (6.7) to equation (6.8), the following is obtained

$$\begin{aligned}
\frac{\delta(x,y,z,t+\Delta t)}{\delta(x,y,z,t)} &= 1 + \alpha\Delta t\left(\frac{e^{i\beta\Delta x}-2+e^{-i\beta\Delta x}}{(\Delta x)^2}\right) \\
&\quad + \alpha\Delta t\left(\frac{e^{i\gamma\Delta y}-2+e^{-i\gamma\Delta y}}{(\Delta y)^2}\right) \\
&\quad + \alpha\Delta t\left(\frac{e^{i\eta\Delta z}-2+e^{-i\eta\Delta z}}{(\Delta z)^2}\right) \\
&= 1 + \alpha\Delta t\left(\frac{2cos(\beta\Delta x)-2}{(\Delta x)^2}\right) \\
&\quad + \alpha\Delta t\left(\frac{2cos(\gamma\Delta y)-2}{(\Delta y)^2}\right) \\
&\quad + \alpha\Delta t\left(\frac{2cos(\eta\Delta z)-2}{(\Delta z)^2}\right)
\end{aligned}$$

To insure the stability, $|G|$ must be ≤ 1. Therefore,

$$\left|1+2\alpha\Delta t\left[\frac{cos(\beta\Delta x)-1}{(\Delta x)^2}+\frac{cos(\gamma\Delta y)-1}{(\Delta y)^2}+\frac{cos(\eta\Delta z)-1}{(\Delta z)^2}\right]\right| \leq 1$$

$$\left|1 - 4\alpha\Delta t\left[\frac{sin^2(\beta\frac{\Delta x}{2})}{(\Delta x)^2} + \frac{sin^2(\gamma\frac{\Delta y}{2})}{(\Delta y)^2} + \frac{sin^2(\eta\frac{\Delta z}{2})}{(\Delta z)^2}\right]\right| \leq 1$$

And from this condition, the stability criterion can be found that

$$\Delta t \leq \frac{1}{2\alpha}\left[\frac{1}{(\Delta x)^2} + \frac{1}{(\Delta z)^2} + \frac{1}{(\Delta z)^2}\right]^{-1}$$

If $\Delta x = \Delta y = \Delta z = \Delta$,

$$\Delta t \leq \frac{\Delta^2}{6\alpha}$$

Chapter 7

Microwave Heating Model

7.1 Introduction

The microwave heating model combines power dissipation and heat transfer models together in order to simulate microwave heating process. For curing of concrete with microwave energy, the developed permittivity-maturity relation is included in the heating model in addition to the update of thermal properties.

To simulate the microwave heating process, it is necessary to know what value of the input field strength, which is needed to generate electric and magnetic fields used in power dissipation model, is equivalent to certain power in the real microwave cavity. To achieve this, calibration of power in laboratory microwave cavity is simulated by the model and the equivalent input field strength can be identified. The microwave heating model is then verified by comparison to the experimental results with several materials.

This chapter includes (i) overview of the complete model of microwave curing of concrete, (ii) calibration of input power and model verification, (iii) simulation of microwave curing of concrete and (iv) conclusion.

7.2 Overview of Microwave Heating Model of Concrete

Figure 7-1 illustrates the overview of microwave heating model of concrete which basically combines power dissipation model, heat transfer model, and permittivity-maturity relation together.

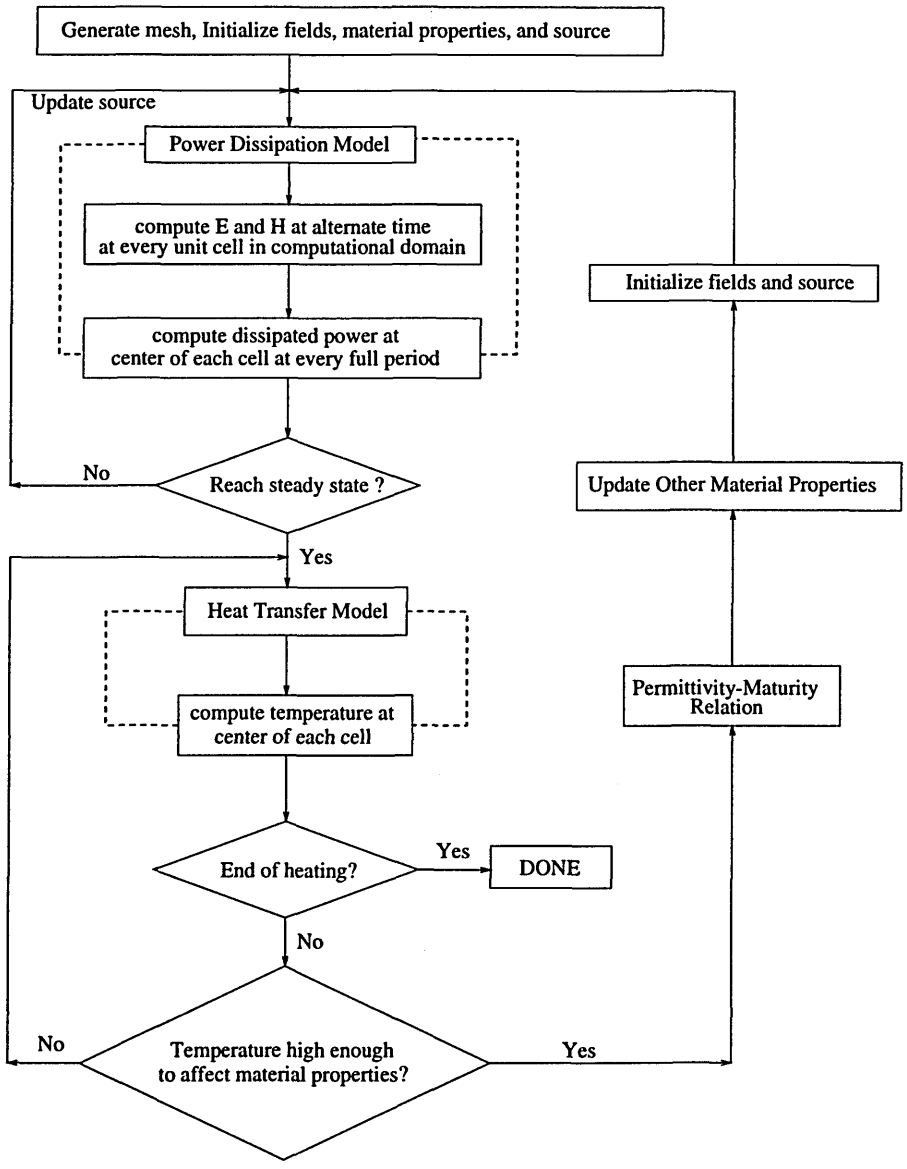

Figure 7-1: Overview of microwave heating model of concrete

7.3 Calibration for Input Power

As mentioned before, to simulate the microwave heating process, the value of the input field strength in the rectangular waveguide, where the microwave source is located, must be determined for its equivalent value in terms of the real microwave power. For example, what will be the input field strength equivalent to 100 watts of microwave heating?

To achieve this, the calibration of power in laboratory microwave cavity is simulated by the numerical model and the temperature rise obtained from the model can be used to determine the equivalent microwave power based on the calorimetry equation (see below).

In practice, power calibration is done by heating a 1 liter of water in the cavity for 1 minute. According to IEC (The International Electrotechnical Commission) Publication 705 [51], the initial temperature of water is required to be $10 \pm 2°C$. The final temperature is then measured and used to calculate the absorbed power which actually is the power in the microwave cavity. The related equation based on the calorimetry method is as follows:

$$P = mc_p \frac{(T_{final} - T_{init})}{t} \tag{7.1}$$

where P = power (watt),

m = mass (gram),

c_p = specific heat (J/(Celsius g)),

T_{final} = final temperature (Celsius),

T_{init} = initial temperature (Celsius), and

t = heating duration (second).

Therefore, the power calibration process in laboratory microwave cavity is numerically modeled. Figure 7-2 shows the parameters concerning the cavity, the rectangular waveguide, and the loaded dielectric materials used in the model. The related properties of the materials in the model are shown in Table 7.1.

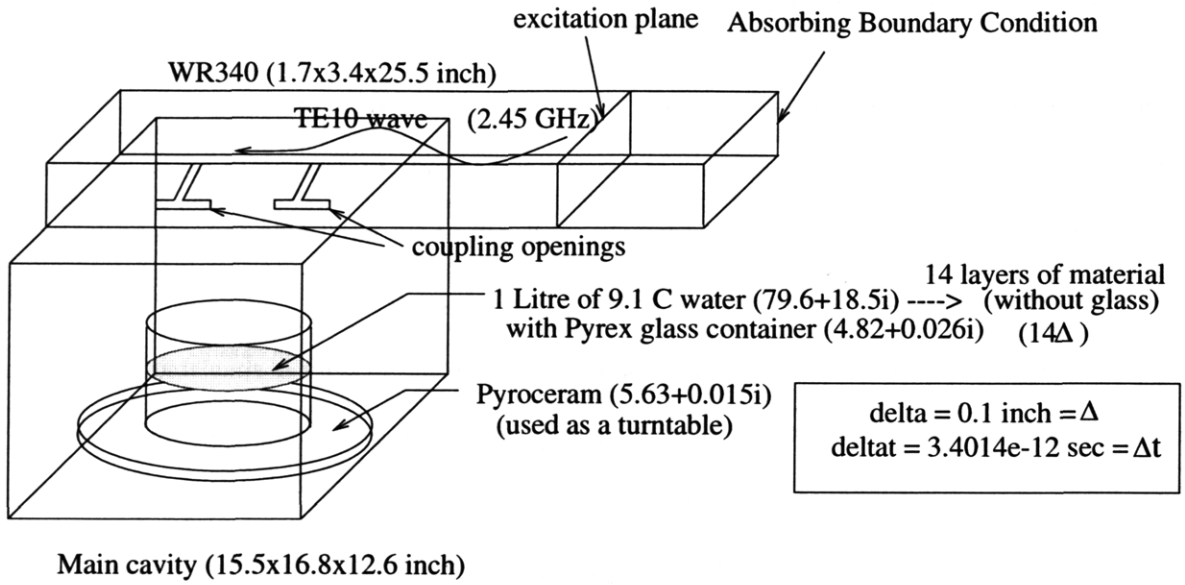

Figure 7-2: Laboratory microwave cavity with loaded dielectric materials used in numerical model to calibrate input power

7.3.1 Result

In this investigation, a load of 9.1°C water is modeled first to approximate the equivalent microwave power. From the plot of total dissipated power versus time step obtained from the power dissipation model as shown in Figure 7-3, it is clear that the steady state dissipated power used in this calibration process can be obtained after 6,000th time step. The time increment in power dissipation model is 3.4014 picosecond while that in heat transfer model is 1 second.

Since only one minute of heating which is such a short time is performed in the calibration, it is therefore valid to assume that the change in relative permittivity and related thermal properties which can affect the dissipated power is so minimal that there will be no need to obtain a new steady state dissipated power. Thus, the thermal properties of 9.1°C water are kept constant throughout the numerical computation.

By varying the input field strengths in the numerical model, several average temperature rises inside the material are obtained and used to compute microwave input powers. As a result, Figure 7-4 shows a plot of input field strength versus microwave input power. It is noted that the heat transfer coefficient and the

Table 7.1: Properties of several materials used in the numerical model

Property	Pyrex	Pyroceram	9.1°C water (282.25 K)	21.4°C water (294.55 K)	20°C concrete (293.15 K)
dielectric constant (3 GHz)[9]	4.82	5.63 (2.45 GHz)	79.6	77.5	16.8 (2.45 GHz)
loss factor (3 GHz)[9]	0.026	0.015 (2.45 GHz)	18.5	13.5	4.7 (2.45 GHz)
density ($kg/(m^3)$)	2230	2610	997	997	2450
specific heat (joule/(kg K))	750	963	4184	4184	880
thermal conductivity (watt/(m °C))	1.2	3.64	0.58	0.60	1.4

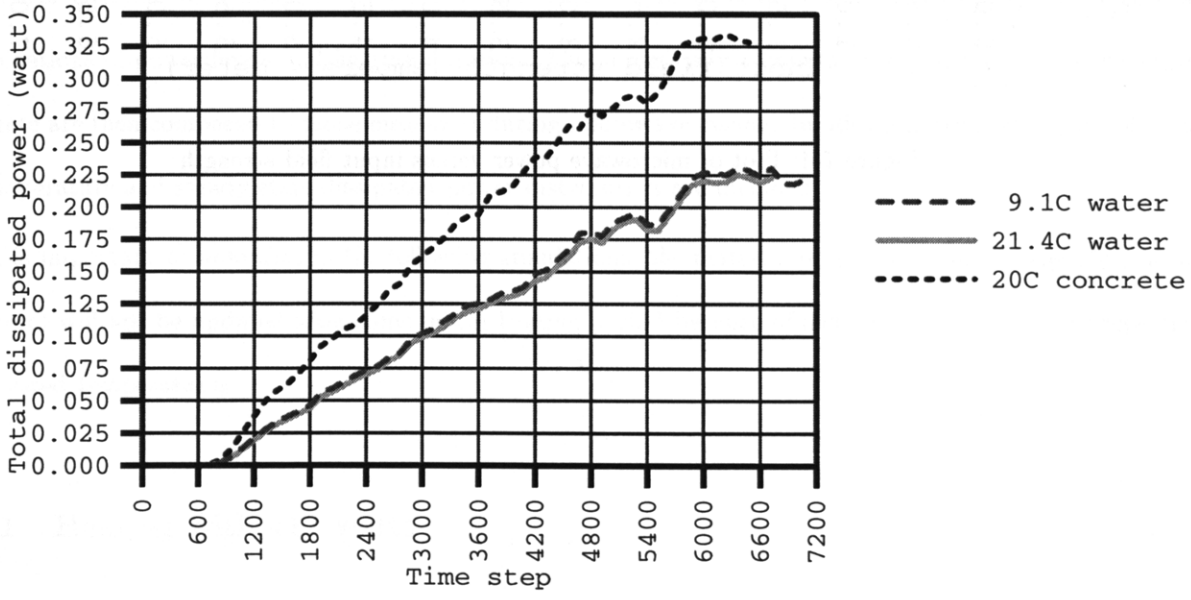

Figure 7-3: Plots of total dissipated power versus time step for 9.1°C water, 21.4°C water and 20°C concrete due to microwave heating(1 time step = 3.4014×10^{-12} second and input field strength = 1 ampere/m)

temperature of the surrounding air used in this model are 25 watt/(m^2 K) and 20°C, respectively.

Figures 7-5 and 7-6 illustrate the dissipated power and temperature profiles of several layers of 9.1°C water after 1 minute of heating with input field strength of 6.5 ampere/m equivalent to 412 watts. As expected, the dissipated powers of the elements at the boundary and at the top layer of material are high because those elements are exposed to the microwave more than those in the interior region. For similar reason, their temperatures are high as well.

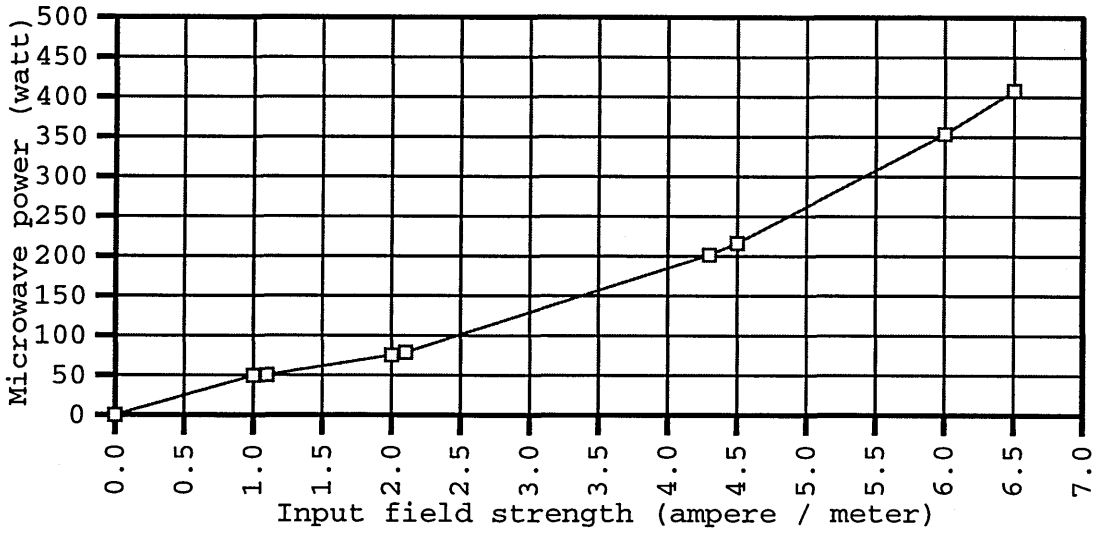

Figure 7-4: Plot of microwave power versus input field strength

7.3.2 Verification

Once each input field strength is determined for its equivalent microwave input power, 1 liter of 21.4°C water is used as an example to verify the input field strength experimentally and numerically. From experiment, 21.4°C water is heated with 412 watts for 1 minute and its measured temperature rise is 5.2°C. To compare, the average temperature rise of the same water in the numerical model is 5.1°C.

Therefore, the microwave heating model is ready to be used with any materials with known properties. In the next section, several simulations of microwave curing of concrete are done numerically and compared with the experiments.

7.4 Simulation of Microwave Curing of Concrete

Since the microwave heating model is verified and its equivalent input field strength is determined, simulation of microwave curing of concrete is proceeded and verified with experiments. In this section, a liter of 0.50 w/c fresh concrete in cylindrical Pyrex container is cured in laboratory microwave cavity under several combinations of power levels and heating duration. The numerically computed temperatures in the center of concrete are then compared to those measured during microwave curing. In addition, some examples of plots of temperature and steady state dissipated power distribution are included.

It is important to note that in the following simulations, the material properties (such as specific heat of concrete) will not be updated after some initial heating period because of lack of available related properties at elevated temperatures.

7.4.1 Heating with 412 watts

Figure 7-7 shows the comparison between the temperatures in the center of concrete in cylindrical Pyrex container obtained from numerical model with those obtained from experiment. It is clear that the results within the first two minutes agree quite well.

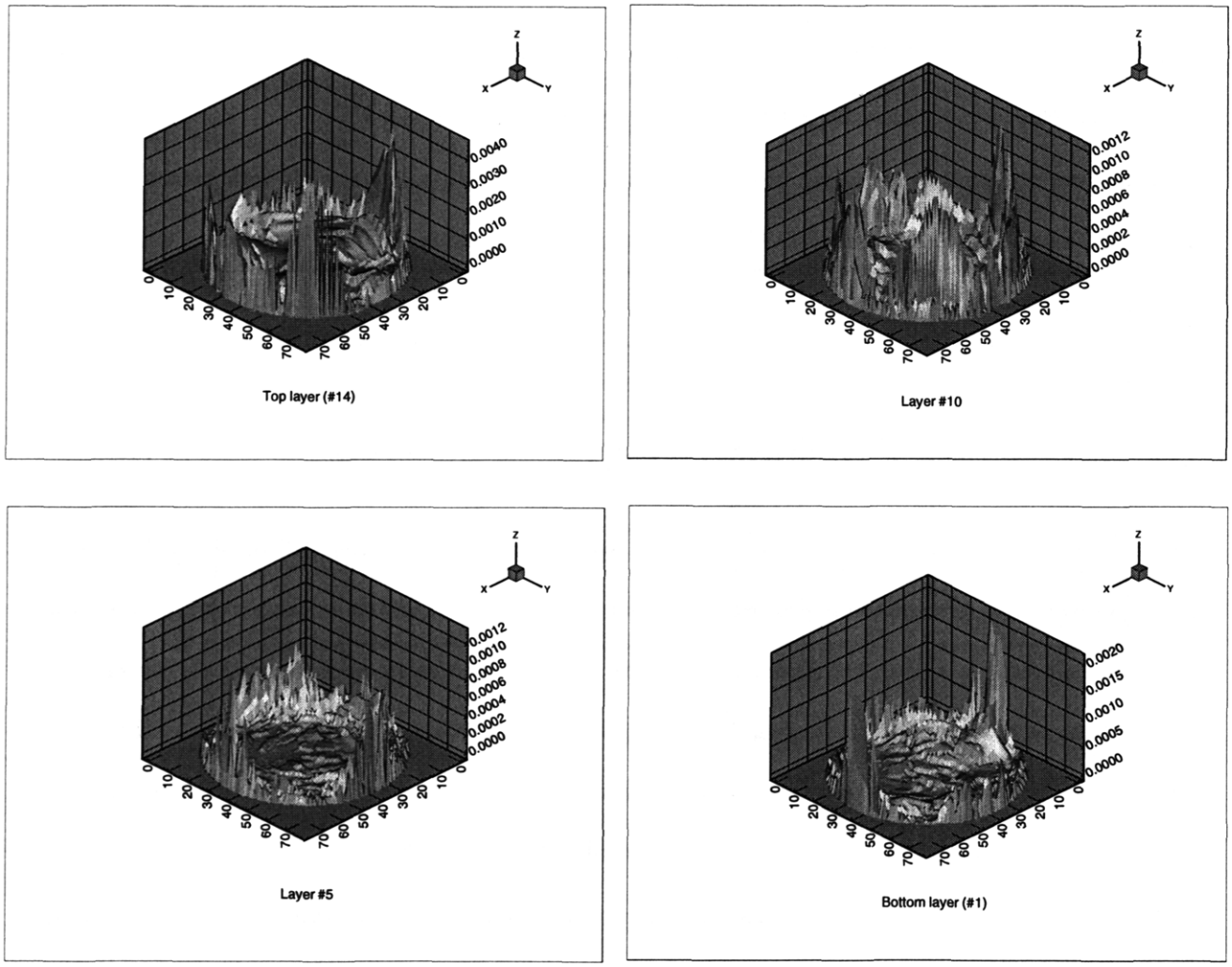

Figure 7-5: Dissipated power profiles of several layers of 9.1°C water after 1 minute of heating with input field strength of 6.5 ampere/m equivalent to 412 watts (with convection and power on z-axis in watt)

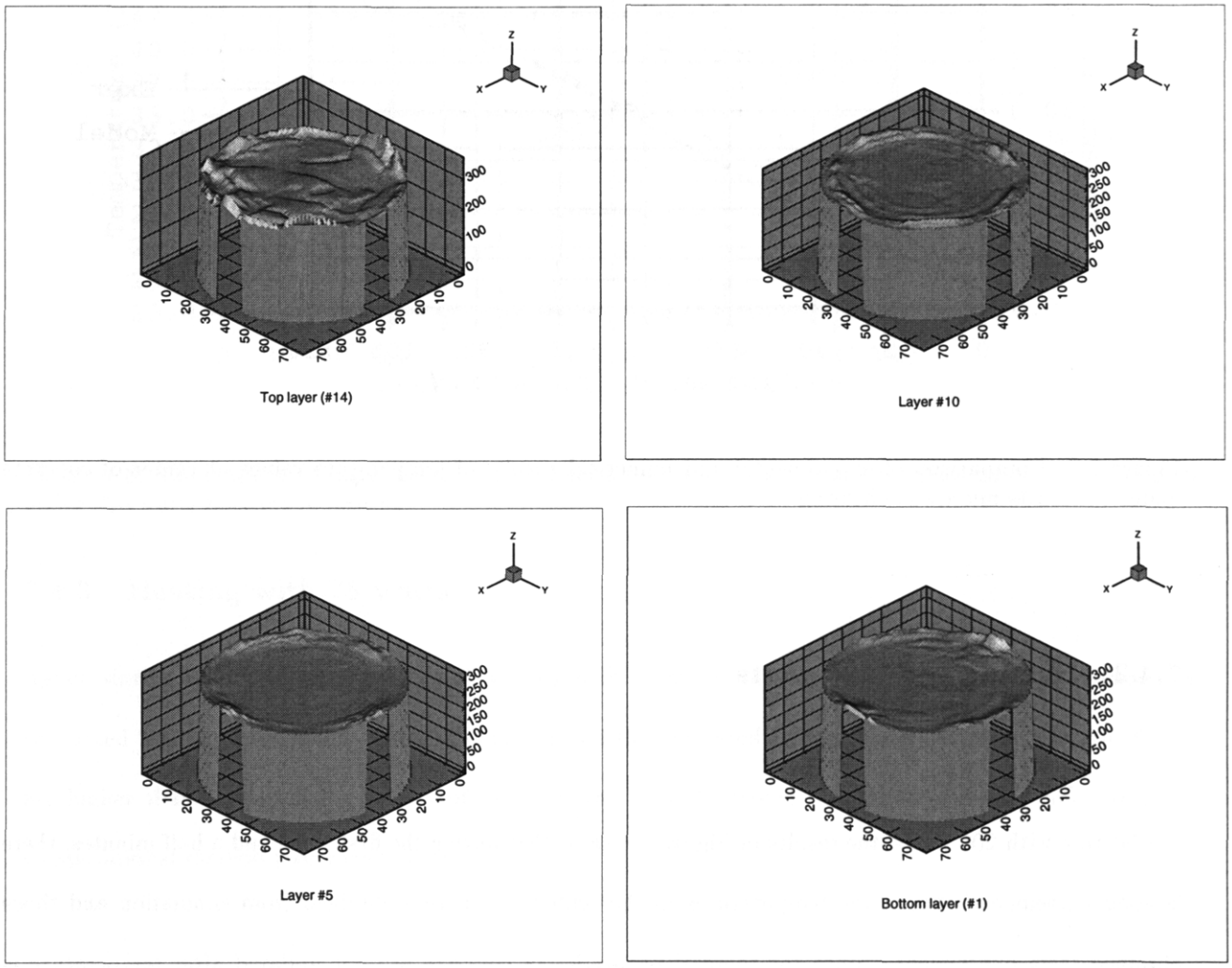

Figure 7-6: Temperature profiles of several layers of 9.1°C water after 1 minute of heating with input field strength of 6.5 ampere/m equivalent to 412 watts (with convection and temperature on z-axis in Kelvin)

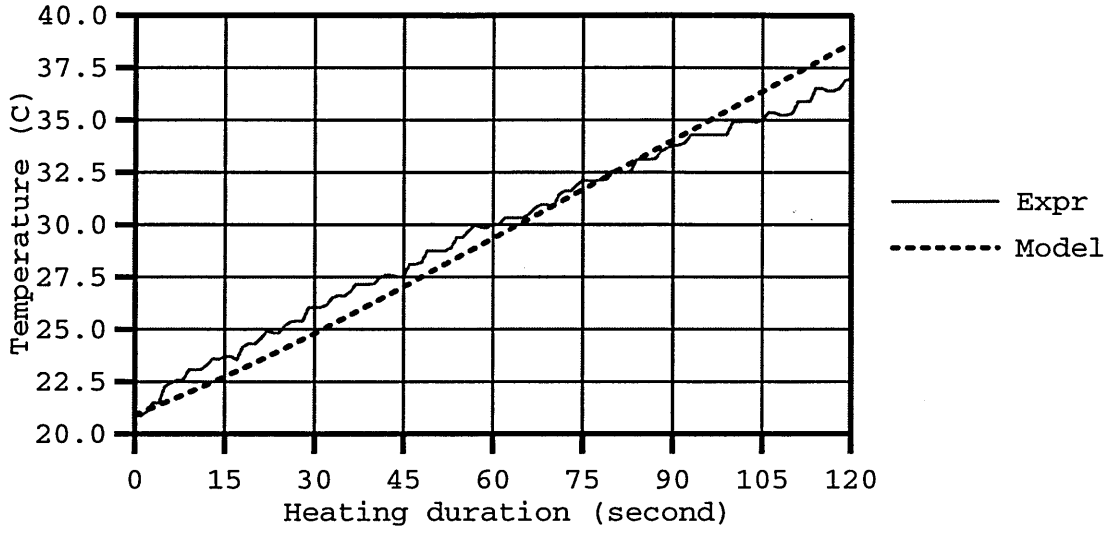

Figure 7-7: Comparison of experimental and numerical results of temperature values at center of concrete under 412 watts microwave heating

7.4.2 Heating with 200 watts

For heating with 200 watts, the results in Figure 7-8 show that during the first three and a half minutes, there is good agreement between the temperatures in the center of concrete obtained from simulation and those obtained from experiment. Since the thermal properties of concrete are not updated after temperature is increased (i.e., after three and a half minutes of heating), the numerically computed temperatures are greater than the measured temperatures.

Figures 7-9 and 7-10 illustrate the dissipated power and temperature profiles of several layers of 22°C concrete after 3 minutes of heating with input field strength of 4.3 ampere/m equivalent to 200 watts. As shown before, the dissipated powers and temperatures of the elements at the boundary and at the top layer of material are high.

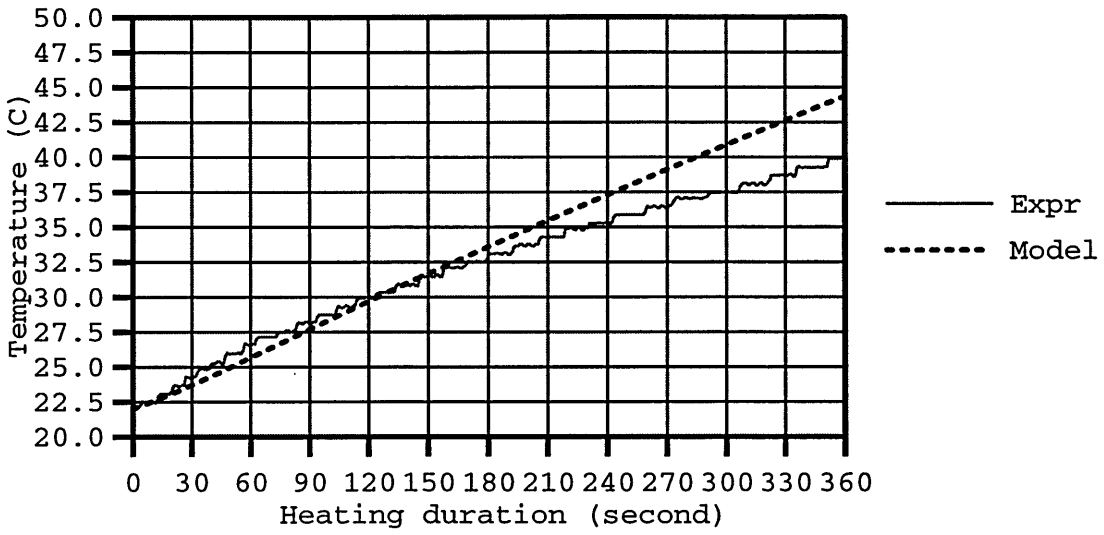

Figure 7-8: Comparison of experimental and numerical results of temperature values at center of concrete under 200 watts microwave heating

7.4.3 Heating with 75 watts

Again, during the first twelve minutes of heating with 75 watts, there is very good agreement between the computed temperatures in the center of concrete and the measured temperatures but after that, the former are higher than the latter due to lack of the updating step of thermal properties of heated concrete in the computational method (see Figure 7-11).

7.4.4 Discussion

According to the results from heating concrete with 200 and 75 watts, it is noticed that there is good agreement between the computed temperatures from the model and the experimentally measured temperatures only in the initial period of heating.

The discrepancy between computed and experimental results cannot be explained by the change in permittivity of concrete (with use of the permittivity-maturity relation) because the calculated change in maturity during the experiments is not sufficient to cause significant changes. The discrepancy is probably due to lack

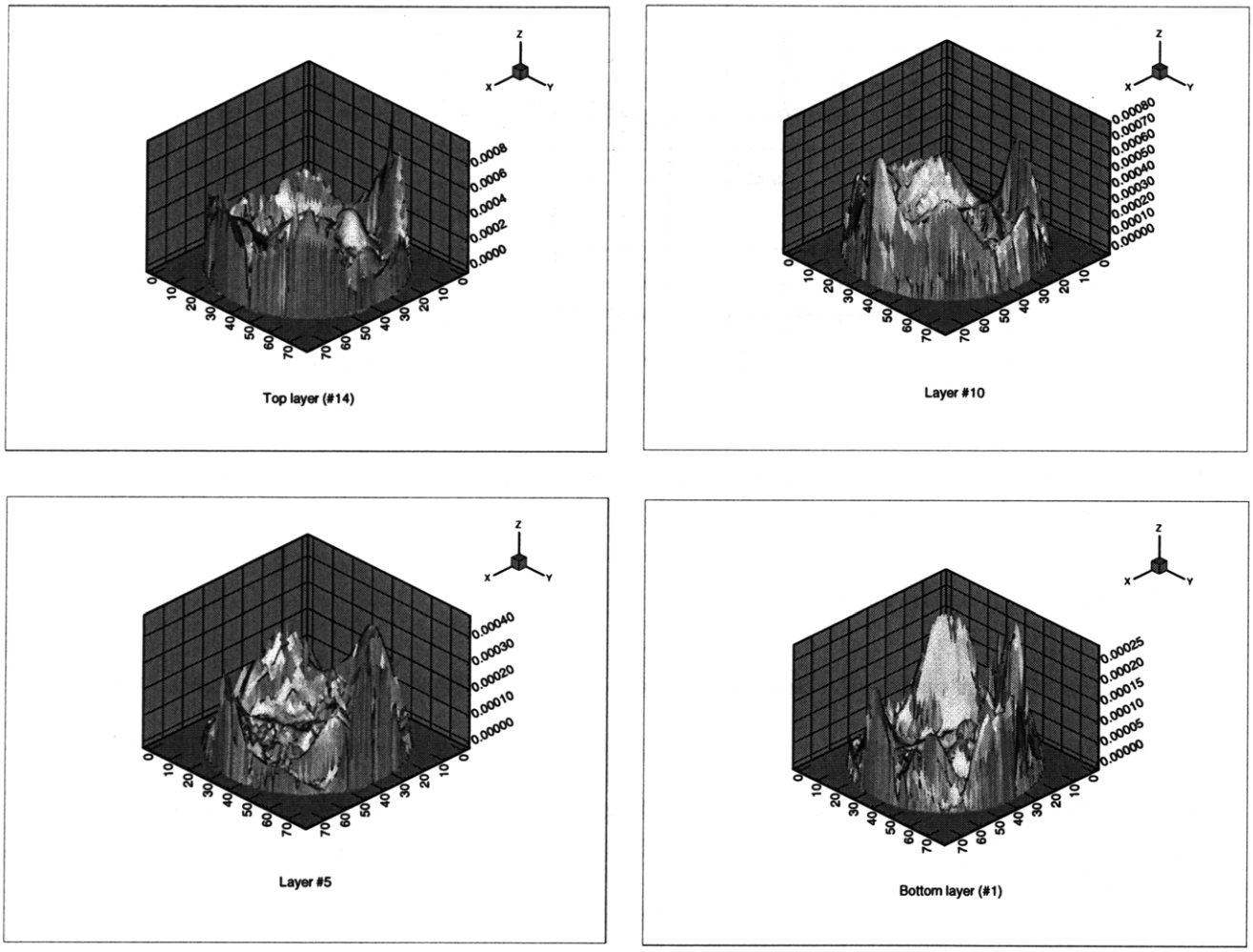

Figure 7-9: Dissipated power profiles of several layers of 22°C concrete after 3 minutes of heating with input field strength of 4.3 ampere/m equivalent to 200 watts (with convection and power on z-axis in watt)

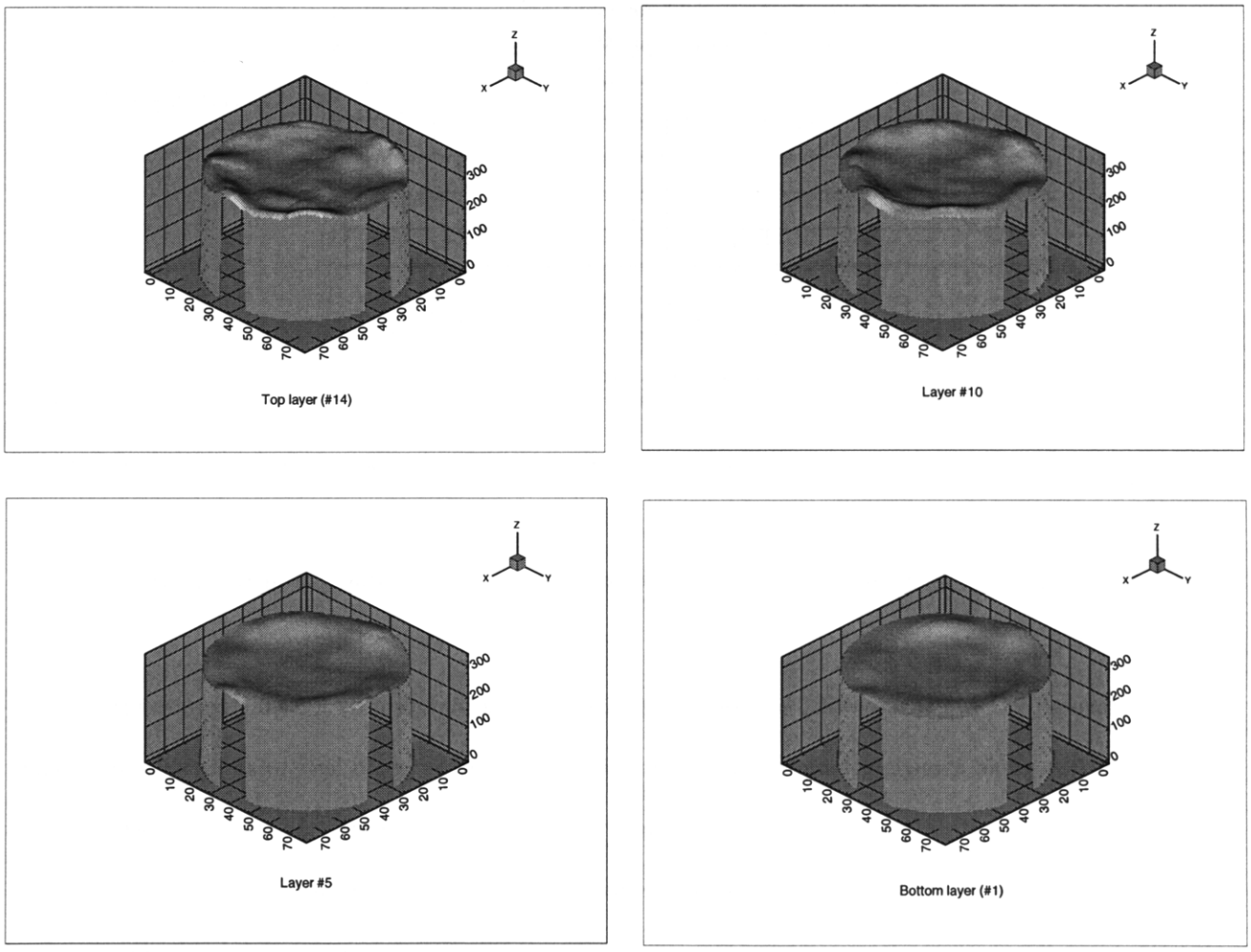

Figure 7-10: Temperature profiles of several layers of 22°C concrete after 3 minutes of heating with input field strength of 4.3 ampere/m equivalent to 200 watts (with convection and temperature on z-axis in Kelvin)

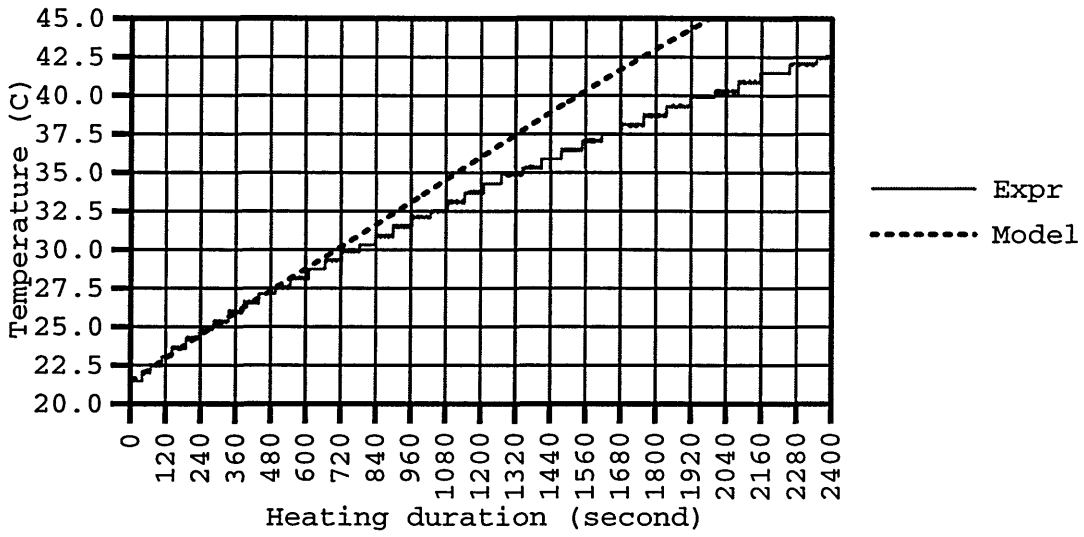

Figure 7-11: Comparison of experimental and numerical results of temperature values at center of concrete under 75 watts microwave heating

of the updating step of thermal properties of heated concrete in the computational method, particularly the specific heat.

It is generally known that specific heat of concrete can increase significantly if its temperature is elevated (see Table 7.2), rapid change in temperature due to microwave heating would lead to an increase in specific heat. Referring to heat diffusion difference-equation, if specific heat is increased, the rate of temperature rise will be reduced; therefore, the computed temperatures from numerical model will tend to agree well with the measured temperatures from experiment once the new specific heat is reassigned to each element after the proper initial heating period. And since there is no published data of specific heat of concrete at high temperatures, no attempt has been made to check for this argument.

7.5 Conclusion

To summarize, the microwave heating model can be used to successfully simulate microwave heating process of any material if its related properties are known and provided. In this chapter, water and concrete are used

Table 7.2: Specific heats of pastes and concretes [adapted from Mindess et al., 1981]

Material	w/c ratio	Temperature (°C)	Specific heat (joule/(kg °C))
Paste	0.25	21	1140
	0.25	65	1680
	0.60	21	1600
	0.60	65	2460
Concrete	-	-	800-1200

as examples to illustrate the validity of the model. However, to improve the microwave curing process for concrete, its thermal properties such as specific heat should be provided at various temperatures.

Chapter 8

Conclusion and Future Work

8.1 Research Summary

In this work, we investigate the determination of optimization for microwave curing process of concrete, the freeze-thaw durability of microwave-cured air-entrained concrete, the approximation of permittivity of microwave-cured concrete, and the numerical model for microwave curing process of concrete.

The temperature control of the heated specimen is carried out with a feedback loop to obtain the most favorable temperature for cement to hydrate rapidly under microwave curing so that the early strength gain is high and the later strength gain is not impaired much. Optimal process with high energy efficiencies can then be obtained. Furthermore, we use superplasticizer and low w/c ratio to obtain higher early strength. Microwave-cured concrete with air-entraining admixture is also tested for strength development.

After the completeness of the study on strength development of microwave-cured concrete, test on its freeze-thaw resistance is carried out to make sure that microwave curing can be applied to concrete exposed to frost attack (e.g. concrete for pavement repair).

The concept of maturity used widely in concrete construction is applied to approximate the permittivity of concrete during microwave curing process. Then the complete model of microwave curing process of concrete, including microwave power dissipation model, heat transfer model, and permittivity-maturity relation, is

developed and verified with experiments.

8.2 Conclusion

The conclusions of this research are as follows:

1. Microwave curing technique exhibits high strength development at both early and later stages at optimized process. Early compressive strength at 4.5 hours can be as high as 5,129 psi while its 7-day strength of 8,259 psi is comparable to that of normal-cured concrete with 8,322 psi. High early strength is also obtained for splitting tension except that the later strength of microwave-cured concrete is about 12% less than that of normal-cured concrete.

2. Process with discrete power levels simulates the optimal process with continuous power levels well, showing the possibility of using low cost microwave applicators in practical applications. Moreover, when discrete power is applied without using the temperature probe, the discrete power process gives better results than the continuous power process.

3. It is recommended to apply a relatively high heating power at the beginning of microwave curing process and low heating power at the end so that free water can be removed as much as possible without destructing the structure of the hardening concrete.

4. Based on the results of strength and freeze-thaw durability, concrete with a lower w/c ratio responds to microwave curing well.

5. The microwave-cured air-entrained concrete need an adequate air-void system, similar to the normal-cured concrete. For high w/c air-entrained concrete, microwave can cause small air voids to coalesce and become larger during the initial stage of microwave curing, resulting in bigger voids and larger spacing factor, which can be detrimental to the frost resistance. On the other hand, for microwave-cured low w/c air-entrained concrete, the reduced freezable water, increased air content, and increased formation of cracks and voids help resisting frost attack.

6. The complex permittivity-maturity relation of concrete cured under different temperature histories can be roughly established with the use of maturity concept, although different maturity relation are required for different temperature ranges.

7. The discrepancy between computed and experimental results cannot be explained by the change in permittivity of concrete (with use of the permittivity-maturity relation) because the calculated change in maturity during the experiments is not sufficient to cause significant changes. The discrepancy is probably due to lack of the updating step of thermal properties of heated concrete in the computational method, particularly the specific heat.

8. The numerical model of microwave curing of concrete is shown to be promising if the related thermal properties of concrete such as specific heat at higher temperatures are provided.

8.3 Recommendations for Future Work

Several recommendations for future work include the followings:

- Reduce the computational effort in the microwave heating model by assigning the initial field values so that the steady state is reached faster. The initial field values can be obtained by initially simulating the microwave heating in the empty cavity up to a certain time step. The values at several locations are saved to be used as initial field values. It is noticed that it is not practical to save all the field values so interpolation will be used to assign initial field values to every element in the case with the dielectric material.

- Determine the related thermal properties of concrete at various temperatures to fully complete the numerical modeling of microwave curing of concrete.

- Determine optimal processes for larger-size specimens using the developed numerical model and the experimental results from small-size specimens.

- Include the effects of mode stirrer and turntable in microwave heating model to completely simulate a realistic microwave cavity.

- Design low-cost microwave applicators for concrete pavement repairs and precast concrete fabrication after completeness of the numerical modeling of microwave curing of concrete.

Bibliography

[1] Aïtcin, P.-C. and D. Vezina, "Resistance to freezing and thawing of silica fume concrete," *Cement, Concrete, and Aggregates*, CCAGDP, Vol. 6, No. 1, pp. 38-42, Summer 1984.

[2] American Society for Testing and Materials, "Standard Practice for Making and Curing Concrete Test Specimens in the Laboratory," Designation: C 192-90a, *1993 Annual Book of ASTM Standards*, Section 4, Vol. 04.02, Philadelphia, pp. 117-123, 1993.

[3] American Society for Testing and Materials, "Standard Test Method for Air Content of Freshly Mixed Concrete by the Pressure Method," Designation: C 231-91b, *1993 Annual Book of ASTM Standards*, Section 4, Vol. 04.02, Philadelphia, pp. 140-147, 1993.

[4] American Society for Testing and Materials, "Standard Test Method for Microscopical Determination of Parameters of the Air-Void System in Hardened Concrete," Designation: C 457-90, *1993 Annual Book of ASTM Standards*, Section 4, Vol. 04.02, Philadelphia, pp. 234-246, 1993.

[5] American Society for Testing and Materials, "Standard Specification for Chemical Admixtures for Concrete," Designation: C 494-92, *1993 Annual Book of ASTM Standards*, Section 4, Vol. 04.02, Philadelphia, pp. 260-268, 1993.

[6] American Society for Testing and Materials, "Standard Test Method for Resistance of Concrete to Rapid Freezing and Thawing," Designation: C 666-92, *1993 Annual Book of ASTM Standards*, Section 4, Vol. 04.02, Philadelphia, pp. 326-331, 1993.

[7] Application Note 1217-1, "Basics of measuring the dielectric properties of materials," *Hewlett Packard Literature number 5091-3300E*, March 1992.

[8] Carette, G.G. and V.M. Malhotra, "Mechanical properties, durability, and drying shrinkage of Portland cement concrete incorporating silica fume," *Cement, Concrete, and Aggregates*, CCAGDP, Vol. 5, No. 1, pp. 3-13, Summer 1983.

[9] *Dielectric materials and applications,* edited by Arthur R. Von Hippel, The Technology Press of M.I.T and John Wiley & Sons, Inc., 1958.

[10] Double, D.D., "New developments in understanding the chemistry of cement hydration," *Phil. Trans. R. Soc. Lond.*, A 310, pp. 53-66, 1983.

[11] Engquist, Bjorn, and Andrew Majda, "Absorbing boundary conditions for the numerical simulation of waves," *Mathematics of Computation*, Vol. 31,No. 139, pp. 629-651, July 1977.

[12] Foy, C., M. Pigeon, and N. Banthia, "Freeze-thaw durability and deicer salt scaling resistance of a 0.25 water-cement ratio concrete," *Cement and Concrete Research*, Vol. 18, No. 4, pp. 604-614, 1988.

[13] Harnik, A.B., U. Meier, and A. Rösli, "Combined influence of freezing and deicing salt on concrete-Physical aspects," *Durability of Building Materials and Components, ASTM STP 691*, edited by P.J. Sereda and G.G. Litvan, American Society for Testing and Materials, pp. 474-484, 1980.

[14] "Materials Measurement: Measuring the dielectric constant of solids with the HP 8510 network analyzer," *Hewlett Packard Product Note 8510-3.*

[15] "Network Analysis: Specifying calibration standards for the HP 8510 network analyzer," *Hewlett Packard Product Note 8510-5A.*

[16] Hutchison, R.G., J.T. Chang, H.M. Jennings, and M.E. Brodwin, "Thermal Acceleration of Portland Cement Mortars with Microwave Energy," *Cement and Concrete Research*, Vol. 21, pp 795-799, 1991.

[17] Janna, William S., *Engineering heat transfer,* SI edition prepared by Morgan Heikal, Van Nostrand Reinhold (international) Co. Ltd, 1988.

[18] Kafry, I.D., *Direct Electric Curing of Concrete: Basic Design*, Whittles Publishing Services, Scotland, 1993.

[19] Khali, S.M., M.A. Ward, and D.R. Morgan, "Freeze-thaw durability of nonair-entrained high strength concretes containing superplasticizers," *Durability of Building Materials and Components, ASTM STP 691*, edited by P.J. Sereda and G.G. Litvan, American Society for Testing and Materials, pp. 509-519, 1980.

[20] Kong, Jin Au, *Electromagnetic wave theory*, 2nd edition, Wiley, New York, 1990.

[21] *Labtech Notebook Reference Manual*, Laboratory Technologies Corporation, Wilmington Massachusetts, 1992.

[22] Leung, C.K.Y. and T. Pheeraphan, "Very high early strength of microwave cured concrete," *Cement and Concrete Research*, Vol. 25, No. 1, pp. 136-146, 1995.

[23] Leung, C.K.Y. and T. Pheeraphan, "Microwave curing of concrete: experimental results and feasibility for practical applications," *Construction and Building Materials*, Vol. 9, No. 2, pp. 67-73, 1995.

[24] Litvan, G.G., "Freeze-thaw durability of porous building materials," *Durability of Building Materials and Components, ASTM STP 691*, edited by P.J. Sereda and G.G. Litvan, American Society for Testing and Materials, pp. 455-463, 1980.

[25] Liu, F. I. Turner, and M. Bialkowski, "A finite-difference time-domain simulation of power density distribution in a dielectric loaded microwave cavity," *Journal of Microwave Power and Electromagnetic Energy*, Vol. 29, No. 3, pp. 138-148, 1994.

[26] mcIntosh, J.D., "Electrical curing of concrete," *Magazine of Concrete Research*, Vol. 1, No. 1, pp. 21-28, Jan 1949.

[27] Mehta, P. Kumar, *Concrete: Structure, Properties, and Materials*, 2nd edition, Prentice-Hall Inc., 1993.

[28] Metaxas, A.C. and R.J. Meredith, *Industrial Microwave Heating*, Peter Peregrinus Ltd., London, 1983.

[29] Mindess, Sidney, and J. Francis Young, *Concrete*, Prentice-Hall, Inc. Englewood Cliffs, New Jersey, 1981.

[30] Minkowycz, W.J., E.M. Sparrow, G.E. Schneider, and R.H. Pletcher, *Handbook of numerical heat transfer*, John Wiley & Sons, Inc., 1988.

[31] Mur, G., "Absorbing boundary conditions for the finite-difference approximation of the time-domain electromagnetic-field equations," *IEEE Transactions on Electromagnetic Compatibility*, Vol. EMC-23, No. 4, pp. 377-382, Nov. 1981.

[32] Neville, A.M., *Properties of Concrete*, Longman Singapore Publishers, 3rd edition, 1981.

[33] Neas, E.D. and M.J. Collins, "Microwave heating: Theoretical concepts and equipment design," *Introduction to microwave sample preparation:theory and practice*, edited by H.M. Kingston and L.B. Jassie, ACS professional reference book, pp. 7-32, 1988.

[34] Nurse, R.W., "Stream curing of concrete," *Magazine of Concrete Research*, Vol. 1, No. 2, pp. 79-88, June 1949.

[35] Pheeraphan, Thanakorn, "Microwave Curing of Cementitious Materials,"S.M.C.E., Thesis, Dept. of Civil and Environmental Engineering, M.I.T., 1993.

[36] Pigeon, M., J. Prevost, and J.-M. Simard, "Freeze-thaw durability versus freezing rate," *Journal of the American Concrete Institute*, Vol. 82, No. 5, pp. 684-692, Sept.-Oct. 1985.

[37] Pigeon, M., R. Pleau, and P.-C. Aïtcin, "Freeze-thaw durability of concrete with and without silica fume in ASTM C666 (Procedure A) Test Method: internal cracking and scaling," *Cement, Concrete, and Aggregates*, CCAGDP, Vol. 8, No. 2, pp. 76-85, Winter 1986.

[38] Pigeon, M., R. Gagné, and C. Foy, "Critical air-void spacing factors for low water-cement ratio concretes with and without condensed silica fume," *Cement and Concrete Research*, Vol. 17, No. 6, pp. 896-906, 1987.

[39] Rhim, Hong C., "Nondestructive evaluation of concrete using wideband microwave techniques," Ph.D., Thesis, Dept. of Civil and Environmental Engineering, M.I.T., Feb 1995.

[40] Rodway, Lloyd E., "Durability of concrete," *Cement, Concrete, and Aggregates*, CCAGDP, Vol. 7, No. 1, pp. 43-48, Summer 1985.

[41] Saul, A.G.A., "Principles underlying the stream curing of concrete at atmospheric pressure," *Magazine of Concrete Research*, Vol. 2, No. 6, pp. 127-140, March 1951.

[42] Schmidt, F.W., R.E. Henderson, and C.H. Wolgemuth, *Introduction to Thermal Sciences*, 2nd edition, John Wiley & Sons, p. 455, 1993.

[43] Shen, Liang Chi and Jin Au Kong, *Applied Electromagnetism,* Brooks/Cole Engineering Division, 1983.

[44] Soroka, I., *Portland Cement Paste and Concrete*, The Macmillan Press Ltd, 1979.

[45] Sutton, Willard H., "Microwave Processing of Ceramic Materials," *Ceramic Bulletin*, Vol. 68, No. 2, pp. 376-386, 1989

[46] Taflove, A., "Review of the formulation and applications of the finite-difference time-domain method for numerical modeling of electromagnetic wave interactions with arbitrary structures," *Wave Motion*, Vol. 10, pp. 547-582, 1988.

[47] Taflove, A., *Computational Electrodynamics: The Finite-Difference Time-Domain Method*, Artech House, Inc., Boston, 1995.

[48] Taflove, A., and M.E. Brodwin, "Numerical solution of steady-state electromagnetic scattering problems using the time-dependent Maxwell's equations," *IEEE Transactions on Microwave Theory and Techniques*, Vol. MTT-23, No. 8, pp. 623-630, August 1975.

[49] Thuéry, Jacques, *Microwaves: Industrial, Scientific, and Medical Applications*, edited by E.H. Grant, Artech House, Inc., 1992.

[50] Volz, C.K., R.L. Tucker, N.H. Burns, and H.S. Lew, "Maturity effects on concrete strength," *Cement and Concrete Research*, Vol. 11, No. 1, pp. 41-50, 1981.

[51] Voss, W.A.G. and T. Greenwood-Madsen, "Brief communication: A simple instrument for measuring microwave oven power," *Journal of Microwave Power and Electromagnetic Energy*, Vol. 22, No. 4, pp. 209-211, 1987.

[52] Wu, Xuequan, Jianbgo Dong, and Mingshu Tang , "Microwave Curing Technique in Concrete Manufacture," *Cement and Concrete Research*, Vol. 17, pp. 205-210, 1987.

[53] Yee, K.S., "Numerical solution of initial boundary value problems involving Maxwell's equations in isotropic media," *IEEE Transactions on Antennas and Propagation*, Vol. AP-14, No. 3, pp. 302-307, May 1966.

5646-64